NASA TECHNICAL NOTE

NASA TN D-8235

NASA TN D-8235 c.1

WIND-TUNNEL INVESTIGATION OF AERODYNAMIC PERFORMANCE, STEADY AND VIBRATORY LOADS, SURFACE TEMPERATURES, AND ACOUSTIC CHARACTERISTICS OF A LARGE-SCALE TWIN-ENGINE UPPER-SURFACE BLOWN JET-FLAP CONFIGURATION

Staff of Langley Research Center

Langley Research Center
Hampton, Va. 23665

NATIONAL AERONAUTICS AND SPACE ADMINISTRATION • WASHINGTON, D. C. • NOVEMBER 1976

1. Report No.	2. Government Accession No.	3. Recipient's Catalog No.
NASA TN D-8235		

4. Title and Subtitle	5. Report Date
WIND-TUNNEL INVESTIGATION OF AERODYNAMIC PERFORMANCE, STEADY AND VIBRATORY LOADS, SURFACE TEMPERATURES, AND ACOUSTIC CHARACTERISTICS OF A LARGE-SCALE TWIN-ENGINE UPPER-SURFACE BLOWN JET-FLAP CONFIGURATION	November 1976
	6. Performing Organization Code
7. Author(s)	8. Performing Organization Report No.
Staff of Langley Research Center	L-10753
	10. Work Unit No.
9. Performing Organization Name and Address	505-10-44-01
NASA Langley Research Center Hampton, Va. 23665	11. Contract or Grant No.
	13. Type of Report and Period Covered
12. Sponsoring Agency Name and Address	Technical Note
National Aeronautics and Space Administration Washington, D.C. 20546	14. Sponsoring Agency Code

15. Supplementary Notes

16. Abstract

This report contains the results of a wind-tunnel investigation conducted in the Langley full-scale tunnel to determine the aerodynamic performance, steady and vibratory aerodynamic loads, surface temperatures, and acoustic characteristics of a large-scale twin-engine upper-surface blown jet-flap configuration. The investigation was conducted by the staff of Langley Research Center and the results are presented in four parts, each part covering one aspect of the study. The first and second parts of the report cover the aerodynamic performance and steady aerodynamic loads, respectively. The third part deals with temperatures and vibratory loads caused by jet impingement on the wing, and the fourth part presents the acoustic characteristics of the model.

17. Key Words (Suggested by Author(s))	18. Distribution Statement
Aerodynamic characteristics Static and vibratory loads Acoustic characteristics Upper-surface blowing	FEDD Distribution Subject Category 02

19. Security Classif. (of this report)	20. Security Classif. (of this page)	21. No. of Pages	22. Price*
Unclassified	Unclassified	152	

FEDD DOCUMENT

IT SHOULD BE NOTED THAT THIS DOCUMENT BEARS THE LABEL FEDD WHICH IS AN ACRONYM FOR "FOR EARLY DOMESTIC DISSEMINATION." THE FEDD LABEL IS AFFIXED TO DOCUMENTS WHICH MAY CONTAIN INFORMATION HAVING HIGH COMMERCIAL POTENTIAL.

THE FEDD CONCEPT DEVELOPED AS A RESULT OF THE DESIRE TO MAINTAIN U.S. LEADERSHIP IN WORLD TRADE MARKETS AND THUS ENCOURAGE A FAVORABLE BALANCE OF TRADE. READY AVAILABILITY OF U.S. TECHNOLOGY TO FOREIGN BUSINESS INTERESTS COULD REPRESENT AN UNFAIR COMPETITIVE ADVANTAGE FOR THEM IF THEY RECEIVE THE RESULTS OF U.S. TAX-SUPPORTED TECHNOLOGY AT THE SAME TIME AS OUR OWN BUSINESS INTERESTS. FOR THIS REASON, RESEARCH RESULTS THAT MAY HAVE HIGH COMMERCIAL POTENTIAL ARE BEING DISTRIBUTED TO U.S. OWNED AND MANAGED INDUSTRY AT THE EARLIEST POSSIBLE TIME AND IN ADVANCE OF GENERAL RELEASE.

IT IS THUS REQUIRED THAT THE RECIPIENT OF THIS REPORT TREAT THE INFORMATION ACCORDING TO THE CONDITIONS OF THE FEDD LABEL ON THE FRONT COVER.

CONTENTS

WIND-TUNNEL INVESTIGATION OF AERODYNAMIC PERFORMANCE, STEADY AND VIBRATORY LOADS, SURFACE TEMPERATURES, AND ACOUSTIC CHARACTERISTICS OF A LARGE-SCALE TWIN-ENGINE UPPER-SURFACE BLOWN JET-FLAP CONFIGURATION

Staff of Langley Research Center

SUMMARY

This report contains the results of a wind-tunnel investigation conducted in the Langley full-scale tunnel to determine the aerodynamic performance, steady and vibratory aerodynamic loads, surface temperatures, and acoustic characteristics of a large-scale twin-engine upper-surface blown jet-flap configuration. The investigation was conducted by the staff of Langley Research Center and the results are presented in four parts, each part covering one aspect of the study. The first and second parts of the report cover the aerodynamic performance and steady aerodynamic loads, respectively. The third part deals with temperatures and vibratory loads caused by jet impingement on the wing, and the fourth part presents the acoustic characteristics of the model.

INTRODUCTION

There is considerable interest in the upper-surface blown (USB) jet-flap concept as a means of achieving the high lift necessary for efficient powered-lift operations while providing acceptable noise levels in the airport terminal area through using the wing as a shield to diminish some of the engine noise. Recent aerodynamic and noise studies of the concept show promising results in both areas. The USB concept produces high lift by exhausting the jet-engine efflux above the wing in such a manner that it becomes attached to the wing upper surface and turns downward over a trailing-edge flap. Although the results of previous investigations of the USB concept have been encouraging, the work, in general, was conducted with small models using cold jet engine simulators which cannot be used to obtain information on the environment of the wing upper surface regarding temperature effects. Since this information is considered to be extremely important for the design of USB configurations, the present investigation was undertaken to provide fundamental information on aerodynamic loads and temperatures on the wing of a large-scale USB configuration powered with actual turbofan engines. The investigation also included

tests to determine the acoustic characteristics of the model. The main purpose of the aerodynamic tests was to provide a reference base for relating the measured temperature and loads information and also for providing a convenient reference for application of the results to other USB configurations. The investigation was conducted by the staff of Langley Research Center and the results are presented in four parts covering areas of (1) aerodynamic performance, (2) static pressures and loads, (3) temperatures and vibratory loads, and (4) acoustic characteristics.

The model had a full-span leading-edge Krueger flap equipped with boundary-layer control (BLC) and three spanwise trailing-edge flap segments – an inboard USB flap located behind the engine, a double-slotted midspan flap, and a drooped aileron equipped with blowing BLC. Two Pratt & Whitney Aircraft of Canada Limited JT15D-1 turbofan engines used to power the model were equipped with rectangular nozzles having an aspect ratio (width/height) of 6.0. The internal contour of the nozzle exit was designed so that the exhaust flow was deflected slightly downward toward the top of the wing to insure that the jet sheet was attached to the upper surface of the wing. Most of the tests were made with a deflector attached to the nozzle to improve the spreading and turning of the jet exhaust.

The aerodynamic information presented herein was obtained by means of static force tests in the Langley full-scale tunnel. The tests were made over an angle-of-attack range from -6° to 28°, a thrust-coefficient range from 0 to 4, flap deflections of 32° and 72°, and symmetrical and asymmetrical (one engine inoperative) power conditions. The investigation also included tests to determine the effects of BLC at the leading edge of the wing and the ailerons. In addition to the wind-on force tests, static tests were conducted to measure the static turning performance of the USB jet-flap system. All data in the investigation were obtained for the model with the horizontal and vertical tails off.

The model was instrumented with static-pressure orifices for measuring the static-pressure distribution on the fuselage and wing, including the leading-edge and trailing-edge flaps. The static-pressure data were used to evaluate the steady aerodynamic loads acting on the wing. The effects of one engine inoperative on the pressure distribution on the wing were also determined.

One of the major objectives of the investigation was to obtain basic information to help in establishing the structural environment on the wing and flaps caused by using turbofan engines in the USB jet-flap concept. To accomplish this objective, the wing and flaps were instrumented with experimental dual-sensing transducers. Each transducer unit included a fluctuating pressure gage, a vibratory accelerometer, and a surface-mounted chromel-alumel thermocouple. It was anticipated that the transducers on the flap would be subjected to both high temperatures and high vibration levels. Therefore, a

new transducer designed to withstand the temperatures and to compensate for the vibrations was selected. Unfortunately, the pressure transducer proved to be unsatisfactory because of sensitivity drift (probably due to the high temperatures). This problem of sensitivity drift made it impossible to obtain even relative levels of pressure or to separate the signal due to fluctuating pressure from that due to vibration of the transducer. However, data were obtained on the temperatures and vibratory accelerations on the wing and flaps.

Acoustic tests were made to provide baseline noise data for a large-scale USB configuration having real turbofan engines. These tests included noise directivity and spectral content measurements for various flap configurations and various engine thrust settings.

I. AERODYNAMIC PERFORMANCE

Charles C. Smith, Jr., James P. Shivers,
and William G. Sewall

SUMMARY

The results of static force tests showed that the aerodynamic performance of the large-scale model with hot engine exhaust was generally similar to that obtained from small-scale models with cold-air jet-engine simulators in previous investigations; this indicates that the effects of Reynolds number and engine exhaust temperature on aerodynamic characteristics were relatively small. Full-span trailing-edge flaps were much more effective for achieving good high-lift performance than partial-span flaps alone. The use of leading-edge boundary-layer control (BLC) generally improved the overall aerodynamic performance of the model. Large rolling and yawing moments were introduced with one engine inoperative. The use of differential aileron deflection in combination with asymmetric BLC appeared to be a promising method of achieving roll trim for the engine-inoperative condition, but very high values of BLC are required for roll trim at high lift coefficients.

INTRODUCTION

This part of the report presents the results of wind-tunnel static force tests to determine the aerodynamic performance characteristics of a large-scale upper-surface blown (USB) jet-flap model. Previous investigations of the USB jet flap have shown this concept to have high aerodynamic efficiency and to provide some noise benefits because the engine noise is shielded by the wing (see refs. 1 to 6). The tests were performed over a range of angles of attack and thrust coefficients, for symmetrical power and one-engine-inoperative conditions, for two different trailing-edge flap deflections, and with and without blowing boundary-layer control on the wing leading edge and drooped ailerons. The longitudinal aerodynamic data are presented as plots of lift, drag, and pitching-moment coefficients as functions of angle of attack. The pitching-moment data are also plotted against lift coefficient, and drag polars are presented for performance analysis. Lateral-directional data in the form of side-force, yawing-moment, and rolling-moment coefficients are plotted against angle of attack to illustrate the engine-out trim problem and to show the effectiveness of various methods for providing trim.

SYMBOLS

Dimensional data were obtained in U.S. Customary Units and are presented herein in both the International System of Units (SI) and U.S. Customary Units. Conversion factors between the two systems are given in reference 7. The longitudinal aerodynamic data are referred to the wind-axis system and the lateral-directional aerodynamic data are referred to the body-axis system shown in figure 1. The data presented herein are referred to a center-of-gravity position of 25.30 percent of the mean aerodynamic chord (see fig. 2).

b	wing span, m (ft)
C_D	drag coefficient, $\frac{F_D}{q_\infty S}$
C_L	lift coefficient, $\frac{F_L}{q_\infty S}$
C_l	rolling-moment coefficient, $\frac{M_X}{q_\infty S b}$
C_m	pitching-moment coefficient, $\frac{M_Y}{q_\infty S \bar{c}}$
C_n	yawing-moment coefficient, $\frac{M_Z}{q_\infty S b}$
C_Y	side-force coefficient, $\frac{F_Y}{q_\infty S}$
C_μ	static thrust coefficient, $\frac{T}{q_\infty S}$
$C_{\mu,a}$	static thrust coefficient of boundary-layer-control system for drooped aileron
$C_{\mu,le}$	static thrust coefficient of boundary-layer-control system for wing leading edge

c_a aileron chord, measured in percent local wing chord

c_f flap chord, measured in percent local wing chord

$c_{f,le}$ leading-edge Krueger flap chord, measured in percent local wing chord

c_v vane chord, measured in percent local wing chord

c_w local wing chord, m (ft)

$\bar{c}$ wing mean aerodynamic chord, m (ft)

F_A axial force, N (lb)

F_D drag force, N (lb)

F_L lift force, N (lb)

F_N normal force, N (lb)

F_X, F_Y, F_Z forces along X, Y, and Z body axes, N (lb)

M_X rolling moment, m-N (ft-lb)

M_Y pitching moment, m-N (ft-lb)

M_Z yawing moment, m-N (ft-lb)

q_∞ free-stream dynamic pressure, Pa (lb/ft^2)

S wing area, m^2 (ft^2)

T static thrust force, N (lb)

W model weight, N (lb)

X,Y,Z body reference axes (see fig. 1)

x,y,z	rectangular Cartesian coordinates, m (ft)
α	angle of attack, deg (see fig. 1)
β	angle of sideslip, deg
δ_a	aileron deflection, deg
δ_f	deflection of USB and double-slotted flap (deflected together), deg (see figs. 2 and 3)
δ_j	static-thrust jet deflection, $\tan^{-1}\frac{F_N}{F_A}$, deg
δ_s	spoiler deflection, deg
δ_v	vane deflection, deg (see fig. 4)
γ	flight-path angle, positive for climb, deg
η	static-thrust recovery efficiency, $\frac{\sqrt{F_A^2 + F_N^2}}{T}$

Subscripts:

L	left
l	lower
le	leading edge
R	right
u	upper

Abbreviations:

BLC	boundary-layer control

L.E. leading edge

USB upper-surface blown

WRP wing reference plane

MODEL AND APPARATUS

The investigation was conducted in the 9.12- by 18.3-m (30- by 60-ft) open-throat test section of the Langley full-scale tunnel. Figure 1 shows the body axis system, and figure 2 shows a three-view drawing of the model. Photographs showing the model and the test setup in the Langley full-scale tunnel are presented in figure 3. The model was assembled largely from components of an existing high-wing airplane configuration.

Dimensional characteristics of the model are given in figure 2 and details of the high-lift devices are shown in figure 4. A full-span Krueger flap with a chord equal to 20 percent of the wing chord and a slot for blowing BLC (see fig. 4(a)) was fitted to the leading edge of the wing and set at a deflection of 76^{o} for all tests. The coordinates of the Krueger flap are given in table I. The trailing edge of the wing consisted of three spanwise elements: an inboard USB flap located behind the engine, a midspan double-slotted flap, and ailerons which could be drooped and used as an outboard flap. The inboard flap was covered with a single sheet of metal which was curved so that it conformed to the curvature of the upper surface of the double-slotted flap (see Coanda flap in fig. 4(b)). The inboard flap provided a smooth, large-radius, continuously curved upper surface to enhance the turning of the engine exhaust jet. (See figs. 2 and 4(b).) The inboard flap extended from the side of the fuselage to a station 1.0 nozzle width outboard of the nozzle centerline. The coordinates of the double-slotted flap are given in table II and the gaps, overlaps, and deflections are given in figure 4(a). The coordinates for the ailerons are given in table III. The wing was equipped with two different spoiler arrangements. For one arrangement, a tip spoiler was used which extended spanwise from the inboard aileron station to the wing tip. For the other arrangement, a spoiler was used which extended from the inboard (USB) flap station to the wing tip. These spoiler arrangements and dimensional characteristics are shown in figures 2 and 4(a).

Presented in figure 4(c) are details of a modification that was made to the lower fuselage contour directly aft of the trailing edge of the inboard flap. This modification consisted of a rectangular metal panel which was riveted to the fuselage such that the lower fuselage cross section was rectangular instead of oval. This modification formed a flat surface having a sharp edge in an attempt to prevent the exhaust flow from attaching to the fuselage and turning inboard and beneath the fuselage.

The model was powered by two Pratt & Whitney Aircraft of Canada Limited JT15D-1 turbofan engines mounted in nacelles located high on the wing so that the engine exhaust passed over the upper surfaces of the wing and flaps. The JT15D-1 engine is rated by the manufacturer as having a maximum uninstalled thrust of 9680 N (2200 lb), a fan flow bypass ratio of 3.34, and a fan pressure ratio of 1.36 for standard sea-level conditions at a Mach number of 0. The engine installation and nacelle are given in figure 5. The engine inlets were fitted with acoustical treatment (a liner plus two absorber rings) shown in figures 5 and 6. The engine acoustical treatment was obtained from previous investigations conducted with the JT15D-1 engines. The secondary nozzle (cold-air nozzle) was designed to deflect the jet down on the wing to provide spreading of the jet and attached flow for better turning over the wing and flap (see fig. 5). The secondary nozzle exit was rectangular and had an aspect ratio (width/height) of 6.0. Most of the tests were made with a deflector attached to the nozzle to improve the spreading and turning of the jet exhaust (see figs. 5 and 7). Internal contours for the secondary nozzle are presented in figure 8. The primary nozzle (hot-gas nozzle) was mounted inside the secondary nozzle, had an elliptical exit, and was approximately 1 fan diameter upstream of the secondary nozzle exit (see fig. 5).

TESTS AND PROCEDURES

Wind-Off Tests

In preparation for testing, calibrations of the engines were made to determine the installed static thrust of each engine over the thrust range with and without deflectors on the nozzles. The thrust calibrations were obtained as a function of nozzle exit dynamic pressure with the engines installed on the model in the test section of the Langley full-scale tunnel. In order to prevent the jet exhaust from turning over the wing and flap, a thrust calibration deflector was mounted on the wing directly behind each engine (see fig. 9). The thrust was then determined from the resultant-force readings on the full-scale tunnel scales.

Static-thrust jet deflection angles and thrust-recovery efficiencies were determined from measurements of lift and drag forces for two values of thrust coefficient and for flap settings of 32° and 72°. The static thrust used in computing recovery efficiency was taken directly from the engine calibrations at the appropriate nozzle exit pressure.

Wind-On Tests

Powered wind-on tests were conducted by setting the nozzle exit dynamic pressure to give the desired thrust and holding this pressure constant over an angle-of-attack range. The tests were made for an angle-of-attack range from -6° to 28° and a thrust-coefficient range from 0 to 4.

The longitudinal and lateral-directional aerodynamic characteristics of the model were measured for trailing-edge flap deflections of 32^{o} and 72^{o} with the leading-edge Krueger flap deflected 76^{o}. Included in the investigation were tests to determine the effect of drooped ailerons with BLC in combination with the trailing-edge flap.

Tests to determine the effect of BLC were made by applying boundary-layer blowing at the wing leading edge and at the ailerons. The BLC for the ailerons was used only when the ailerons were drooped. The thrust coefficients of the BLC systems were determined by measuring the static-thrust force produced by the BLC slots for each system in the wind-off condition. Values of the BLC thrust coefficients were 0.013 at the leading edge and 0.021 at the ailerons for symmetrical power conditions. For the engine-inoperative condition, BLC was used asymmetrically with values of 0.015 at the leading edge and 0.030 at the aileron of the engine-inoperative wing, and no BLC was used on the engine-operative wing.

The wind-on tests were made by setting the nominal dynamic pressure range from 82.24 to 166.88 N/m^2 (1.72 to 3.49 lb/ft^2) which corresponds to velocities of 11.59 to 16.82 m/sec (38.03 to 55.17 ft/sec) and Reynolds numbers of 1.575×10^6 to 2.285×10^6 based on the wing mean aerodynamic chord. Jet-boundary-interference corrections caused moderate adjustments to these nominal values, and corrected values were used in reducing the data.

CORRECTIONS

The data were corrected for interference induced by the wind-tunnel jet boundary by using the methods of references 8 and 9. The point at which the model pivoted as the angle of attack was changed caused the wing location relative to the ground plane to vary slightly with angle of attack; this movement has been accounted for in the correction calculations. The correction to angle of attack was found to be small and negative. The dynamic-pressure correction due to the effects of the tunnel boundary was as large as 12 percent for some test conditions.

The model had no horizontal tail; therefore, no corrections were applied to the pitching-moment data other than the overall changes in angle of attack and dynamic pressure. Since the test procedure was to hold the reference engine thrust constant during an angle of attack run and since the corrected dynamic pressure varied during each run, the values of C_μ (thrust coefficient) were found to vary considerably from low to high angle of attack in the basic corrected data. The data presented herein were obtained by interpolation of the basic corrected data for constant values of C_μ.

RESULTS AND DISCUSSION

Longitudinal Aerodynamic Characteristics

Wind-off.- One problem detected in preliminary static turning tests was that the exhaust flow, after leaving the USB flap, attached to the side of the fuselage and turned inward. This problem resulted in poor turning characteristics and, for the engine-out condition, produced side-force and yawing-moment characteristics which aggravated the engine-out condition. As shown in figure 4(c), the lower portion of the fuselage was modified with a rectangular panel to provide a flat surface having a sharp edge in an attempt to prevent the exhaust flow from attaching to the fuselage. With this modification installed, the exhaust flow followed the USB flap and was deflected downward without attaching to the fuselage. All data were recorded with these panels installed.

The results of tests to determine the static turning efficiency and turning angle are presented in figure 10 as a plot of the ratio of lift force to thrust F_L/T as a function of the ratio of drag force to thrust $-F_D/T$. The values of thrust for figure 10 were determined from static tests using the thrust calibration deflector shown in figure 9. Data for the landing flap condition $(\delta_f = 72^o)$ with nozzle deflectors off and on are presented in figure 10(a); data for the take-off flap condition $(\delta_f = 32^o)$ with nozzle deflectors on are presented in figure 10(b). The data show that the use of the nozzle deflector in the landing flap condition increased the turning from about 50^o to about 56^o, but reduced the efficiency from about 92 percent to 87 percent. Because the addition of the deflector increased the static turning for a given flap setting, all subsequent tests were made with the deflectors on unless otherwise noted. The take-off flap setting shows excellent turning performance with a turning angle slightly greater than the upper surface angle of the flap and an efficiency of about 98 percent. The data for the take-off flap setting are shown for a C_μ of 2 since this value of C_μ is generally representative of that for take-off powered-lift operation.

Wind-on.- The basic longitudinal aerodynamic characteristics of the model in the landing configuration are presented in figures 11 and 12. The data of figure 11 show that an increase in thrust coefficient caused the usual increases in lift, lift-curve slope, maximum lift coefficient, stall angle of attack, and negative pitching moments associated with powered-lift operation. The lift performance of the large-scale model with real turbofan engines was generally similar to that obtained from small-scale models using cold-air jet-engine simulators in previous investigations; this indicates that the aerodynamic effects of Reynolds number and engine exhaust temperature were relatively small in the present investigation. (For example, see refs. 1 to 4.)

One significant point to note in the lift-drag polar on the right-hand side of figure 11 is that the basic landing configuration had limited descent capability. For example, at an

approach lift coefficient of 4.0, the angle of attack corresponding to a glide slope of 7.5° is about 20°, which results in essentially no stall margin. The more appropriate angles of attack for approach to insure safety of flight (from $\alpha = 0^{\circ}$ to 10°) are seen to give negative values of C_D (climb conditions). A comparison of the data of figures 11 and 12(a) shows that the addition of the nozzle deflectors reduced the angle of attack for approach $\left(C_L = 4.0\right)$ to about 10° for the 7.5° glide-slope condition. This lower angle of attack for approach provides an adequate stall margin for safety of flight. The improvement in descent capability with the deflectors on is to be expected, based on the increase in jet turning angle provided by the addition of the deflectors as indicated in figure 10(a). The data in figure 12(b) show the aerodynamic characteristics of the landing configuration with the ailerons drooped 50° and with BLC on the ailerons to insure attached flow. A comparison of figures 12(a) and 12(b) shows that the drooped ailerons provided an increase in lift coefficient and provided even more descent capability than was provided by the nozzle deflectors alone. A comparison of the data of figures 12(b) and 12(c) shows that the addition of full-span leading-edge blowing and increased aileron blowing generally provided an increase in lift coefficient at high angles of attack, an indication that leading-edge stall was delayed to a higher angle of attack.

An important point to be noted regarding the lift-coefficient data in figures 11 and 12 is that a change in the lift-curve slope occurred at very low angles of attack, even with full-span leading-edge blowing. This break in the lift-curve slope possibly could be associated with a flow-separation problem on the fuselage and wing between the nacelles. This point is indicated in the tuft photographs presented in figure 13. A close examination of the tufts on the nacelle, fuselage, and wing between the nacelles shows that the airflow was badly disturbed at relatively low angles of attack, apparently because of the close proximity of the nacelles to the fuselage. It appeared from close observation of the tufts that the airflow between the nacelles was turned upward at a very steep angle and a vortex was formed at the wing-fuselage junction. Such a flow field could prove to be very detrimental to the lift carryover from one wing panel to another in the one-engine-inoperative condition and to the spanwise lift distribution for the symmetrical power condition. Recent unpublished data (obtained in the Langley full-scale tunnel) indicated that the addition of a leading-edge Krueger flap in combination with leading-edge boundary-layer control provided much-improved flow conditions between the nacelles and fuselage and gave improvements in the longitudinal aerodynamic characteristics.

Presented in figure 14 is the performance of the model in the landing configuration $\left(\delta_f = 72^{\circ}\right)$ in terms of flight-path angle plotted against trimmed-lift coefficient based on the data of figure 12(c). From figure 14 it can be seen that a landing approach could be made at a lift coefficient of 4 along a glide slope of 7.5° with a thrust-weight ratio of 0.21 and a stall margin of about 19°. In the event of an engine failure, the configuration would

require a thrust-weight ratio of 0.375 (one engine inoperative) to arrest the descent and maintain level flight. There are no certified requirements at this time for powered-lift operation; but, if it is assumed that the configuration must be able to fly in level flight without changing the approach flap setting, then a two-engine powered-lift airplane such as the test configuration would require an installed thrust-weight ratio of at least 0.75 for safe flight operation. It should be emphasized that the flight-envelope data presented in figure 14 give only approximate thrust requirements for the engine-out condition because performance penalties introduced for engine-out operation and roll trim are not taken into account. The installed thrust-weight ratio requirements indicated by the data of figure 14 are therefore somewhat conservative and should be used primarily for establishing general performance trends only.

Presented in figures 15(a) to 15(e) are the longitudinal aerodynamic characteristics of the model with the flaps set at $\delta_f = 32^o$ for the take-off condition. The data of figure 15 show, in general, that the effects of boundary-layer control at the wing leading edge and with drooped ailerons provided improvements in performance generally similar to those shown for the landing condition (fig. 12). That is, the data show that an increase in thrust coefficient produced increases in lift, lift-curve slope, maximum lift coefficient, stall angle of attack, and negative pitching moments. The use of BLC at the wing leading edge gave an improvement in the stall characteristics whereas aileron BLC generally improved the lift at the lower angles of attack. The combination of BLC at the wing leading edge and ailerons appeared to give the best performance in that the beneficial effects of each were additive, with the result that the lift characteristics of the basic configuration were improved over the angle-of-attack range.

Presented in figure 16 are the lift-drag data of figure 15(e) summarized in terms of flight-path angle plotted against trim-lift coefficient. As pointed out in the discussion of the characteristics of the landing configuration, this particular configuration would require a thrust-weight ratio of at least 0.75 in order to arrest the descent with one engine inoperative, assuming an approach at a lift coefficient of 4.0 without changing landing flap position. The data in figure 16 show that with this high thrust-weight ratio, a climb angle of about 6^o could be maintained for the take-off configuration with one engine inoperative $\left(\text{indicated by the circle at } T/W = 0.375 \text{ and } C_{L,trim} = 4.0\right)$. The data of figure 15 show that the stall angle of attack was above 25^o, indicating that the performance data of figure 16 are well within the angle-of-attack stall margin for safe flight operation. It should be emphasized that the take-off performance estimates of figure 16 do not take into account the penalties introduced for engine-out operation or roll trim. The data are therefore somewhat conservative and should be used for establishing general performance trends only.

Lateral-Directional Characteristics With One Engine Inoperative

Basic lateral-directional characteristics obtained for the configuration with one engine inoperative are presented in figures 17 to 19 for the landing condition and in figure 20 for the take-off condition. Since loss of an engine results in loss of lift in a powered-lift system, plots of the lateral characteristics with one engine inoperative are accompanied by plots of the corresponding longitudinal aerodynamic characteristics.

The data in figure 17(a) show that, as expected, large positive rolling moments and yawing moments existed for the configuration with the right engine inoperative. These data also show that the moments with one engine inoperative increased abruptly in value near $\alpha = 15^{\circ}$. The longitudinal aerodynamic data in figure 17(b) show that the configuration stalled near $\alpha = 15^{\circ}$; the abrupt increase in moments with one engine inoperative in figure 17(a) is therefore probably associated with early stall of the engine-out wing. A comparison of figures 17 and 18 shows that the use of symmetrical BLC on the wing leading edge and aileron delayed the wing stall, and the accompanying abrupt increases in rolling-moment and yawing-moment asymmetries, to a higher angle of attack. Figure 19 presents data for the configuration with flap slots open behind the inoperative engine. A comparison of the data in figures 19(a) and 19(b) with the data in figures 18(a) and 18(b) shows that opening the slots behind the inoperative engine produced only minor improvements in the longitudinal and lateral-directional characteristics.

The data in figures 20(a) and 20(b) show that the out-of-trim moments for the engine inoperative case were also large for the take-off condition, with the yawing moments generally being somewhat greater and the rolling moments somewhat less than those of the landing configuration (fig. 18).

Presented in figures 21 to 24 are data obtained with differential flap and/or aileron deflection and asymmetrical BLC in attempts to achieve roll trim for the one-engine-inoperative condition. The data in figure 21(a) show that the use of differential aileron deflection in combination with increased BLC on the engine-inoperative wing and no BLC on the engine-operative wing essentially provided roll trim for $C_{\mu} = 1.0$ and reduced the engine-out rolling moments for $C_{\mu} = 2.0$ by about one-half (compare figs. 17(a) and 21(a)). Figure 22 shows data obtained after the addition of a wing-tip spoiler (see fig. 2) to the model with differential ailerons and asymmetrical BLC. A comparison of the data in figures 21(a) and 22(a) shows that the tip spoiler provided very little additional roll trim. Figure 23(a) shows results for the configuration with differential midspan flaps and open flap slots behind the inoperative engine in combination with differential aileron deflection and asymmetrical BLC for attempted roll trim. A comparison of the data of figures 23(a) and 21(a) shows little effect on the roll-trim problem of differential midspan flaps and opening the flap slots behind the inoperative engines. A comparison of the data of figures 21 to 24 indicates that differential ailerons and asymmetrical BLC

(see fig. 21) were the most effective means of those investigated for counteracting the engine-out problem. On this basis, it would appear that an increase in BLC on the engine-inoperative wing above the values used $\left(C_{\mu,a} = 0.03, \quad C_{\mu,le} = 0.015\right)$ may be one method for providing roll trim at the higher lift coefficients. In tests of a 1/5-scale model of the present USB configuration with larger span ailerons (reported in ref. 4), it was found that the additional span of the ailerons was very beneficial in increasing the effectiveness of differential aileron deflection and asymmetrical BLC for roll control in the engine-inoperative condition.

The data of figure 24 show that the model with the take-off flaps produced engine-out moments that could not be trimmed with the amount of differential aileron deflection and asymmetrical BLC used in the tests. Preliminary analysis indicates that for engine-out roll trim of the take-off flap configuration, the asymmetrical BLC used in the tests would have to be increased by a factor of 2 or 3.

Spoiler Effectiveness With Symmetrical Power

Although no engine-out tests were made using the semispan spoiler (midspan and tip) for roll trim, some tests were made to determine the lateral and longitudinal characteristics of the model with symmetrical power and with the left semispan spoiler deflected 60°. The data of figure 25 show that increasing thrust had only small effects on the rolling and yawing moments produced by spoiler deflection. The data also show that the effectiveness of the spoiler remained about constant with increasing angle of attack up to about $\alpha = 20^{\circ}$, beyond which the rolling effectiveness of the spoiler decreased. A comparison of the rolling-moment data of figures 21 to 23 with those of figure 25 indicates that the use of the semispan spoiler in combination with the other methods of trim investigated may have provided the additional rolling moment required for trim at $C_{\mu} = 2.0$. It should be noted, however, that the lift losses associated with the use of the semispan spoiler are large. For example, a comparison of figures 12(b) and 25(b) indicates that the lift loss produced by the semispan spoiler was about 0.5 at $C_{\mu} = 2.0$.

SUMMARY OF RESULTS

A wind-tunnel investigation to measure the aerodynamic performance of a large-scale twin-engine upper-surface blown jet-flap model has produced the following results:

The lift performance of the large-scale model with real turbofan engines was generally similar to that obtained from small-scale models with cold-air jet-engine simulators in previous investigations; this indicates that the aerodynamic effects of Reynolds number and engine exhaust temperature were relatively small in the present investigation. Full-span trailing-edge flaps, which were simulated by the addition of drooped

ailerons and boundary-layer control (BLC) to the inboard flaps, were much more effective for achieving good high-lift performance than partial-span inboard flaps alone. The use of leading-edge boundary-layer control generally improved the overall lift performance of the model. Large rolling and yawing moments were introduced by engine-out operation. The use of differential aileron deflection in combination with asymmetrical BLC appeared to be the most promising method investigated for engine-out roll trim; but the results indicated that very high values of BLC will be required for roll trim at high lift coefficients.

REFERENCES

1. Phelps, Arthur E.; Letko, William; and Henderson, Robert L.: Low-Speed Wind-Tunnel Investigation of a Semispan STOL Jet Transport Wing-Body With an Upper-Surface Blown Jet Flap. NASA TN D-7183, 1973.

2. Phelps, Arthur E., III; and Smith, Charles C., Jr.: Wind-Tunnel Investigation of an Upper Surface Blown Jet-Flap Powered-Lift Configuration. NASA TN D-7399, 1973.

3. Smith, Charles C., Jr.; Phelps, Arthur E., III; and Copeland, W. Latham: Wind-Tunnel Investigation of a Large-Scale Semispan Model With an Unswept Wing and an Upper-Surface Blown Jet Flap. NASA TN D-7526, 1974.

4. Phelps, Arthur E., III: Wind-Tunnel Investigation of a Twin-Engine Straight-Wing Upper-Surface Blown Jet-Flap Configuration. NASA TN D-7778, 1975.

5. Reshotko, Meyer; Olsen, William A.; and Dorsch, Robert G.: Preliminary Noise Tests of the Engine-Over-the-Wing Concept. I. 30^{o}-60^{o} Flap Position. NASA TM X-68032, 1972.

6. Reshotko, Meyer; Olsen, William A.; and Dorsch, Robert G.: Preliminary Noise Tests of the Engine-Over-the-Wing Concept. II. 10^{o}-20^{o} Flap Position. NASA TM X-68104, 1972.

7. Mechtly, E. A.: The International System of Units – Physical Constants and Conversion Factors (Second Revision). NASA SP-7012, 1973.

8. Heyson, Harry H.: Use of Superposition in Digital Computers To Obtain Wind-Tunnel Interference Factors for Arbitrary Configurations, With Particular Reference to V/STOL Models. NASA TR R-302, 1969.

9. Heyson, Harry H.: FORTRAN Programs for Calculating Wind-Tunnel Boundary Interference. NASA TM X-1740, 1969.

TABLE I.- AIRFOIL COORDINATES FOR LEADING-EDGE KRUEGER FLAP

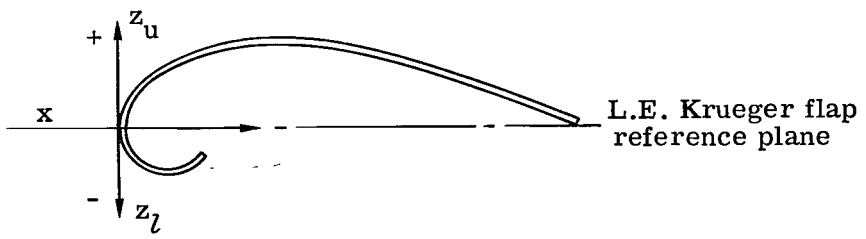

x, percent $c_{f,le}$	z_u, percent $c_{f,le}$	z_l, percent $c_{f,le}$
0	0	
2.50	5.590	-7.250
5.00	8.615	-9.125
10.00	12.075	-9.900
15.00	14.550	-8.475
20.00	16.550	
30.00	19.125	
40.00	19.975	
50.00	20.025	
60.00	18.650	
70.00	16.250	
80.00	12.650	
90.00	7.360	
100.00	0	

$c_{f,le} = 0.20c_w$

TABLE II.- COORDINATES OF DOUBLE-SLOTTED TRAILING-EDGE FLAPS

(a) Vane

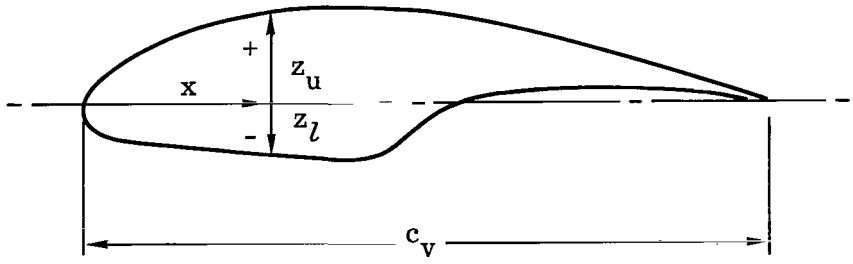

x, percent c_v	z_u, percent c_v	z_l, percent c_v
0	0	0
1.25	3.392	-2.167
2.50	4.715	-2.883
5.00	6.852	-3.739
7.25	8.412	-4.308
10.00	9.950	-4.761
20.00	12.925	-5.868
30.00	14.416	-6.852
40.00	14.743	-7.801
45.00	14.697	-5.664
50.00	14.298	-1.797
60.00	12.814	2.374
70.00	10.488	3.934
80.00	7.264	3.694
90.00	3.709	2.103
100.00	.203	0
$c_v = 0.18c_w$		

TABLE II.- Concluded

(b) Flap

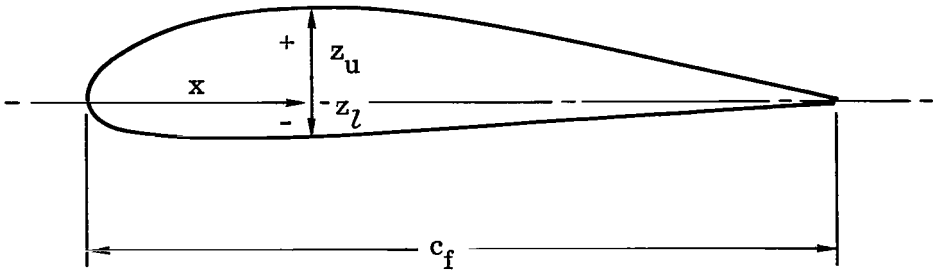

x, percent c_f	z_u, percent c_f	z_l, percent c_f
0	0	0
1.25	2.366	-1.670
2.50	3.444	-2.226
5.00	5.516	-2.783
7.25	6.491	-2.922
10.00	7.849	-2.957
20.00	10.925	-2.841
30.00	12.070	-2.676
40.00	12.348	-2.500
45.00	12.175	-2.370
50.00	11.862	-2.276
60.00	10.475	-2.087
70.00	8.077	-1.782
80.00	5.446	-1.465
90.00	2.844	-.976
100.00	.173	-.173
$c_f = 0.175c_w$		

TABLE III.- COORDINATES OF AILERON

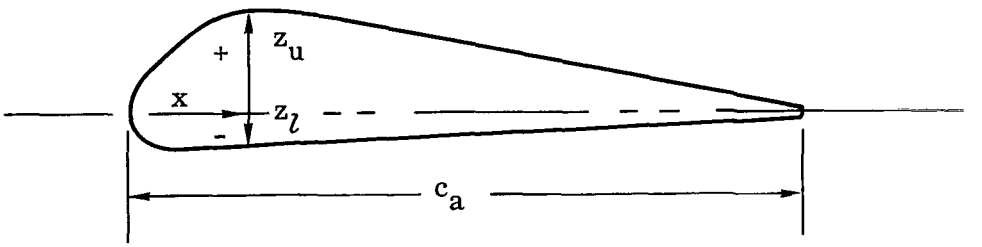

x, percent c_a	z_u, percent c_a	z_l, percent c_a
0	-0.0471	-0.0471
1.25	-.0067	-.0774
2.50	.0135	-.0875
5.00	.0397	-.0956
7.50	.0694	-.0956
10.00	.0875	-.0943
20.00	.1205	-.0842
25.00	.1131	-.0801
30.00	.1051	-.0741
40.00	.0909	-.0653
50.00	.0768	-.0545
60.00	.0606	-.0458
70.00	.0471	-.0337
80.00	.0330	-.0222
90.00	.0168	-.0128
100.00	.0034	-.0034
$c_a = 0.267c_w$		

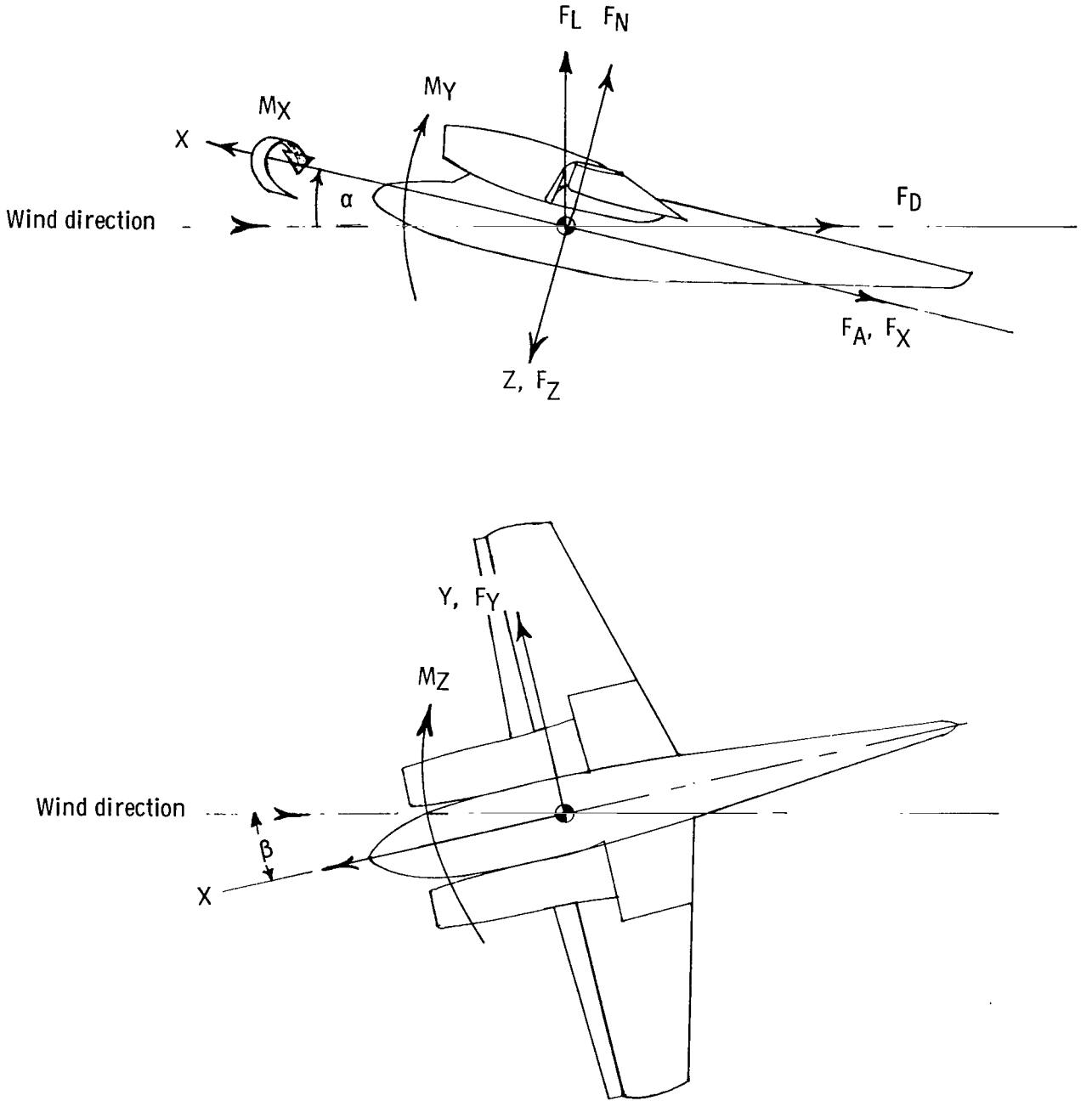

Figure 1.- Body-axis system. Arrows indicate positive direction of forces and moments.

DIMENSIONAL CHARACTERISTICS OF MODEL

Wing:	
Area, m^2 (ft^2)	19.75 (212.5)
Span, m (ft)	10.67 (35.0)
Mean aerodynamic chord, m (ft)	1.96 (6.42)
Incidence:	
Root, deg	3
Tip, deg	-0.17
Leading-edge sweep, deg	0
Taper ratio	0.47
Aspect ratio	5.76
Airfoil section:	
Root	NACA 23012
Tip	NACA 23012
Dihedral, deg	4
Root chord, m (ft)	2.54 (8.33)
Tip chord, m (ft)	1.19 (3.92)
Aileron chord, percent local wing chord	20
Flap:	
Span, percent wing span	60
Chord, percent wing chord	17.5
Vane chord, percent wing chord	18
Leading-edge flap:	
Span, percent wing span	62.9
Chord, percent wing chord	20
Engines:	
Spanwise location, percent wing span	16.9
Nozzles:	
Height, m (ft)	0.156 (0.52)
Width, m (ft)	0.940 (3.084)
Area, m^2 (ft^2)	0.147 (1.576)
Aspect ratio	6.0
Location of center of gravity, longitudinal distance from front of fuselage, m (ft)	4.0 (13.15)
Spoiler:	
Chordwise location, percent wing chord	0.66
Height, percent wing chord	0.104
Deflection angle, deg	60

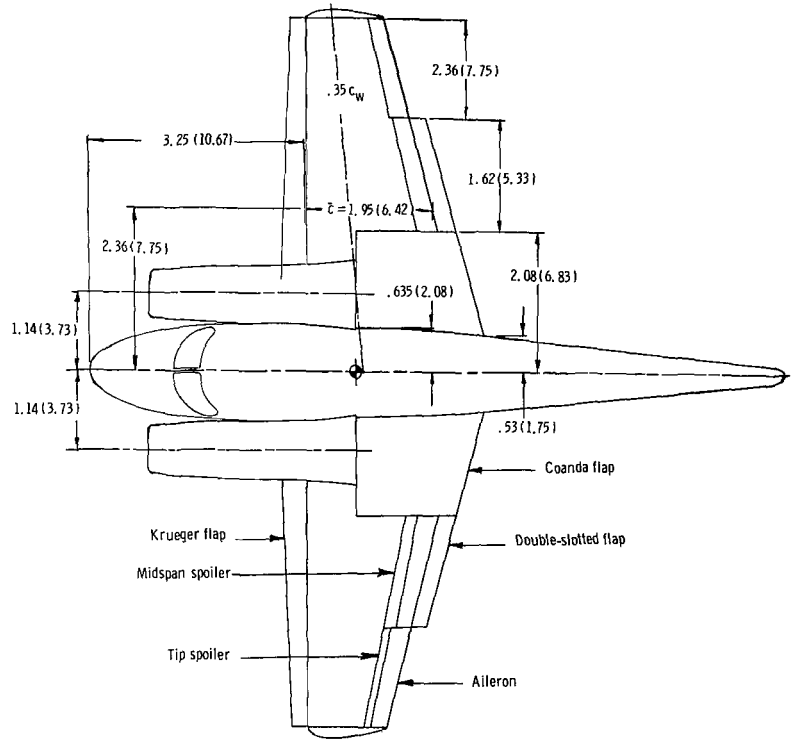

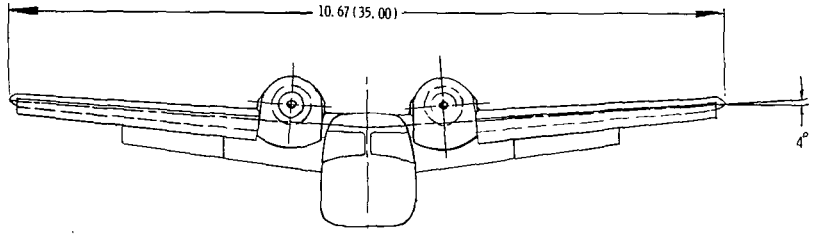

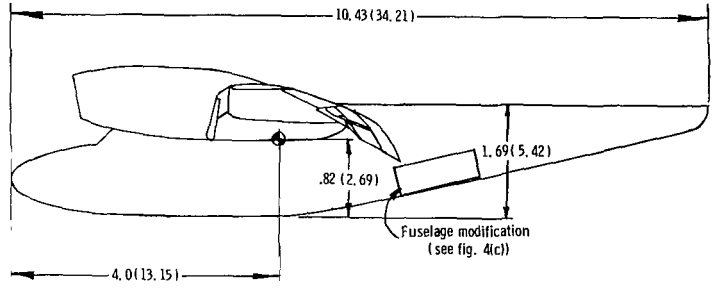

Figure 2.- Three-view sketch and dimensional characteristics of model. All dimensions in the sketch are in meters (feet).

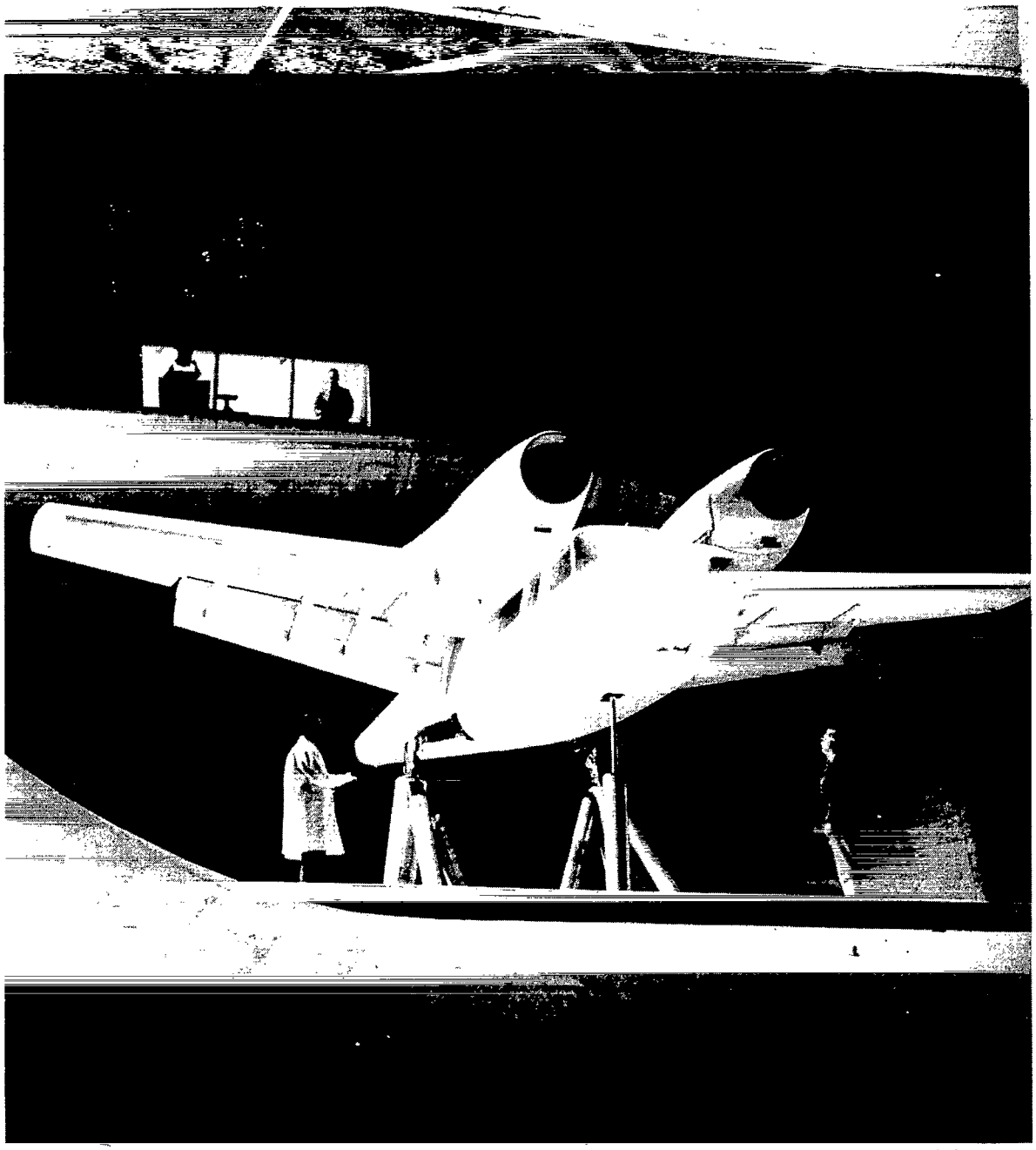

L-74-1835

(a) Front view.

Figure 3.- Model in test section of Langley full-scale tunnel.

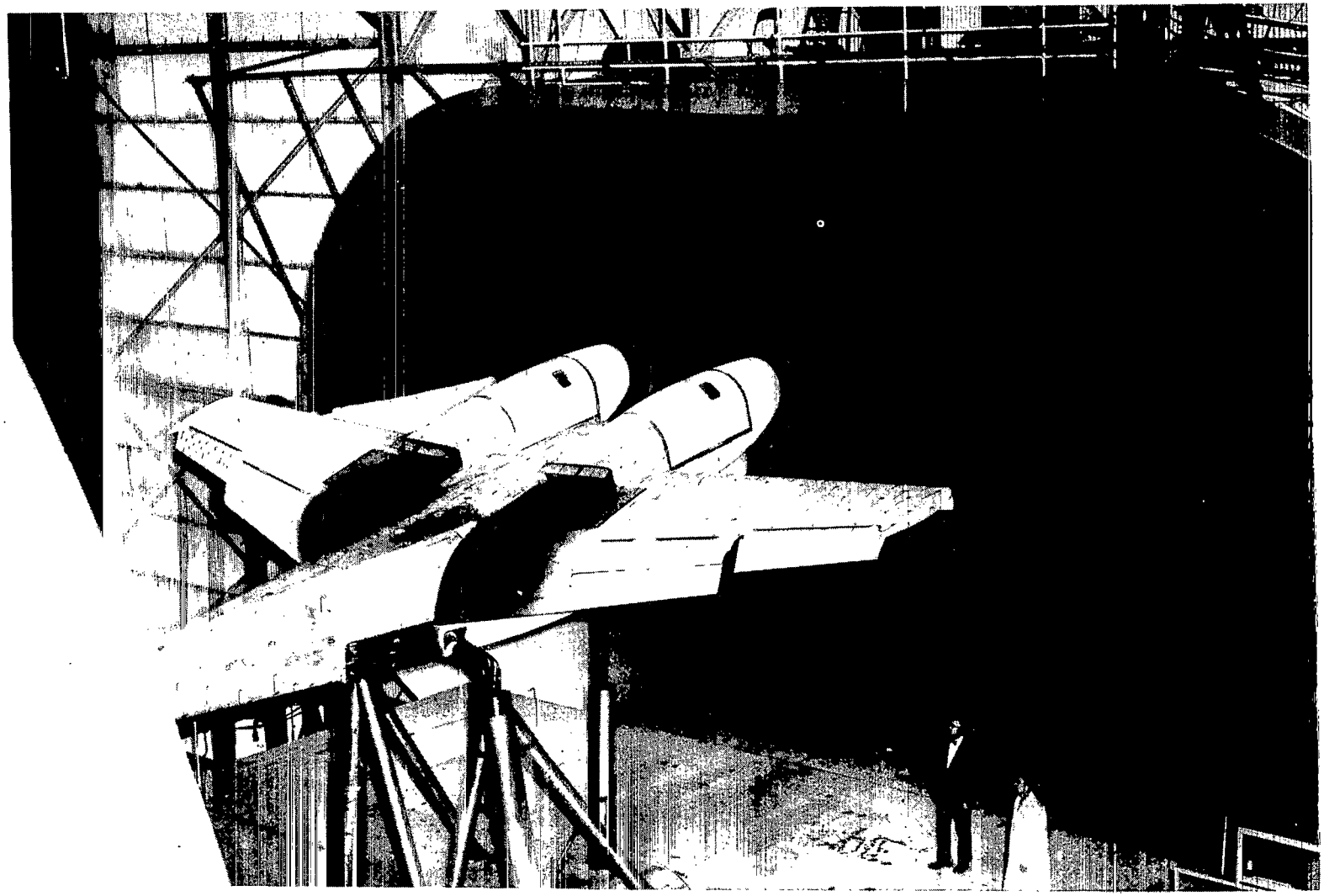

L-74-3231

(b) Three-quarter rear view.

Figure 3.- Concluded.

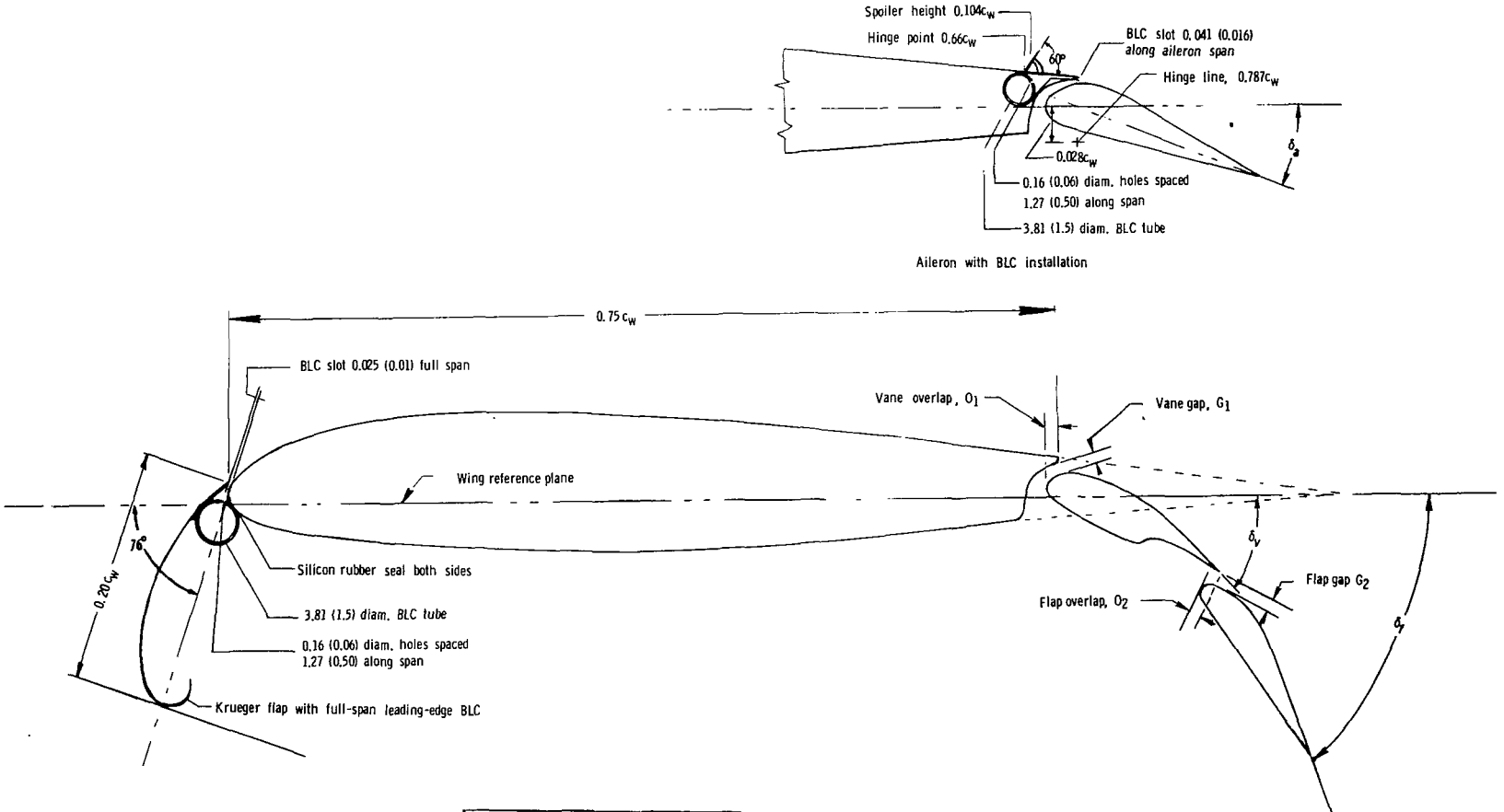

δ_v / δ_f, deg	O_1	G_1	O_2	G_2
15 / 32	0.98	1.67	1.54	1.26
40 / 72	1.12	1.54	1.54	1.26

(a) Leading- and trailing-edge flap deflection and BLC installation. Dimensions are in percent local wing chord and centimeters (inches).

Figure 4.- Details of high-lift system.

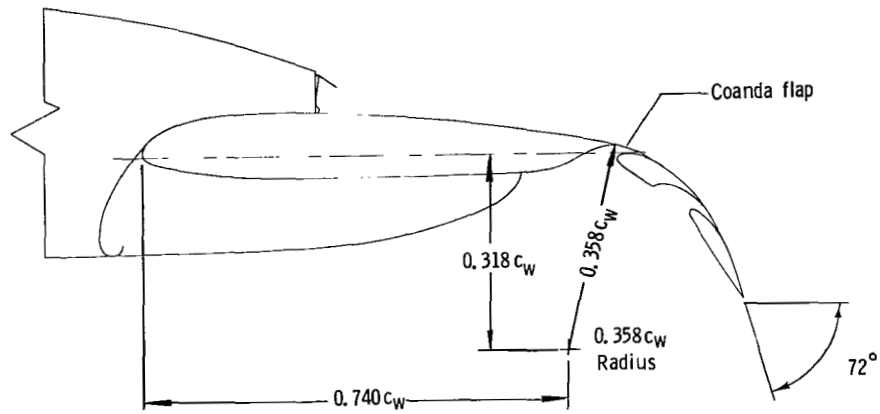

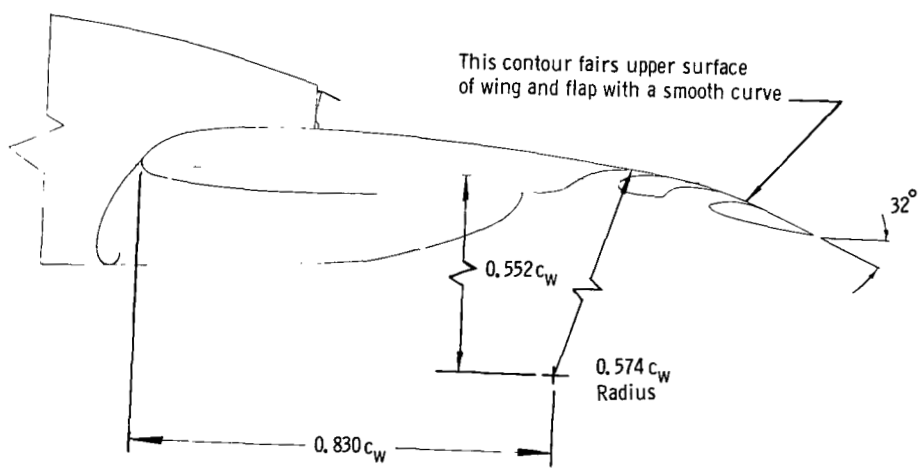

(b) Details of inboard flap.

Figure 4.- Continued.

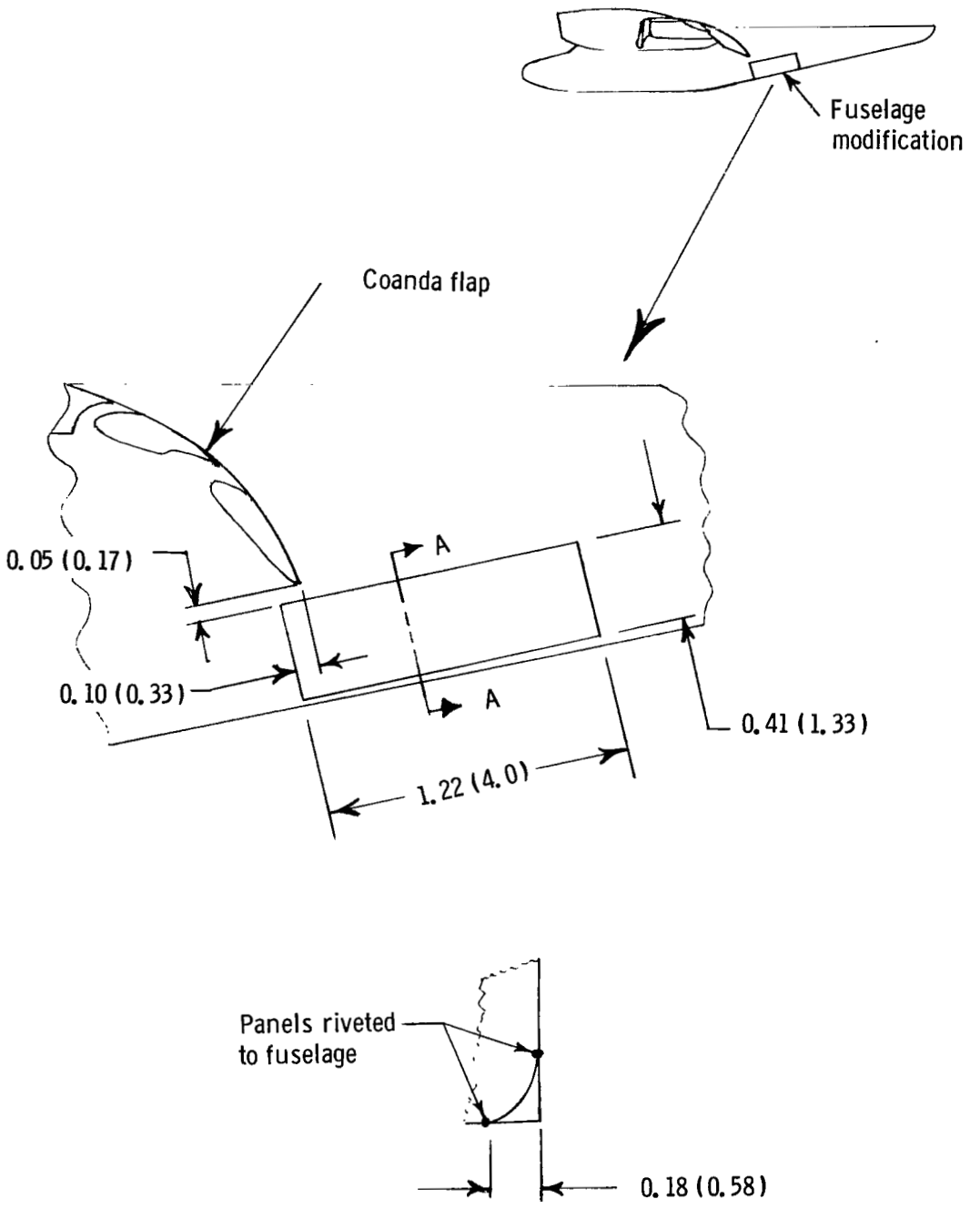

(c) Details of fuselage modification. Dimensions are in meters (feet).

Figure 4.- Concluded.

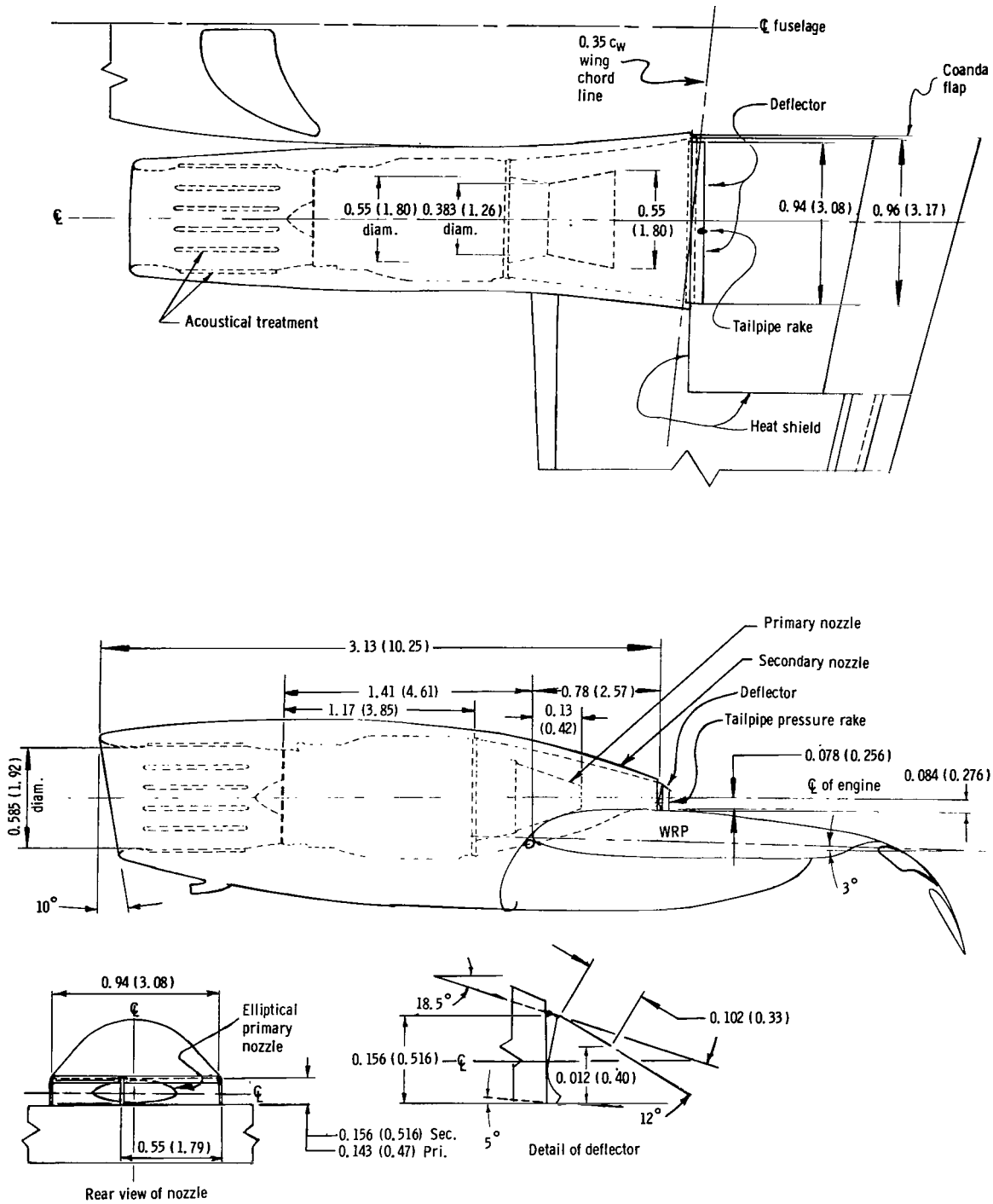

Figure 5.- Sketch of engine and nacelle showing installation on wing. All linear dimensions are in meters (feet).

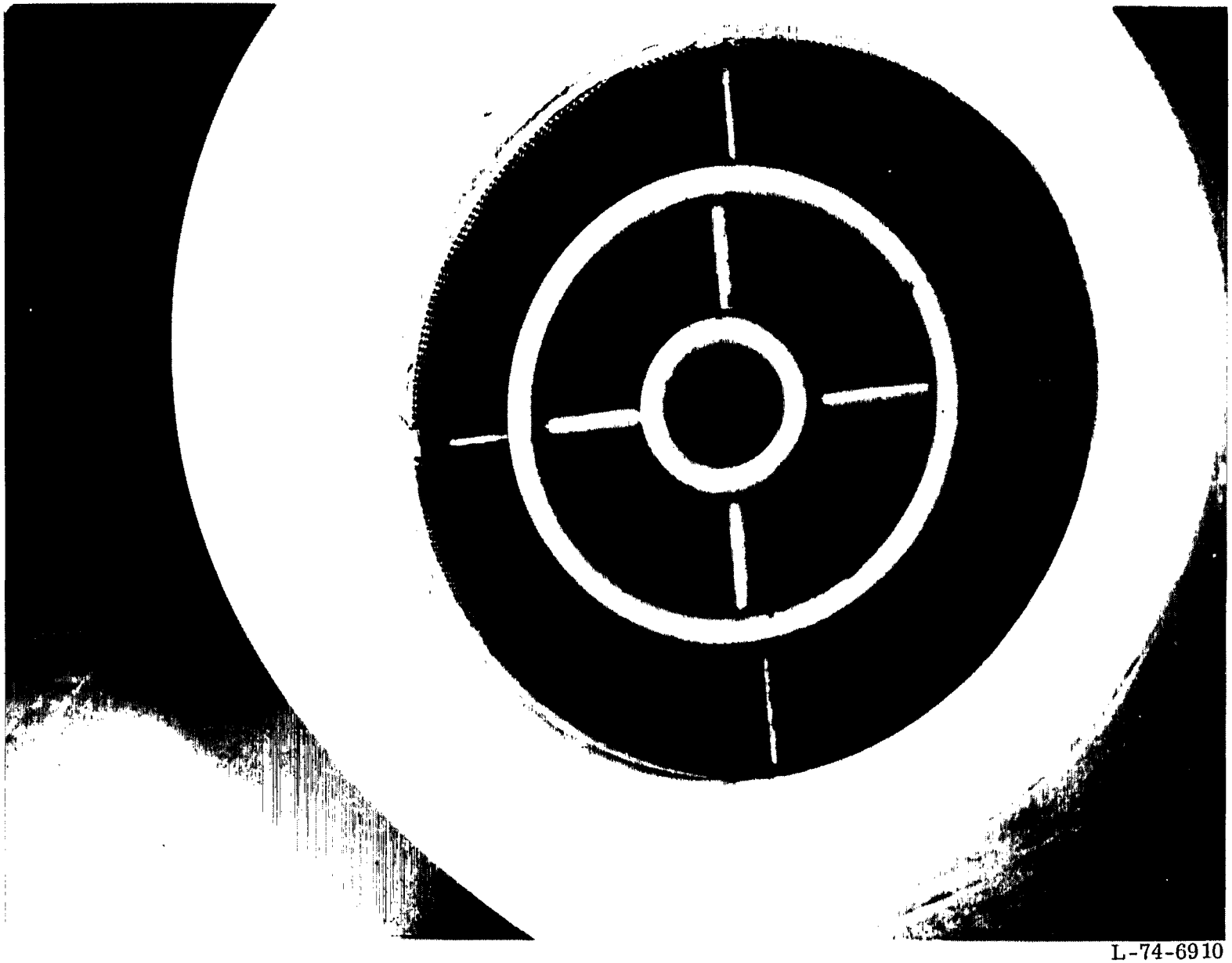

L-74-6910

Figure 6.- Engine inlet acoustical treatment.

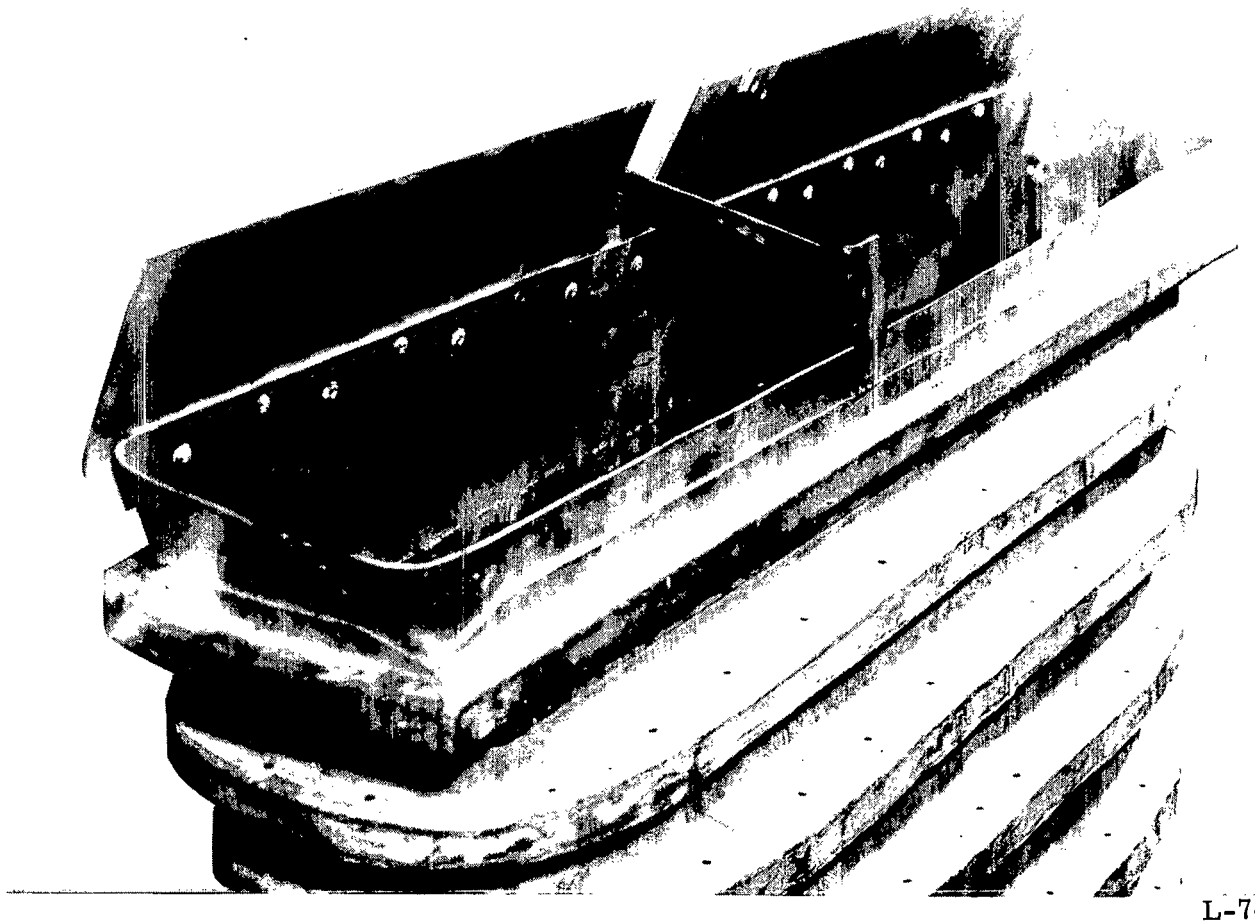

L-74-6911

Figure 7.- Nozzle exit showing deflector and rake.

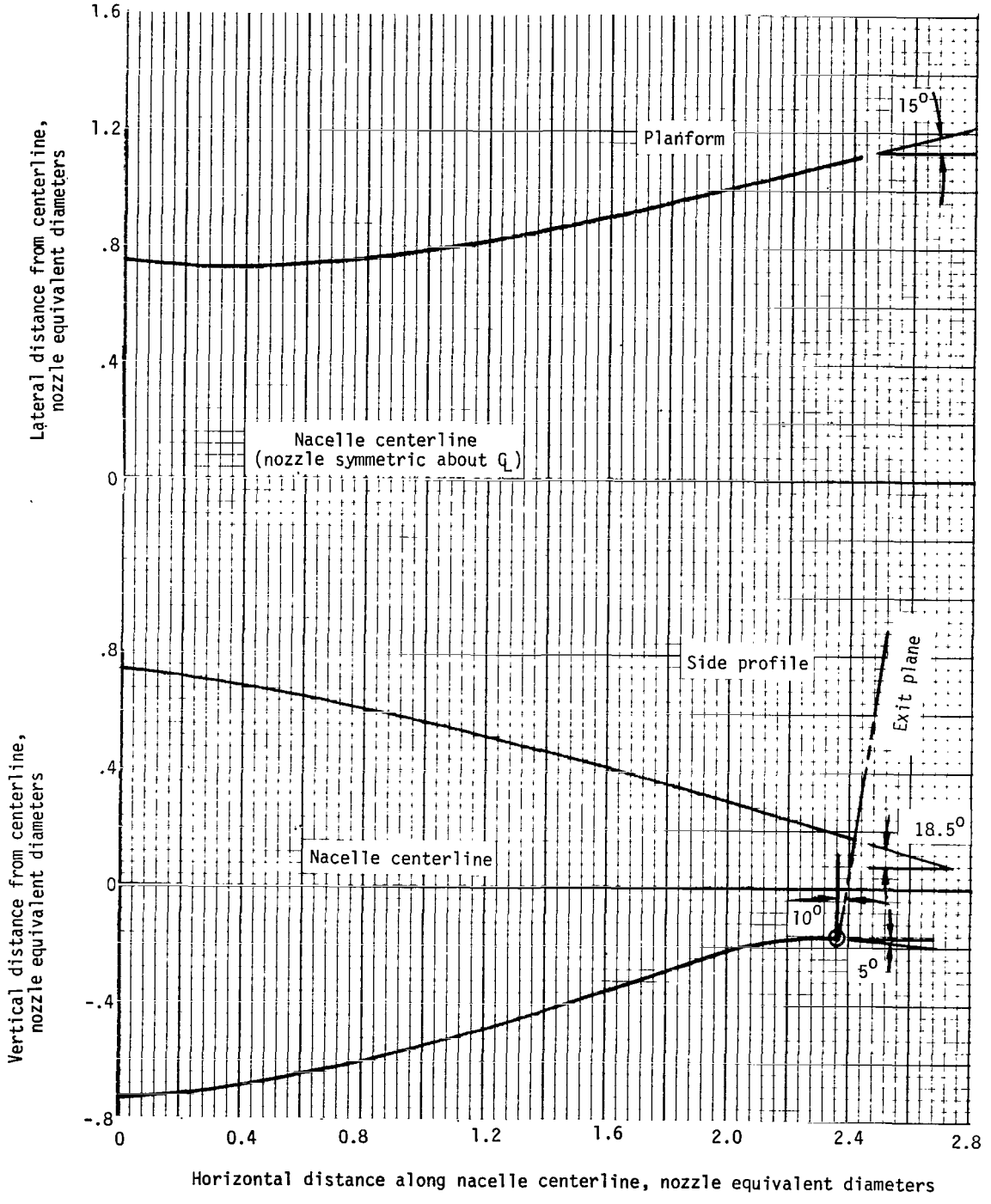

Figure 8.- Internal contours for secondary nozzle.

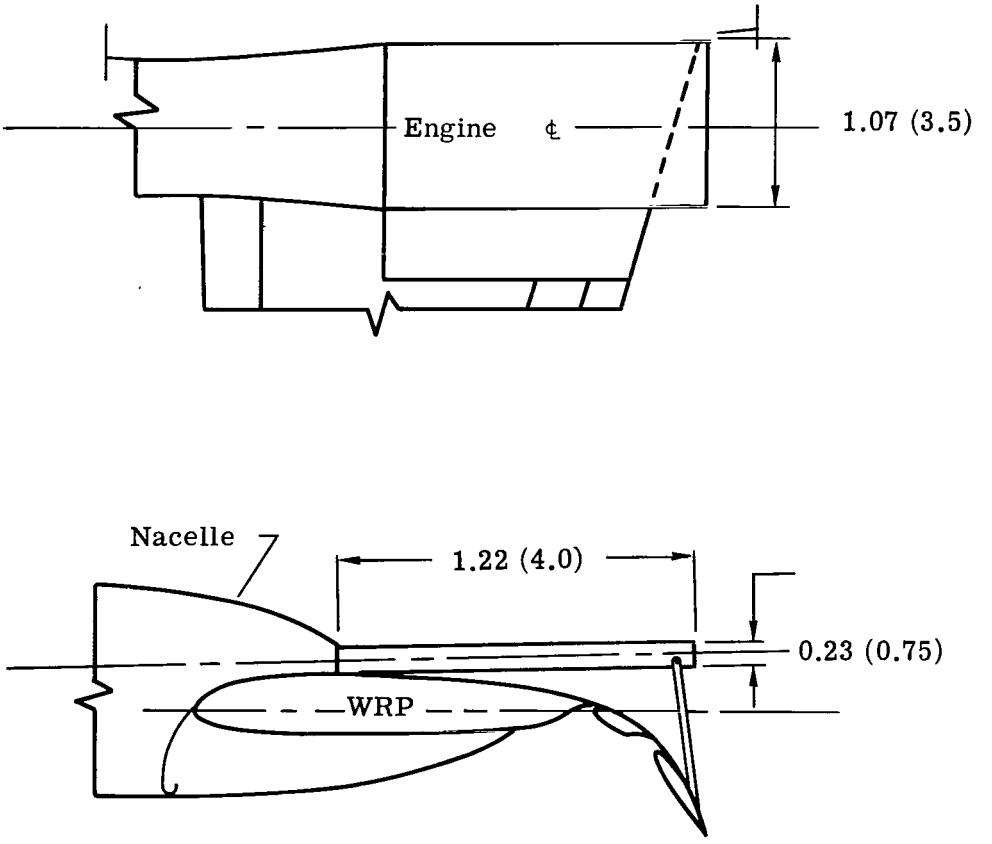

Figure 9.- Thrust calibration deflector used in static thrust measurements. Dimensions are given in meters (feet).

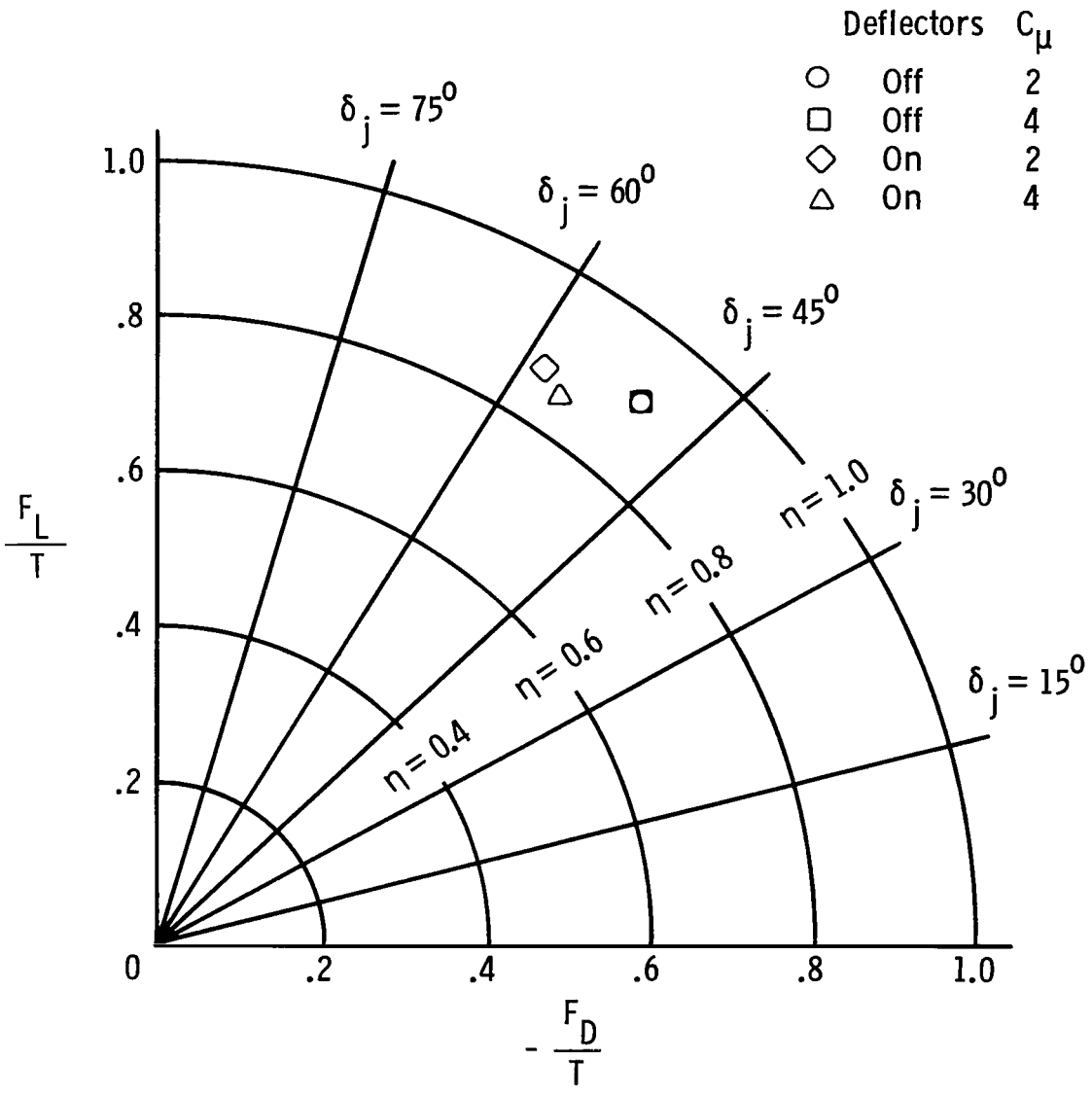

(a) $\delta_f = 72^o$.

Figure 10.- Summary of static turning characteristics. (For values of C_μ quoted, a free-stream dynamic pressure of 143.64 Pa (3.00 lb/ft^2) was assumed.)

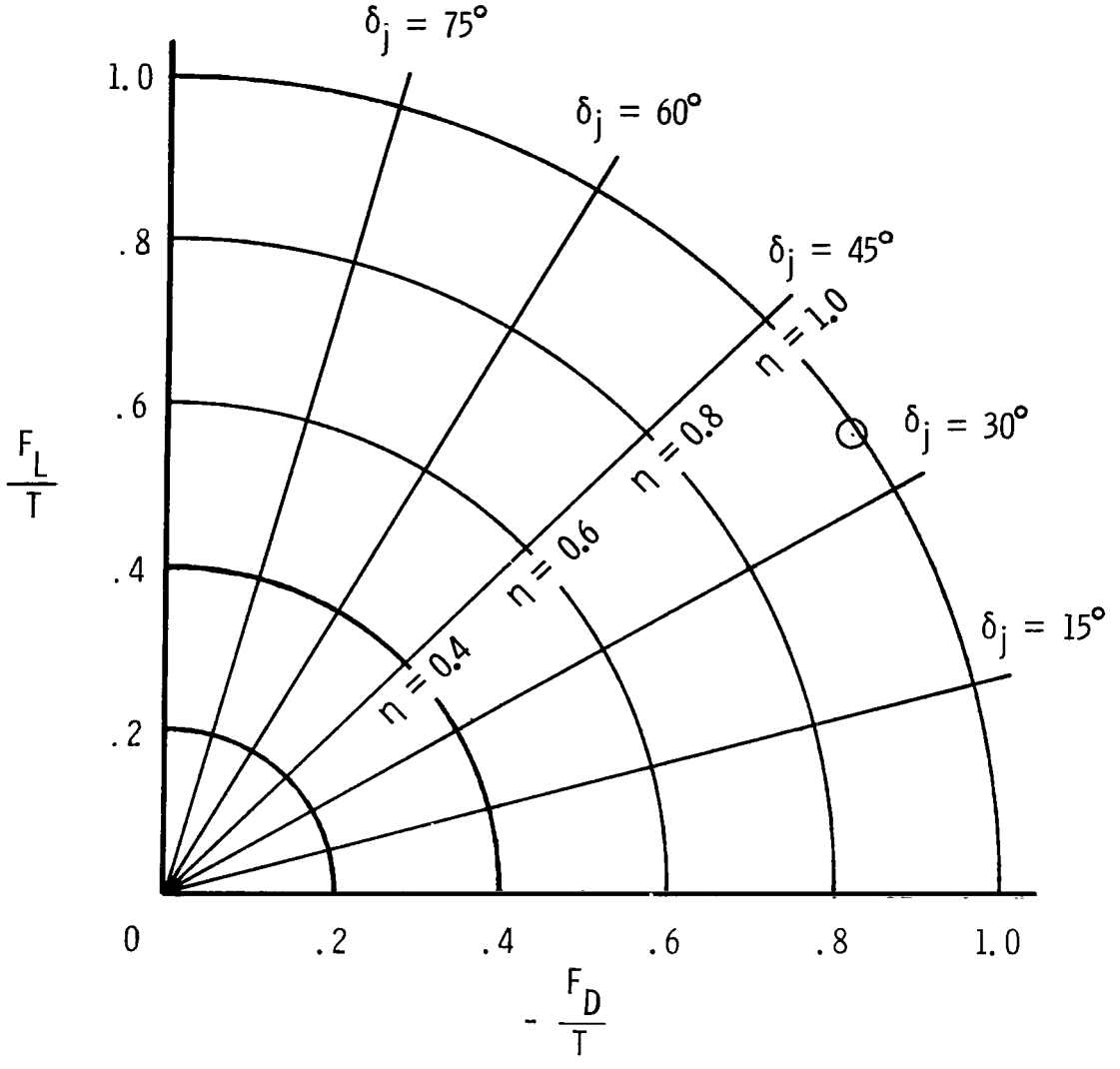

(b) $\delta_f = 32^o$, $C_\mu = 2$, deflectors on.

Figure 10.- Concluded.

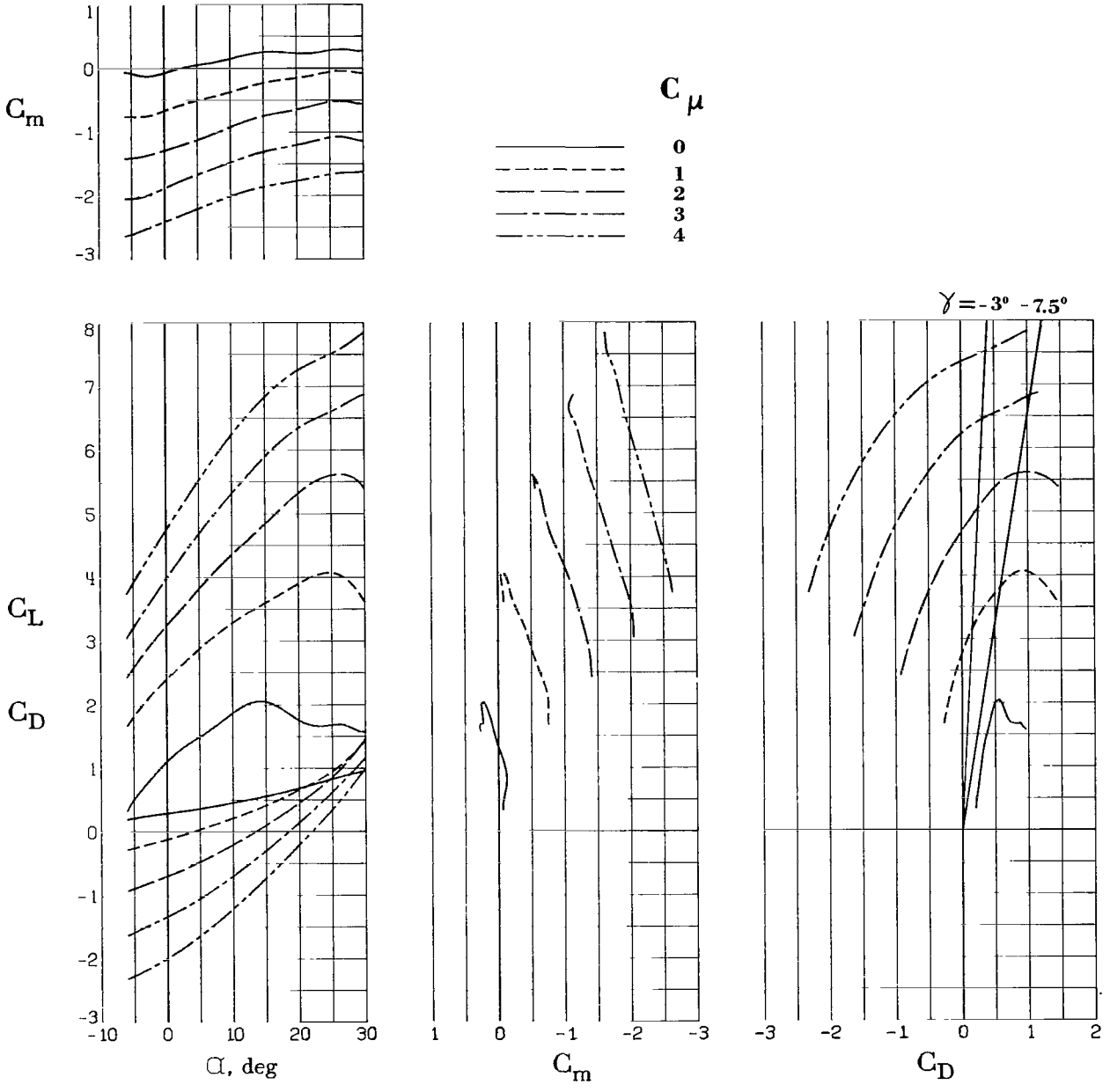

Figure 11.- Longitudinal aerodynamic characteristics of model with nozzle deflectors off. $\delta_f = 72^o$; $C_{\mu,le} = 0$; $C_{\mu,a} = 0$; $\delta_a = 0^o$.

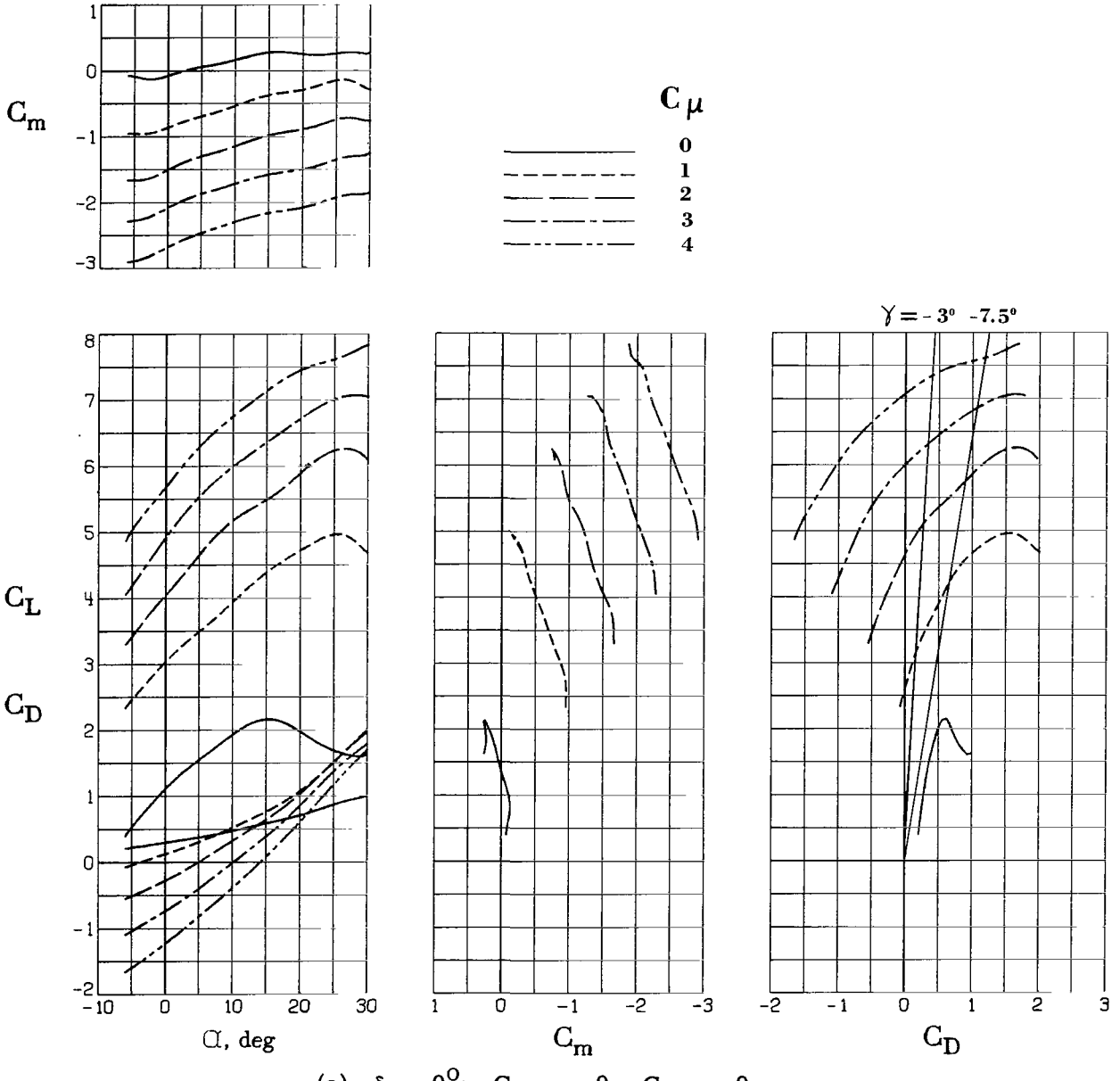

(a) $\delta_a = 0^o$; $C_{\mu,le} = 0$; $C_{\mu,a} = 0$.

Figure 12.- Longitudinal aerodynamic characteristics of model with nozzle deflectors on. $\delta_f = 72^o$.

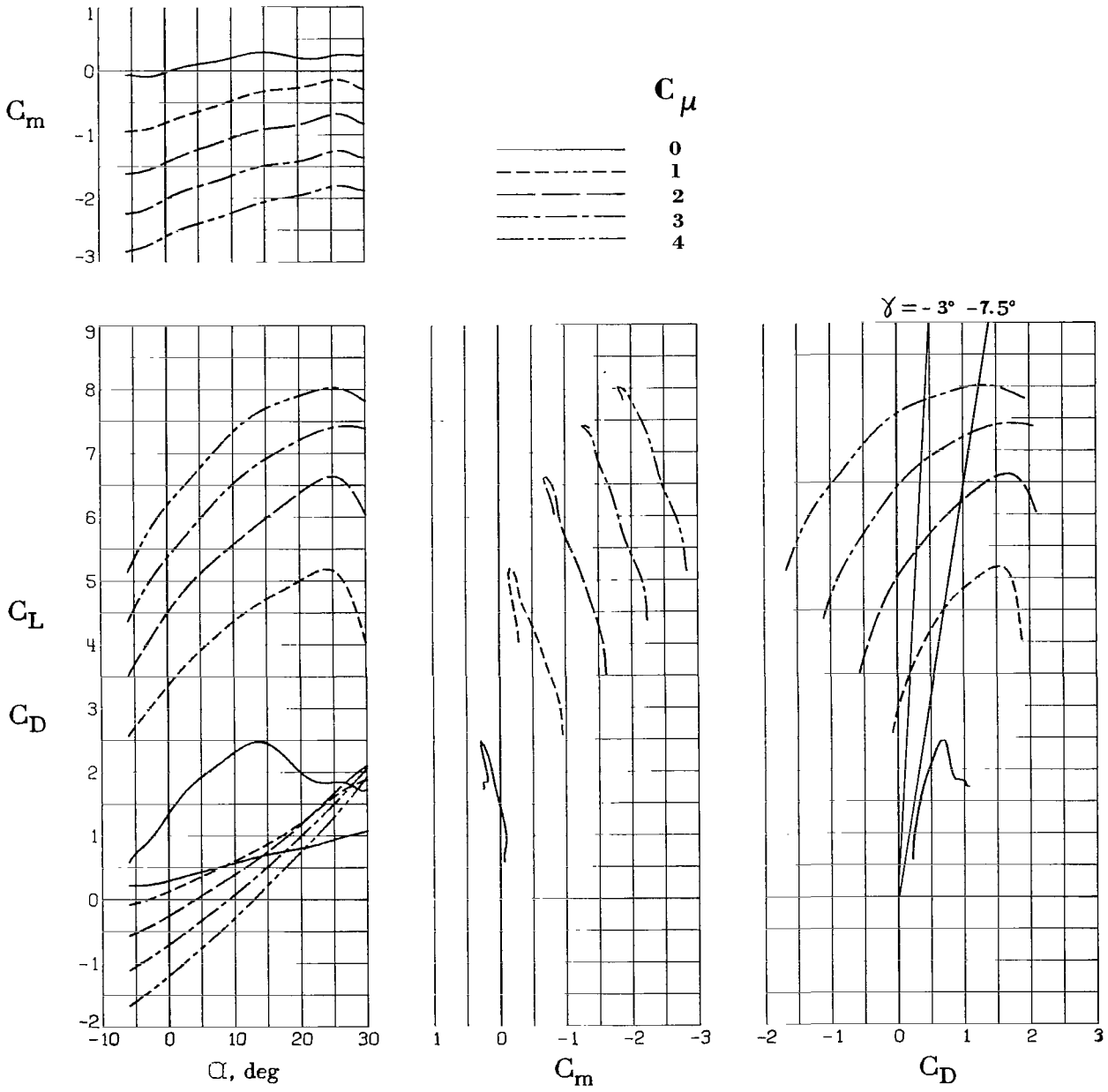

(b) $\delta_a = 50^o$; $C_{\mu,le} = 0$; $C_{\mu,a} = 0.015$.

Figure 12.- Continued.

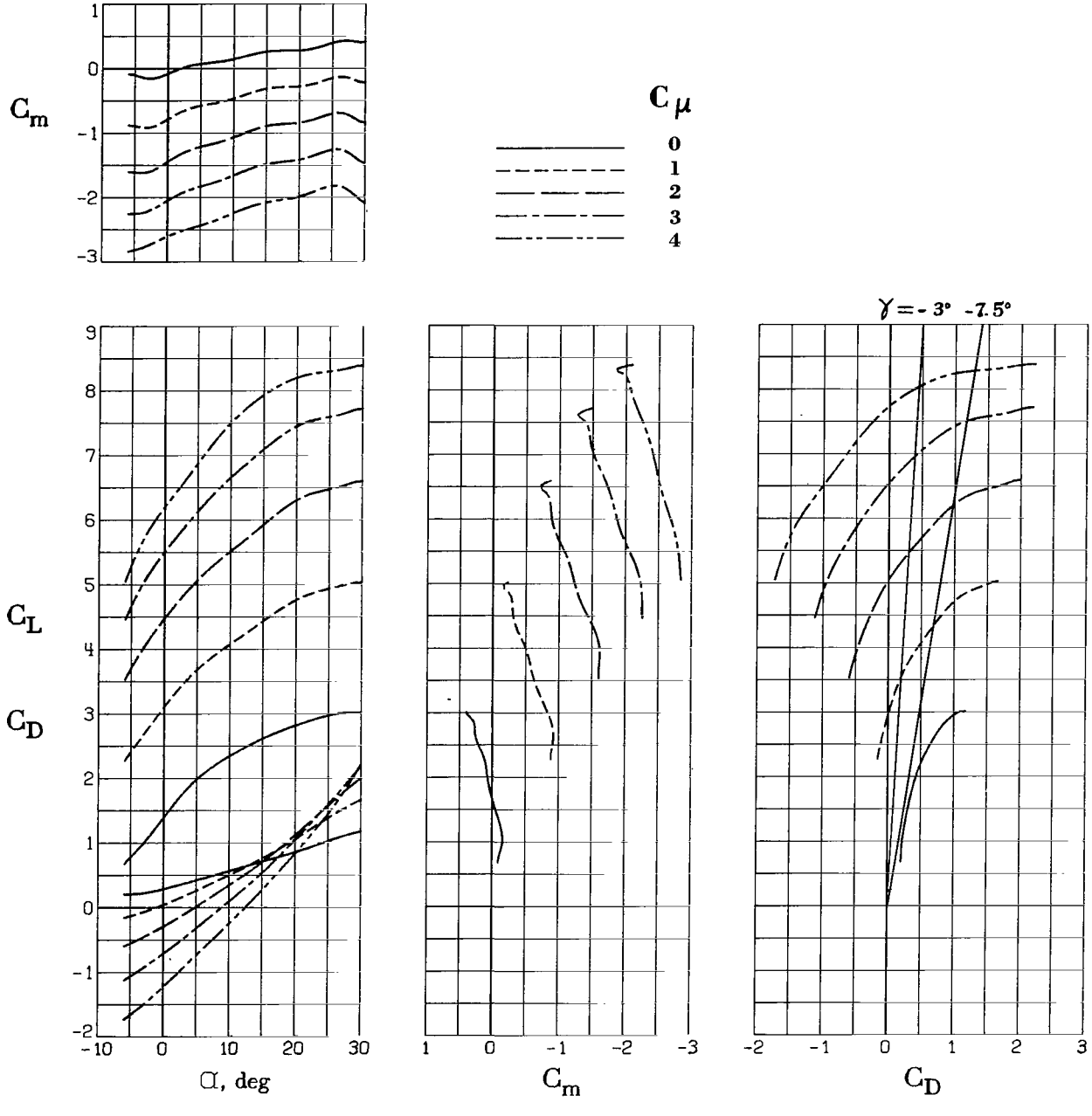

(c) $\delta_a = 50^o$; $C_{\mu,le} = 0.013$; $C_{\mu,a} = 0.021$.

Figure 12.- Concluded.

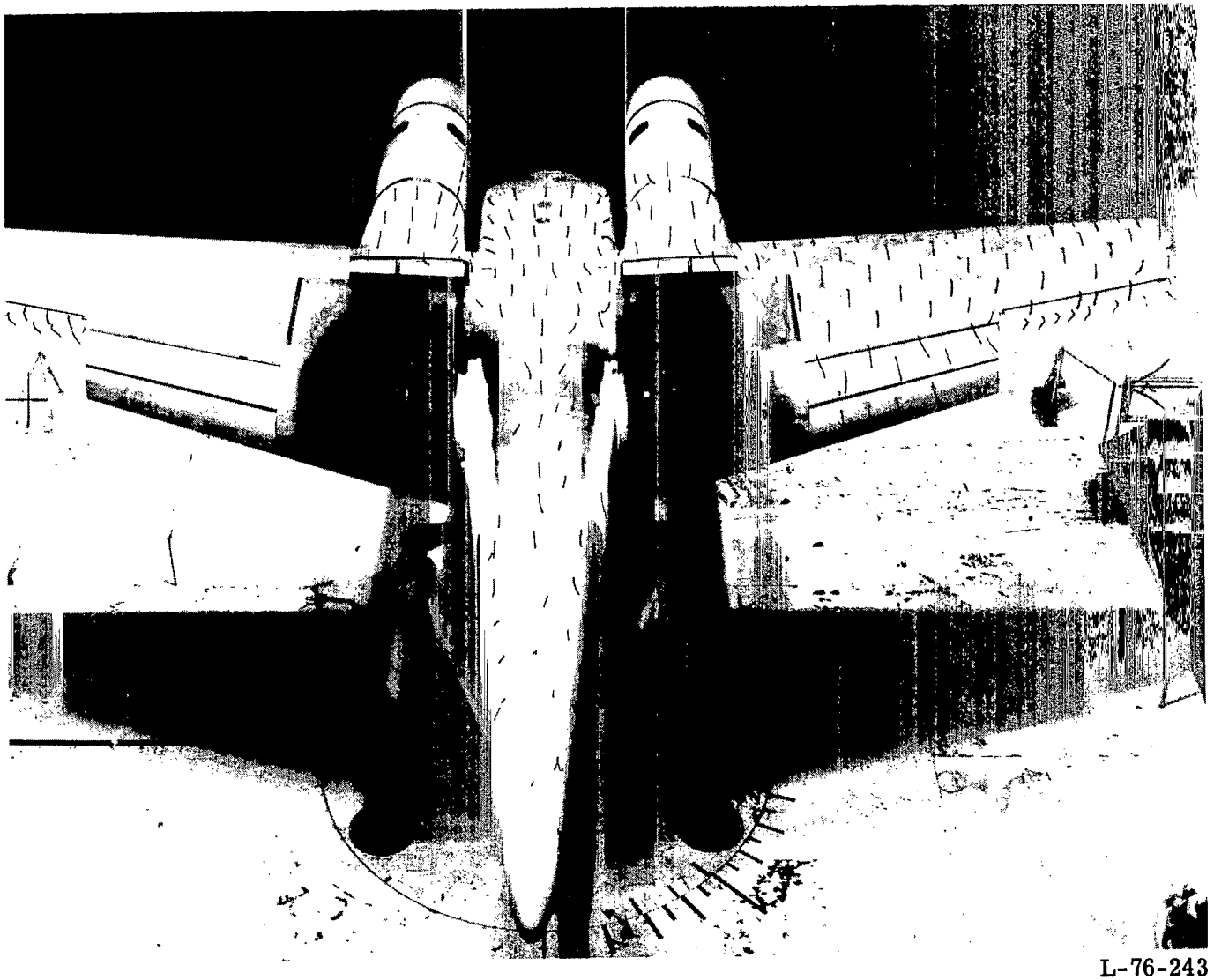

L-76-243

(a) $\alpha = -1^{o}$.

Figure 13.- Tuft photographs of model. $C_{\mu} = 2$; $\delta_f = 72^{o}$; $\delta_a = 0^{o}$; $C_{\mu,le} = 0$; $C_{\mu,a} = 0$.

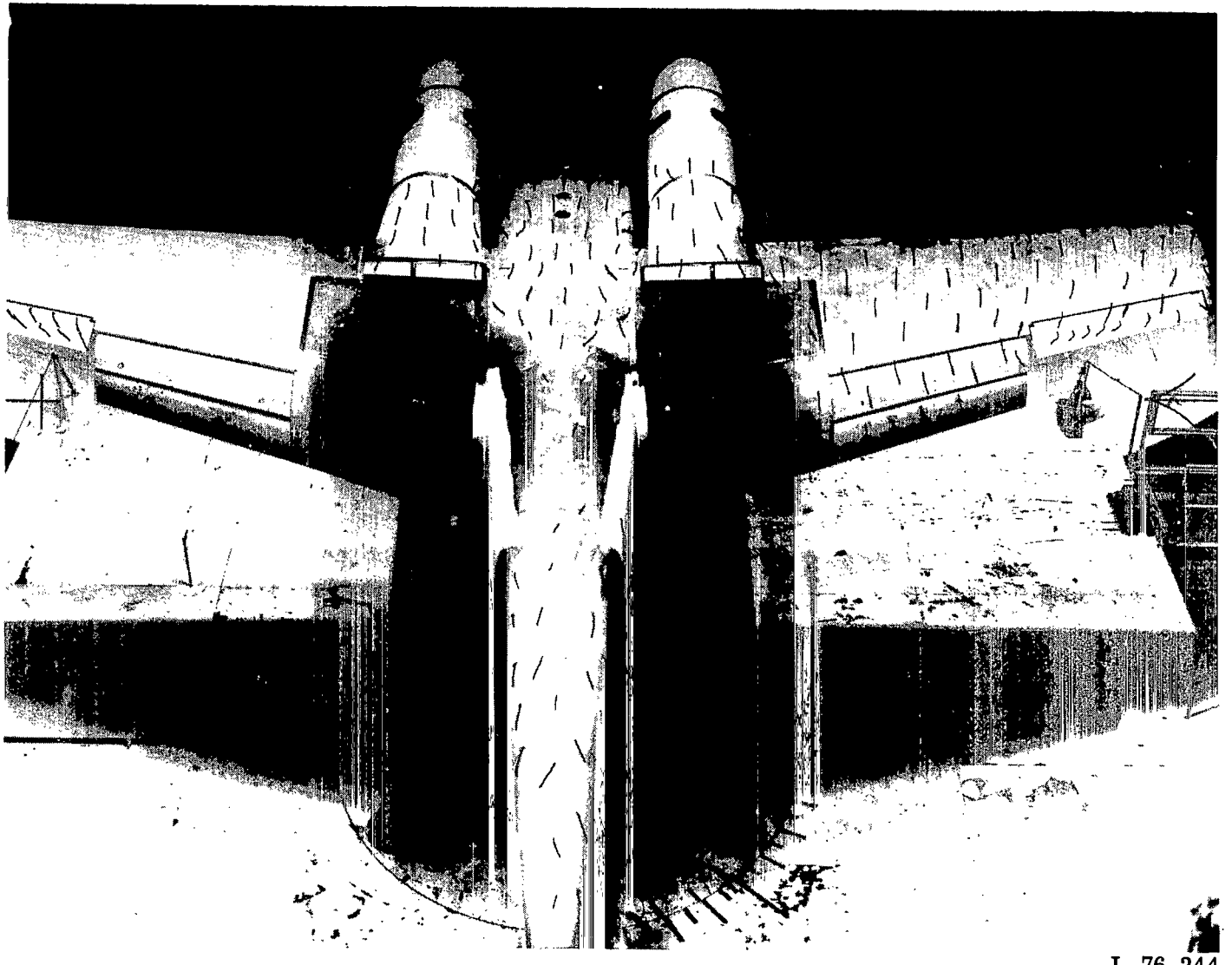

L-76-244

(b) $\alpha = 4^{o}$.

Figure 13.- Continued.

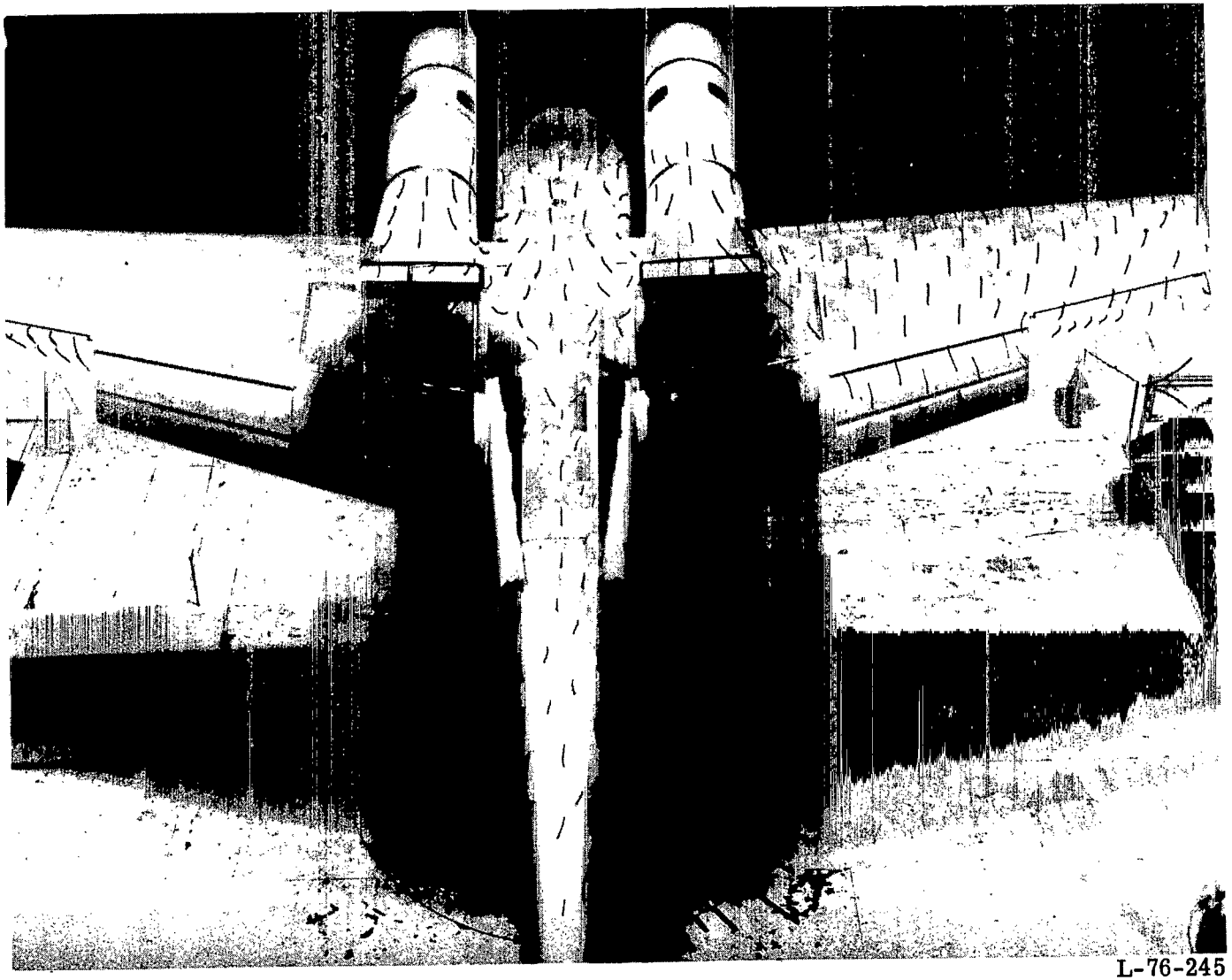

(c) $\alpha = 9^{o}$.

Figure 13.- Continued.

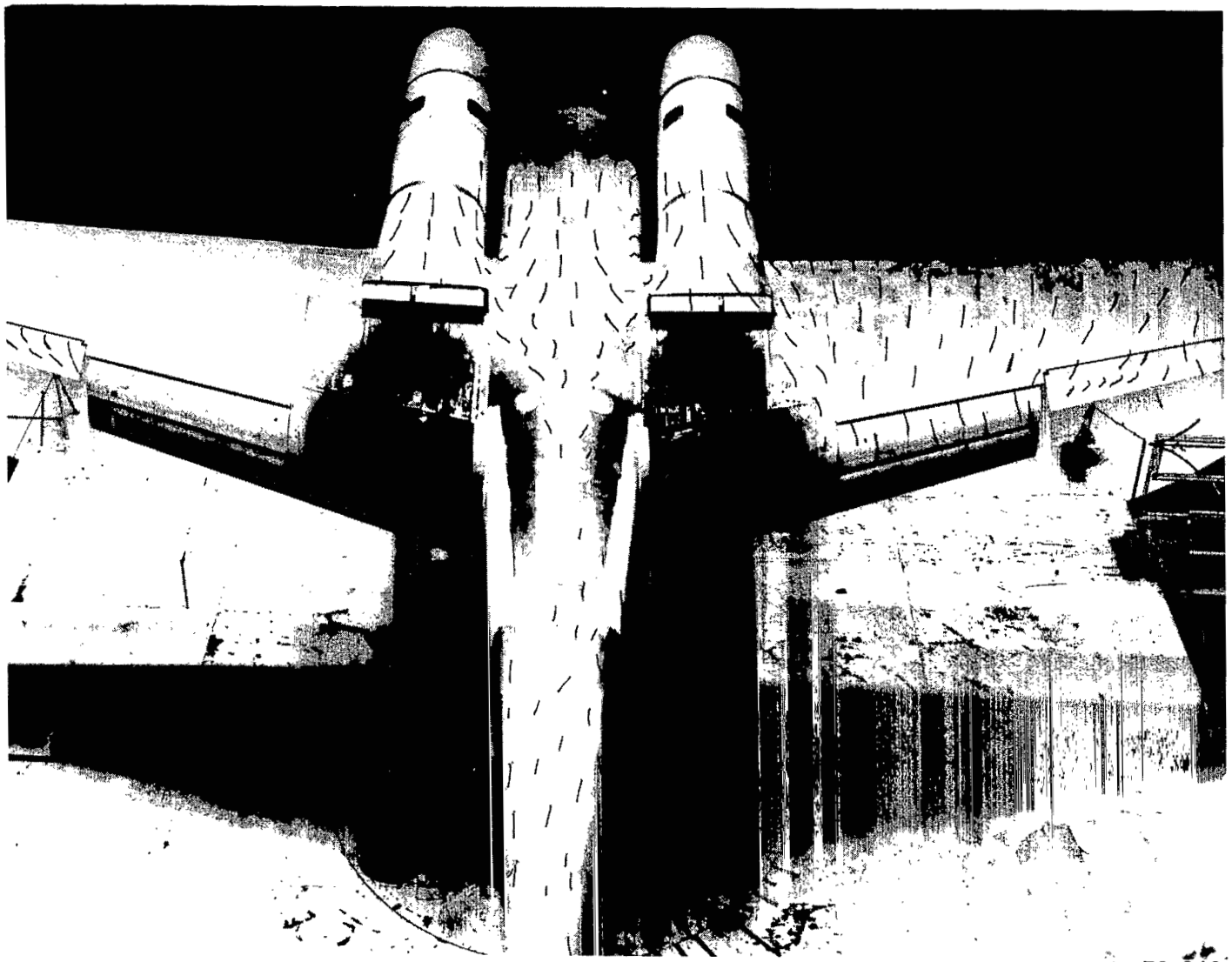

L-76-246

(d) $\alpha = 14^{o}$.

Figure 13.- Continued.

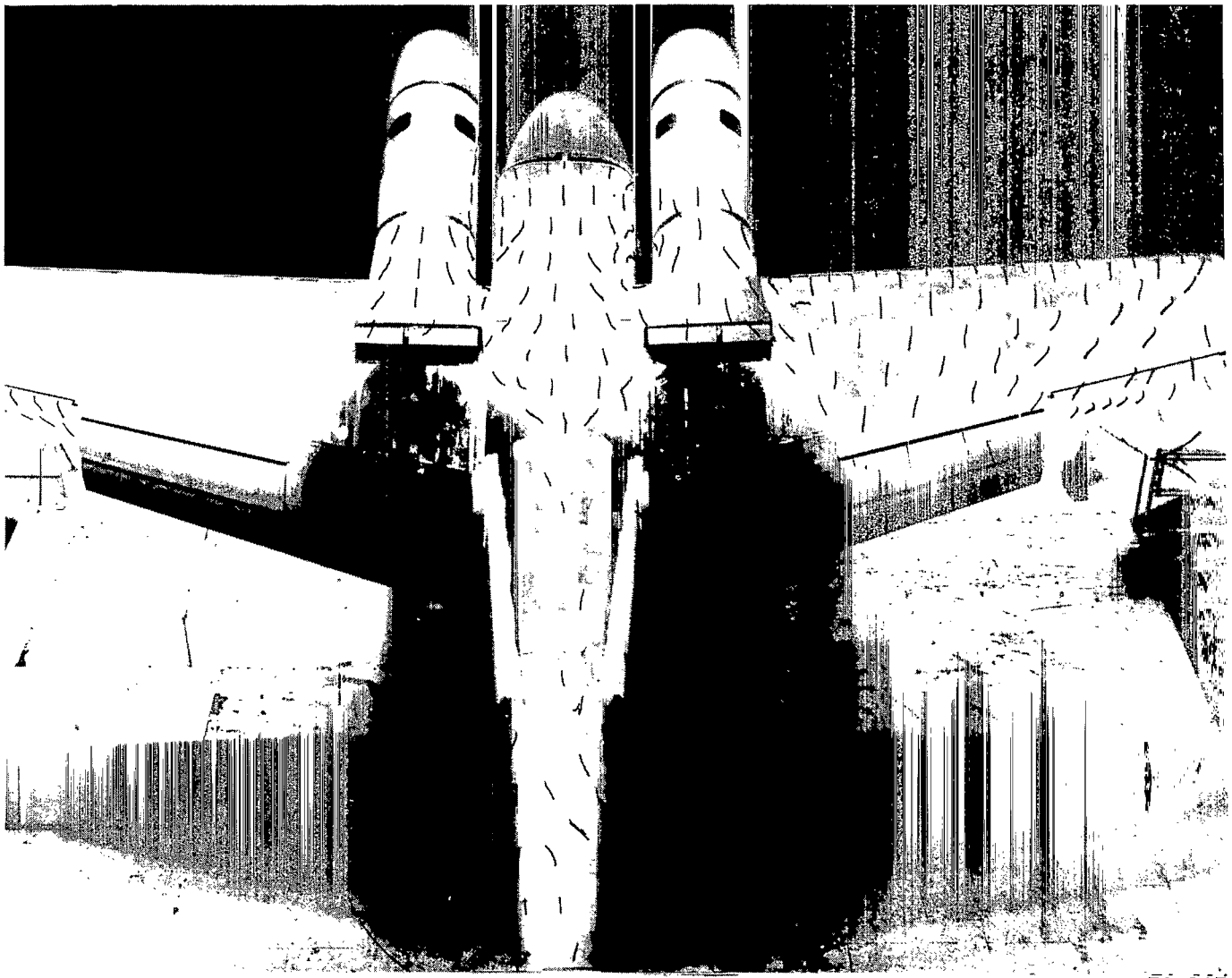

L-76-247

(e) $\alpha = 19^{\circ}$.

Figure 13.- Concluded.

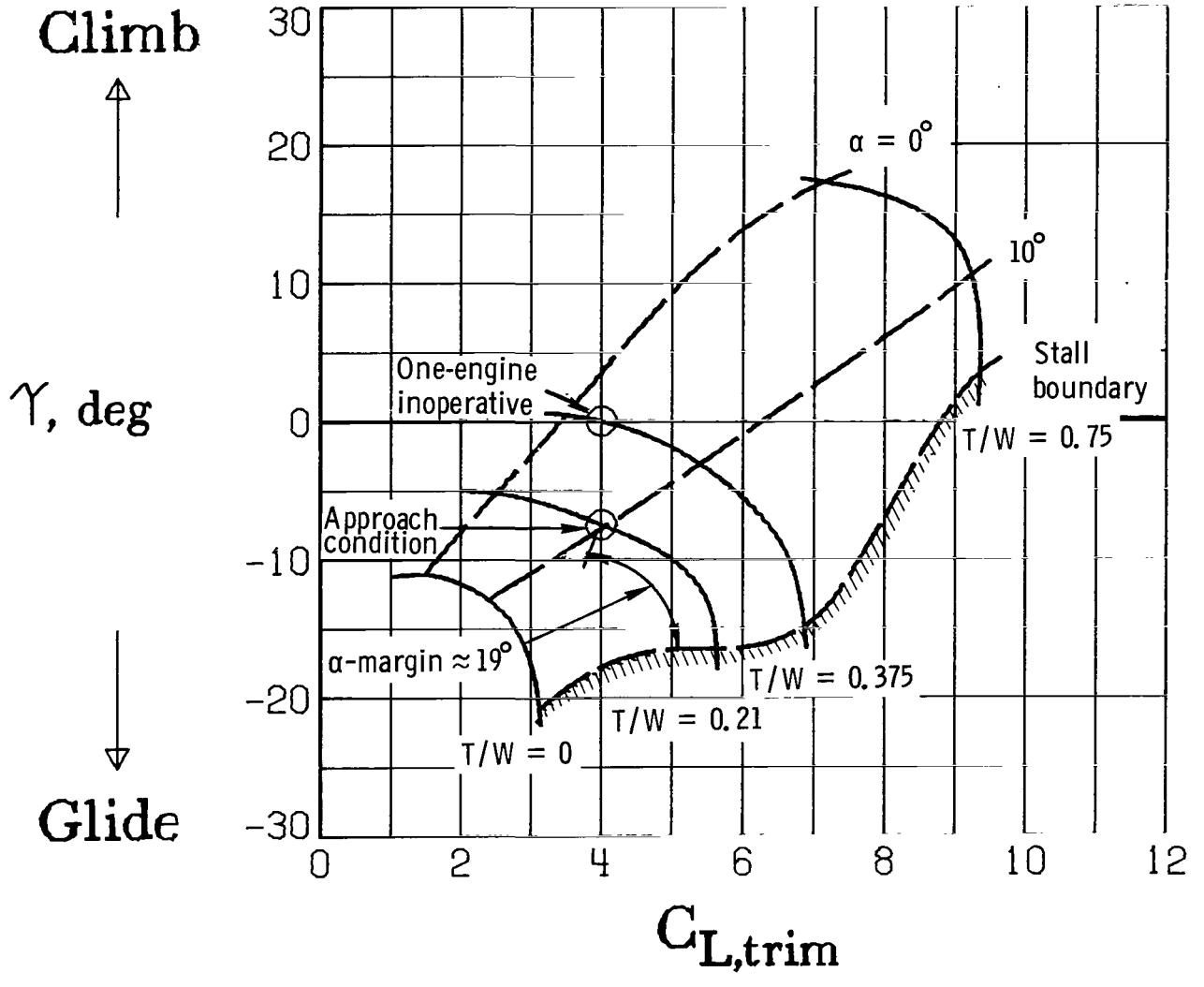

Figure 14.- Flight-path envelope of model with $\delta_f = 72^\circ$. $\delta_a = 50^\circ$; $C_{\mu,le} = 0.013$; $C_{\mu,a} = 0.021$.

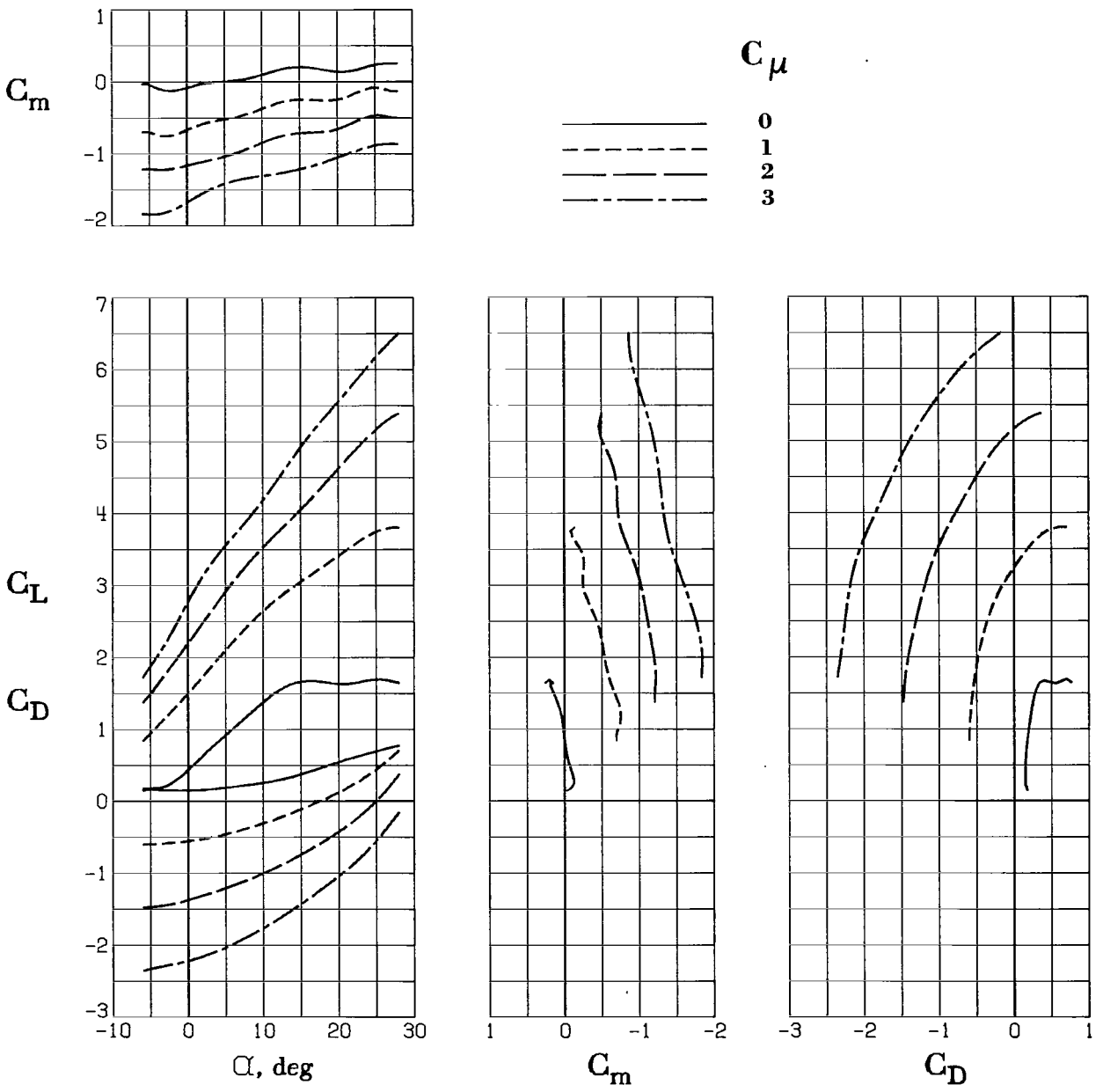

(a) $\delta_a = 0^o$; $C_{\mu,le} = 0$; $C_{\mu,a} = 0$.

Figure 15.- Longitudinal aerodynamic characteristics of model with $\delta_f = 32^o$.

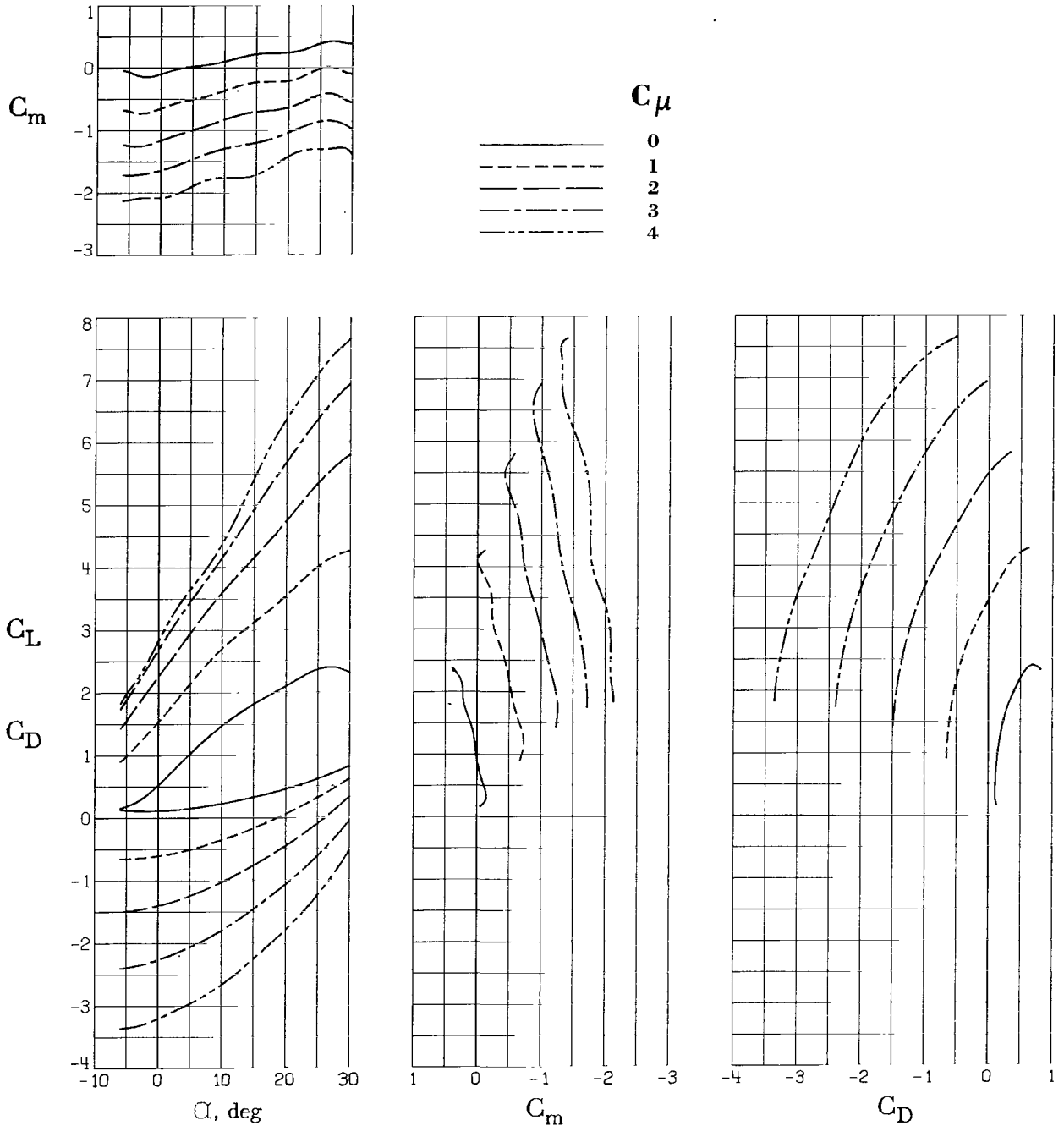

(b) $\delta_a = 0^o$; $C_{\mu,le} = 0.013$; $C_{\mu,a} = 0$.

Figure 15.- Continued.

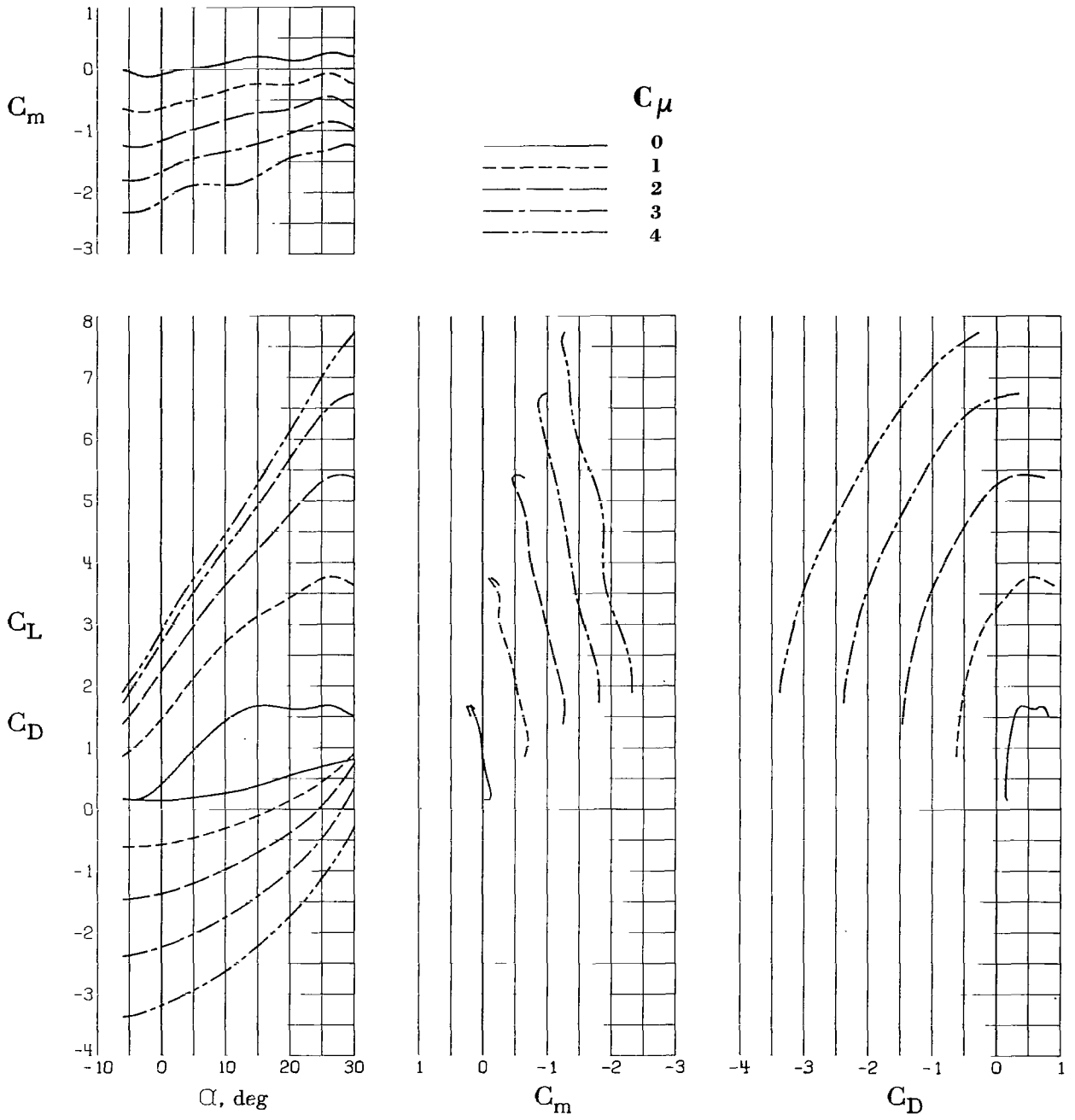

(c) $\delta_a = 20^o$; $C_{\mu,le} = 0$; $C_{\mu,a} = 0.021$.

Figure 15.- Continued.

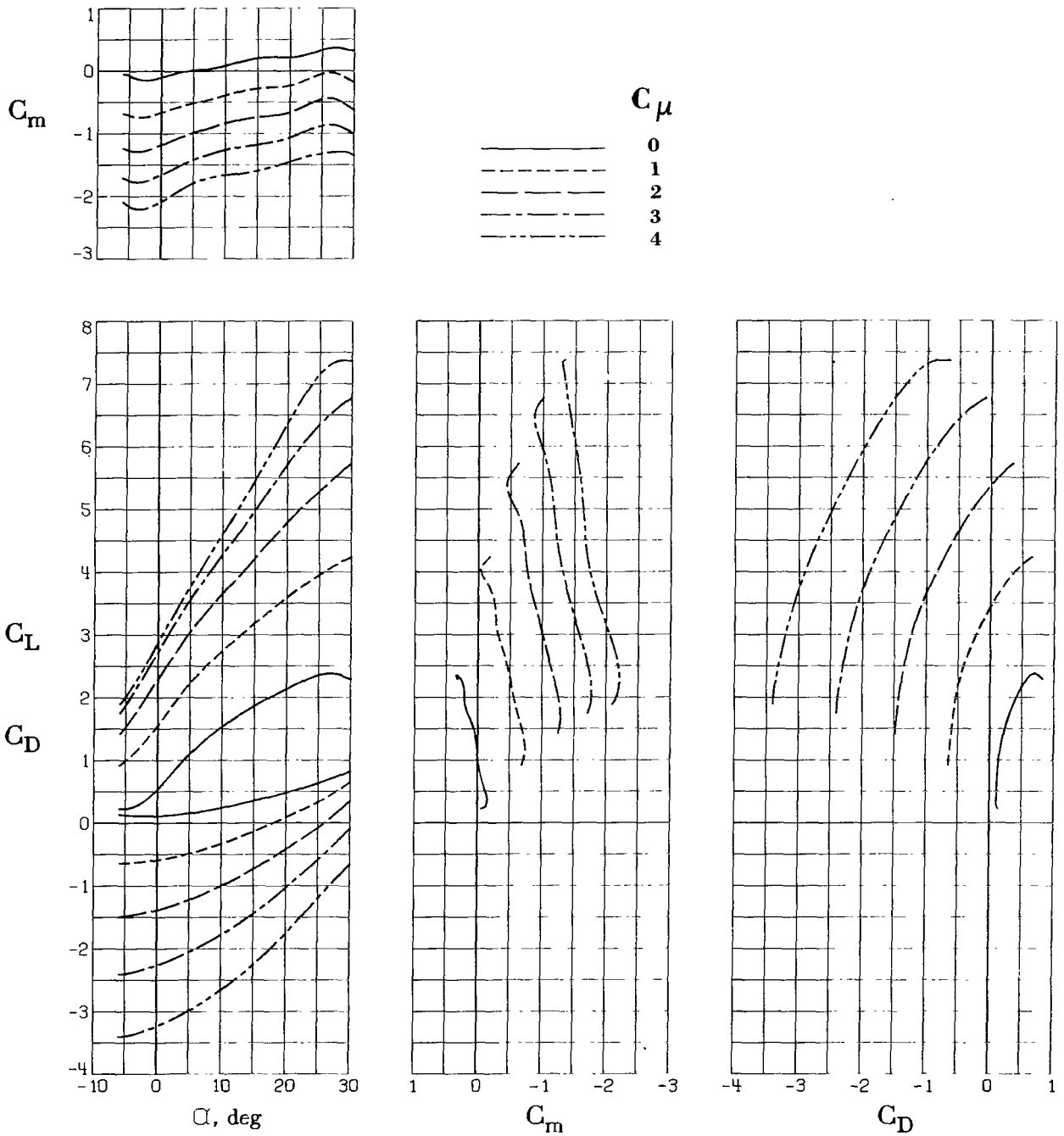

(d) $\delta_a = 20^o$; $C_{\mu,le} = 0.013$; $C_{\mu,a} = 0.$

Figure 15.- Continued.

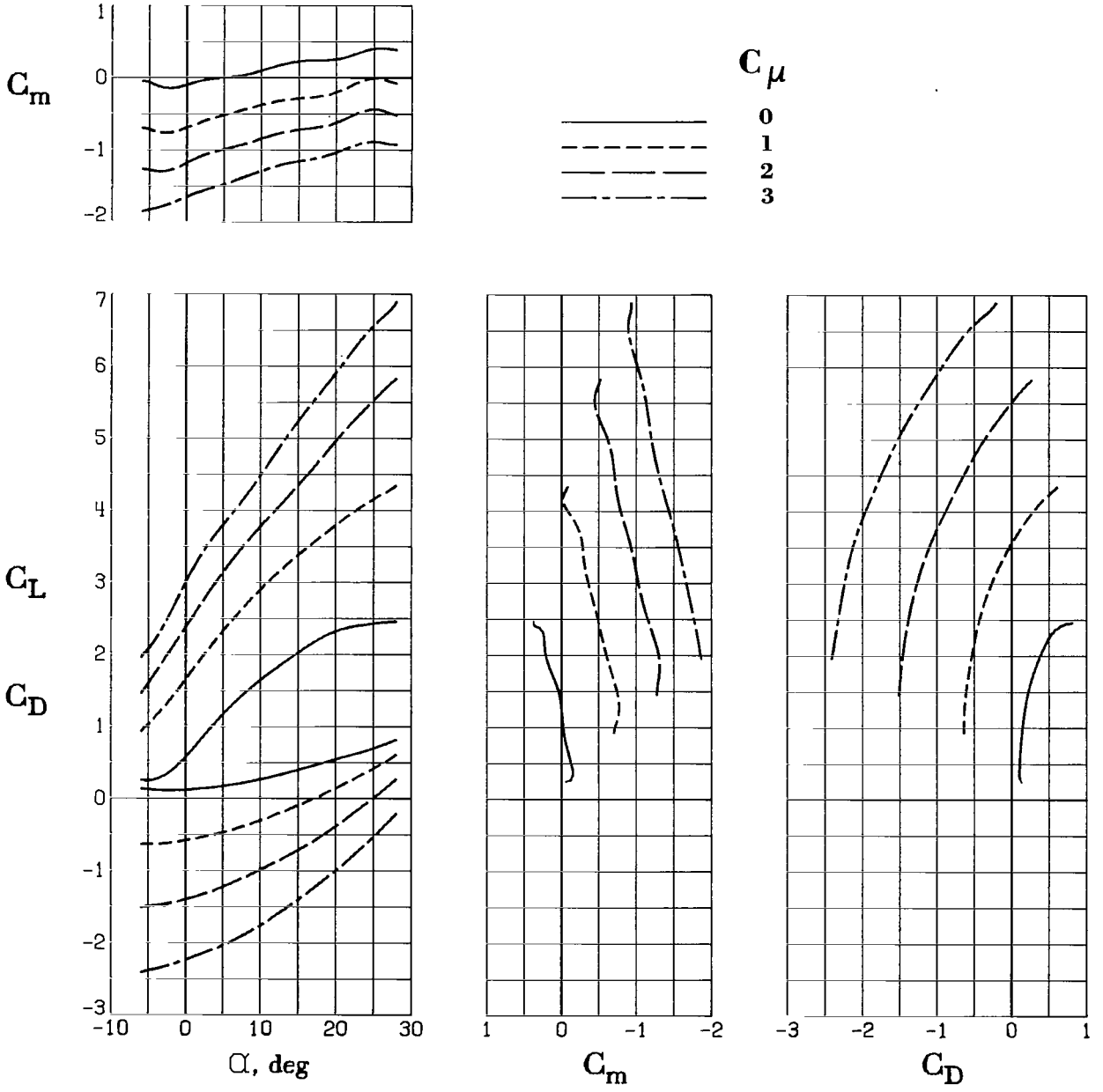

(e) $\delta_a = 20^o$; $C_{\mu,le} = 0.013$; $C_{\mu,a} = 0.021$.

Figure 15.- Concluded.

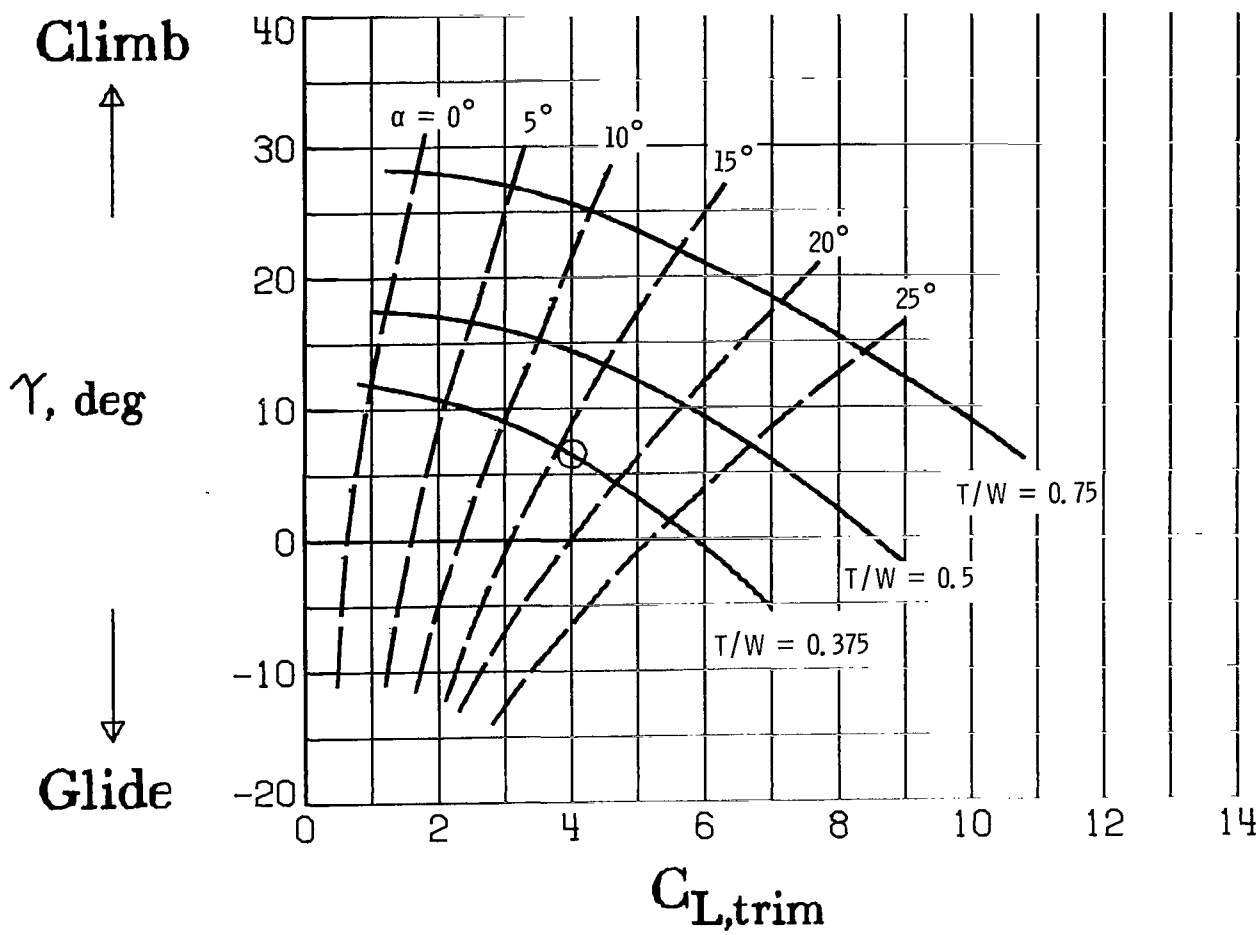

Figure 16.- Flight-path envelope of model with $\delta_f = 32^o$. $\delta_a = 20^o$; $C_{\mu,le} = 0.013$; $C_{\mu,a} = 0.021$.

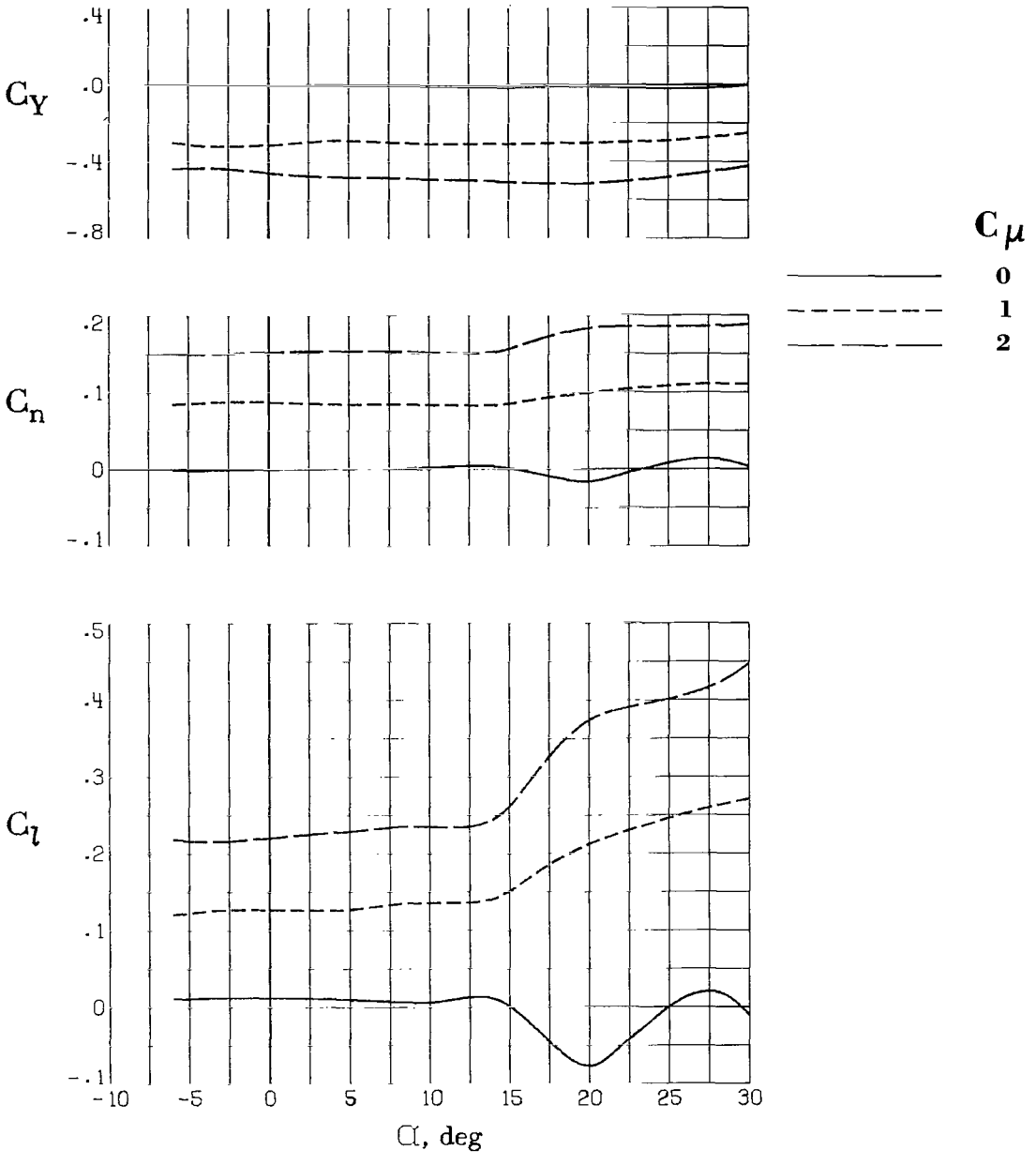

(a) Lateral-directional characteristics.

Figure 17.- Lateral-directional and longitudinal aerodynamic characteristics of the model with right engine inoperative, $\delta_f = 72^o$, and $\delta_a = 0^o$. $C_{\mu,le} = 0$; $C_{\mu,a} = 0$.

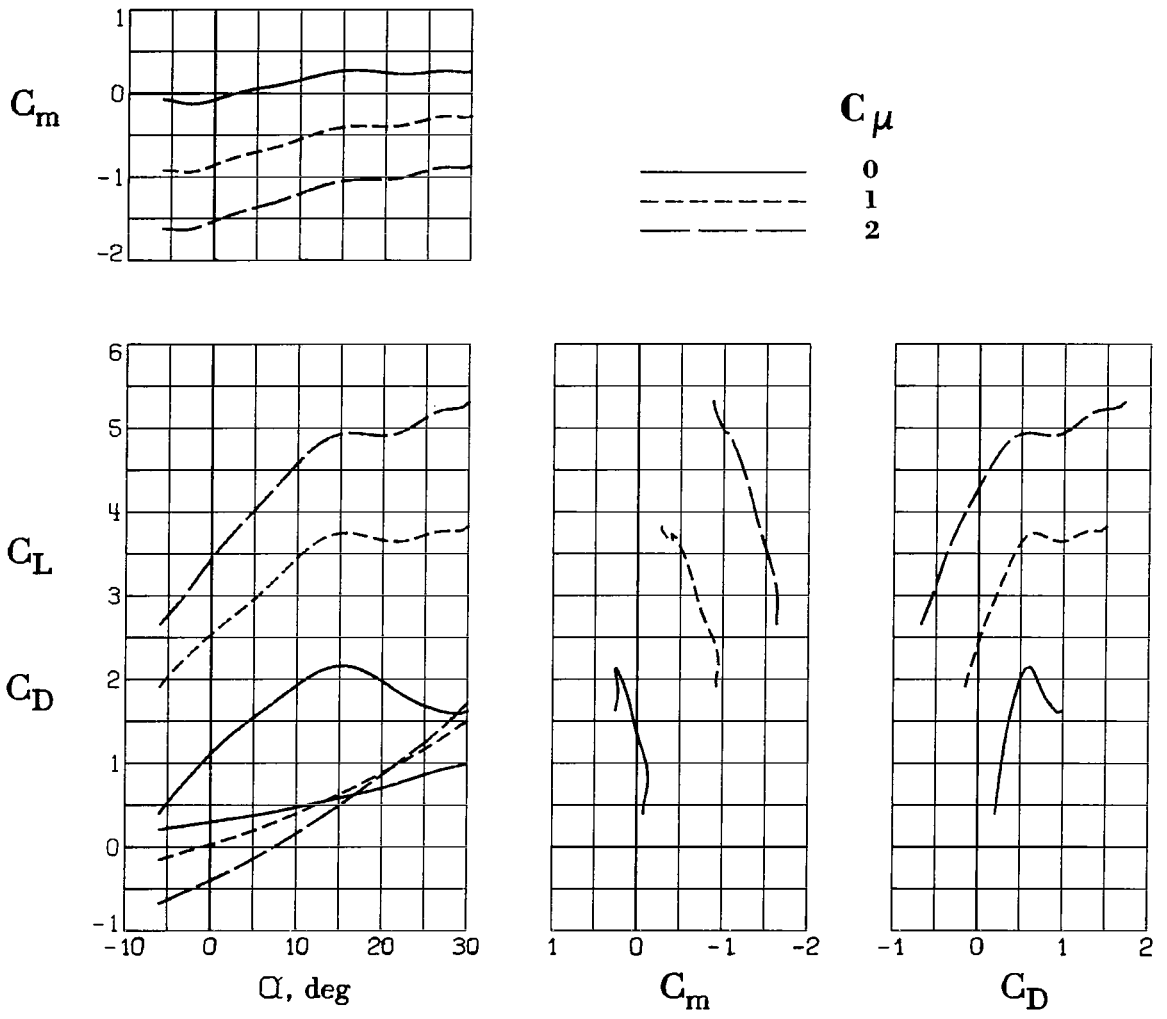

(b) Longitudinal characteristics.

Figure 17.- Concluded.

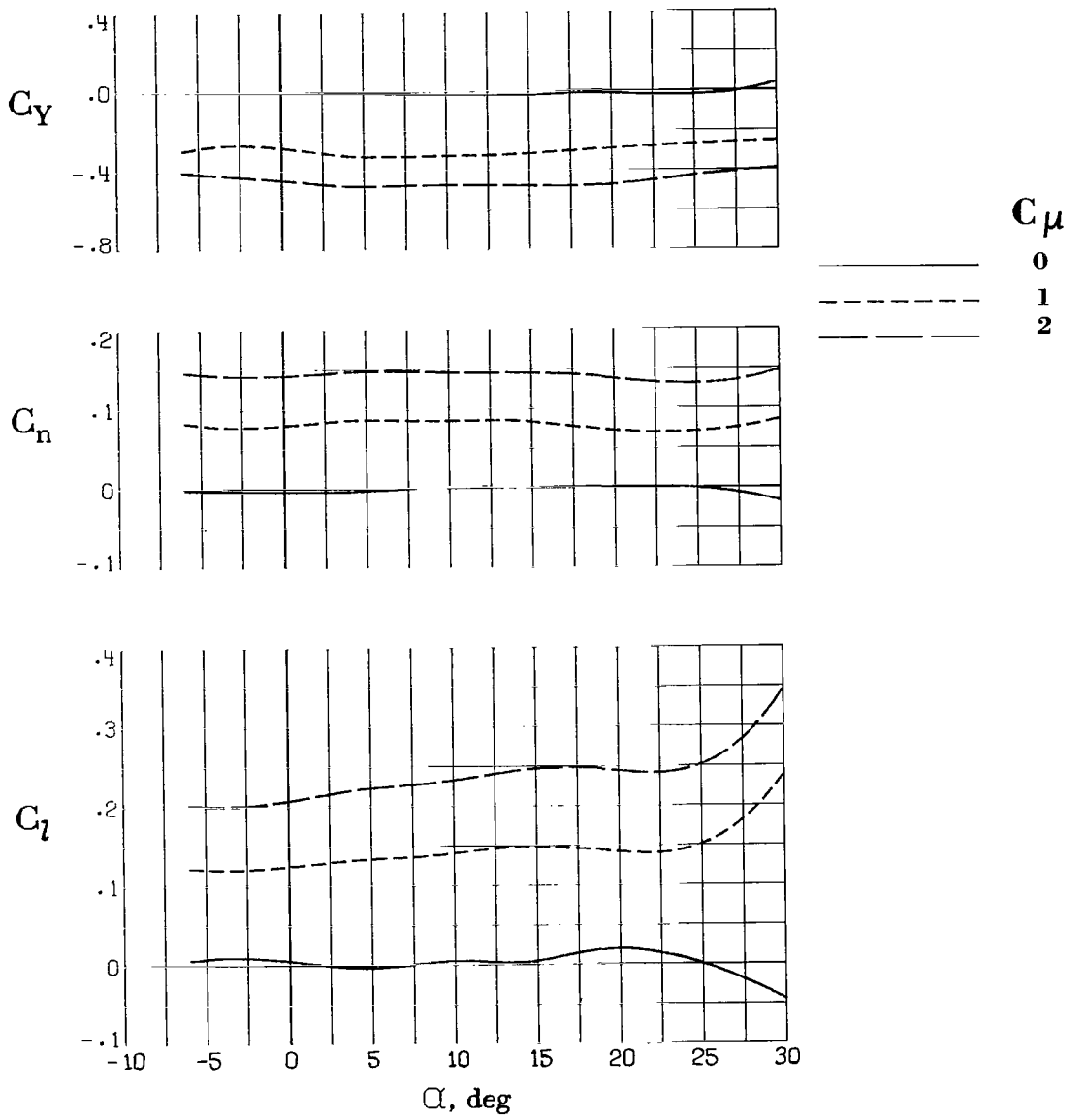

(a) Lateral-directional characteristics.

Figure 18.- Lateral-directional and longitudinal aerodynamic characteristics of model with right engine inoperative, $\delta_f = 72^o$, and $\delta_a = 50^o$. $C_{\mu,le} = 0.013$; $C_{\mu,a} = 0.021$.

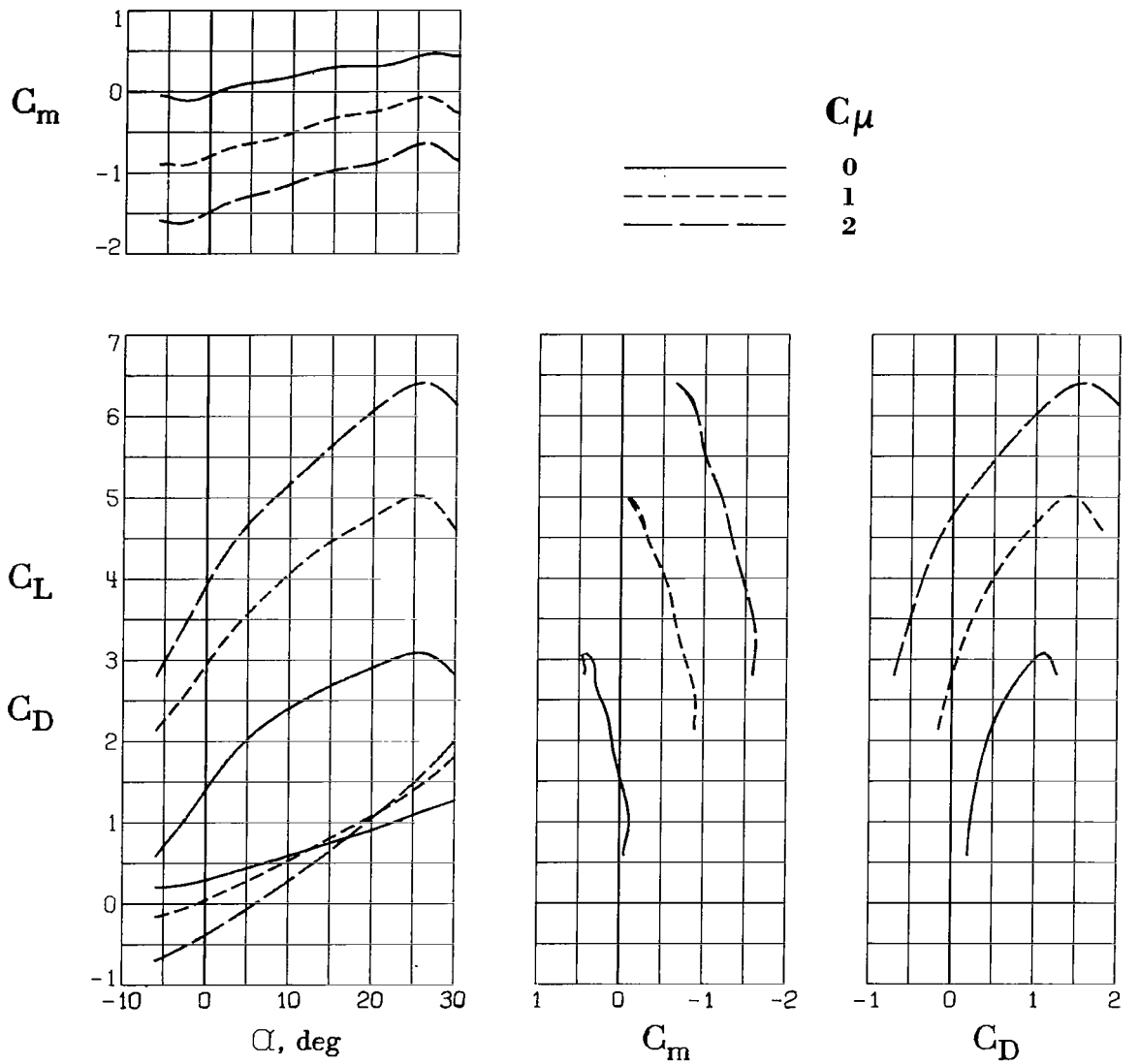

(b) Longitudinal characteristics.

Figure 18.- Concluded.

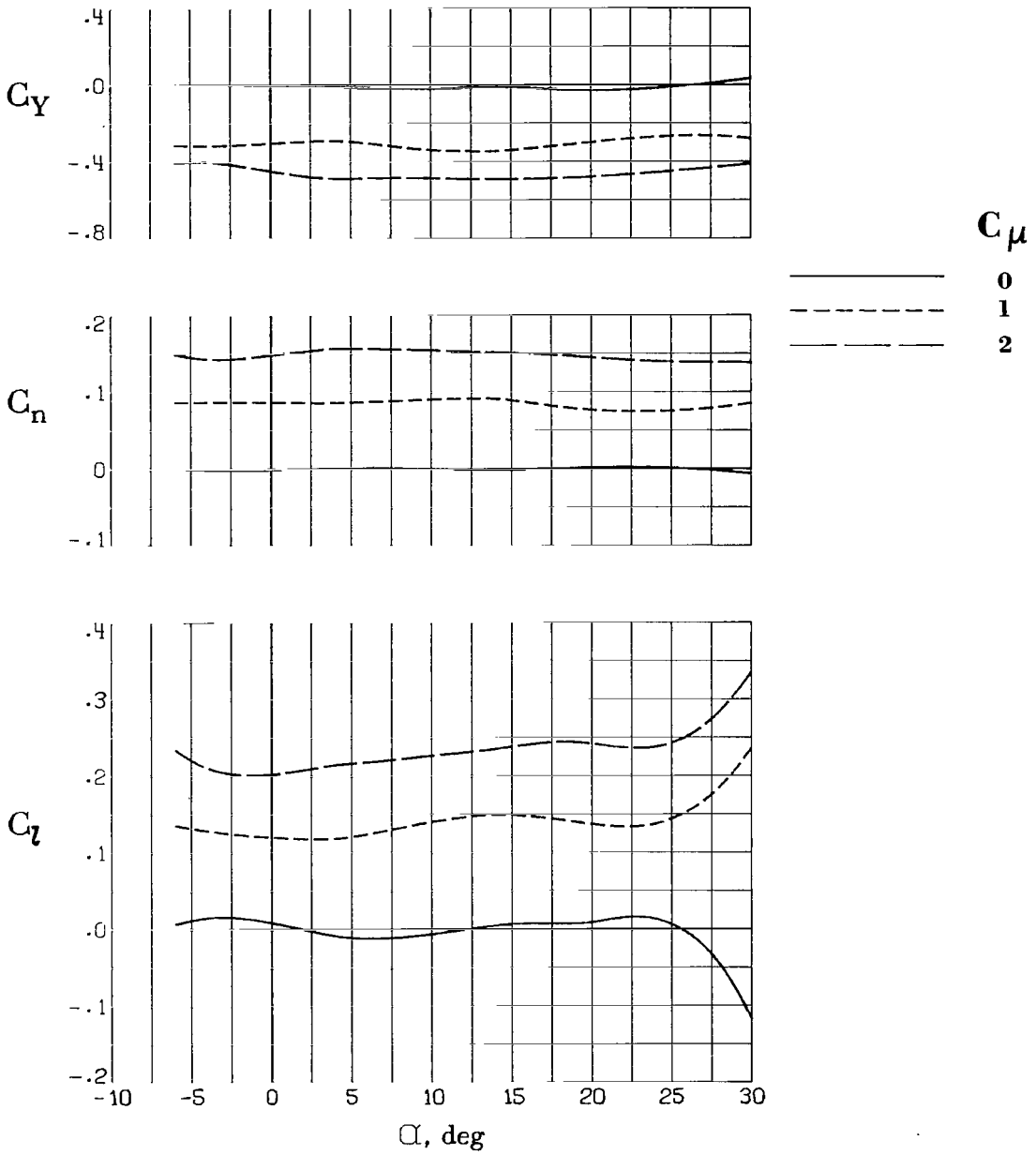

(a) Lateral-directional characteristics.

Figure 19.- Lateral-directional and longitudinal aerodynamic characteristics of model with right engine inoperative and flap slots open behind inoperative engine. $\delta_f = 72^o$; $\delta_a = 50^o$; $C_{\mu,le} = 0.013$; $C_{\mu,a} = 0.021$.

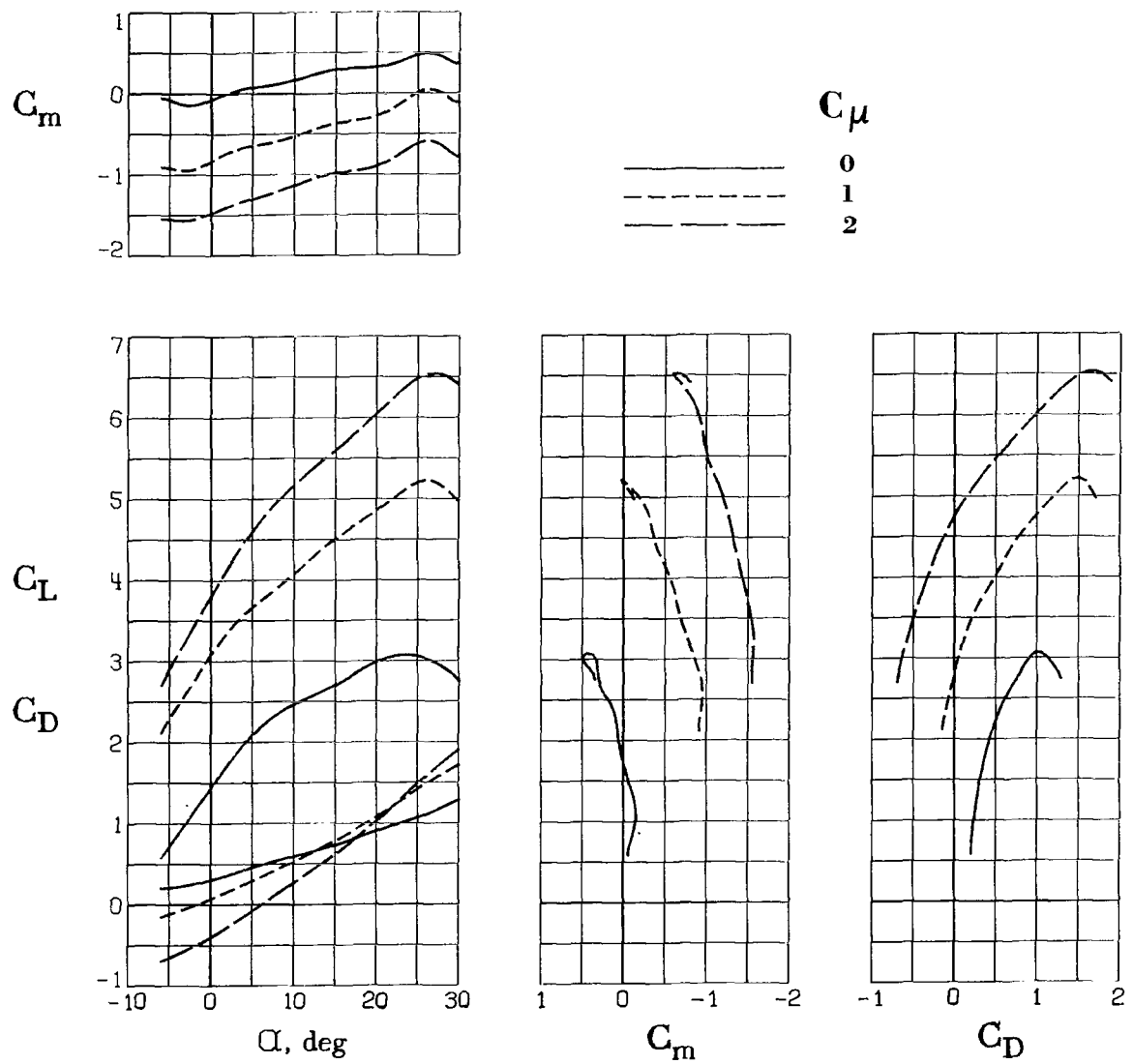

(b) Longitudinal characteristics.

Figure 19.- Concluded.

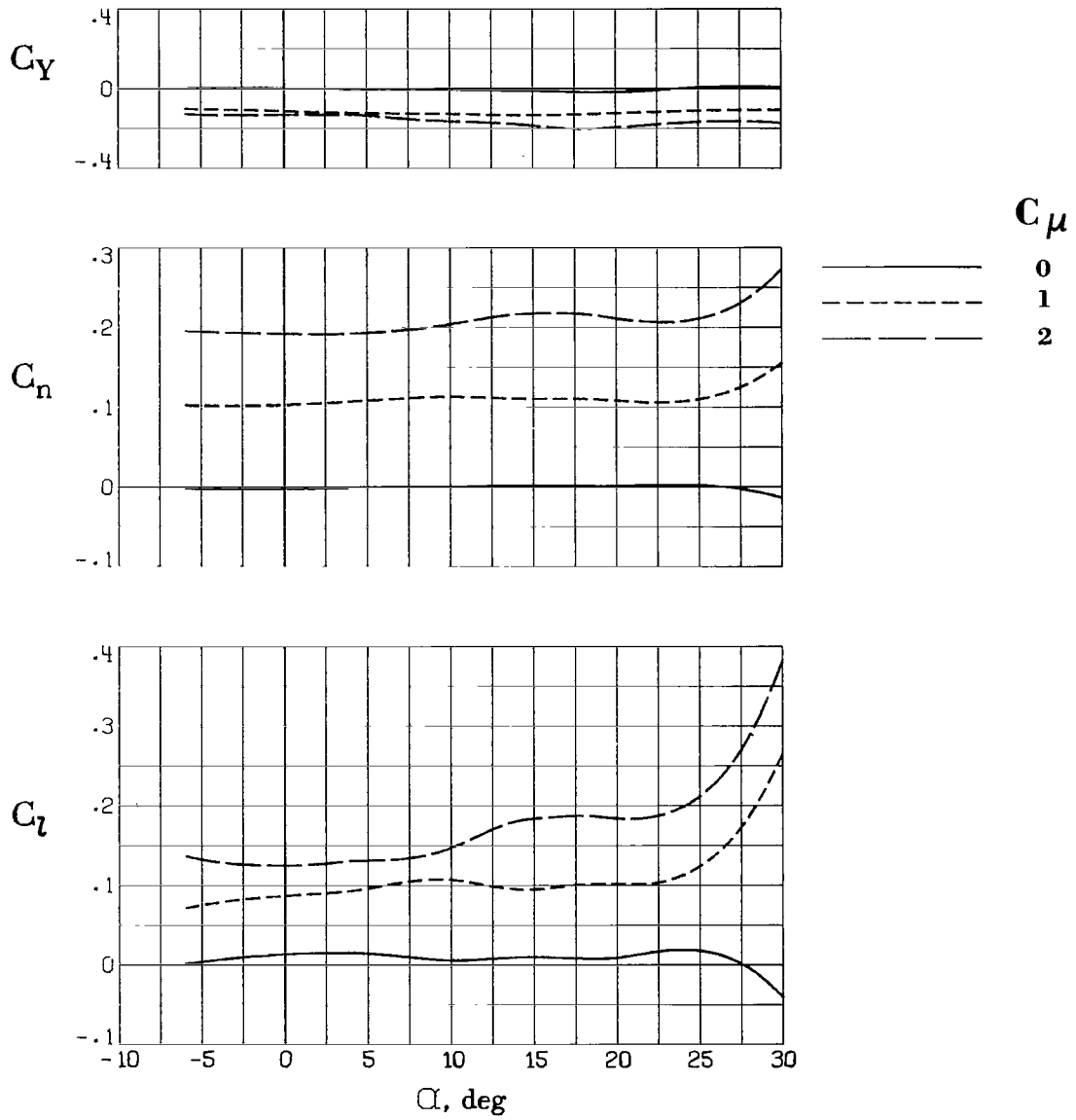

(a) Lateral-directional characteristics.

Figure 20.- Lateral-directional and longitudinal aerodynamic characteristics of model with right engine inoperative, $\delta_f = 32^o$, and $\delta_a = 20^o$. $C_{\mu,le} = 0.013$; $C_{\mu,a} = 0.021$.

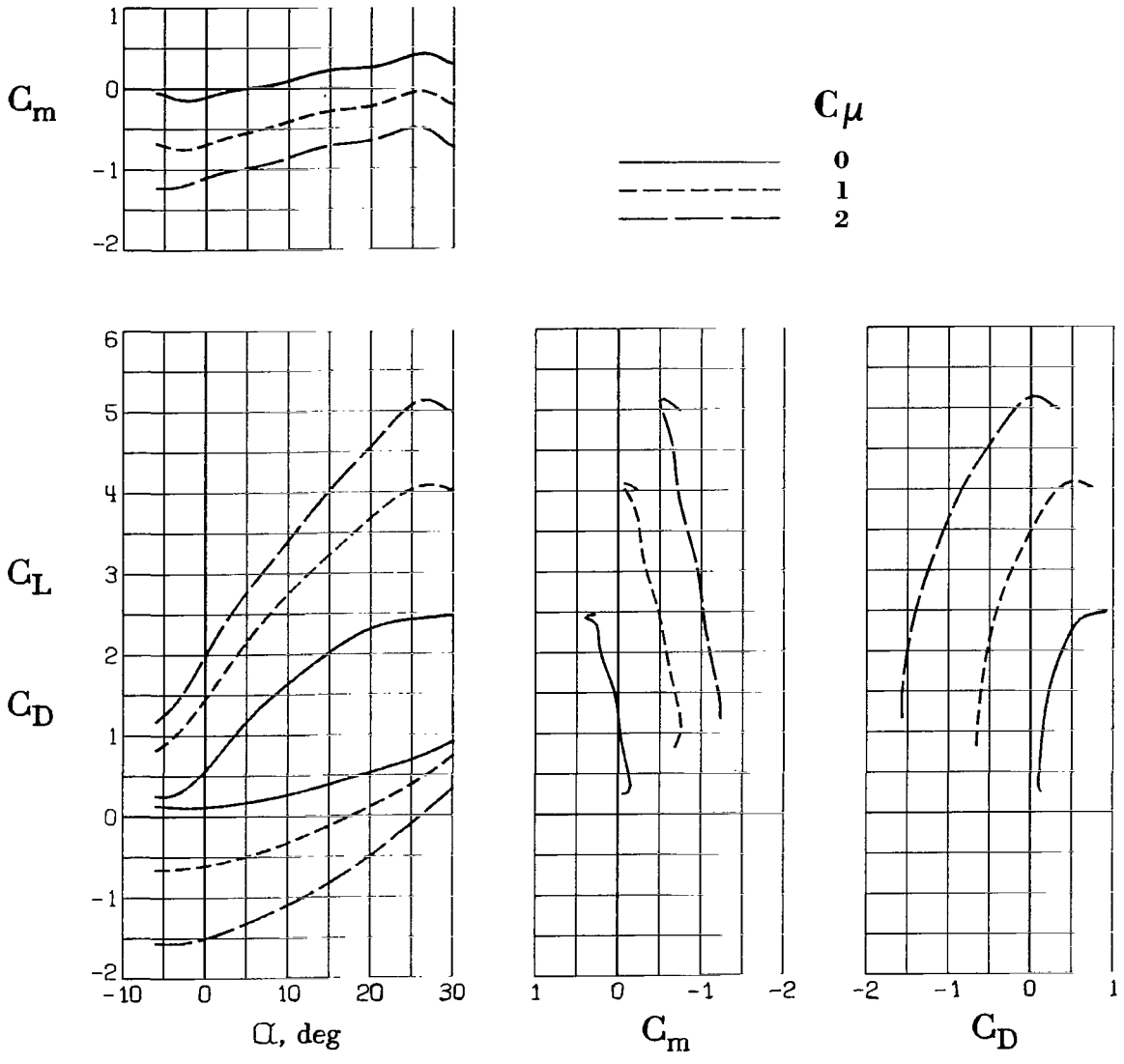

(b) Longitudinal characteristics.

Figure 20.- Concluded.

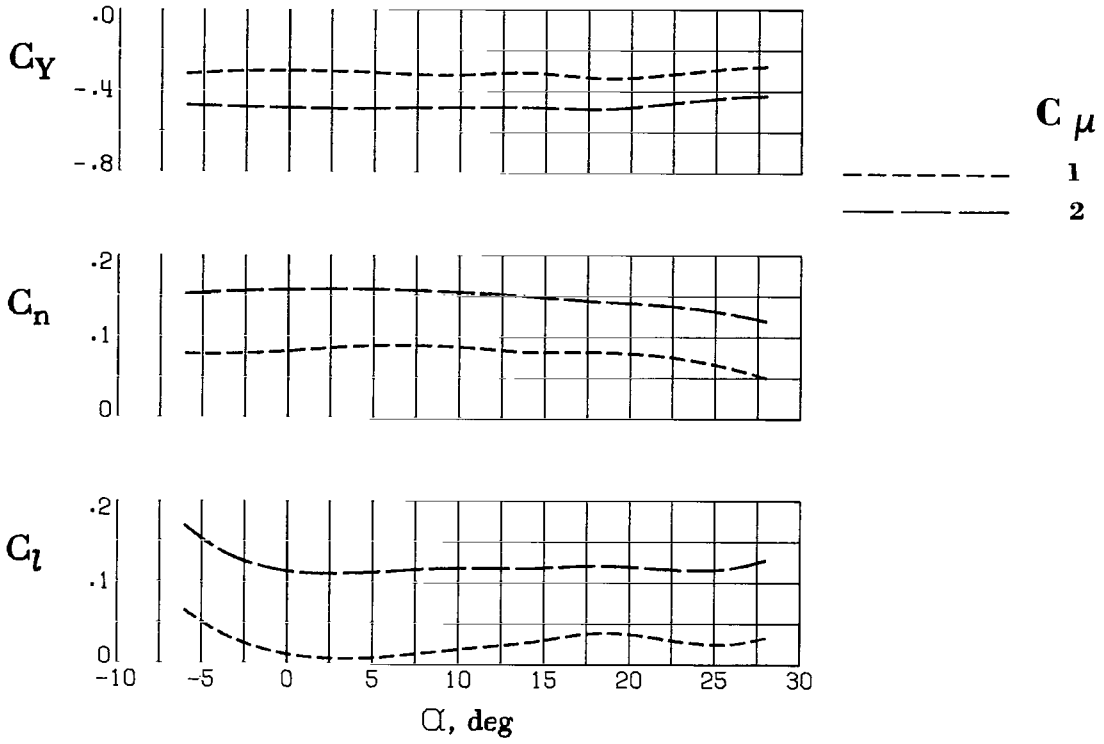

(a) Lateral-directional characteristics.

Figure 21.- Lateral-directional and longitudinal aerodynamic characteristics of model with right engine inoperative, differential ailerons, and asymmetrical BLC. $\delta_f = 72^o$; $\delta_{a,L} = 0^o$; $\delta_{a,R} = 50^o$; $C_{\mu,le,L} = 0$; $C_{\mu,le,R} = 0.015$; $C_{\mu,a,L} = 0$; $C_{\mu,a,R} = 0.03$.

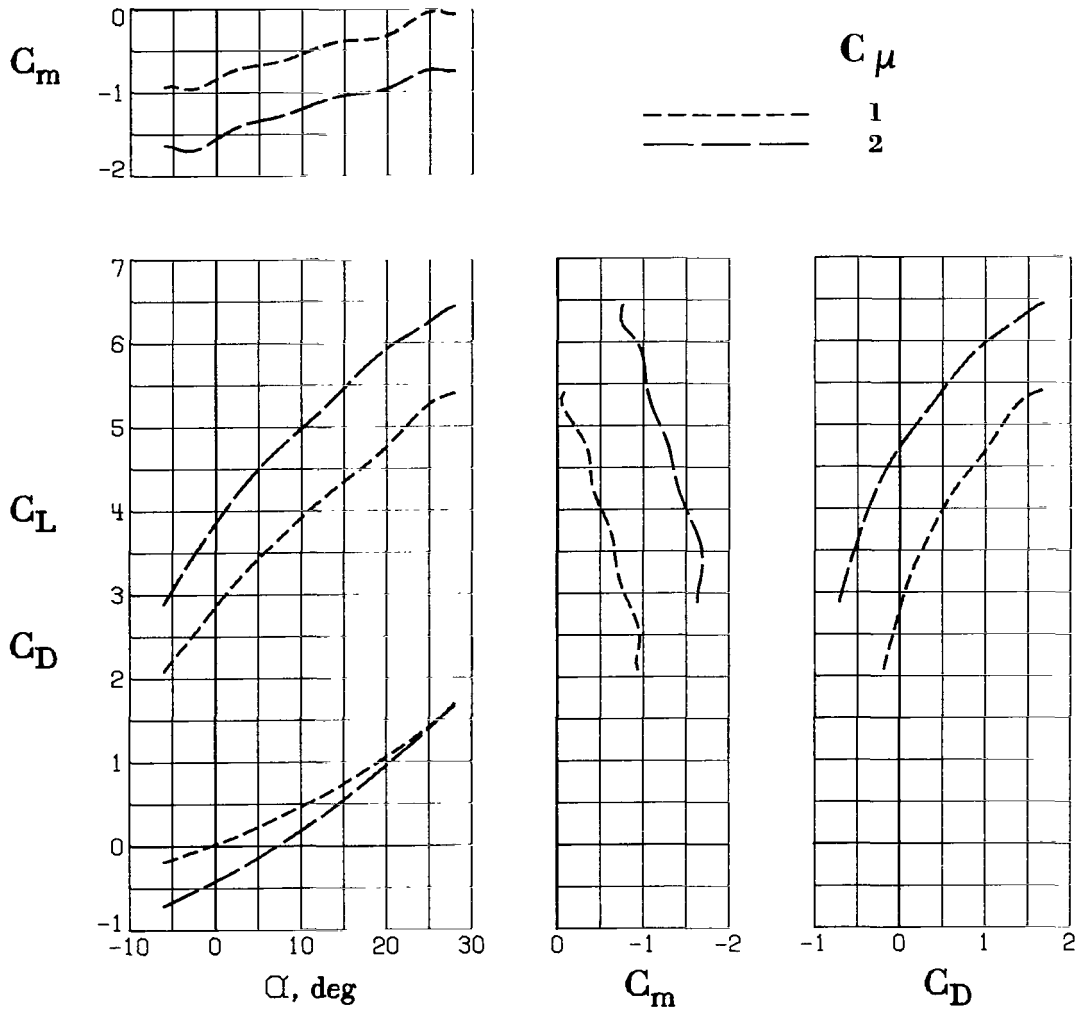

(b) Longitudinal characteristics.

Figure 21.- Concluded.

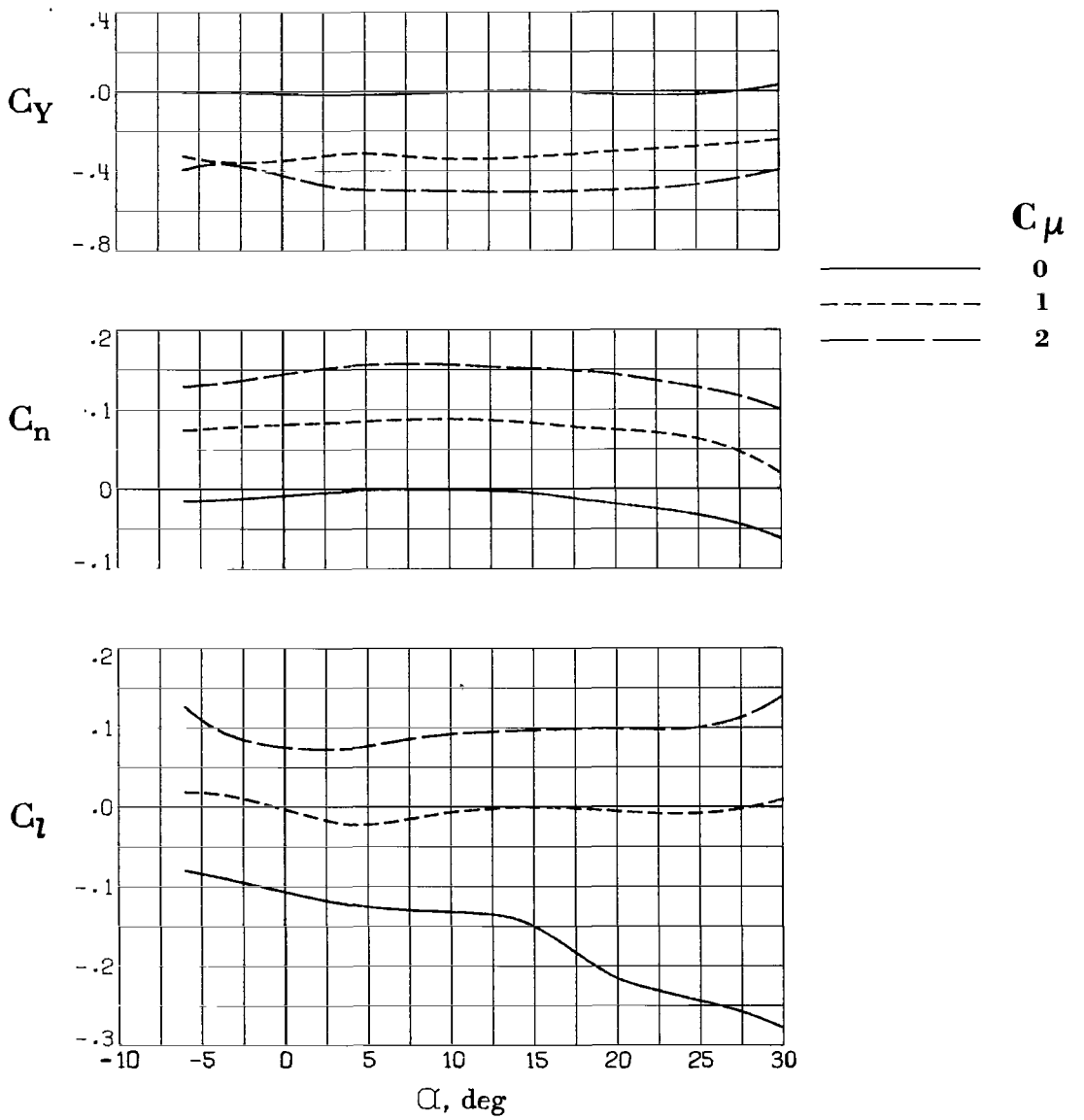

(a) Lateral-directional characteristics.

Figure 22.- Lateral-directional and longitudinal aerodynamic characteristics of model with right engine inoperative, wing-tip spoiler deflected, differential ailerons, and asymmetrical BLC. $\delta_f = 72^o$; $\delta_{a,L} = 0^o$; $\delta_{a,R} = 50^o$; $C_{\mu,le,L} = 0$; $C_{\mu,le,R} = 0.015$; $C_{\mu,a,L} = 0$; $C_{\mu,a,R} = 0.03$; $\delta_{s,L} = 60^o$; $\delta_{s,R} = 0^o$.

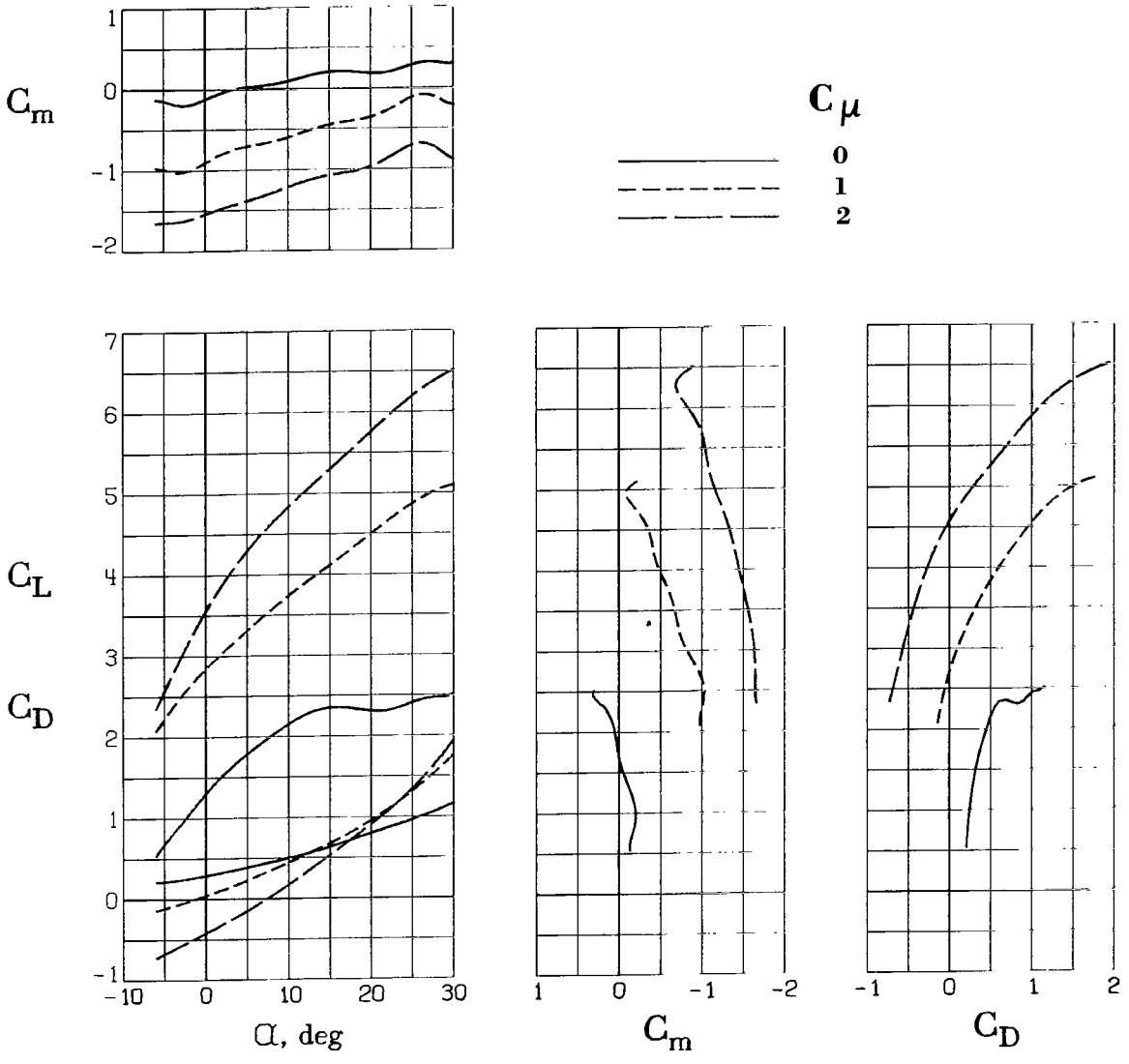

(b) Longitudinal characteristics.

Figure 22.- Concluded.

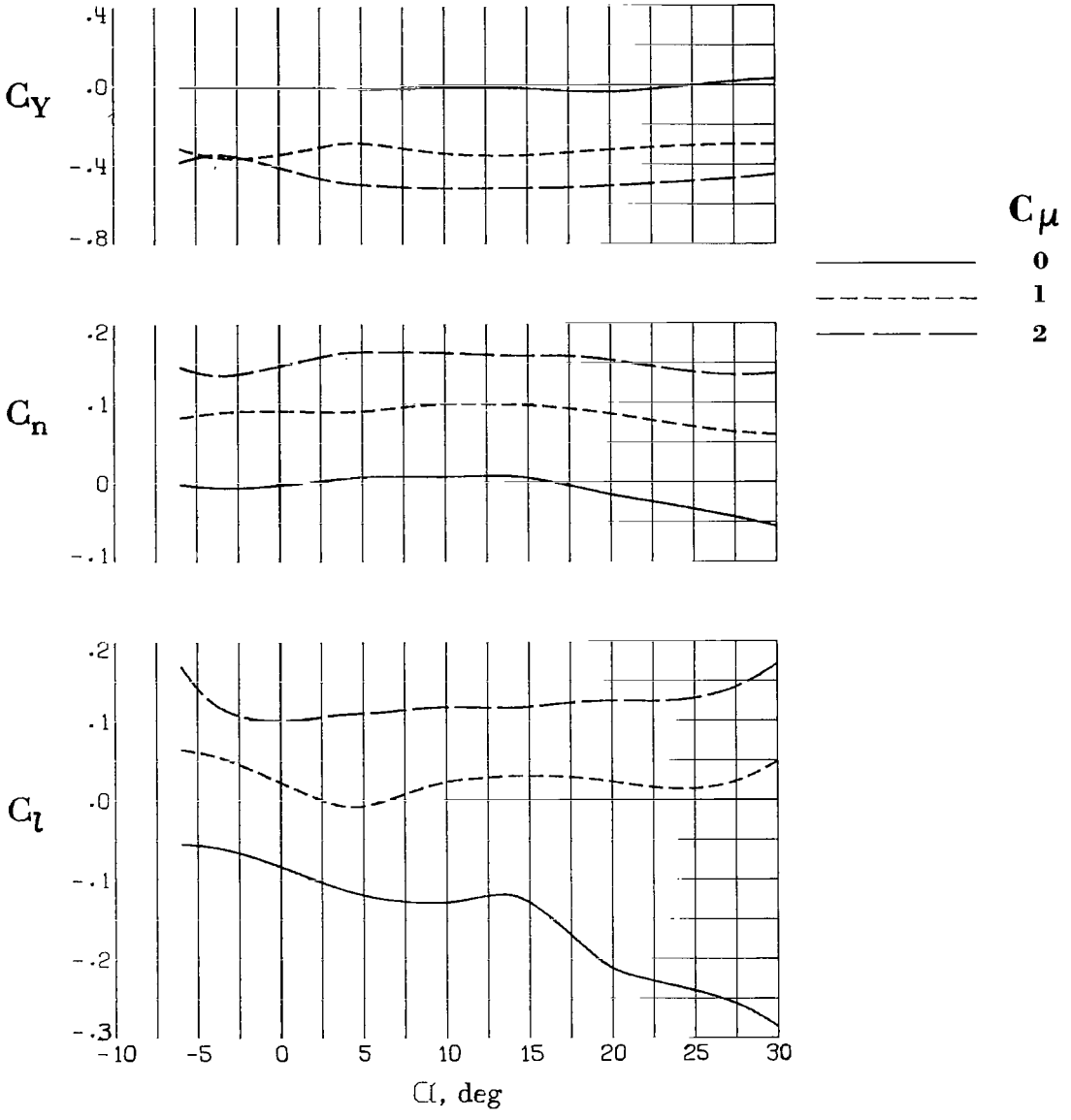

(a) Lateral-directional characteristics.

Figure 23.- Lateral-directional and longitudinal aerodynamic characteristics of model with right engine inoperative, differential flaps, open flap slots behind inoperative engine, differential ailerons, and asymmetrical BLC. $\delta_f = 72^o$; $\delta_{a,L} = 0^o$; $\delta_{a,R} = 50^o$; $\delta_{f,L(midspan)} = 50^o$; $\delta_{f,R(midspan)} = 70^o$; $C_{\mu,le,L} = 0$; $C_{\mu,le,R} = 0.015$; $C_{\mu,a,L} = 0$; $C_{\mu,a,R} = 0.03$.

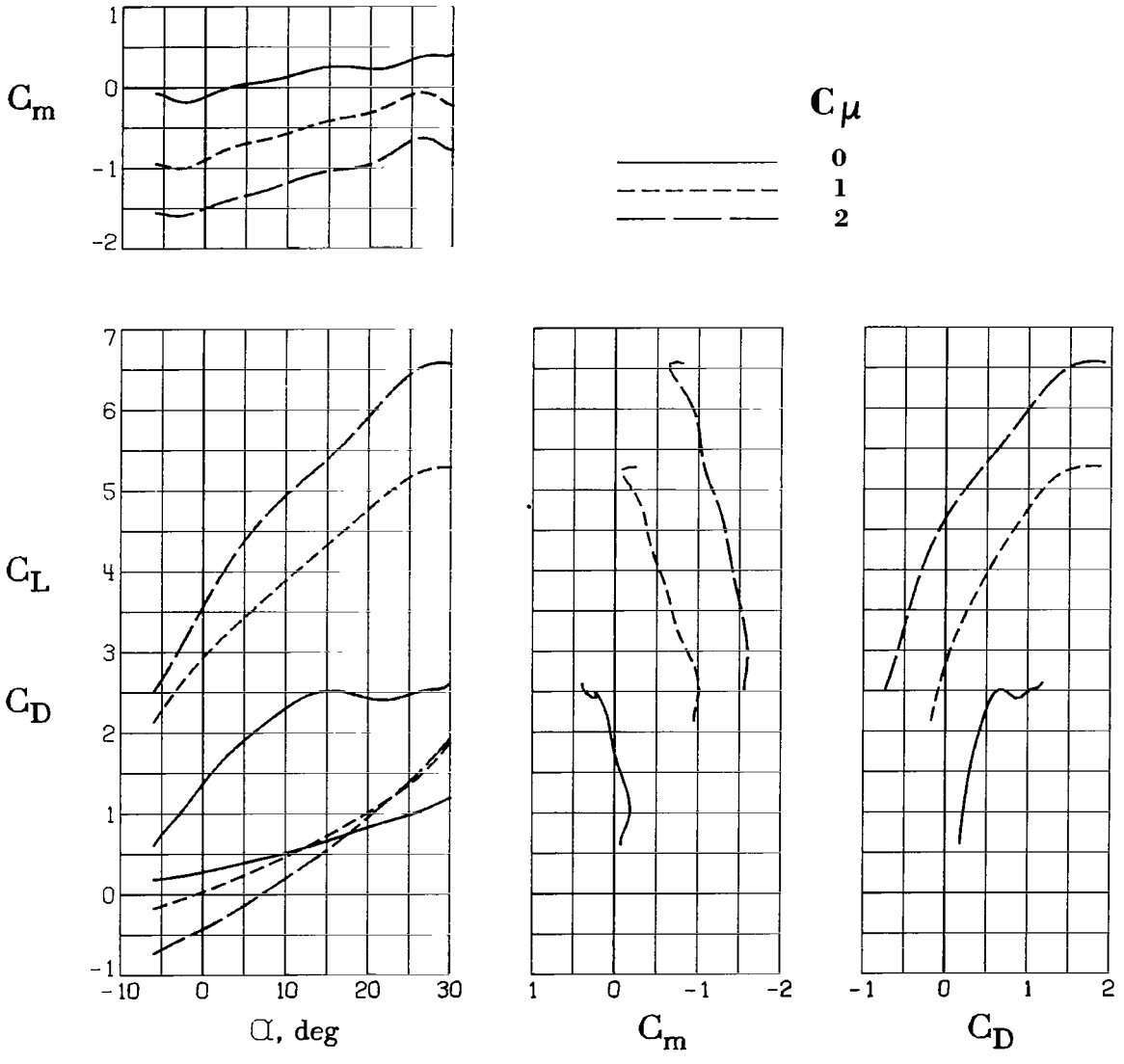

(b) Longitudinal characteristics.

Figure 23.- Concluded.

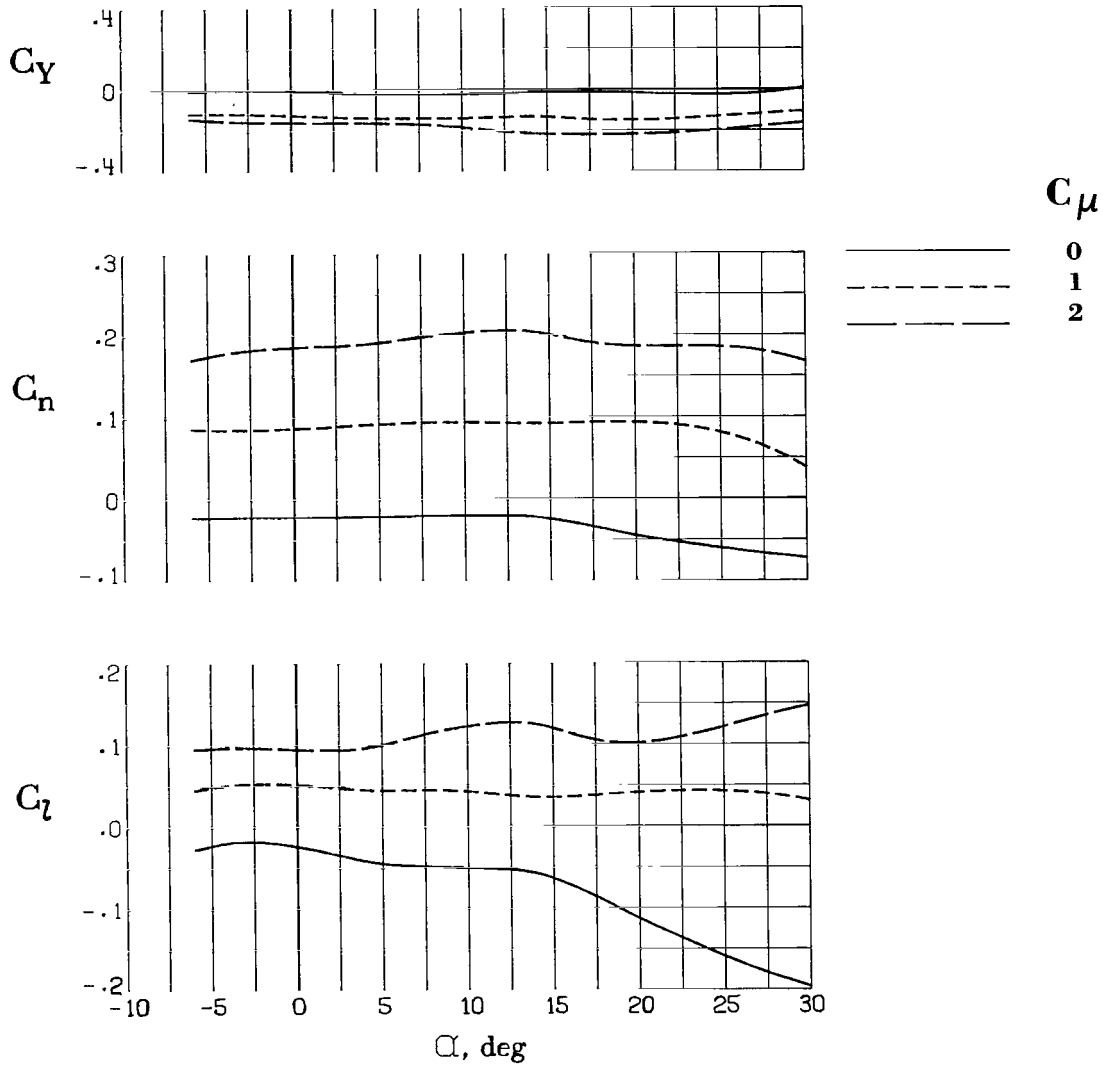

(a) Lateral-directional characteristics.

Figure 24.- Lateral-directional and longitudinal aerodynamic characteristics of model with right engine inoperative, differential ailerons, and asymmetrical BLC. $\delta_f = 32^o$; $\delta_{a,L} = 0^o$; $\delta_{a,R} = 20^o$; $C_{\mu,le,L} = 0$; $C_{\mu,le,R} = 0.015$; $C_{\mu,a,L} = 0$; $C_{\mu,a,R} = 0.03$.

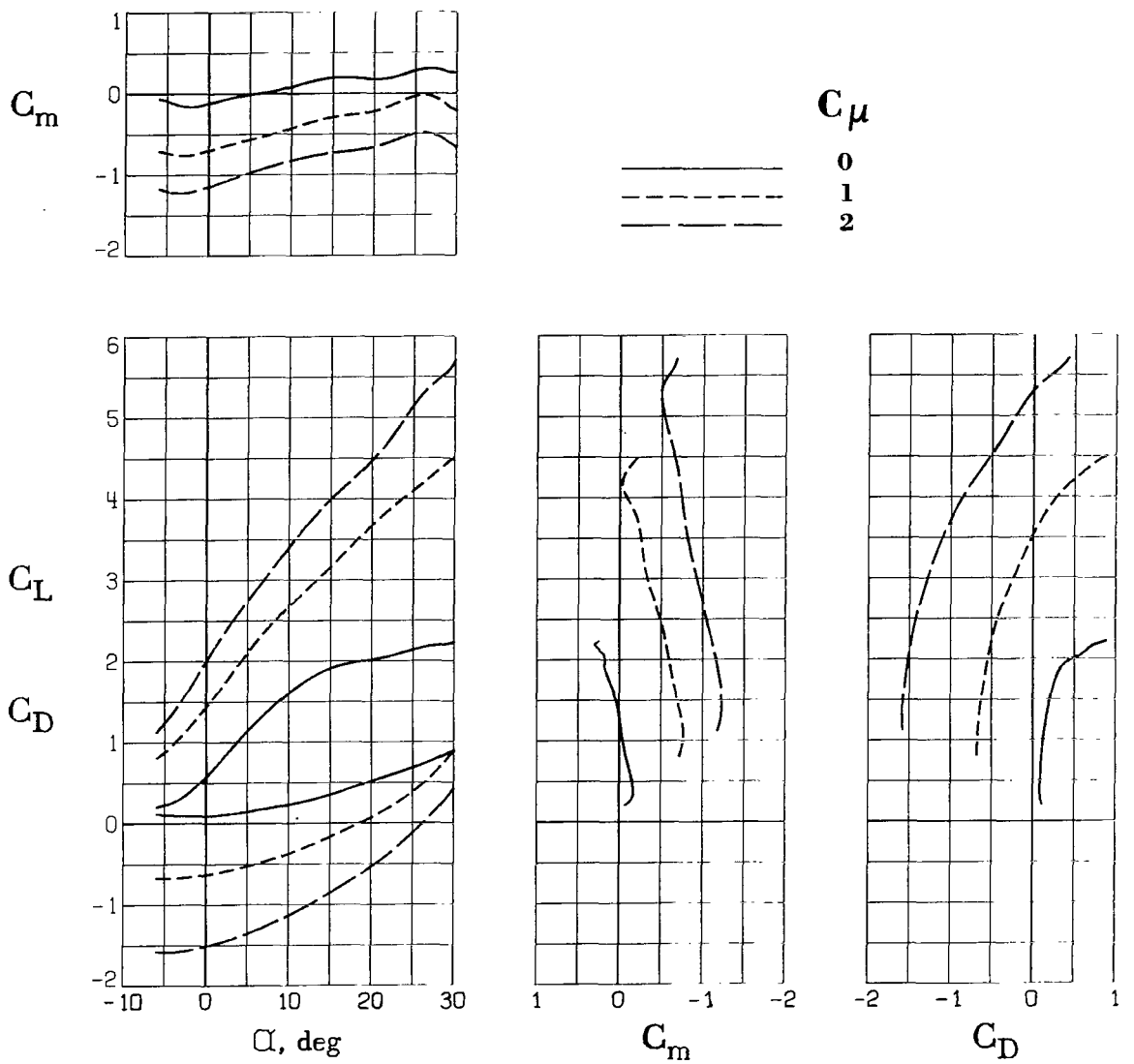

(b) Longitudinal characteristics.

Figure 24.- Concluded.

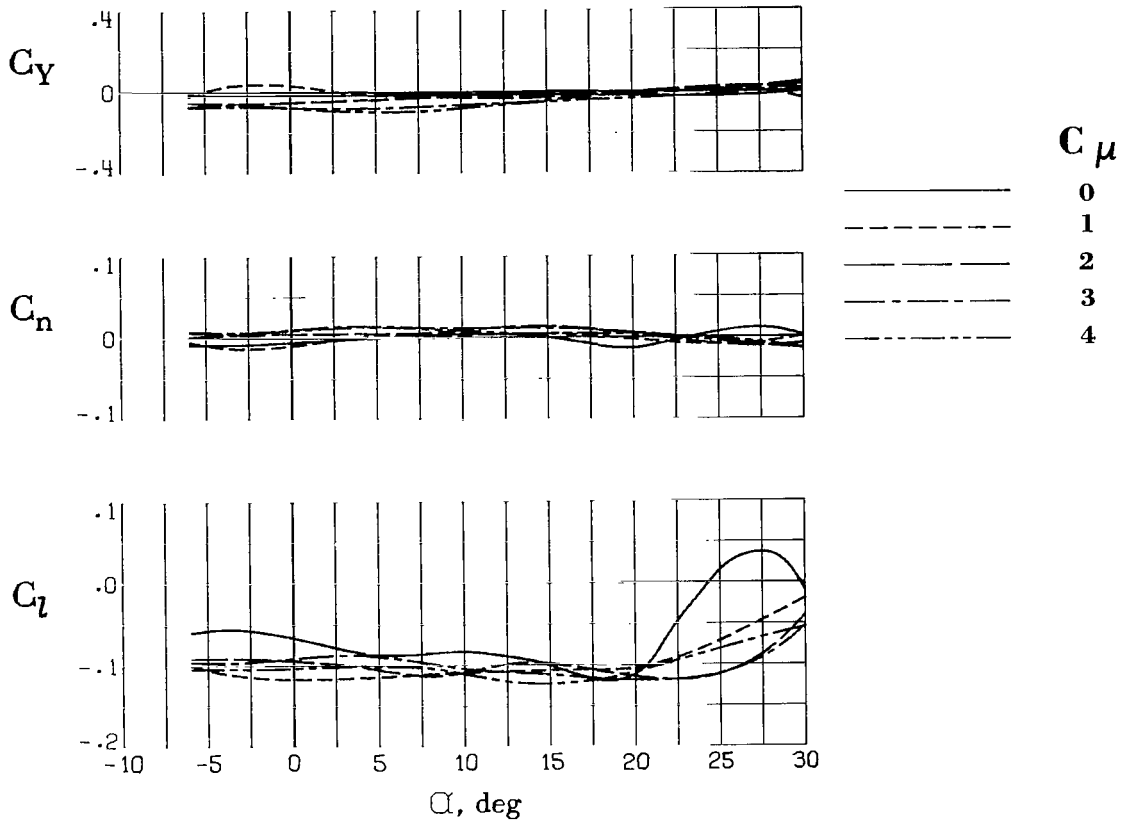

(a) Lateral-directional characteristics.

Figure 25.- Lateral-directional and longitudinal aerodynamic characteristics of model with symmetrical power and semispan spoiler. $\delta_f = 72^o$; $\delta_a = 50^o$; $C_{\mu,le} = 0$; $C_{\mu,a} = 0.021$; $\delta_{s,L} = 60^o$; $\delta_{s,R} = 0^o$.

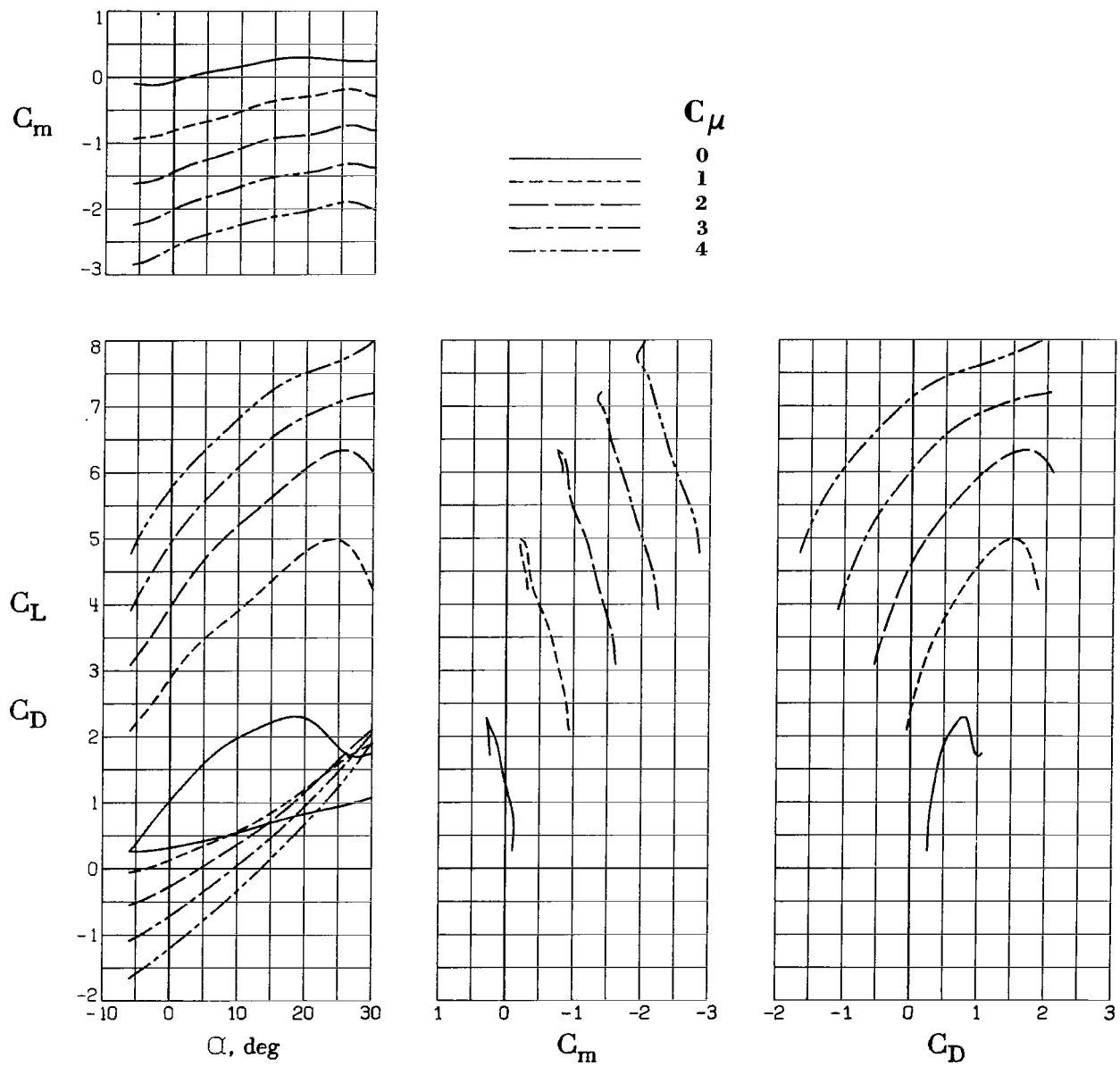

(b) Longitudinal characteristics.

Figure 25.- Concluded.

II. STATIC-PRESSURE CHARACTERISTICS

Boyd Perry III

SUMMARY

An experimental investigation has been performed to determine the static-pressure distributions on the fuselage, leading-edge Krueger flap, wing, upper-surface blown flap, double-slotted flap, and aileron of a large-scale upper-surface blown jet-flap model with turbofan engines. Section normal-force coefficients, which are a measure of the static loading, were determined from the static-pressure data. Results of the investigation indicated that the highest section normal-force coefficients were obtained at spanwise wing locations behind the engine exhaust nozzles. The magnitudes of the section normal-force coefficients behind the nozzle were very sensitive to both flap deflection angle and engine power setting, but fairly insensitive to angle of attack. Tests with one engine inoperative indicated very little lift carryover from the powered to the unpowered side of the model.

INTRODUCTION

This part of the report presents chordwise static-pressure distributions and spanwise normal-force-coefficient variations for the large-scale upper-surface blown jet-flap (USB) model described in part I. Investigations giving the results of some previous pressure-distribution studies for USB configurations are presented in references 1 to 3. The investigation included tests to determine the effects of angle of attack, flap deflection angle, engine power setting, and one engine inoperative on the static-pressure distributions of the wing. Results are presented as plots of pressure coefficient against the nondimensional chordwise coordinate and plots of section normal-force coefficient against the nondimensional spanwise coordinate.

SYMBOLS

Dimensional data were obtained in U.S. Customary Units and are presented herein in both the International System of Units (SI) and U.S. Customary Units.

a' integration limit corresponding to location of leading edge of either wing or Krueger flap projected onto wing reference plane and expressed as fraction of local wing chord

b	wing span, m (ft)
b'	integration limit corresponding to location of trailing edge of USB flap, double-slotted flap, or aileron, projected onto wing reference plane and expressed as fraction of local wing chord
C_p	pressure coefficient, $\frac{p - p_\infty}{q_\infty}$
C_μ	static thrust coefficient, $\frac{T}{q_\infty S}$
$C_{\mu,a}$	static thrust coefficient of boundary-layer-control system for drooped aileron
$C_{\mu,le}$	static thrust coefficient of boundary-layer-control system for wing leading edge
c	local wing chord, m (ft)
c_n	section normal-force coefficient, $-\int_{a'}^{b'} \left(C_{p,u} - C_{p,l}\right) d\left(\frac{x}{c}\right)$
p	local static pressure, Pa (lb/ft^2)
p_∞	free-stream static pressure, Pa (lb/ft^2)
q_∞	free-stream dynamic pressure, Pa (lb/ft^2)
S	wing area, m^2 (ft^2)
T	static thrust force, N (lb)
x	chordwise coordinate, m (ft)
y	spanwise coordinate, m (ft)
α	angle of attack, deg (see fig. 1 of part I)
δ_a	aileron deflection, deg

δ_f deflection of USB and double-slotted flap (deflected together), deg (see figs. 2 and 3 of part I)

Subscripts:

l lower

u upper

Abbreviation:

USB upper-surface blown

MODEL

The model used in these tests is shown in figure 2 of part I of this report. Details of the model and model installation are presented in part I.

INSTRUMENTATION

The model was instrumented with static-pressure orifices at eight spanwise stations as shown in figure 1. The instrumentation included a total of 270 pressure orifices on portions of the fuselage, wing, leading-edge Krueger flap, USB flap, double-slotted flap, and aileron. No orifices were located on either the upper or the lower surfaces of the engine nacelles. The chordwise location for each orifice at each station (both upper and lower surfaces) is presented in table I. All 270 orifices were used during tests for a flap deflection angle of 32°. Four of these orifices were not used for the flap deflection angle of 72° (one less orifice per station at stations 3 to 6 on the upper surface of the USB flap) because of the locations of the flap-support hardware.

Forty-eight-port pressure scanning valve transducers were used to sample the pressure data. The transducer pressure range corresponding to pressure orifices on the upper surfaces of the wing and USB flap at stations 3 to 6 was ±34.5 kPa (±5 lb/in^2) and the pressure range corresponding to all other pressure orifices on the model was ±6.9 kPa (±1 lb/in^2). The pressure data obtained are believed to be accurate to ±1 percent of the full pressure range of the pressure transducers used.

TESTS

A detailed description of the wind-tunnel test procedures and test conditions is given in part I of this report. The aerodynamic data presented in part I and the pressure-distribution data presented in this part of the report were obtained for the same test conditions and therefore complement each other. Test conditions for the data presented herein are given in table II.

PROCEDURE

Static-pressure data are presented in figures 2 to 4 as plots of pressure coefficient C_p as a function of nondimensional chordwise position x/c for each pressure station. The nondimensional chordwise position of a given pressure orifice is based on its location when projected onto the reference plane of the basic wing, as illustrated in the following sketch:

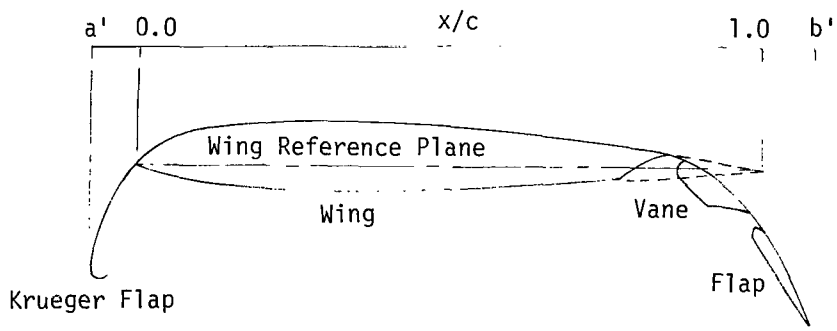

Thus, some nondimensional chordwise positions have values less than 0 and others have values greater than 1. Values less than 0 include those pressure orifices on the fuselage forward of the wing leading edge and those pressure orifices on the Krueger flap. Values greater than 1 include those pressure orifices on the fuselage and those on the vane and flap aft of the projected wing trailing edge.

The section normal-force coefficient c_n represents the force perpendicular to the local wing chord and it is obtained from the chordwise pressure-coefficient distribution. The section normal-force coefficient is expressed as

$$c_n = -\int_{a'}^{b'} \left(C_{p,u} - C_{p,\ell}\right) d\left(\frac{x}{c}\right) \tag{1}$$

where a' and b' are the locations shown in the preceding sketch. (For the two rows of pressure orifices on the fuselage, the integration limits a' and b' correspond to

the projections of the wing leading and trailing edges at those locations; i.e., $a' = 0.0$ and $b' = 1.0$.) Section normal-force coefficients were obtained from the chordwise pressure-coefficient distributions by fairing through plotted points and graphically integrating the faired data to obtain c_n as expressed by equation (1). When c_n is plotted as a function of nondimensional semispan position $y/(b/2)$, a measure of the static aerodynamic loading of the wing is provided.

As discussed in the section "Corrections" of part I of this report, the basic data were corrected for interference induced by the wind-tunnel jet boundary as discussed in references 4 and 5. Values of both section normal-force coefficient c_n and angle of attack α for constant values of thrust coefficient C_μ were obtained by interpolation of the basic corrected data.

RESULTS AND DISCUSSION

Chordwise Pressure-Coefficient Distributions

Figures 2 to 4 contain chordwise static-pressure-coefficient distributions on the upper and lower surfaces of the model. Test conditions for figures 2 to 4 include a range of thrust coefficients for symmetrical power as well as left-engine-inoperative and right-engine-inoperative conditions. The data in these figures indicate that very large pressure coefficients exist on the USB flap in the region behind the engine. All data were obtained with exhaust nozzle deflectors on (see figs. 5 and 7 of part I).

To visualize typical distributions more easily, the pressure coefficients at each station in figure 3(c) have been connected with faired curves. The remarks which follow, although referring specifically to figure 3(c), are also generally applicable to the chordwise distributions for the other power-on conditions. Since spanwise pressure stations 3 to 6 are within or very close to the spanwise extent of the exhaust nozzle, the pressure distributions at these stations are greatly influenced by the engine exhaust. The influence of the engine exhaust appears in the pressure distributions as both modestly large positive pressures and very large negative pressures on the upper surfaces of the wing and USB flap. The positive pressures at stations 3, 4, and 5 from approximately 40 percent to 60 percent chord are due to the deflected jet exhaust impinging directly on the wing upper surface. The positive pressures at stations 3, 4, 5, and 6 at approximately 80 percent chord are not clearly understood but similar results have been reported previously (see refs. 1 and 2). The 80 percent chordwise location corresponds to the knee of the flap, and the magnitudes of the positive pressures at this location are larger for $\delta_f = 32^\circ$ than for $\delta_f = 72^\circ$ (compare figs. 2 and 3). The area of positive pressure on the upper surface at station 1 from approximately 60 percent to 100 percent chord is present only for power-on conditions (compare figs. 2(a) and 2(c), for example). The reason for the

positive pressures along the fuselage centerline is the spreading of the high-velocity exhaust after it impinges on the upper surface of the wing. As before, the magnitudes of the positive pressures at this location are larger for $\delta_f = 32^o$ than for $\delta_f = 72^o$. The area of positive pressure at station 2 at approximately 20 percent chord is present for both power-on and power-off conditions and is attributed to flow separation which was evident from tuft studies. The pressure distributions at stations 7 and 8 are typical of lift-pressure distributions for wings with boundary-layer control and high-lift devices such as the wing of the present model.

Even at angles of attack approaching 30^o the pressure distributions outboard indicate that the wing tip has not stalled. The pressure distributions at stations 7 and 8 in figures 2(j), 2(k), 2(l), 3(d), 3(e), and 3(f) indicate relatively high lift which is attributed to the boundary-layer control used on the ailerons and the wing leading edge.

Figures 2(m) and 2(n) contain chordwise pressure-coefficient distributions which are based on engine-exhaust dynamic pressure (10.49 kPa (219 lb/ft^2)) rather than on free-stream dynamic pressure. Figure 2(m) includes the wind-on condition (q_∞ = 91.0 Pa (1.9 lb/ft^2)) and figure 2(n) includes the wind-off condition (q_∞ = 0 Pa (0 lb/ft^2)). The spanwise location for maximum C_p occurs along the engine centerline (station 5) for both wind-on and wind-off conditions. Except for stations 7 and 8, which are removed from the influence of the engine, the pressure distributions at the remaining six stations compare very well for wind-on and wind-off conditions. The shapes and magnitudes of the distributions, especially at stations 3, 4, and 5, indicate that, for powered-lift systems such as the configuration of the present investigation, it may be possible to determine the critical loads and load distributions from static tests alone.

Spanwise Variation of Section Normal-Force Coefficient

Figures 5 to 8 contain plots of section normal-force coefficient c_n as a function of nondimensional semispan position $y/(b/2)$. Figure 5 presents results relating to variations in angle of attack. In figure 6 a comparison is made for two flap deflection angles. A comparison for three thrust coefficients is given in figure 7. The effects of one engine inoperative are shown in figure 8. Note that the location of the nozzle is identified in each of these figures. Because no pressure orifices were located on the nacelles, c_n does not include contributions from the nacelles. The individual curves in figures 5 to 8 were obtained by fairing curves through values of c_n obtained at the eight locations indicated in figure 1. There is a pronounced dip in most curves in figures 5 to 8 which occurs inboard of the engine centerline at station 4. Because no data were taken at a comparable station outboard of the engine centerline, it is not known if the dip is repeated.

Effect of angle of attack.- Figure 5 shows spanwise variation of section normal-force coefficient for angles of attack of -1.27^o, 8.48^o, 18.30^o, and 28.33^o. Examination of fig-

ure 5 indicates that from the fuselage centerline to a position slightly outboard of the nozzle location, the magnitudes of the spanwise normal-force-coefficient variations are primarily dependent on the engine exhaust and show little dependence on angle of attack. However, outboard of the nozzle location the normal-force coefficient increased with increasing angle of attack as might be expected.

Effect of flap deflection angle.- Figure 6 shows spanwise variation of section normal-force coefficient for flap deflection angles of 72° and 32°. The angles of attack were 27.85° for $\delta_f = 72^{\circ}$ and 26.45° for $\delta_f = 32^{\circ}$ (the difference in α is considered to have a negligible effect on the comparison). Examination of figure 6 indicates that the normal-force coefficients on the fuselage are almost the same for the two flap deflection angles. Outboard near the wing tip, normal-force coefficients for the 72° flap setting are approximately 10 percent larger than those for the 32° flap setting. A significant increase in normal-force coefficient occurs in the region behind the exhaust nozzle, as expected. In this region, normal-force coefficients for the 72° flap setting are considerably larger than those for the 32° flap setting. Also of interest are c_n variations from the midpoint of the exhaust nozzle to slightly outboard of the exhaust nozzle. For the 72° flap deflection, maximum values of c_n occurred within the spanwise extent of the exhaust nozzle; for the 32° flap deflection, maximum values of c_n occurred outboard of the exhaust nozzle. The locations of these maximum values of c_n indicate that there was more spanwise spreading of the high-velocity exhaust for the smaller flap deflection angle than for the higher flap deflection angle.

Effect of engine thrust coefficient.- Figure 7 shows spanwise variation of section normal-force coefficient for thrust coefficients of 0, 2.15, and 3.93. The angles of attack were 9.62°, 8.62°, 7.95° for the three thrust coefficients (the difference in α is considered to have a negligible effect on the comparison). Examination of figure 7 indicates that, from the fuselage centerline to approximately 80 percent semispan, the normal-force coefficients increased with increasing thrust coefficient. At the nozzle centerline, the normal-force coefficient for maximum thrust was an order of magnitude greater than that for zero thrust. Outboard, near the wing tip and well removed from the influence of the engine exhaust, the section normal-force coefficients for the two power-on conditions approached a common value, an indication that near the wing tip c_n is independent of C_μ.

Effect of one engine inoperative.- Figure 8 shows spanwise variation of section normal-force coefficient on the right wing of the model for both engines operating, left engine inoperative, right engine inoperative, and both engines inoperative. Figure 8 indicates that the normal-force-coefficient variations for both engines on and right engine only are very nearly the same, with maximum variations isolated to the region behind the exhaust nozzle. The spanwise normal-force-coefficient variations for right engine

inoperative and both engines inoperative are almost the same, which indicates that there is very little lift carryover for this model. This result is not in agreement with results from other USB configurations with one engine inoperative (for example, see ref. 3). One reason for the absence of lift carryover for the present model could be the severe flow-separation problem on the fuselage due to the interference between the fuselage and nacelles, as pointed out in part I of this report.

SUMMARY OF RESULTS

Static pressures were measured on the fuselage, Krueger flap, wing, upper-surface blown (USB) flap, double-slotted flap, and aileron of a large-scale USB model equipped with turbofan engines. Section normal-force coefficients were determined from the static-pressure data, and the highest section normal-force coefficients occurred directly behind the exhaust nozzle. The magnitudes of the section normal-force coefficients were relatively insensitive to angle of attack within the spanwise extent of the exhaust nozzle, but were very sensitive to both flap deflection angle and thrust coefficient. Greater spanwise spreading was observed with the flaps deflected for the take-off configuration than for the landing configuration. Pressure coefficients based on engine-exhaust dynamic pressure (rather than tunnel free-stream dynamic pressure) indicated that wind-on and wind-off conditions compared very well; therefore, it may be possible to determine the critical loads and load distributions from static tests alone. For the present configuration, it was observed that for the condition of one engine inoperative there was very little lift carryover.

REFERENCES

1. Shivers, James P.; and Smith, Charles C., Jr.: Static Tests of a Simulated Upper Surface Blown Jet-Flap Configuration Utilizing a Full-Size Turbofan Engine. NASA TN D-7816, 1975.

2. Wimpress, John K.: Upper Surface Blowing Technology as Applied to the YC-14 Airplane. [Preprint] 730916, Soc. Automot. Eng., Oct. 1973.

3. Smith, Charles C., Jr.; and White, Lucy C.: Pressure Distribution of a Twin-Engine Upper-Surface Blown Jet-Flap Model. NASA TM X-71937, 1974.

4. Heyson, Harry H.: Use of Superposition in Digital Computers To Obtain Wind-Tunnel Interference Factors for Arbitrary Configurations, With Particular Reference to V/STOL Models. NASA TR R-302, 1969.

5. Heyson, Harry H.: FORTRAN Programs for Calculating Wind-Tunnel Boundary Interference. NASA TM X-1740, 1969.

TABLE I.- LOCAL CHORDWISE LOCATIONS OF STATIC-PRESSURE ORIFICES

(a) Fuselage

Location of pressure orifices, in fraction of local wing chord, at station –							
1	2	3	4	5	6	7	8
Fuselage upper surface							
-0.5530	0.0100						
-.4320	.0500						
-.3120	.2000						
-.1910	.4000						
-.0700	.5000						
.0500	.6000						
.1710	.7000						
.2910	.8000						
.4120	.8500						
.5530	.9000						
.6530							
.7740							
.8940							
1.0150							
1.1360							
1.2560							
1.3770							
1.4970							
1.6180							
Fuselage lower surface							
-0.5530	0.0100						
-.4320	.0500						
-.3120	.1000						
-.1910	.2000						
-.0700	.3000						
.0500	.4000						
.1710	.5000						
.2910	.6000						
.4120	.7000						
.5530	.8000						
.7740	.8500						
.8940	.9000						
1.0150							
1.1360							
1.2560							
1.3770							
1.4970							

TABLE I.- Continued

(b) Krueger flap and wing

Location of pressure orifices, in fraction of local wing chord, at station –							
1	2	3	4	5	6	7	8
Krueger flap upper surface							
					-0.0432	-0.0432	-0.0432
					-.0760	-.0760	-.0760
					-.0728	-.0728	-.0728
					-.0551	-.0551	-.0551
					-.0266	-.0266	-.0266
Wing upper surface							
					0.0500	0.0500	0.0500
					.1000	.1000	.1000
					.2000	.2000	.2000
					.3000	.3000	.3000
		0.4000	0.4000	0.4000	.4000	.4000	.4000
		.5000	.5000	.5000	.5000	.5000	.5000
		.6000	.6000	.6000	.6000	.6000	.6000
		.7000	.7000	.7000	.7000	.7000	.7000
						.8000	
Wing lower surface							
		0.0050	0.0050	0.0050	0.0050	0.0050	
					.0100	.0100	0.0100
		.0500	.0500	.0500	.0500	.0500	.0500
		.1000	.1000	.1000	.1000	.1000	.1000
		.2000	.2000	.2000	.2000	.2000	.2000
		.3000	.3000	.3000	.3000	.3000	.3000
		.4000	.4000	.4000	.4000	.4000	.4000
		.5000	.5000	.5000	.5000	.5000	.5000
		.6000	.6000	.6000	.6000	.6000	.6000
			.7000	.7000	.7000	.7000	.7000

TABLE I.- Continued

(c) Vane, flap, and aileron; $\delta_f = 72^o$

Location of pressure orifices, in fraction of local wing chord, at station –							
1	2	3	4	5	6	7	8
Vane upper surface							
						0.8350	
						.8430	
						.8487	
						.8592	
						.9264	
						.9547	
						.9624	
						.9805	
Vane lower surface							
		0.8364		0.8364	0.8364	0.8364	
		.8396		.8396	.8396	.8396	
		.8468		.8468	.8468	.8468	
		.8691		.8691	.8691	.8691	
		.9127		.9127	.9127	.9127	
		.9491		.9491	.9491	.9491	
		.9793		.9793	.9793	.9793	
Flap upper surface							
		0.8000	0.8000	0.8000	0.8000	0.9760	
		.8550	.8550	.8550	.8550	.9884	
		1.0090	1.0090	1.0090	1.0090	.9967	
		1.0790	1.0770	1.0740	1.0700	1.0165	
						1.0407	
						1.0543	
						1.0658	
Flap lower surface							
		0.9753		0.9753	0.9753	0.9753	
		.9768		.9768	.9768	.9768	
		.9812		.9812	.9812	.9812	
		.9956		.9956	.9956	.9956	
		1.0207		1.0207	1.0207	1.0207	
		1.0399		1.0399	1.0399	1.0399	
		1.0601		1.0601	1.0601	1.0601	
Aileron upper surface							
							0.8196
							.8367
							.8572
							.8874
							.9121
							.9212
Aileron lower surface							
							0.7869
							.7943
							.8824
							.9056
							.9095

TABLE I.- Concluded

(d) Vane, flap, and aileron; $\delta_f = 32^o$

Location of pressure orifices, in fraction of local wing chord, at station –							
1	2	3	4	5	6	7	8
Vane upper surface							
						0.8340	
						.8387	
						.8434	
						.8526	
						.9067	
						.9248	
						.9605	
						.9961	
Vane lower surface							
		0.8383		0.8383	0.8383	0.8383	
		.8427		.8427	.8427	.8427	
		.8517		.8517	.8517	.8517	
		.8786		.8786	.8786	.8786	
		.9239		.9239	.9239	.9239	
		.9602		.9602	.9602	.9602	
		.9960		.9960	.9960	.9960	
Flap upper surface							
		0.8000	0.8000	0.8000	0.8000	1.0000	
		.8550	.8550	.8550	.8550	1.0110	
		1.0000	1.0000	1.0000	1.0000	1.0206	
		1.0320	1.0320	1.0320	1.0320	1.0477	
		1.1300	1.1300	1.1300	1.1300	1.0897	
						1.1212	
						1.1521	
Flap lower surface							
		1.0031		1.0031	1.0031	1.0031	
		1.0070		1.0070	1.0070	1.0070	
		1.0153		1.0153	1.0153	1.0153	
		1.0404		1.0404	1.0404	1.0404	
		1.0826		1.0826	1.0826	1.0826	
		1.1162		1.1162	1.1162	1.1162	
		1.1501		1.1501	1.1501	1.1501	
Aileron upper surface							
							0.7695
							.7862
							.8139
							.8848
							.9437
							.9662
Aileron lower surface							
							0.7566
							.7694
							.8828
							.9337
							.9615

TABLE II.- TEST CONDITIONS

Figure	Test conditions							Figure	Test conditions						
	Deflector	α, deg	δ_f, deg	q_∞, Pa (lb/ft^2)	C_μ	$C_{\mu,a}$	$C_{\mu,le}$		Deflector	α, deg	δ_f, deg	q_∞, Pa (lb/ft^2)	C_μ	$C_{\mu,a}$	$C_{\mu,le}$
2(a)	On	-0.02	72	83.3 (1.74)	0	0.026	0.013	2(m)	On	0	72	91.0 (1.90)	[a]0.0259	[a]0.000323	[a]0.000195
2(b)	On	-1.02	72	93.8 (1.96)	1.89	.024	.013	2(n)	On	0	72	0 (0)	[a].0258	[a].000320	[a].000188
2(c)	On	-1.60	72	106 (2.22)	3.48	.022	.012	3(a)	On	9.64	32	82.4 (1.72)	0	.024	.013
2(d)	On	9.63	72	79.5 (1.66)	0	.025	.014	3(b)	On	8.71	32	102 (2.14)	1.40	.021	.010
2(e)	On	8.62	72	88.1 (1.84)	2.15	.027	.015	3(c)	On	7.98	32	121 (2.53)	2.61	.018	.009
2(f)	On	7.95	72	101 (2.11)	3.93	.024	.014	3(d)	On	29.47	32	76.6 (1.60)	0	.027	.014
2(g)	On	19.52	72	76.1 (1.59)	0	.027	.015	3(e)	On	27.73	32	84.7 (1.77)	2.04	.028	.014
2(h)	On	18.38	72	85.2 (1.78)	2.36	.030	.016	3(f)	On	26.48	32	97.7 (2.04)	3.97	.026	.013
2(i)	On	17.17	72	96.2 (2.01)	4.32	.027	.015	4(a)	On	9.06	32	95.8 (2.00)	[b].84	.021	.010
2(j)	On	29.53	72	73.7 (1.54)	0	.028	.016	4(b)	On	8.55	32	103 (2.16)	[b]1.62	.020	.010
2(k)	On	28.32	72	82.8 (1.73)	2.53	.033	.017	4(c)	On	9.11	32	91.9 (1.92)	[c].77	.022	.012
2(l)	On	27.73	72	94.8 (1.98)	4.61	.028	.016	4(d)	On	8.61	32	102 (2.13)	[c]1.54	.020	.010

[a]Based on engine exhaust dynamic pressure.

[b]Left engine inoperative.

[c]Right engine inoperative.

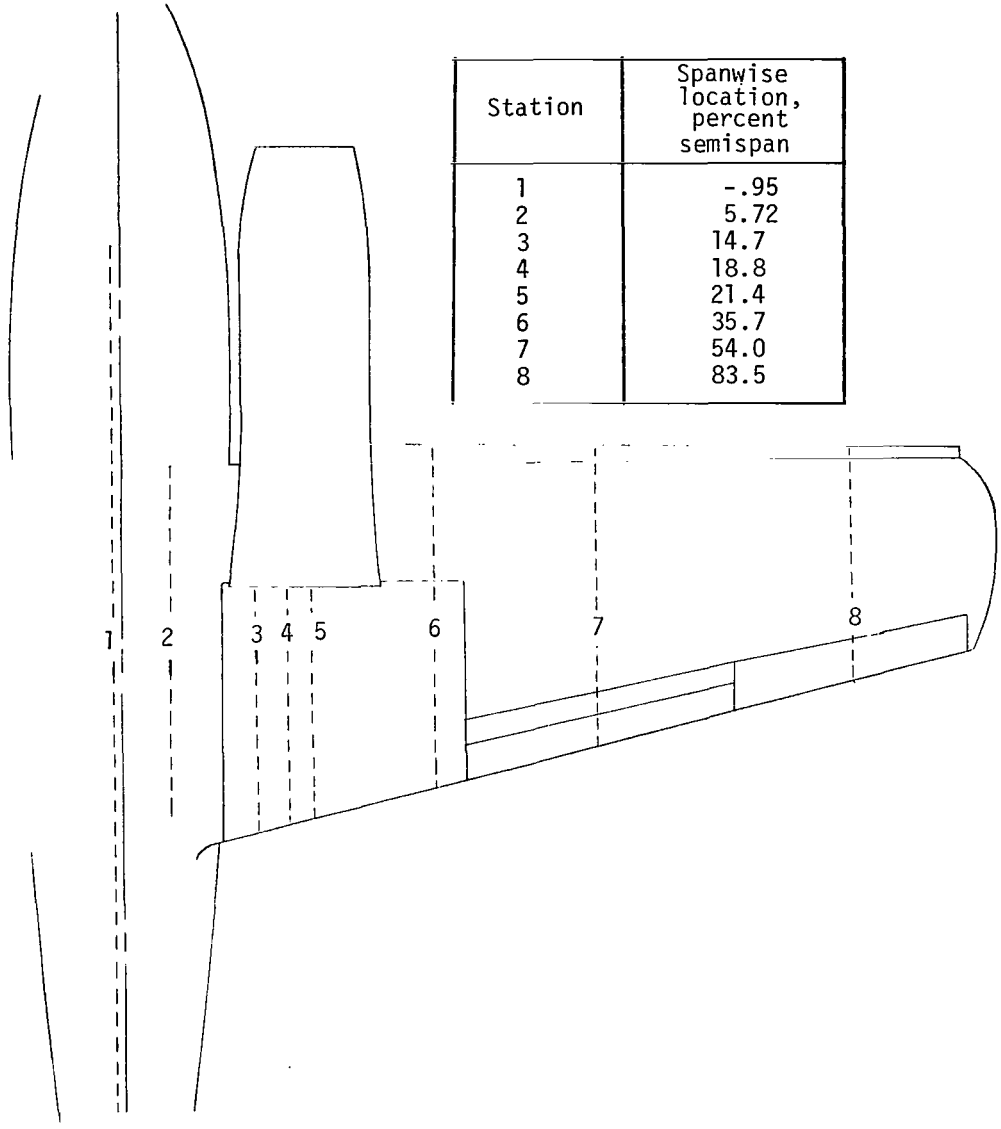

Station	Spanwise location, percent semispan
1	-.95
2	5.72
3	14.7
4	18.8
5	21.4
6	35.7
7	54.0
8	83.5

Figure 1.- Spanwise locations of pressure orifices.

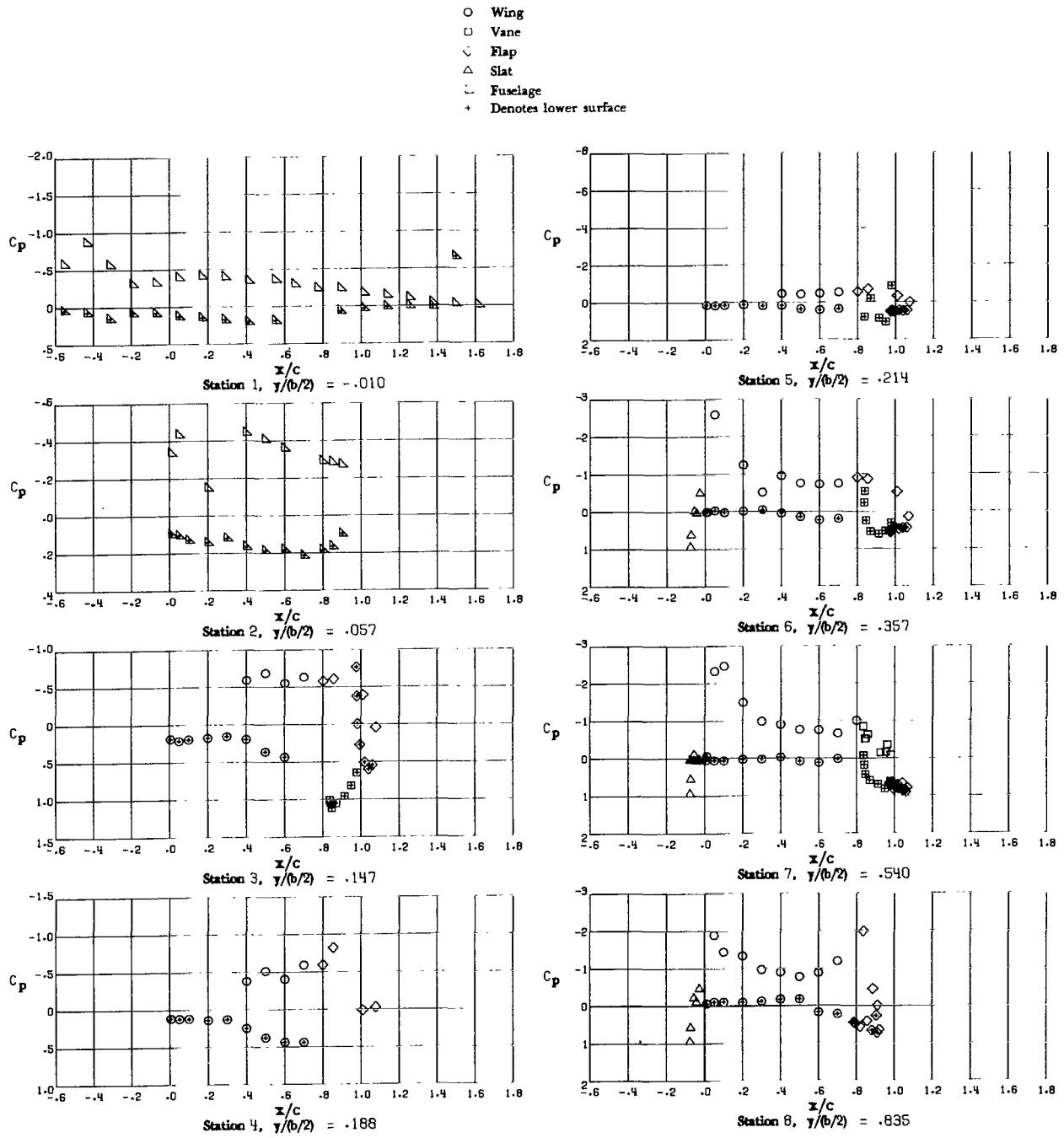

(a) $\alpha = -0.02^{o}$; $C_{\mu} = 0$; $C_{\mu,a} = 0.026$; $C_{\mu,le} = 0.013$.

Figure 2.- Chordwise pressure-coefficient distributions for model with exhaust nozzle deflectors on, symmetrical thrust, $\delta_f = 72^{o}$, and $\delta_a = 59^{o}$.

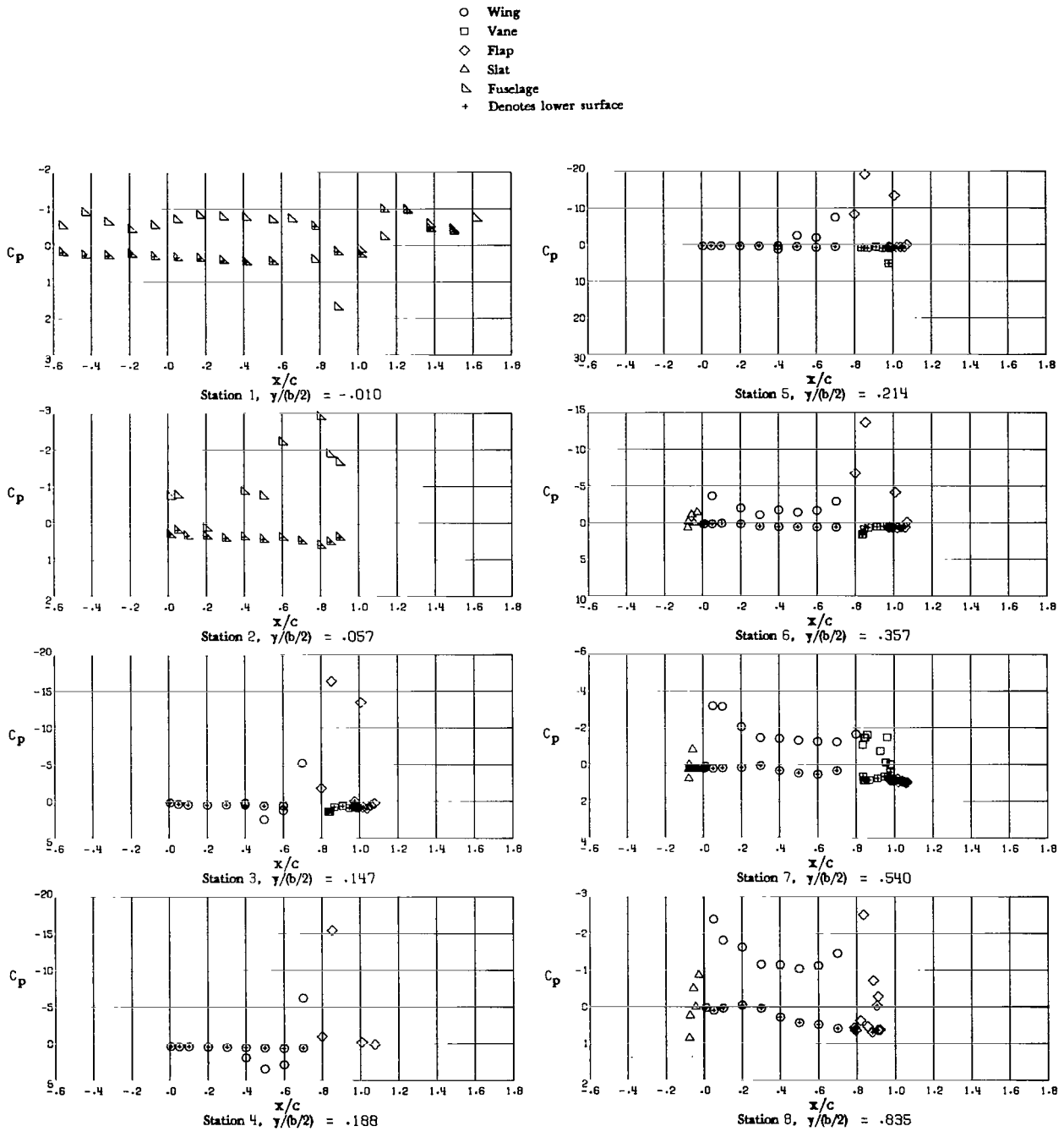

(b) $\alpha = -1.02^{O}$; $C_{\mu} = 1.89$; $C_{\mu,a} = 0.024$; $C_{\mu,le} = 0.013$.

Figure 2.- Continued.

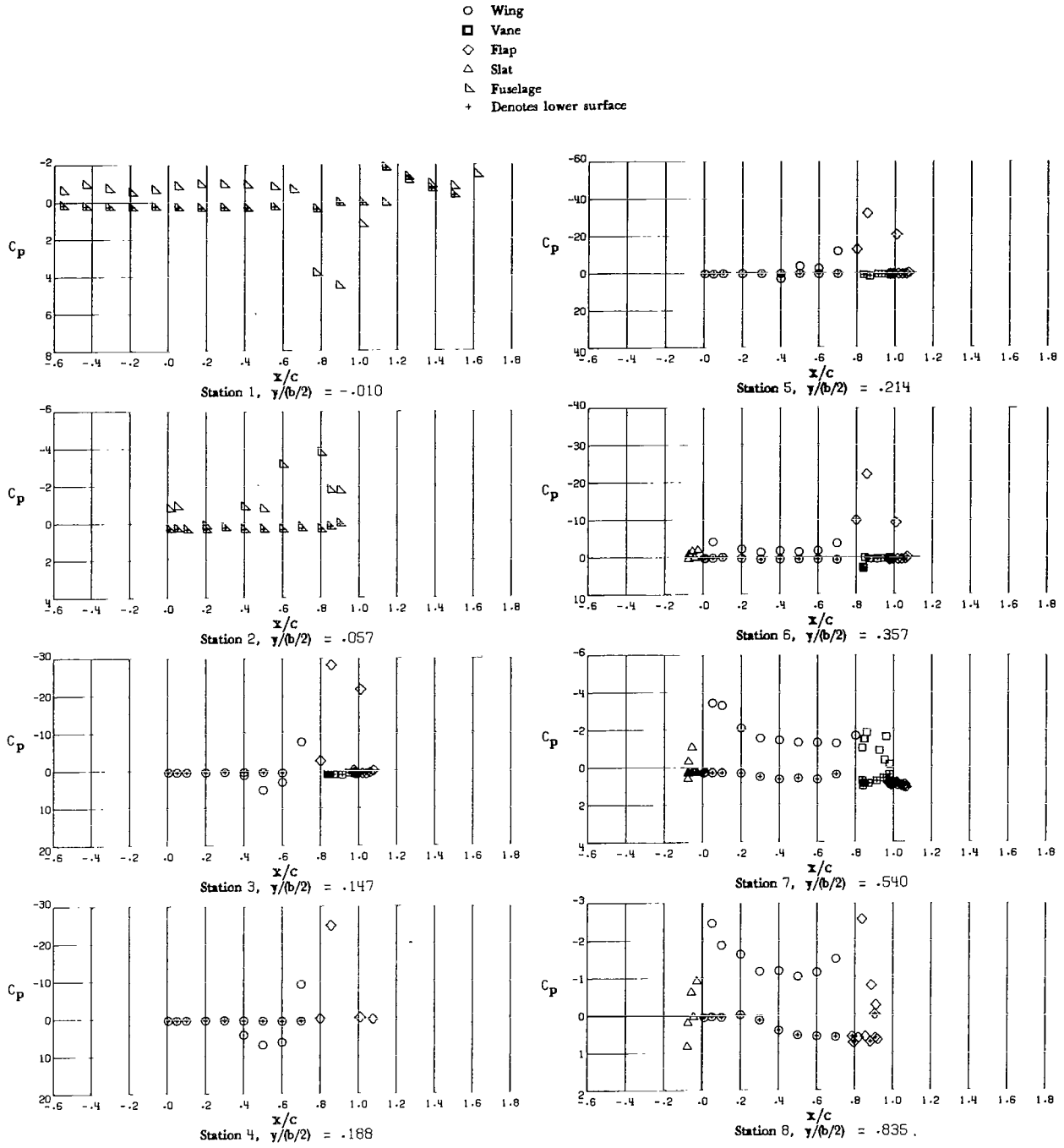

(c) $\alpha = -1.60^{\circ}$; $C_{\mu} = 3.48$; $C_{\mu,a} = 0.022$; $C_{\mu,le} = 0.012$.

Figure 2.- Continued.

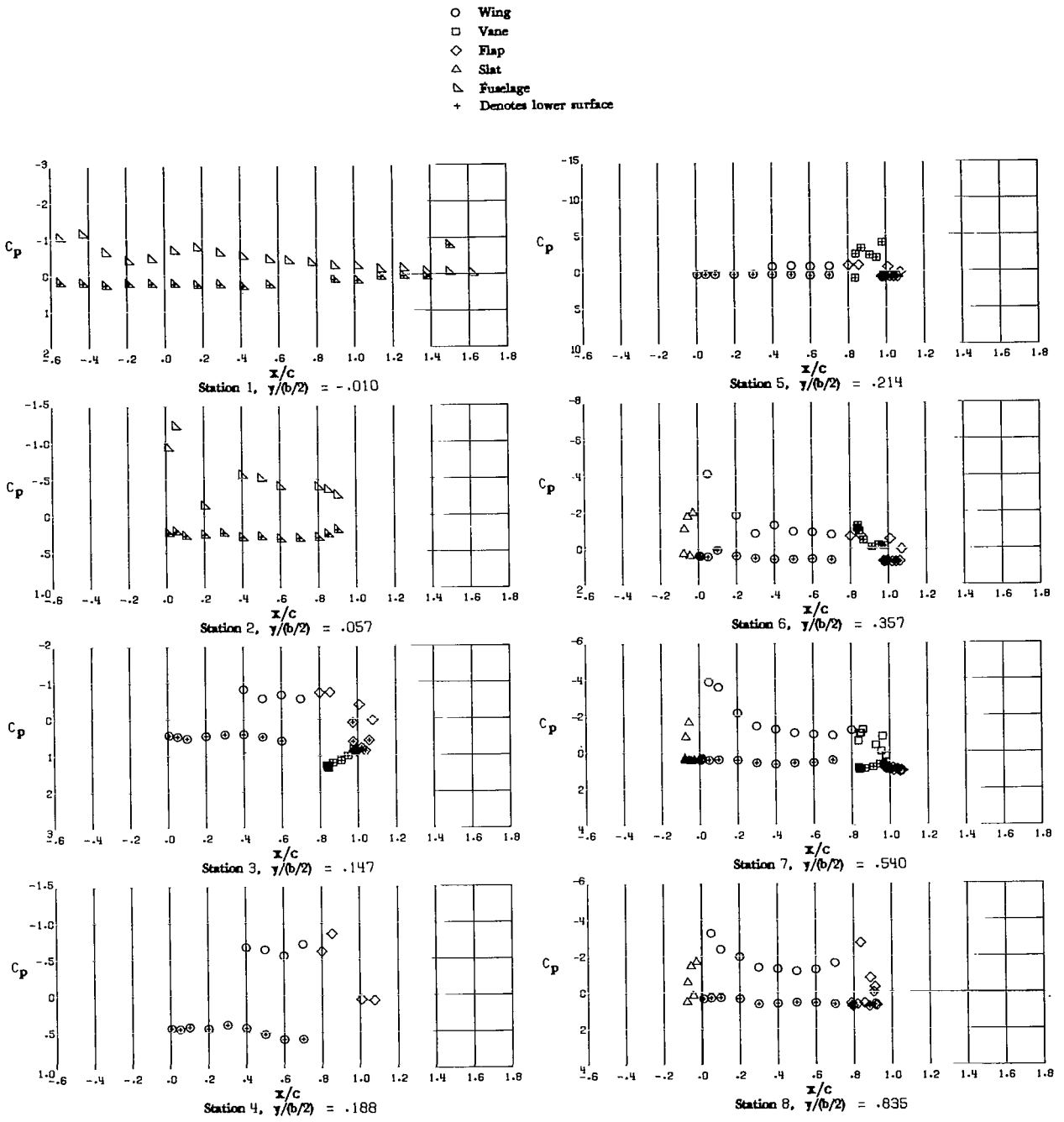

(d) $\alpha = 9.63^{o}$; $C_{\mu} = 0$; $C_{\mu,a} = 0.025$; $C_{\mu,le} = 0.014$.

Figure 2.- Continued.

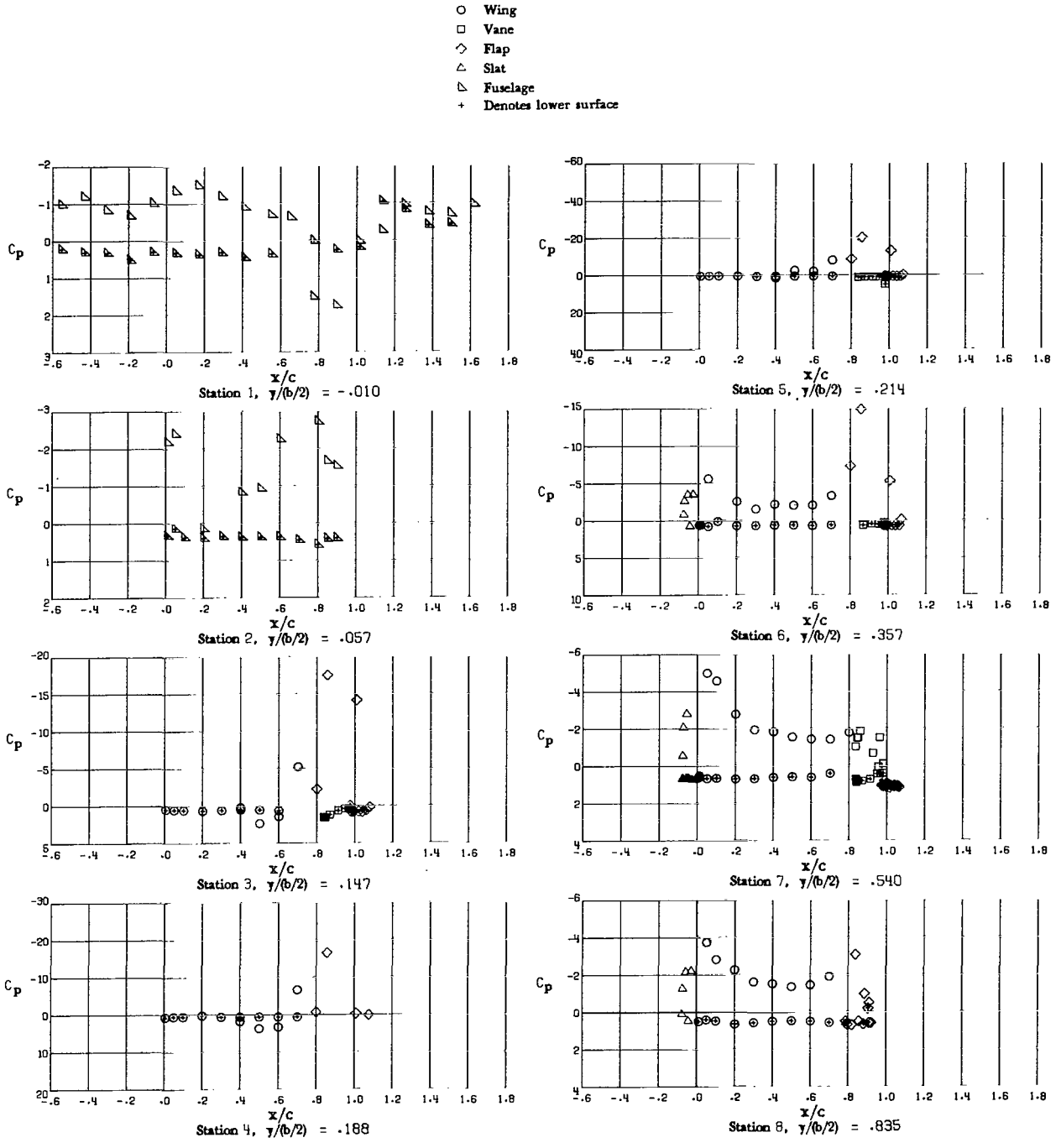

(e) $\alpha = 8.62^{\circ}$; $C_{\mu} = 2.15$; $C_{\mu,a} = 0.027$; $C_{\mu,le} = 0.015$.

Figure 2.- Continued.

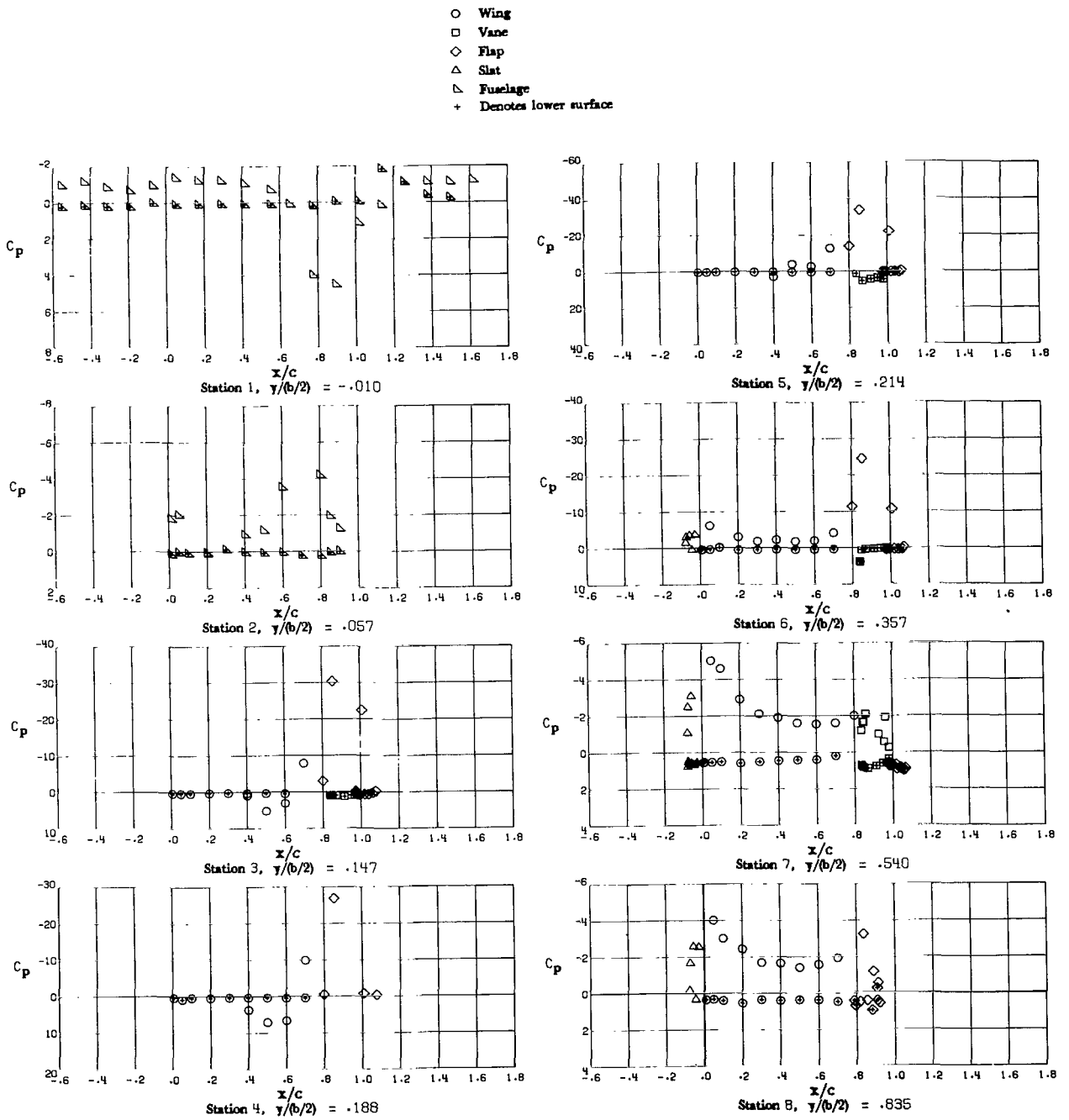

(f) $\alpha = 7.95^{o}$; $C_{\mu} = 3.93$; $C_{\mu,a} = 0.024$; $C_{\mu,le} = 0.014$.

Figure 2.- Continued.

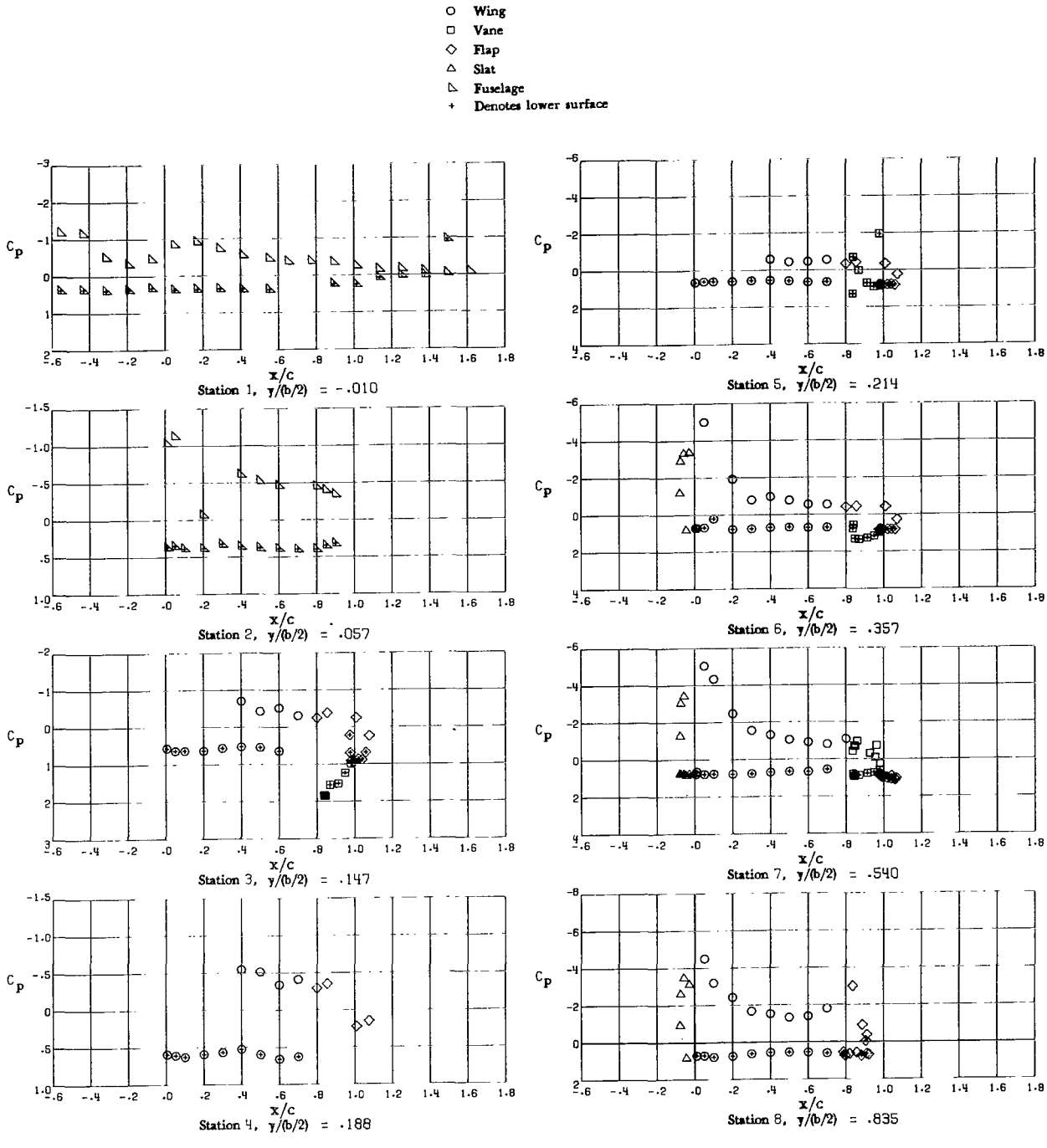

(g) $\alpha = 19.52^{O}$; $C_{\mu} = 0$; $C_{\mu,a} = 0.027$; $C_{\mu,le} = 0.015$.

Figure 2.- Continued.

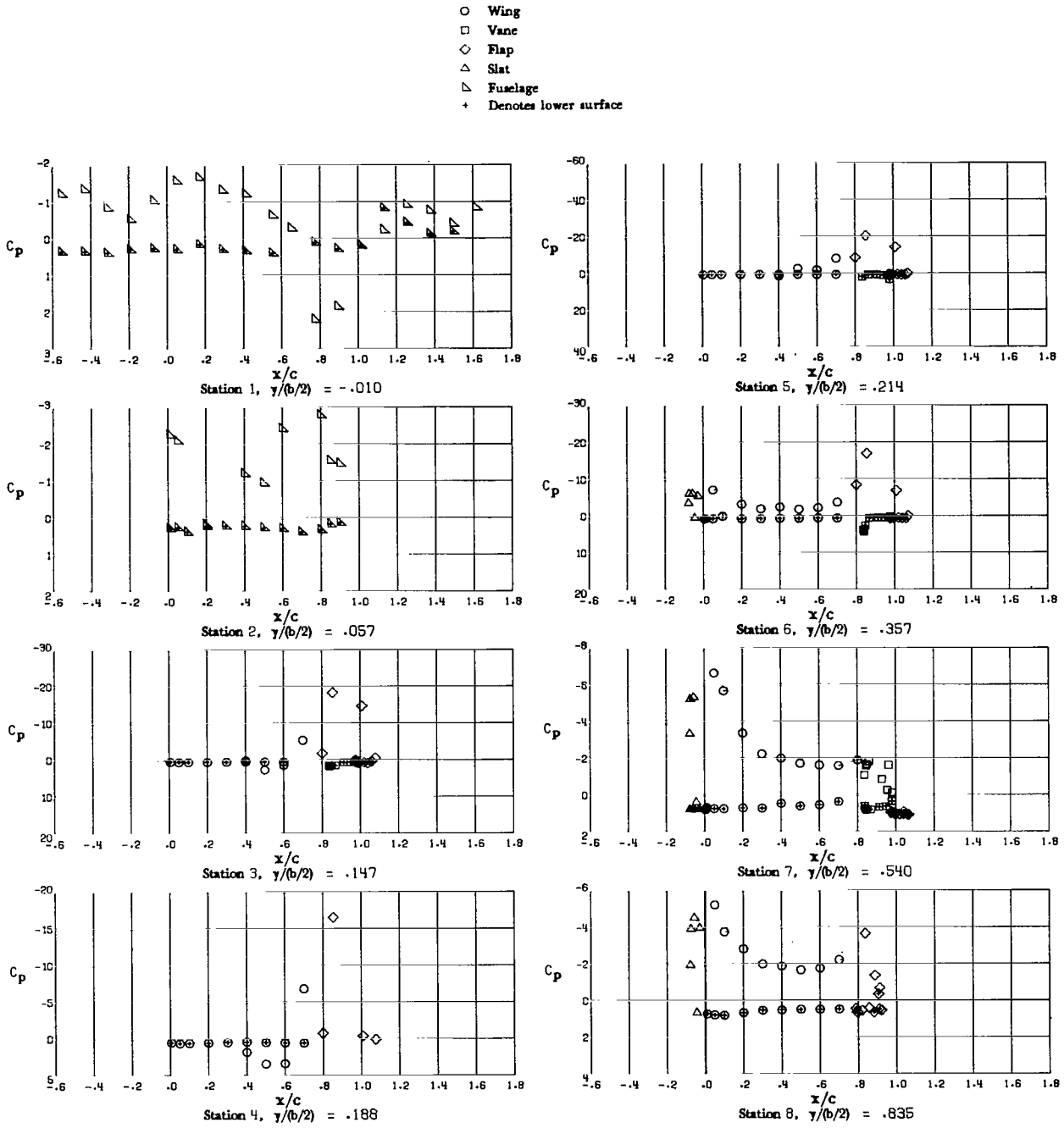

(h) $\alpha = 18.38^{o}$; $C_{\mu} = 2.36$; $C_{\mu,a} = 0.030$; $C_{\mu,le} = 0.016$.

Figure 2.- Continued.

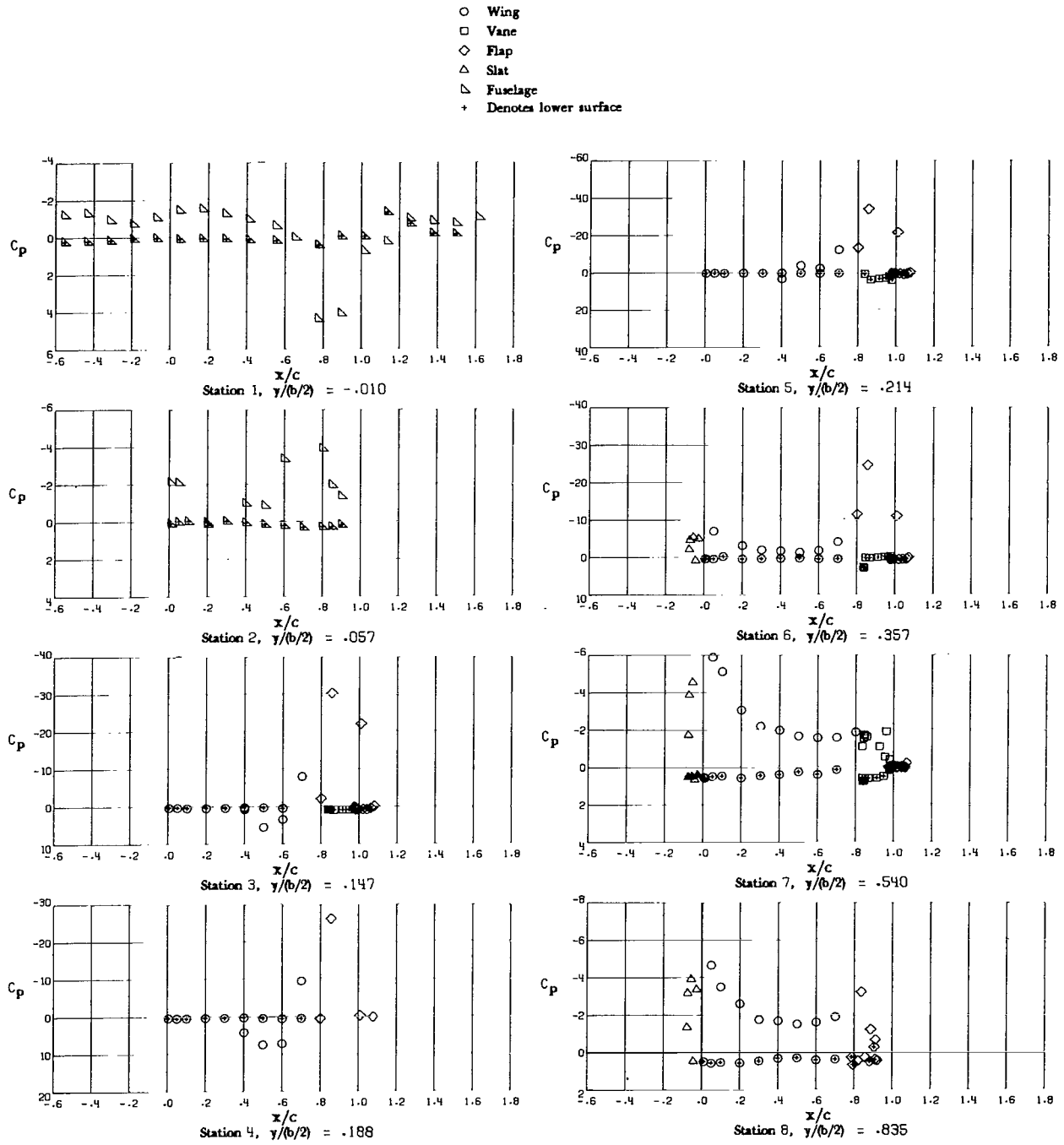

(i) $\alpha = 17.17^{o}$; $C_{\mu} = 4.32$; $C_{\mu,a} = 0.027$; $C_{\mu,le} = 0.015$.

Figure 2.- Continued.

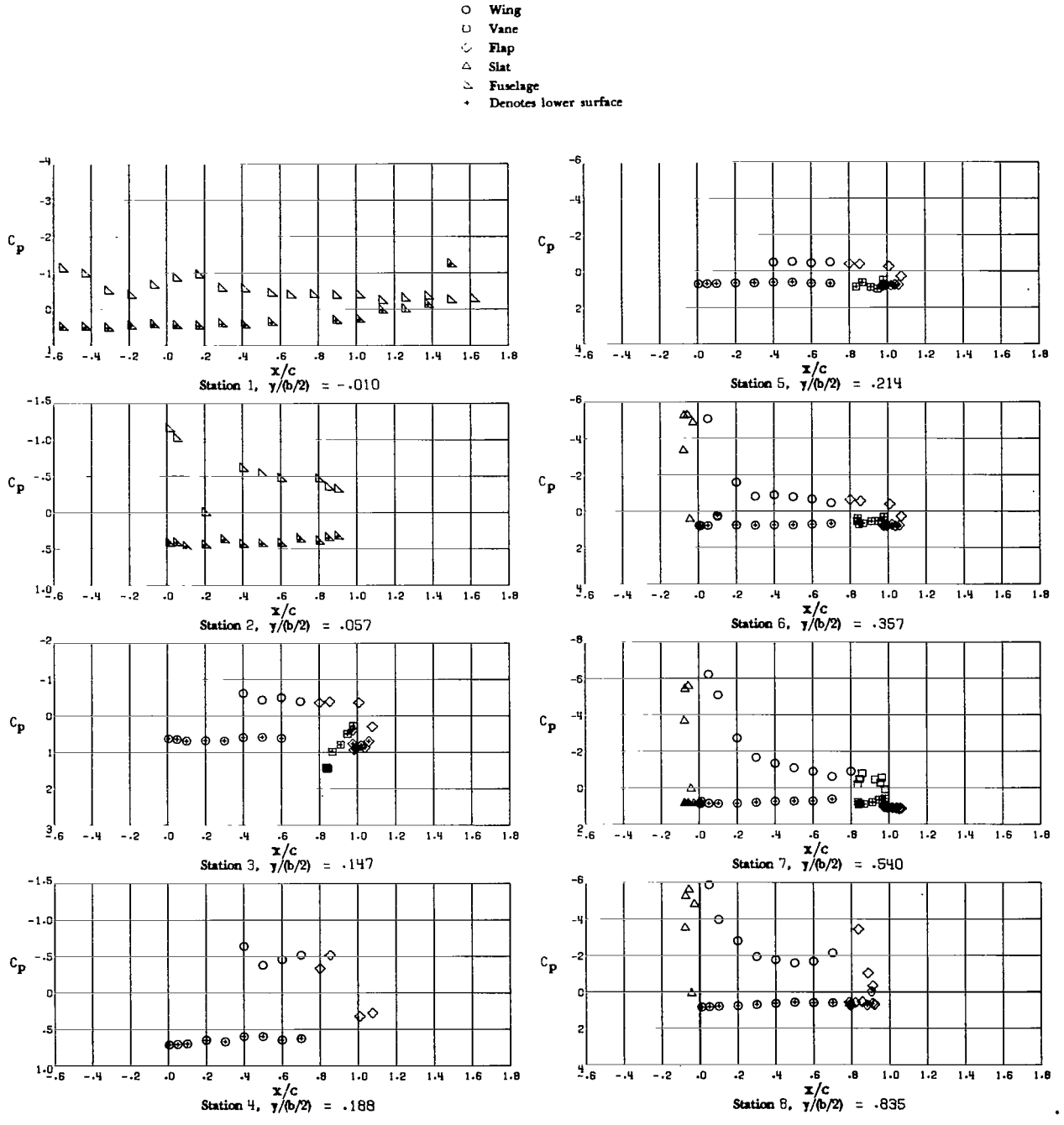

(j) $\alpha = 29.53^{o}$; $C_{\mu} = 0$; $C_{\mu,a} = 0.028$; $C_{\mu,le} = 0.016$.

Figure 2.- Continued.

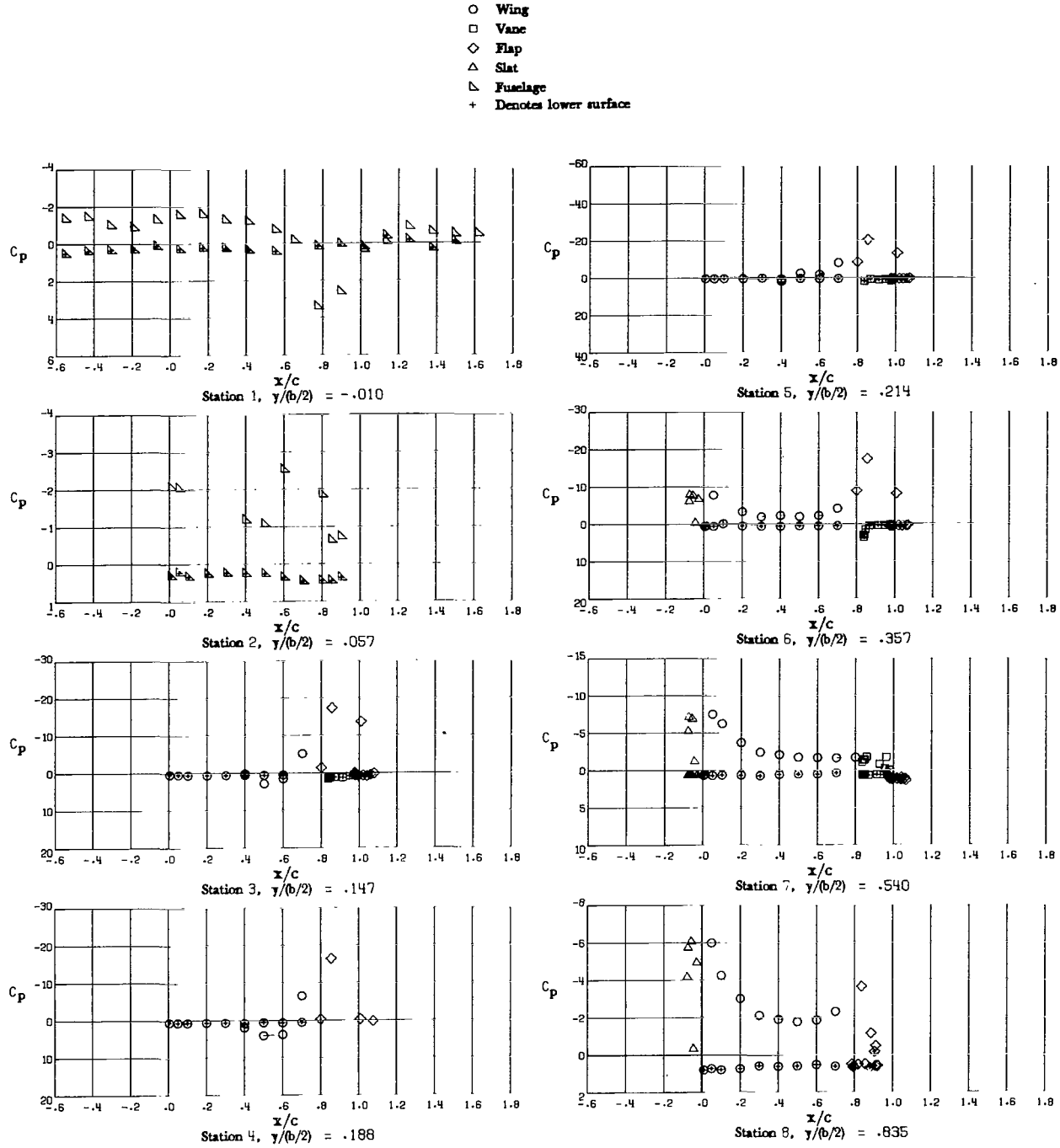

(k) $\alpha = 28.32^{\circ}$; $C_{\mu} = 2.53$; $C_{\mu,a} = 0.033$; $C_{\mu,le} = 0.017$.

Figure 2.- Continued.

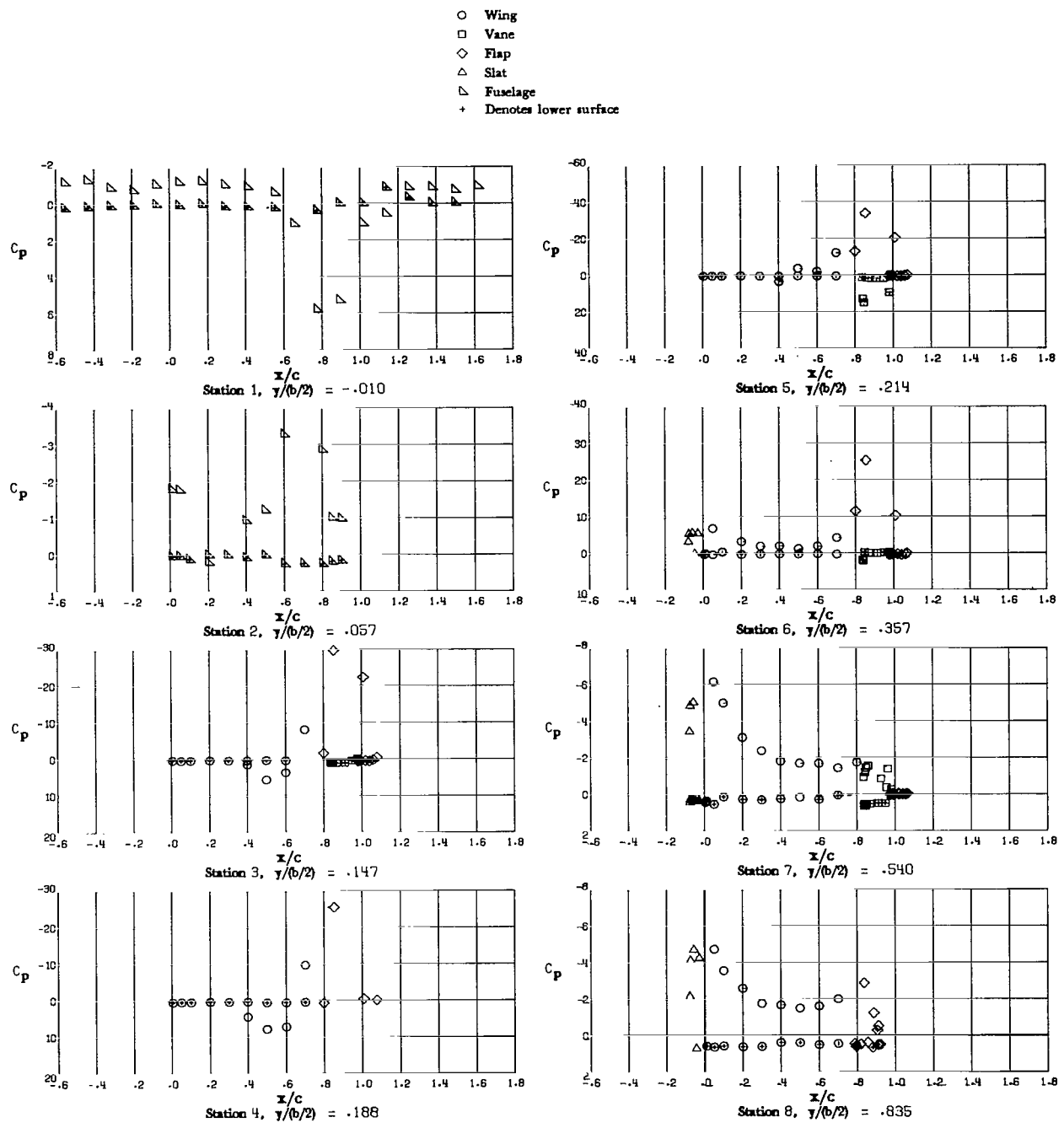

(l) $\alpha = 27.73^{o}$; $C_{\mu} = 4.61$; $C_{\mu,a} = 0.028$; $C_{\mu,le} = 0.016$.

Figure 2.- Continued.

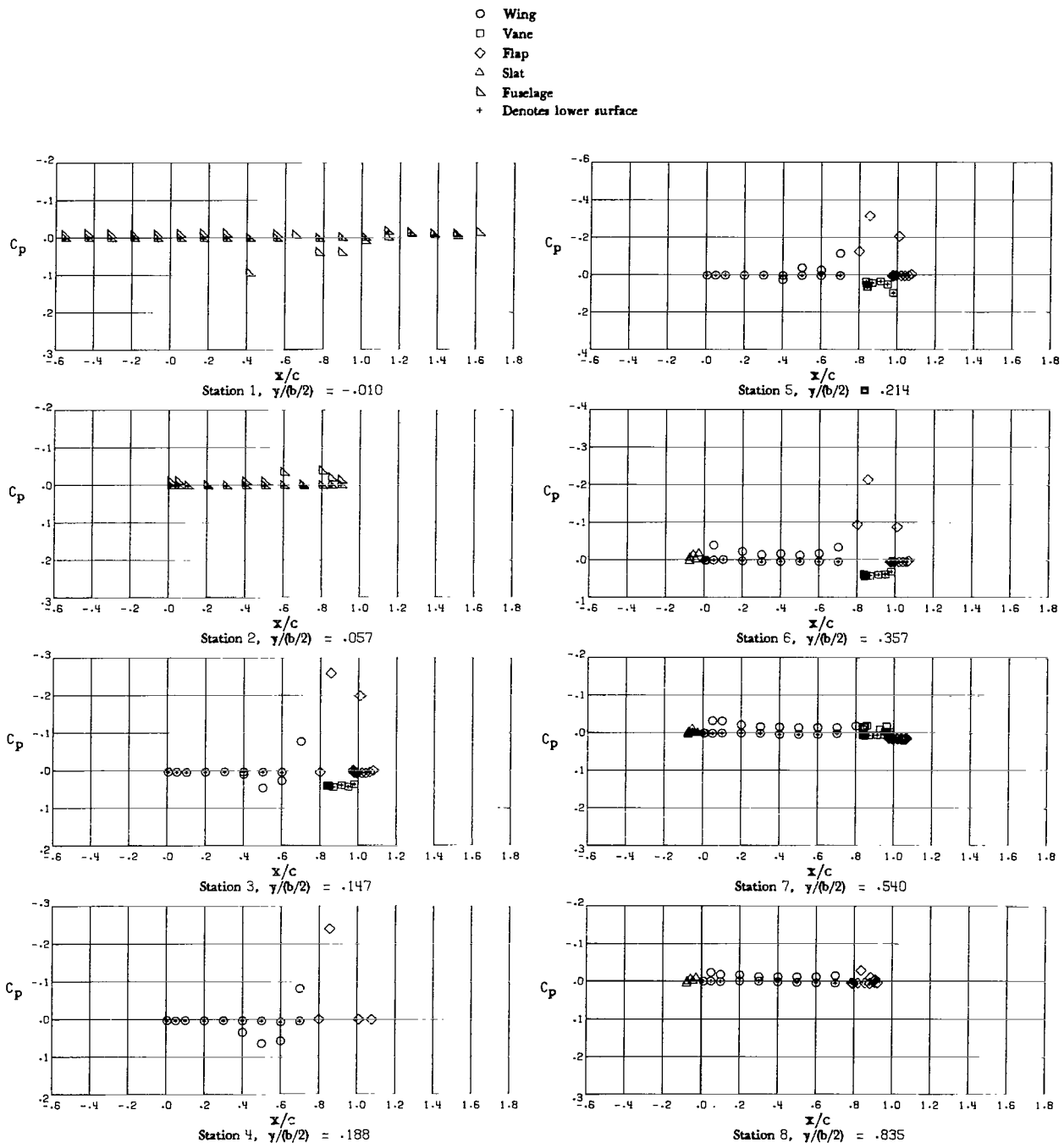

(m) $\alpha = 0^{O}$; $C_{\mu} = 0.0259$; $C_{\mu,a} = 0.000323$; $C_{\mu,le} = 0.000195$; $q_{\infty} = 91.0$ Pa (1.9 lb/ft^2). (These coefficients are based on engine-exhaust dynamic pressure.)

Figure 2.- Continued.

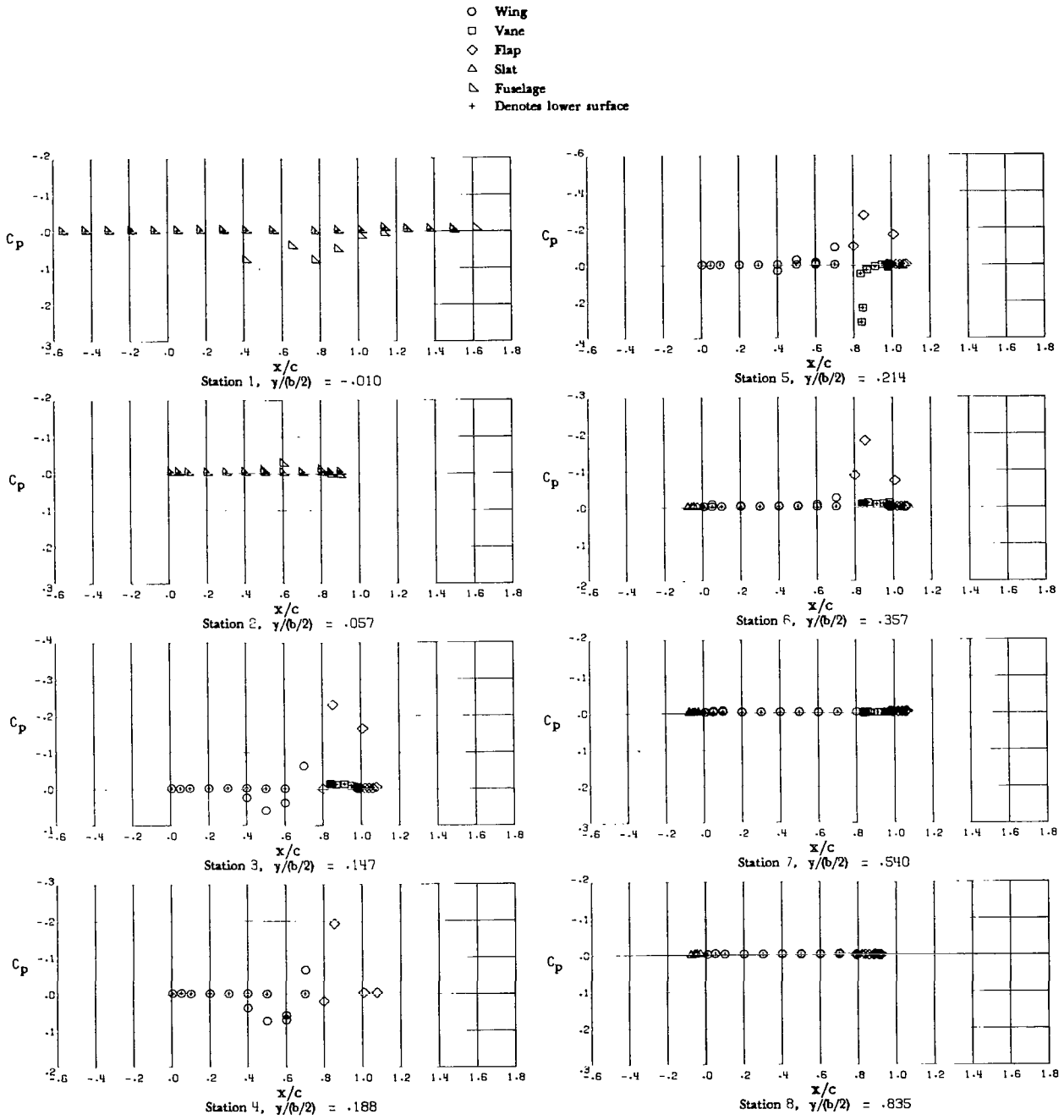

(n) $\alpha = 0^{o}$; $C_{\mu} = 0.0258$; $C_{\mu,a} = 0.000320$; $C_{\mu,le} = 0.000188$; $q_{\infty} = 0$ Pa (0 lb/ft^2). (These coefficients are based on engine-exhaust dynamic pressure.)

Figure 2.- Concluded.

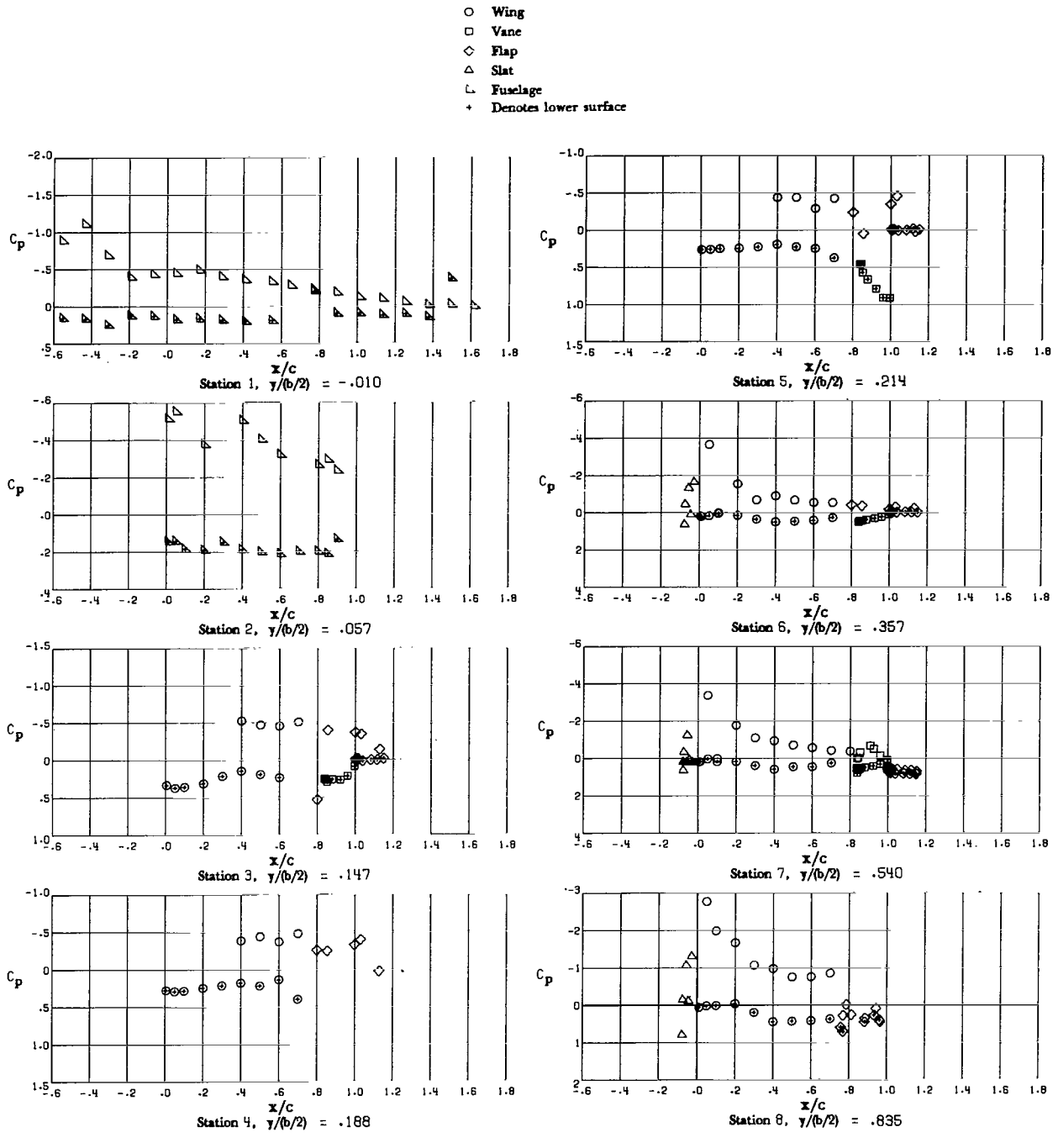

(a) $\alpha = 9.64^{o}$; $C_{\mu} = 0$; $C_{\mu,a} = 0.024$; $C_{\mu,le} = 0.013$.

Figure 3.- Chordwise pressure coefficient distributions for model with exhaust nozzle deflectors on, symmetrical thrust, $\delta_f = 32^{o}$, and $\delta_a = 29^{o}$.

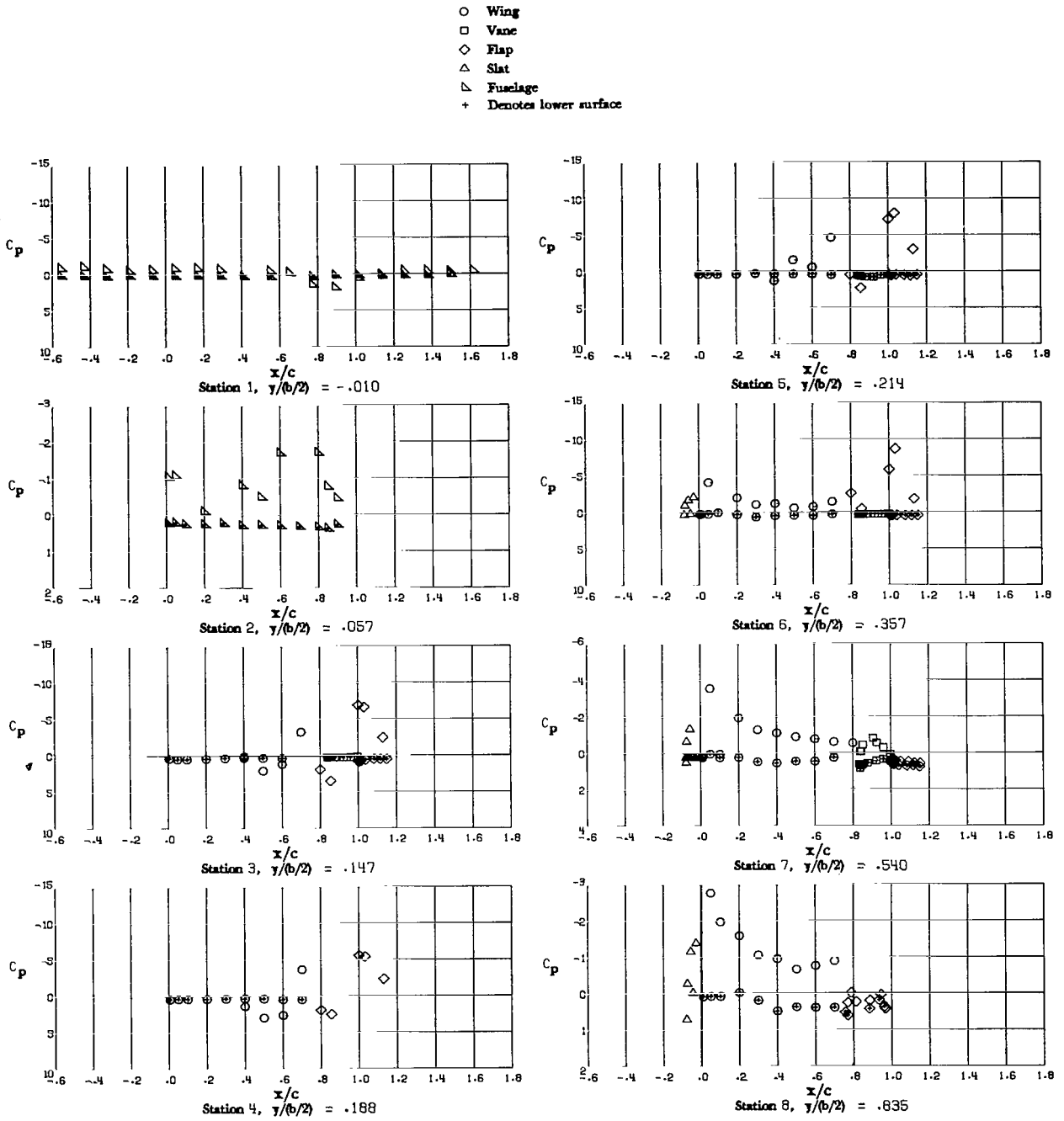

(b) $\alpha = 8.71^{o}$; $C_{\mu} = 1.40$; $C_{\mu,a} = 0.021$; $C_{\mu,le} = 0.010$.

Figure 3.- Continued.

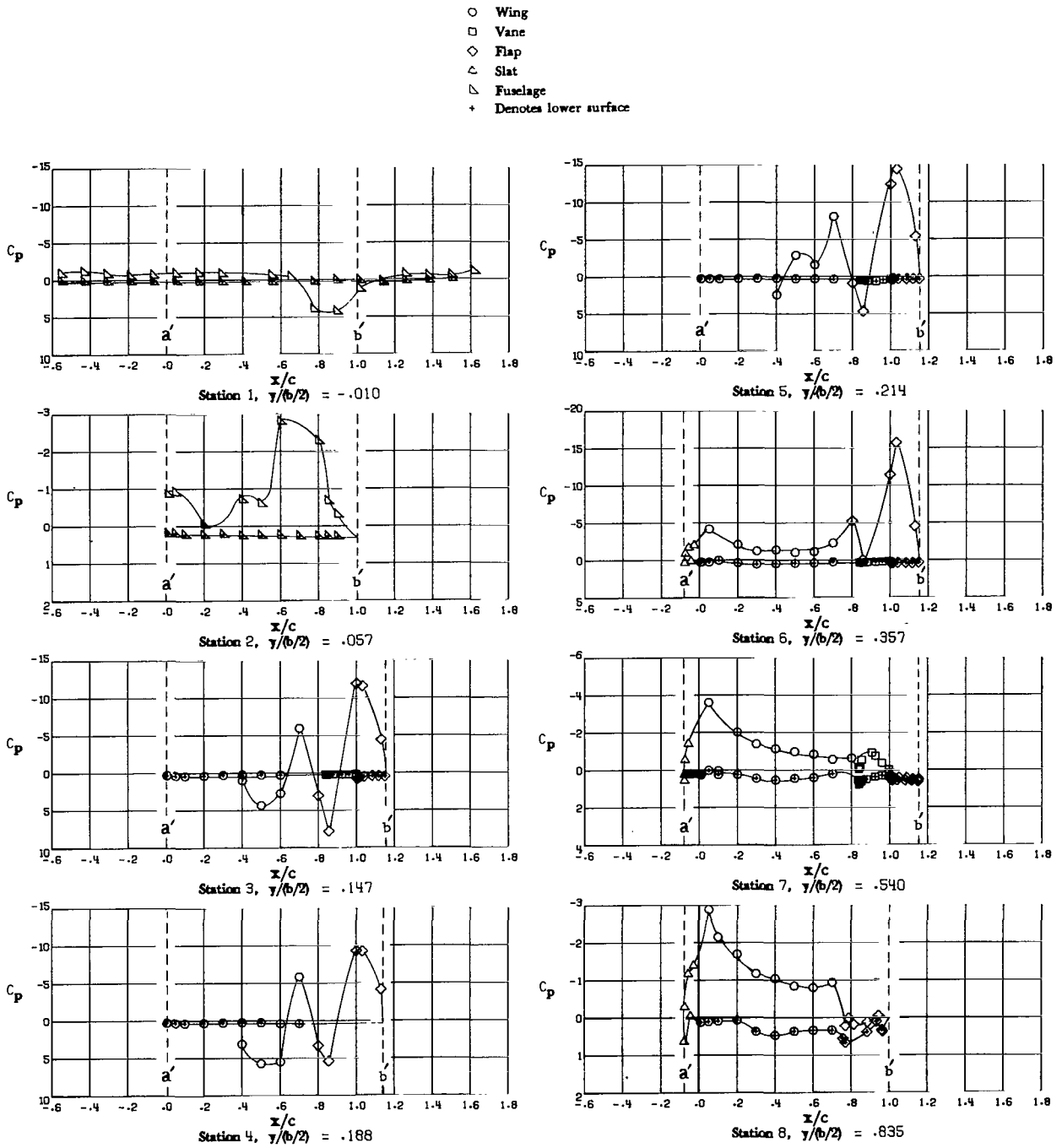

(c) $\alpha = 7.98^{\circ}$; $C_{\mu} = 2.61$; $C_{\mu,a} = 0.018$; $C_{\mu,le} = 0.009$.

Figure 3.- Continued.

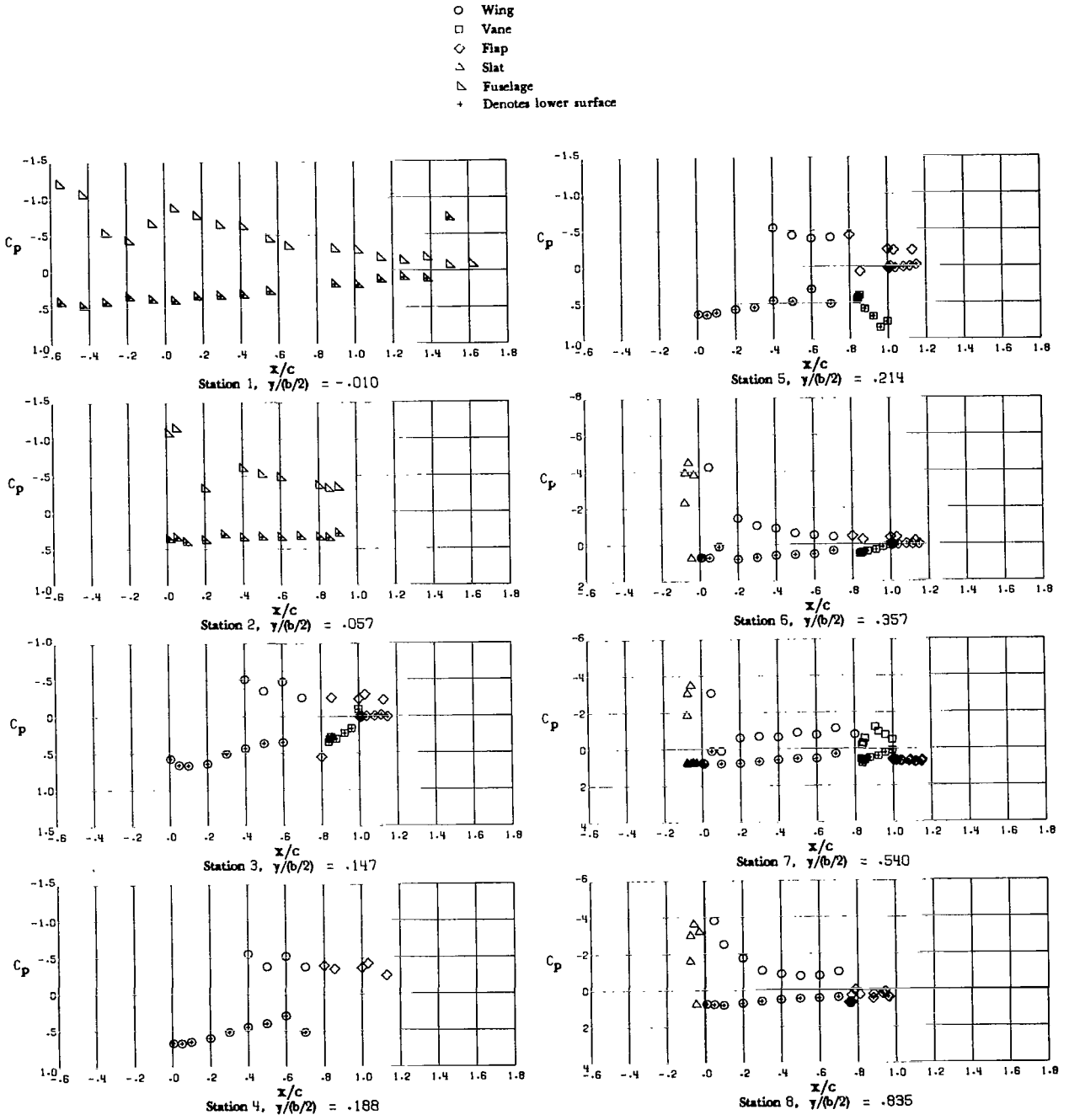

(d) $\alpha = 29.47^{o}$; $C_{\mu} = 0$; $C_{\mu,a} = 0.027$; $C_{\mu,le} = 0.014$.

Figure 3.- Continued.

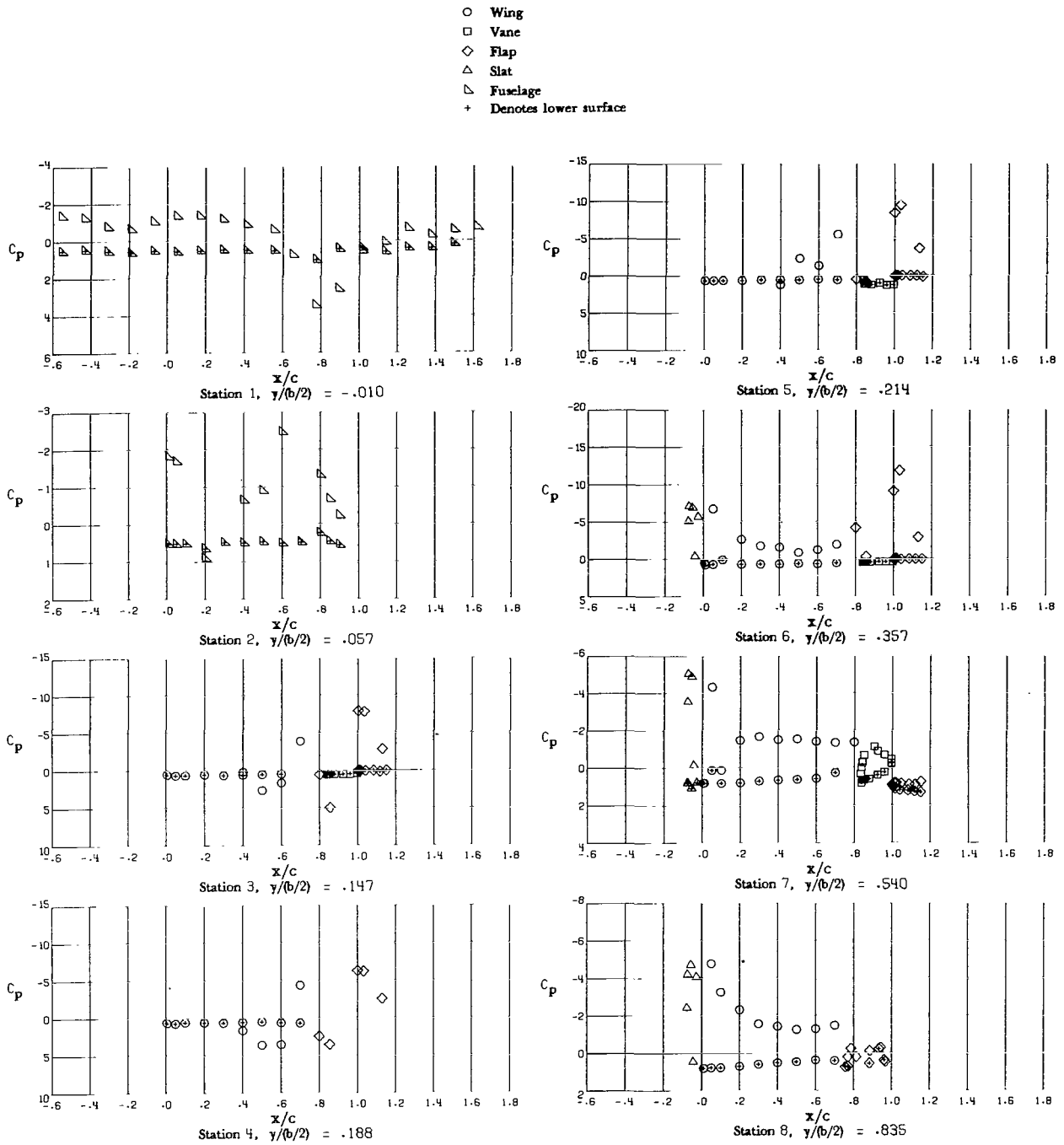

(e) $\alpha = 27.73^{O}$; $C_{\mu} = 2.04$; $C_{\mu,a} = 0.028$; $C_{\mu,le} = 0.014$.

Figure 3.- Continued.

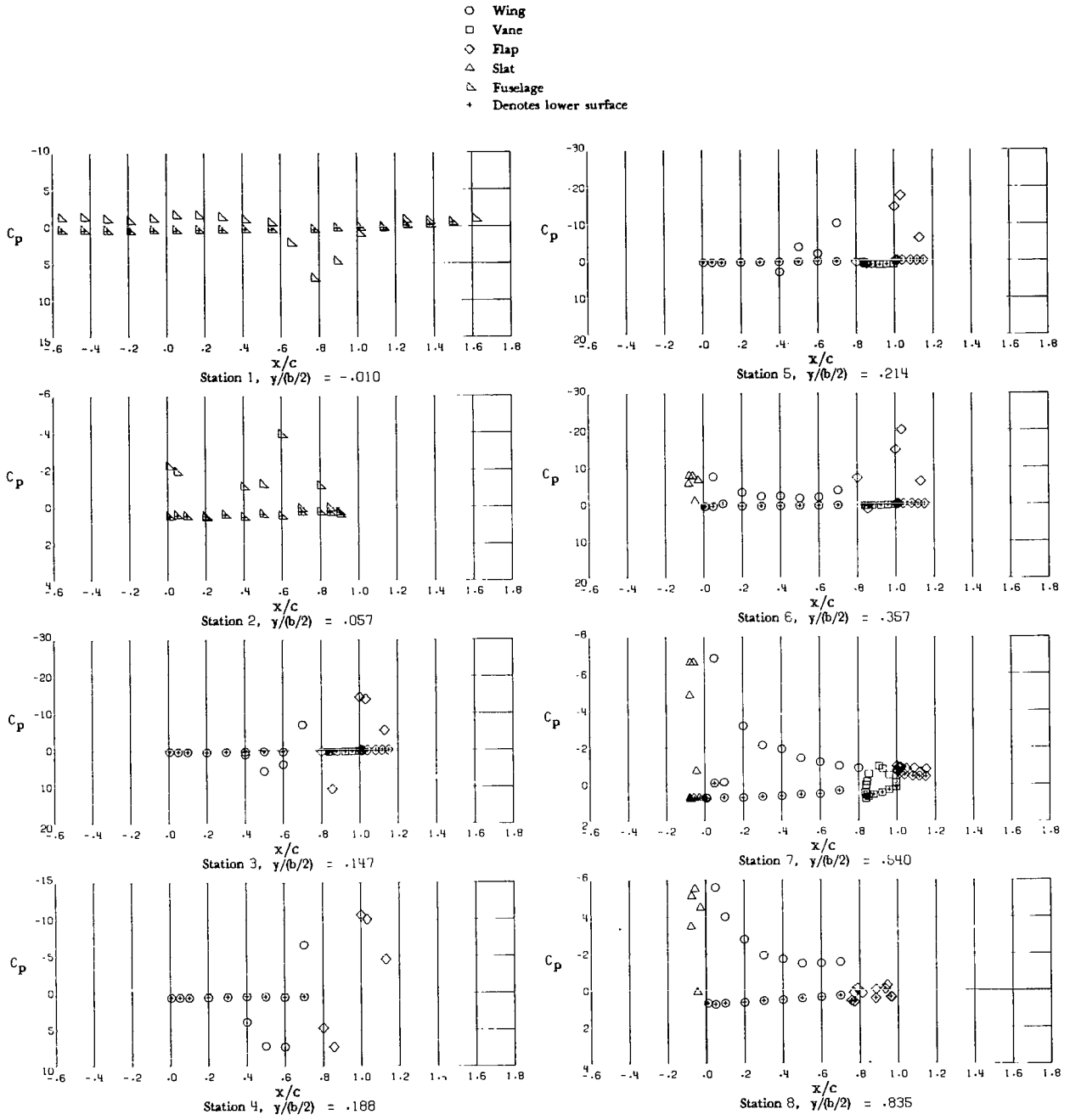

(f) $\alpha = 26.48^{\circ}$; $C_{\mu} = 3.97$; $C_{\mu,a} = 0.026$; $C_{\mu,le} = 0.013$.

Figure 3.- Concluded.

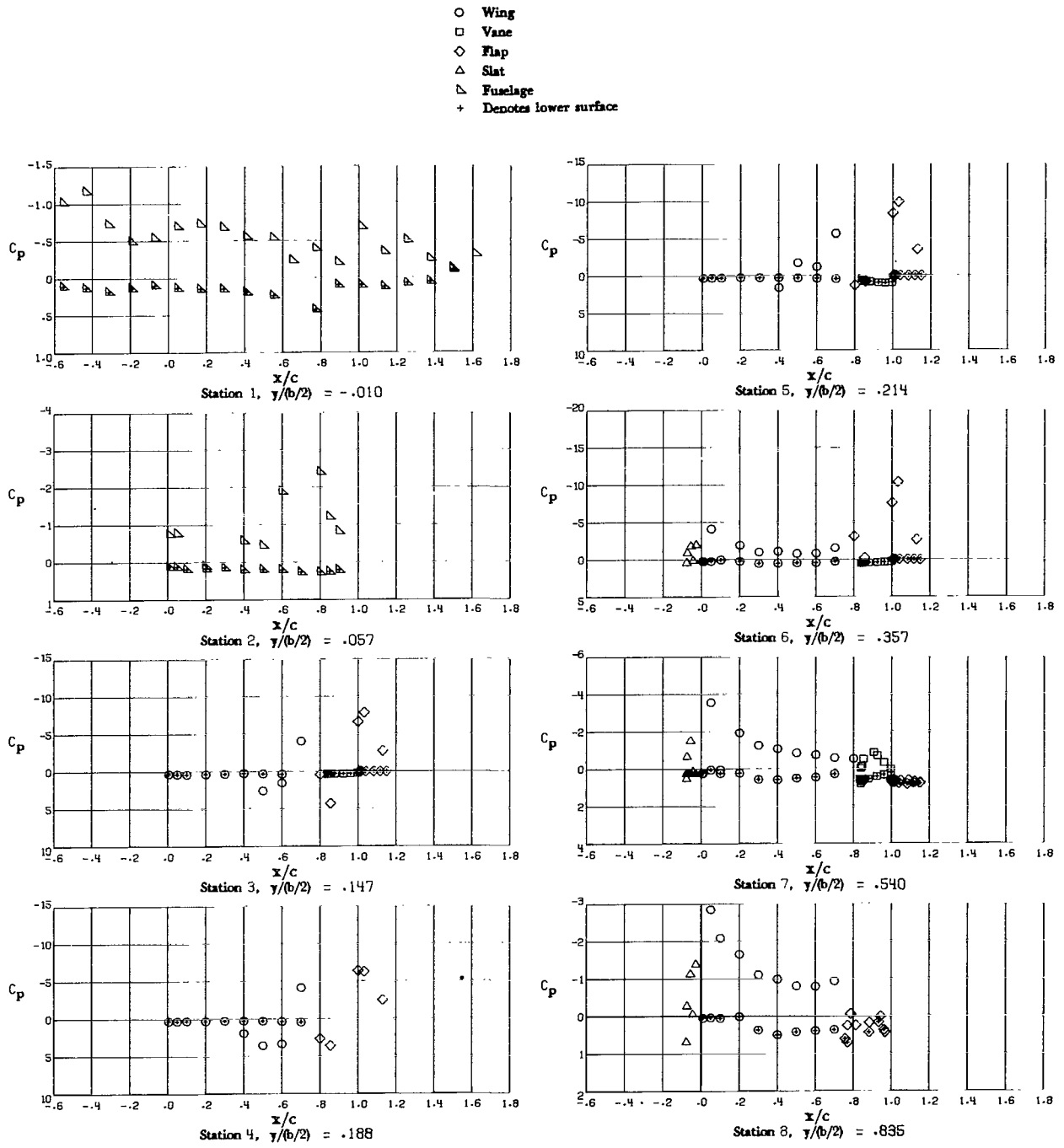

(a) Left engine inoperative; $\alpha = 9.06^{\circ}$; $C_{\mu} = 0.84$; $C_{\mu,a} = 0.021$; $C_{\mu,le} = 0.010$.

Figure 4.- Chordwise pressure-coefficient distributions for model with exhaust nozzle deflectors on, one engine inoperative, $\delta_f = 32^{\circ}$, and $\delta_a = 29^{\circ}$.

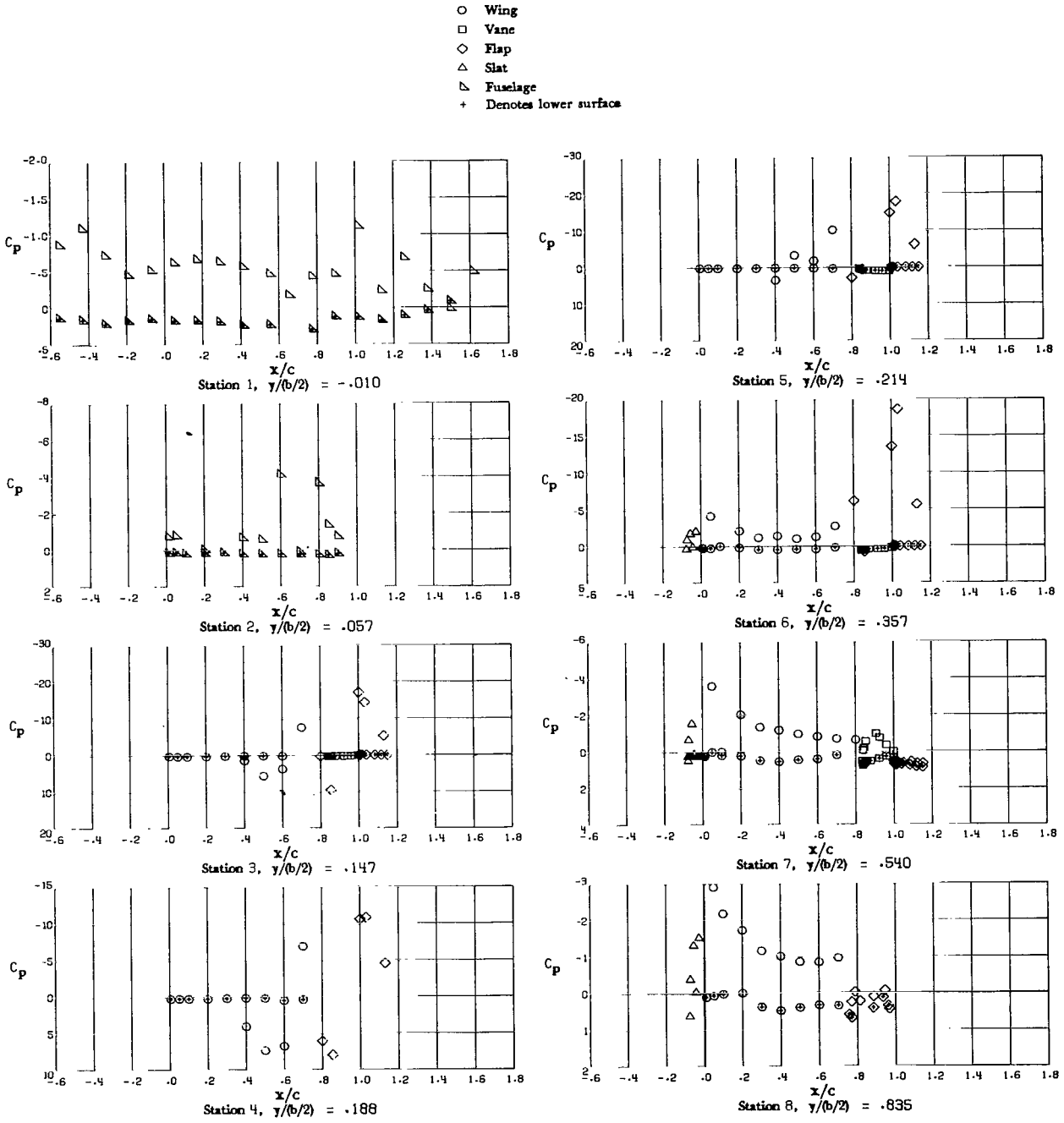

(b) Left engine inoperative; $\alpha = 8.55^{o}$; $C_{\mu} = 1.62$; $C_{\mu,a} = 0.020$; $C_{\mu,le} = 0.010$.

Figure 4.- Continued.

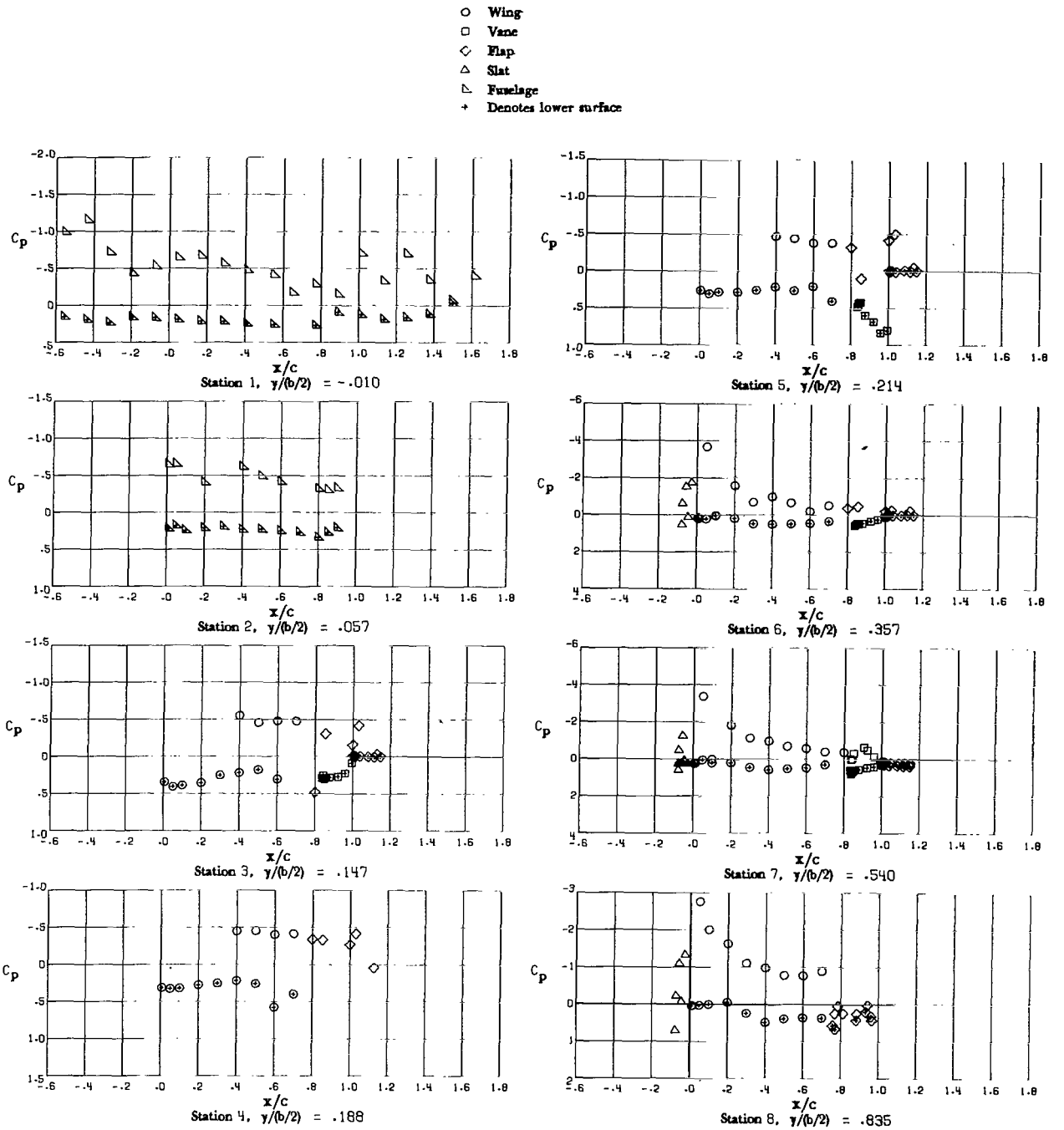

(c) Right engine inoperative; $\alpha = 9.11^{o}$; $C_{\mu} = 0.77$; $C_{\mu,a} = 0.022$; $C_{\mu,le} = 0.012$.

Figure 4.- Continued.

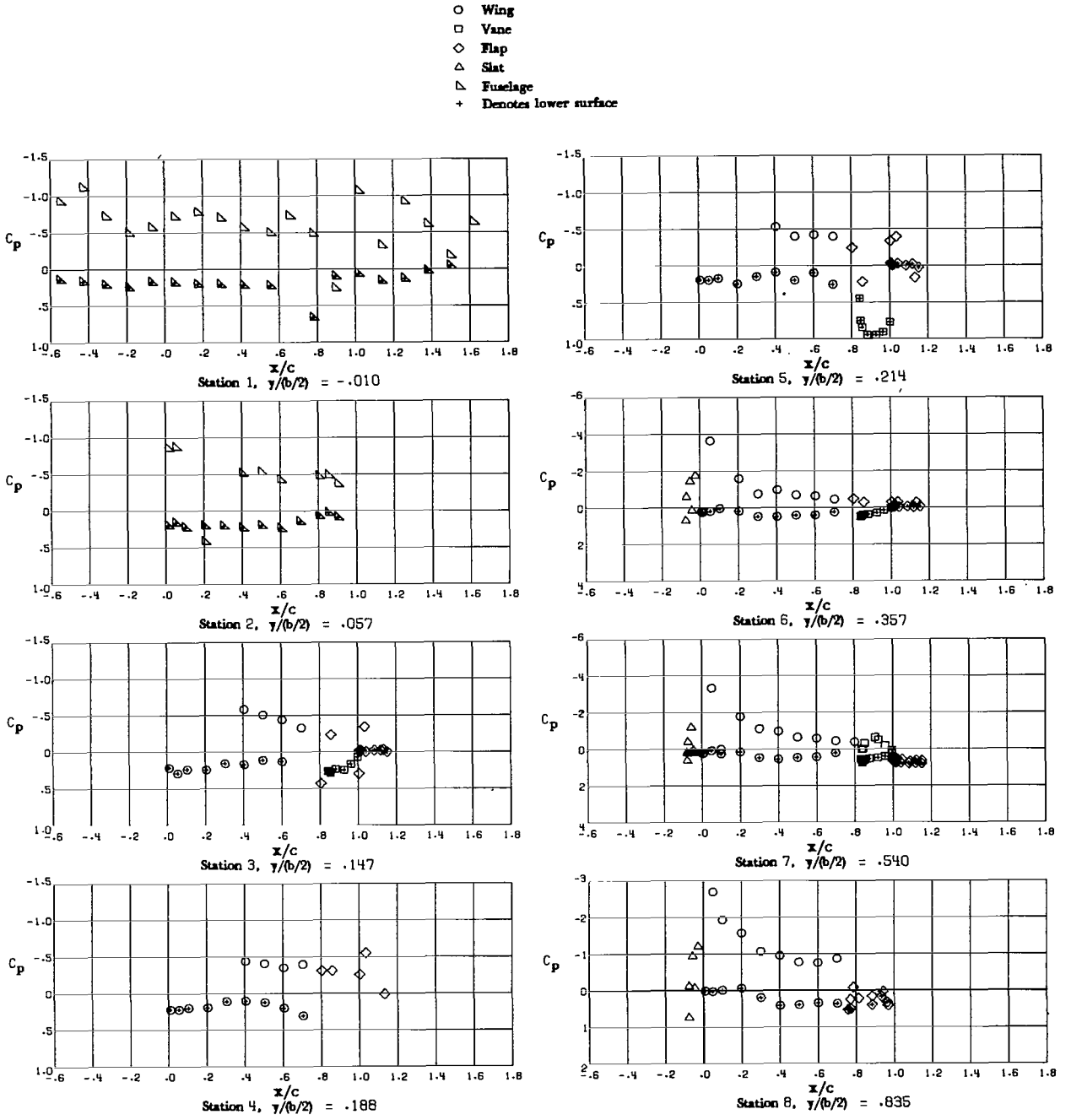

(d) Right engine inoperative; $\alpha = 8.61^{\circ}$; $C_{\mu} = 1.54$; $C_{\mu,a} = 0.020$; $C_{\mu,le} = 0.010$.

Figure 4.- Concluded.

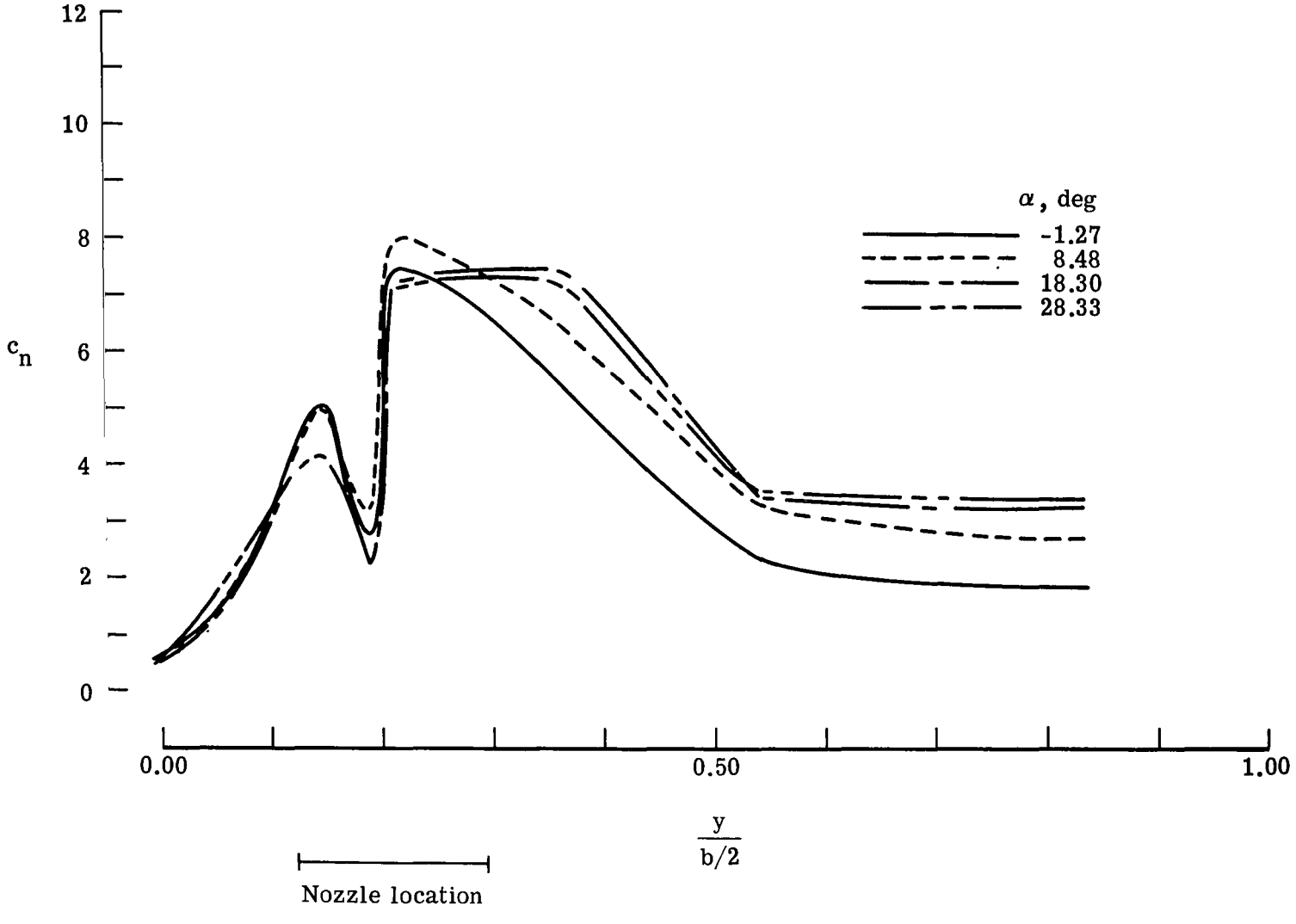

Figure 5.- Effect of angle of attack on spanwise distribution of section normal-force coefficient. Deflectors on; $\delta_f = 72^o$; $\delta_a = 50^o$; $C_\mu = 2.5$; $C_{\mu,a} = 0.020$; $C_{\mu,le} = 0.013$.

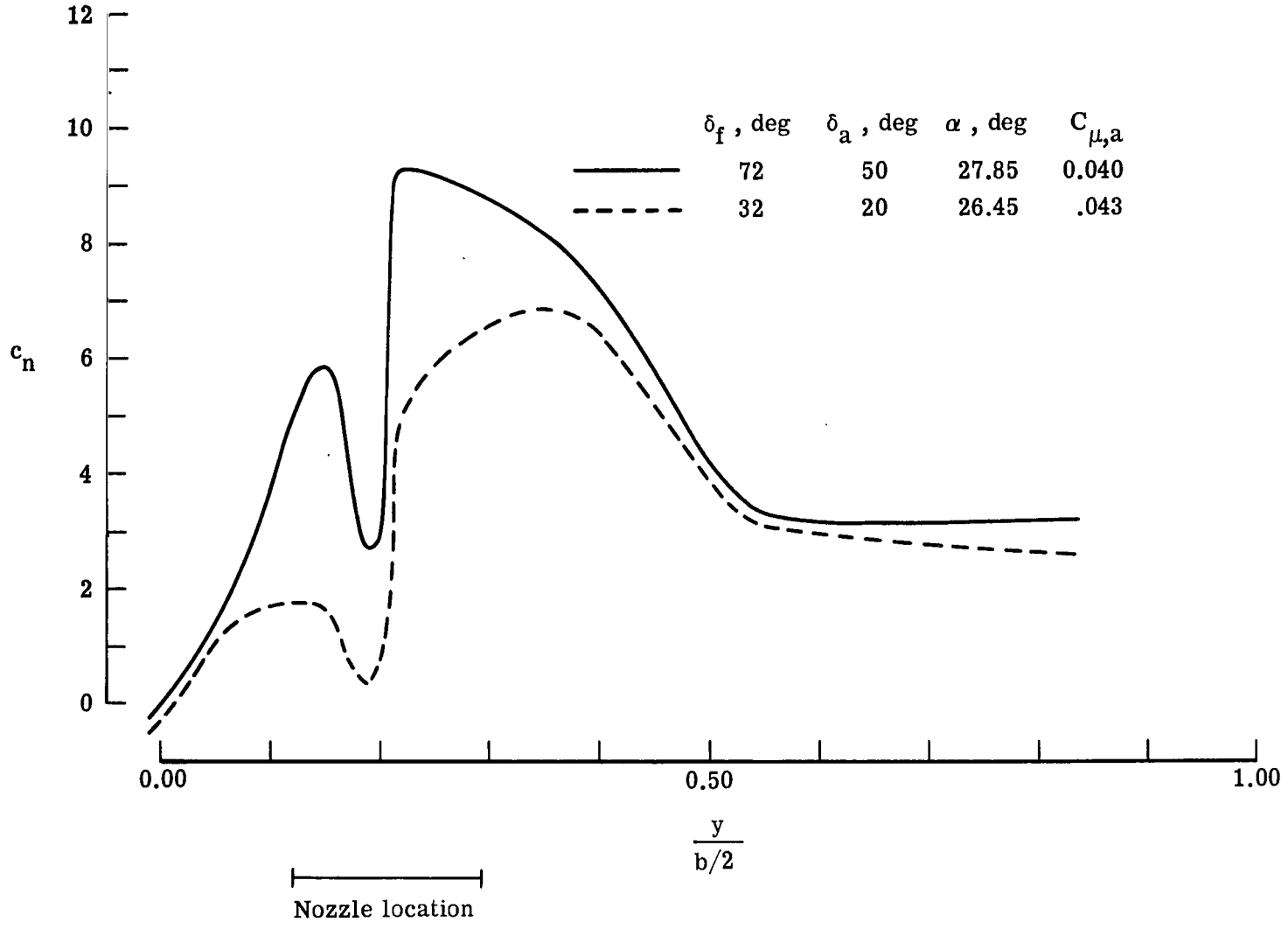

Figure 6.- Effect of flap deflection angle on spanwise distribution of section normal-force coefficient. Deflectors on; $C_\mu = 4.0$; $C_{\mu,le} = 0.020$.

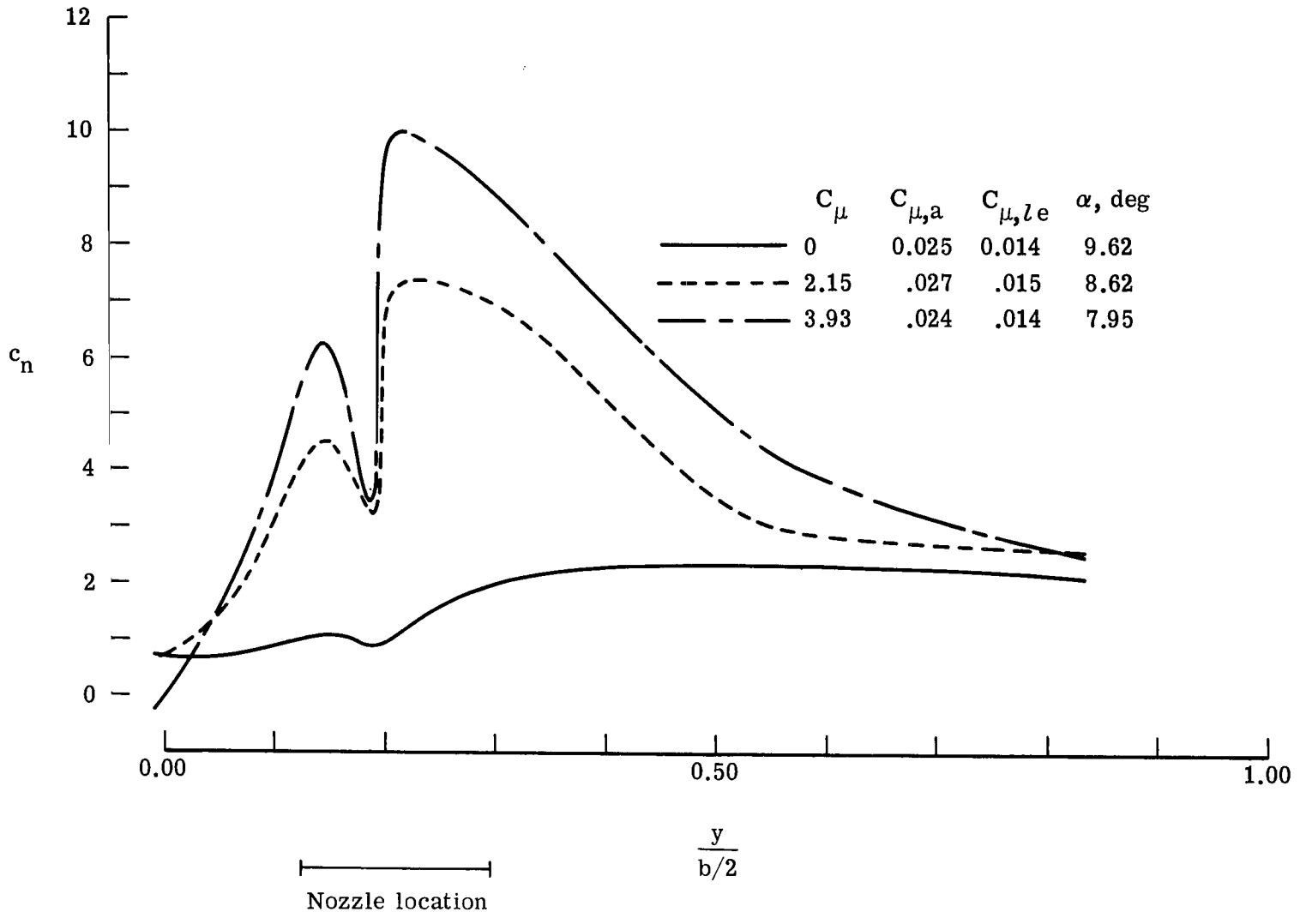

Figure 7.- Effect of thrust coefficient on spanwise distribution of section normal-force coefficient. Deflectors on; $\delta_f = 72^o$; $\delta_a = 50^o$.

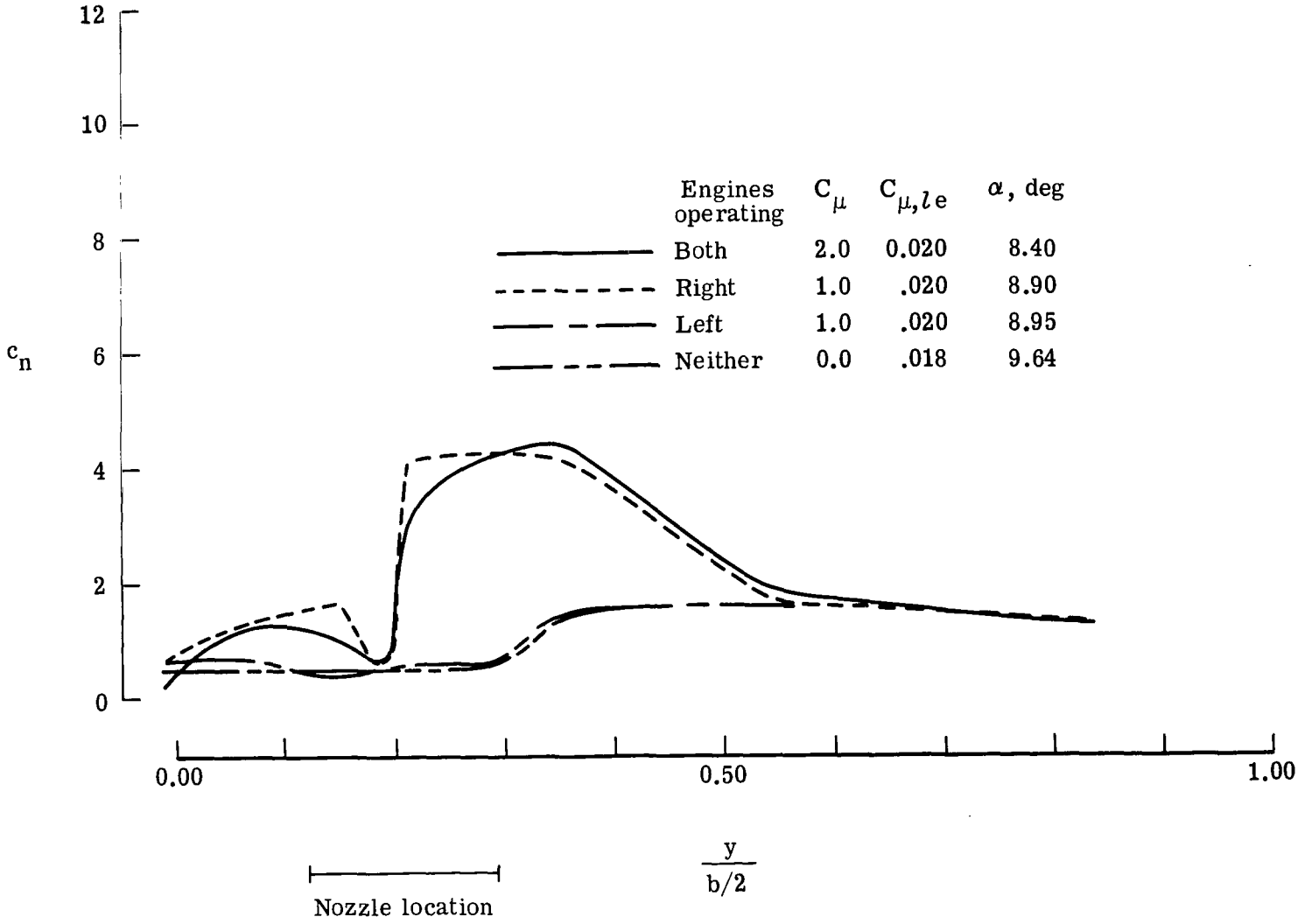

Figure 8.- Effect of engines inoperative on spanwise distribution of section normal-force coefficient. Deflectors on; $\delta_f = 32^o$; $\delta_a = 20^o$; $C_{\mu,a} = 0.043$.

III. TEMPERATURE AND VIBRATION CHARACTERISTICS

James A. Schoenster and Conrad M. Willis

SUMMARY

This part of the report presents the results of tests to measure the temperatures and vibration response due to jet impingement on the upper surface of the wing and flaps of the upper-surface blown model. Results indicate that temperatures up to 250° C occurred on the skin of the wing section and root-mean-square vibratory accelerations up to 38g were obtained on the first flap element. Comparison of the acceleration power spectral densities in the range of tunnel airspeeds and airplane angle of attack of the investigation indicated that there was no noticeable effect of these variables on the response. Although the overall vibratory accelerations appeared to be related to the 3.1 power of the engine-exhaust Mach number, investigation of the power spectral densities indicates that the forcing function on the wing and flap was much too complicated to express in a simple power-law relationship.

INTRODUCTION

One of the problems associated with the use of an upper-surface blown (USB) powered-lift system is the generation of high levels of fluctuating pressures on the surface of the wing and flaps. These fluctuating pressures cause loads which increase the possibility of acoustic fatigue failures, of high vibration levels, and of objectionable cabin interior noise levels. Therefore, plans were made to obtain data on the fluctuating pressures on the wing-flap surfaces so that the effects of forward speed, angle of attack, flap setting, and engine thrust could be evaluated. Unfortunately, the pressure transducers designed to withstand the temperatures and to compensate for the high vibration levels proved to be unsatisfactory because of sensitivity drift (probably due to the high temperatures). This problem of sensitivity drift made it impossible to obtain reliable data. However, data were obtained on the temperatures and vibratory accelerations for the wing and flaps. This part of the report presents the temperature and vibration characteristics of the model and provides analysis of the data to aid in determining the more significant parameters affecting the surface temperatures and vibration response of the wing and flaps of the model.

SYMBOLS

Dimensional data were obtained in U.S. Customary Units and are presented herein in both the International System of Units (SI) and the U.S. Customary Units.

g unit	ratio of vibratory acceleration to acceleration of gravity
M_j	jet Mach number at nozzle exit
T	static thrust force, N (lb)
V_∞	free-stream tunnel velocity, m/sec (ft/sec)
α	angle of attack, deg (see fig. 1 of part I)
δ_f	deflection of USB and double-slotted flap (deflected together), deg (see figs. 2 and 3 of part I)

Abbreviations:

PSD	power spectral density
rms	root mean square
USB	upper-surface blown

APPARATUS

Model

The model used in these tests is shown in figure 2 of part I of this report. Details of the model and model installation are presented in part I.

Instrumentation

The area on the left wing and flaps directly behind the engine was instrumented with an experimental dual-sensing transducer. These transducers, which include both a fluctuating pressure gage and a vibratory accelerometer, were installed in three locations as shown in figure 1. Location 1 is on the main wing, location 2 is on the vane or first flap element, and location 3 is on the aft flap element. It was anticipated that these locations

would experience high temperatures and high vibrations; therefore, the experimental transducer had been designed to withstand this environment. Unfortunately, the pressure transducer proved to be unsatisfactory because of sensitivity drift (probably due to the high temperatures). This problem of sensitivity drift made it impossible to obtain even relative levels of pressure or to separate the signal due to fluctuating pressure from that due to vibration of the pressure transducer. Data from the vibratory accelerometer were considered satisfactory. Located in a common holder with each of these transducers was a surface-mounted chromel-alumel thermocouple. In addition to the three locations of the dual systems, a thermocouple was located behind the exhaust nozzle (location A shown in fig. 1). Signals from each of these transducers were recorded on an FM tape-recording system.

TESTS AND PROCEDURES

Data on the surface temperatures and vibrations were obtained for the test conditions listed in table I. Data for each of the configurations were recorded on magnetic tape. The temperatures are presented in figures 2 and 3. Overall root-mean-square vibratory accelerations (in g units) were obtained and are presented in figures 4(a) and 4(b). These fluctuating vibration data were further analyzed on a narrow-band power-spectral-density (PSD) analyzer using a constant bandwidth of 10 Hz over a frequency range from 0 to 5 kHz. These data were then normalized for comparison purposes. The effects of tunnel speed and airplane angle of attack are presented in figures 5 and 6. The effect of jet-exhaust Mach number is presented in figures 7 and 8.

RESULTS AND DISCUSSION

Temperatures

Shown in figure 2 are the temperature distributions measured on the surface of the wing and flaps for maximum thrust conditions for the 72° and 32° flap settings. The maximum temperature measured on the wing was 250° C at location 1 for the 72° flap. Also, for the 72° flap, the distribution of temperatures measured with a tunnel airspeed of 17 m/sec (54 ft/sec) was about the same as the temperature distribution with zero forward speed. Although the thrust level was lower for the 32° flap setting, the temperatures on the trailing flap were approximately the same, 130° C, for both the 32° flap setting and the 72° flap setting.

A comparison of the temperature data obtained at location 1 over the range of configurations and test conditions indicates that the data are independent of flap angle, tunnel speed, or angle of attack (see fig. 3). For each condition, the temperature increased as

a function of increased engine-exhaust Mach number, that is, increased thrust. The maximum temperatures measured were higher than values considered to be tolerable for most aluminum alloys. These results indicate that special consideration will be required in the selection of materials for a USB configuration of this type.

Vibratory Accelerations

The effect of the nozzle exit Mach number on the vibratory accelerations is shown in figure 4. The accelerations (in g units) are plotted as a function of jet Mach number in log-log coordinates for the test conditions. Little effect of the tunnel forward speed on the accelerations of the structure is apparent for either the 72° flap (fig. 4(a)) or the 32° flap (fig. 4(b)). The highest rms acceleration measured was 38g at location 2 for the 72° flap setting and an exhaust Mach number of 0.56. It is not apparent why these accelerations were the highest at location 2, but it is of interest to note that this area also experienced maximum values of static pressure (see part II). Although the internal structure of this model was considerably modified for these tests and may not represent standard airplane design, these high vibration levels emphasize the need for close attention to the structural design of USB configurations.

Also shown in figure 4 are straight-line fairings of the data which imply a power-law relationship between the vibratory accelerations and the nozzle exit Mach number. Fairings for both flap settings indicate that the accelerations are proportional to jet Mach number to the 3.1 power. To compare the frequency distributions for the various conditions, the power spectral densities were normalized by this relationship and the results are presented in figures 5 to 8. The normalized PSD data were quite similar, and only the envelope encompassing the boundaries is presented except for the data of figure 7(a).

The data of figure 5 indicate that the normalization procedure collapses the 72° flap setting data into a narrow envelope whose width only exceeds 10 dB at location 3 in the upper frequencies. The sharp peaks in the PSD curves at frequencies about 90 Hz, 200 Hz, and 320 Hz for all three locations indicate that some structural modes may be strongly excited. The effects of tunnel airspeed and angle of attack used in this study were minimal for the same jet exhaust Mach number.

Similar results may be seen in figure 6 for the 32° flap setting. The sharp peak at 4500 Hz in figure 6(a) is related to engine fan speed. For this flap setting, however, the low-frequency peaks are not as evident as were those for the 72° flap configuration.

The effects of jet Mach number on the normalized vibration response are shown in figures 7 and 8. Although the PSD amplitudes are normalized by a function of Mach number, the PSD shapes differ considerably at location 1 (fig. 7(a)). Below 300 Hz, the normalized PSD curves are similar and collapse well within a band of 10 dB; however, above 300 Hz, there is considerable difference. Between 300 Hz and 2200 Hz there are no

clearly defined peak amplitudes but, rather, frequency bands of high levels. For an exhaust Mach number of 0.26, the band covers a range of about 500 to 600 Hz; for an exhaust Mach number of 0.39, the range is from about 600 to 900 Hz; for an exhaust Mach number of 0.48, the range is from about 800 to 1300 Hz; and for an exhaust Mach number of 0.56, the range is from about 1100 to 2200 Hz. The sharp peaks at 3250 Hz and 4500 Hz are related to engine fan speeds. This increase in the frequency of peak response with increasing exhaust Mach numbers indicates that a frequency normalization, such as Strouhal number, might be an effective scaling parameter for the frequencies above 300 Hz.

The PSD data collapse quite well with only the amplitude normalization at locations 2 and 3 (figs. 7(b) and 7(c)). This difference in the vibratory accelerations at different locations on the wing flap indicates that the forcing function varies with location. Location 1 is in the area in which the jet exhaust directly impacts on the wing, whereas locations 2 and 3 are farther downstream of this flow. This would imply that there are at least two sources of vibration: (1) the fluctuating pressures caused by the jet exhausting through the nozzle and following a frequency-dependent phenomenon and (2) an independent force governing the low-frequency range of vibrations and the vibration of the structure away from the impact area.

Presented in figure 8 are the data from the 32° flap setting. These data appear to collapse with only PSD normalization at location 1 (fig. 8(a)) and location 3 (fig. 8(b)); however, the range of exhaust Mach numbers of the investigation (0.25 to 0.38) may not have been large enough to observe a relationship between the frequency of maximum response and the jet exit Mach number (see fig. 7(a)).

SUMMARY OF RESULTS

Measurements of temperatures and vibration response were obtained on the wing-flap of an upper-surface blown model in the Langley full-scale tunnel. Temperatures up to 250° C were measured on the skin of the wing section and root-mean-square vibratory accelerations up to 38g were obtained on the first flap element.

Comparisons of the acceleration power spectral densities in the range of tunnel airspeeds and airplane angle of attack of the investigation indicated that there was no noticeable effect of these variables on the response. Although the vibratory accelerations appeared to be related to the 3.1 power of the engine-exhaust Mach number, investigation of the power spectral densities indicates that the forcing function on the wing and flap was too complicated to express in a simple power-law relationship.

TABLE I.- TEST CONFIGURATIONS AND CONDITIONS

Tunnel speed, V_∞		Angle of attack, α, deg	Flap setting, δ_f, deg	Engine		
				Exhaust Mach number, M_j	Thrust per engine	
m/sec	ft/sec				kN	lb
0	0	0	72	0.26	1.4	310
0	0	0	72	.39	2.8	640
0	0	0	72	.48	4.4	980
0	0	0	72	.56	5.8	1300
15	50	0	72	.26	1.4	310
16	51	0	72	.39	2.9	640
16	51	0	72	.48	4.3	960
17	54	0	72	.56	5.8	1300
17	56	-6	72	.55	5.7	1290
15	50	28	72	.55	5.7	1290
0	0	0	32	.25	1.2	280
0	0	0	32	.32	1.9	440
0	0	0	32	.38	2.7	600
12	40	0	32	.27	1.4	320
12	38	0	32	.36	2.1	480
12	38	0	32	.39	2.9	640
13	41	28	32	.37	2.7	600
12	38	28	32	.25	1.2	280

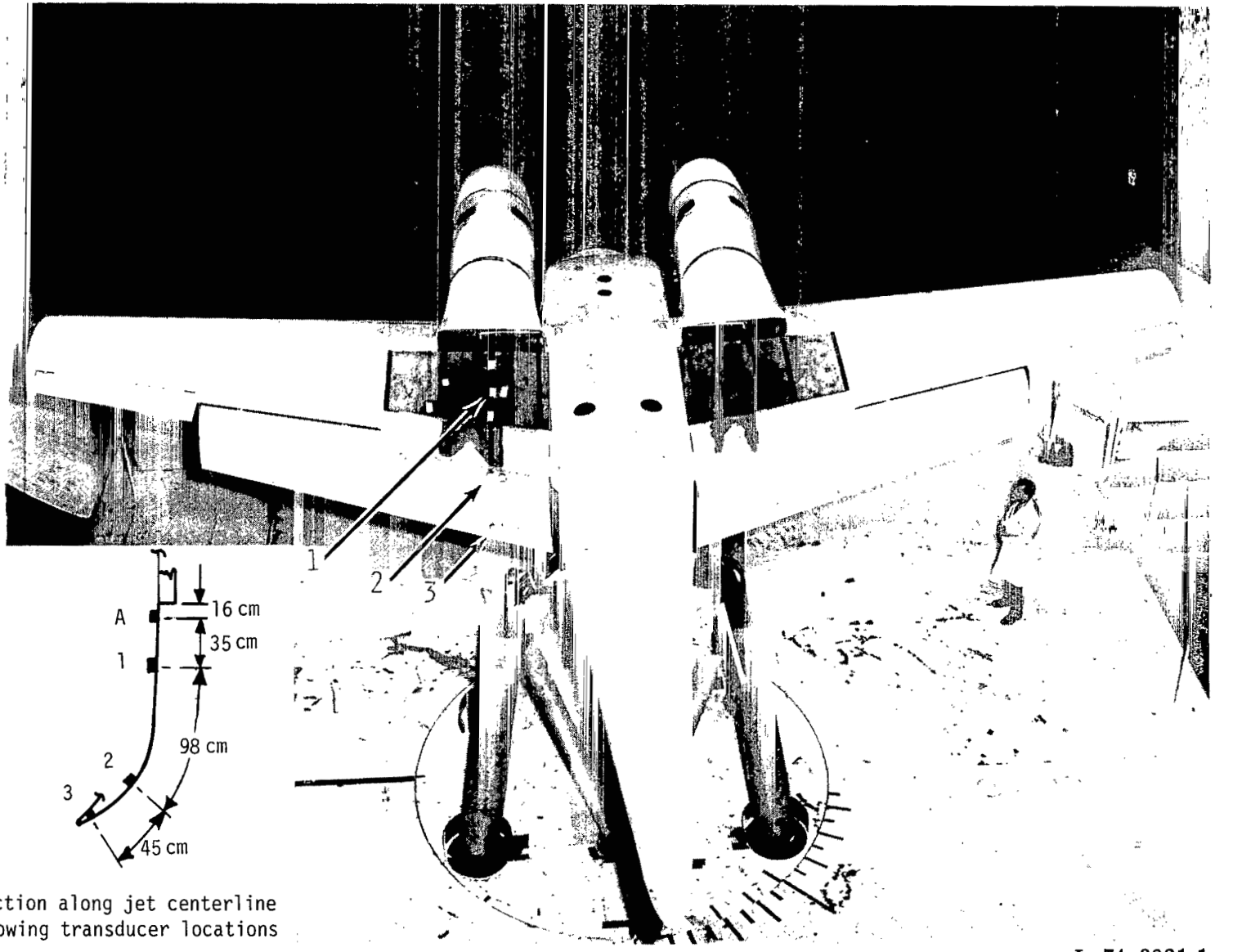

L-74-3021.1

Figure 1.- Test airplane in Langley full-scale tunnel. Arrows indicate transducer locations.

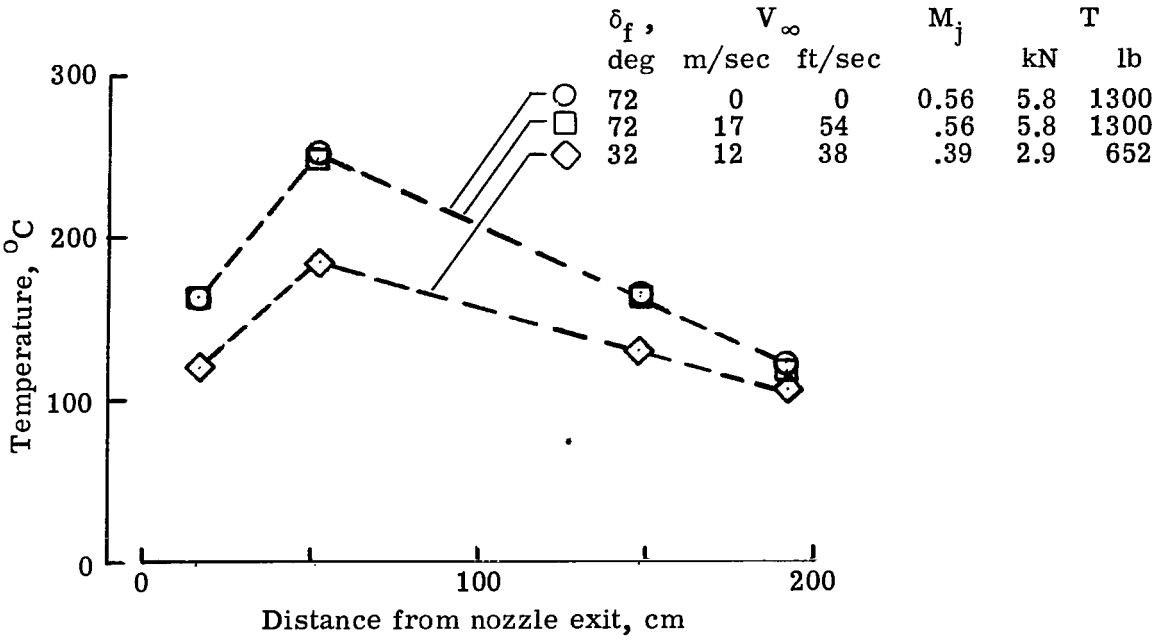

Figure 2.- Upper-surface temperatures along engine centerline. $\alpha = 0^{o}$.

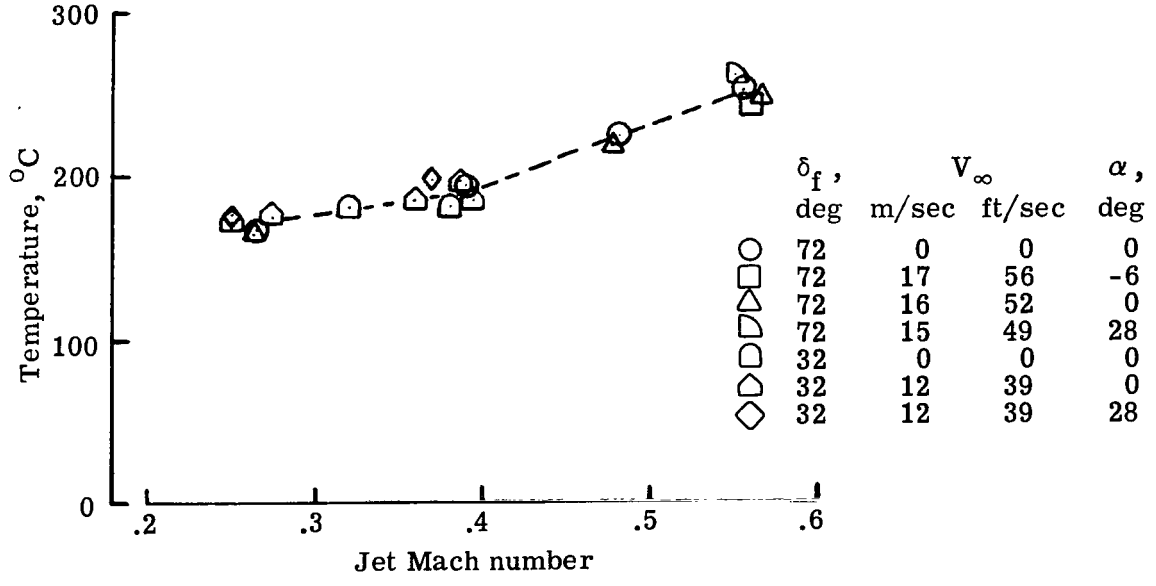

Figure 3.- Variation of surface temperature with jet Mach number. Transducer location 1.

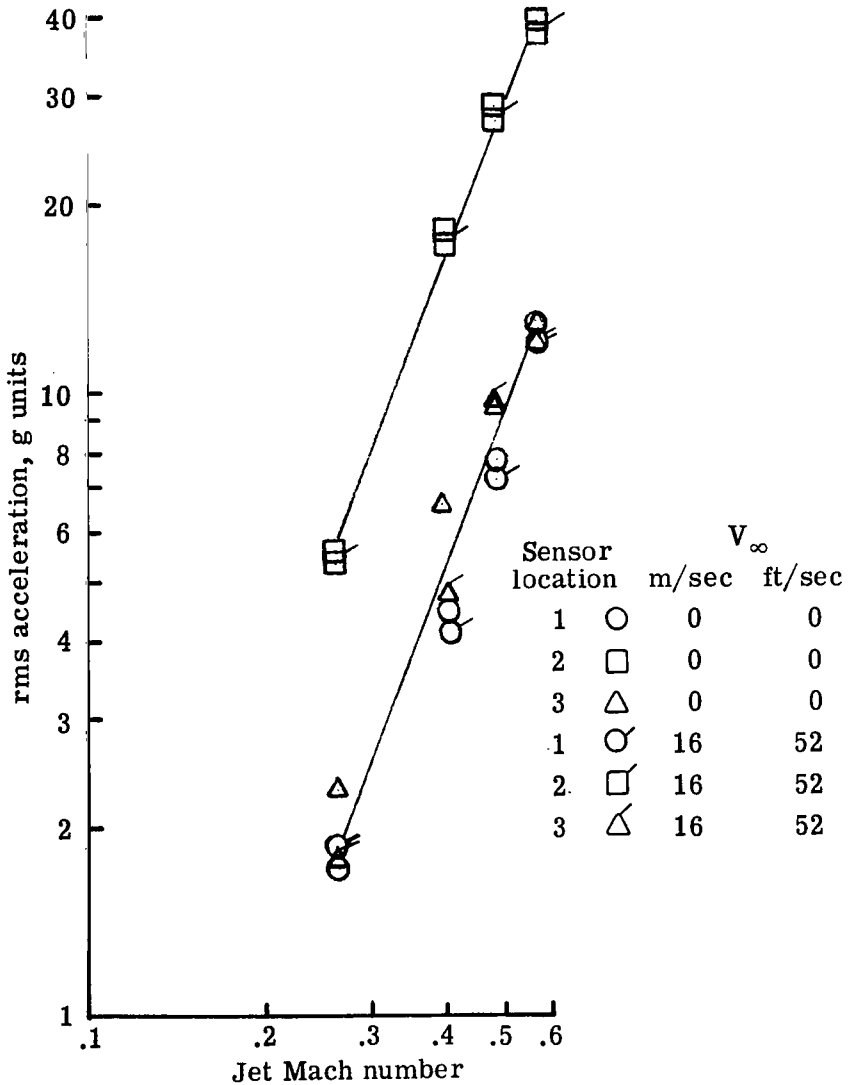

(a) 72^o flap.

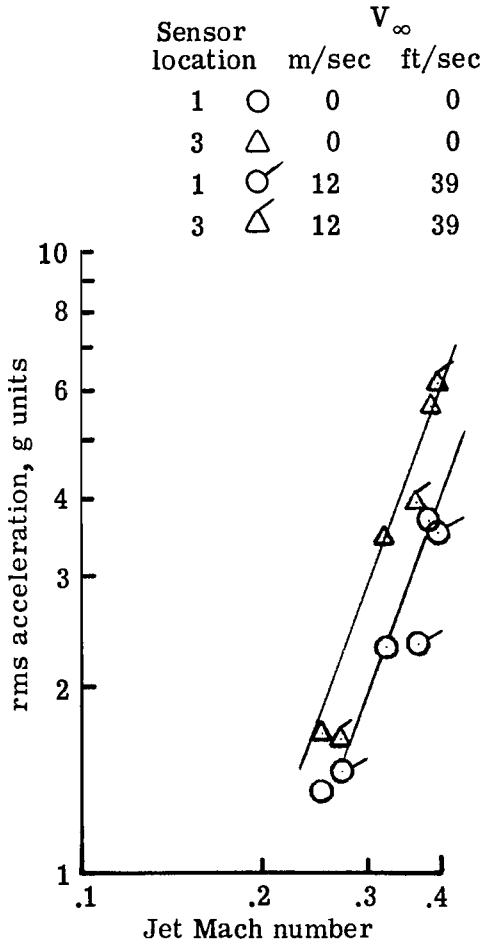

(b) 32^o flap.

Figure 4.- Variation of vibratory accelerations with jet Mach number. $\alpha = 0^o$.

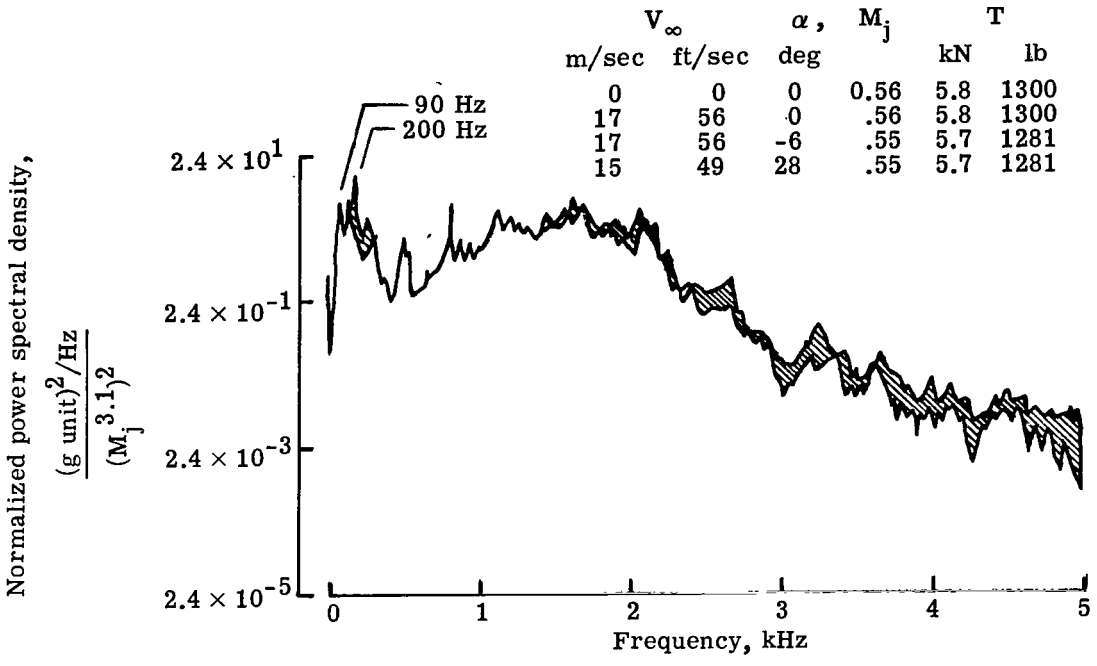

(a) Location 1.

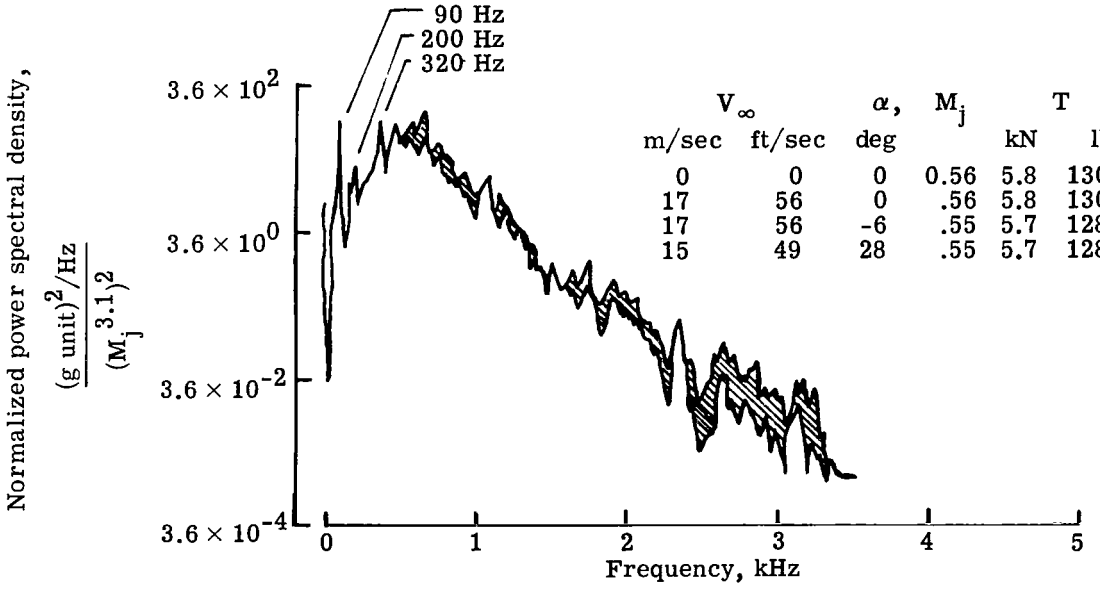

(b) Location 2.

Figure 5.- Effect of airspeed and angle of attack on normalized vibration PSD for 72^{o} flap deflection.

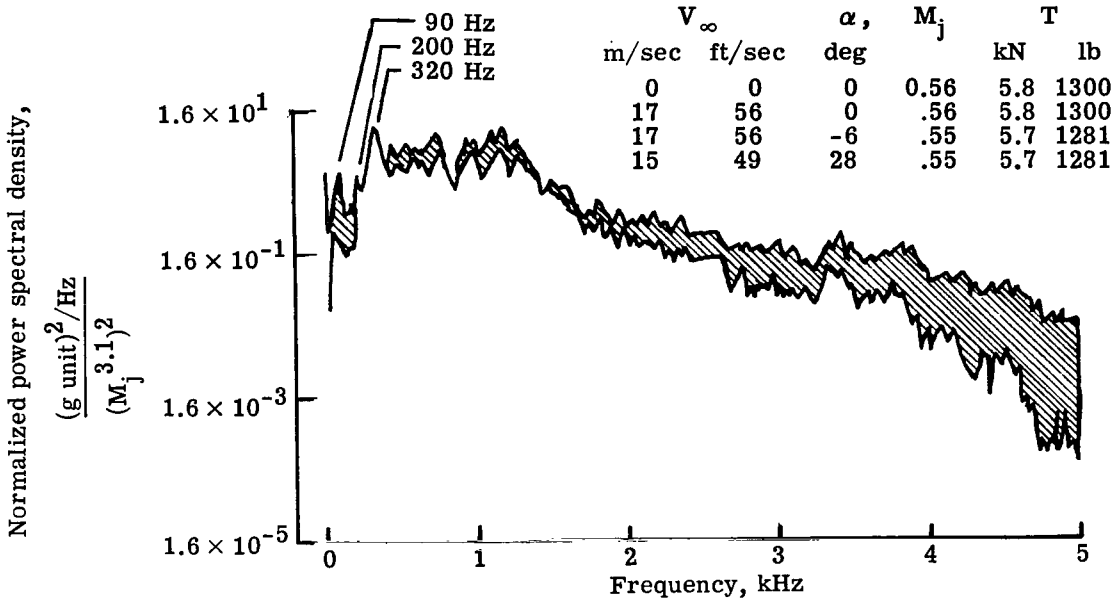

(c) Location 3.

Figure 5.- Concluded.

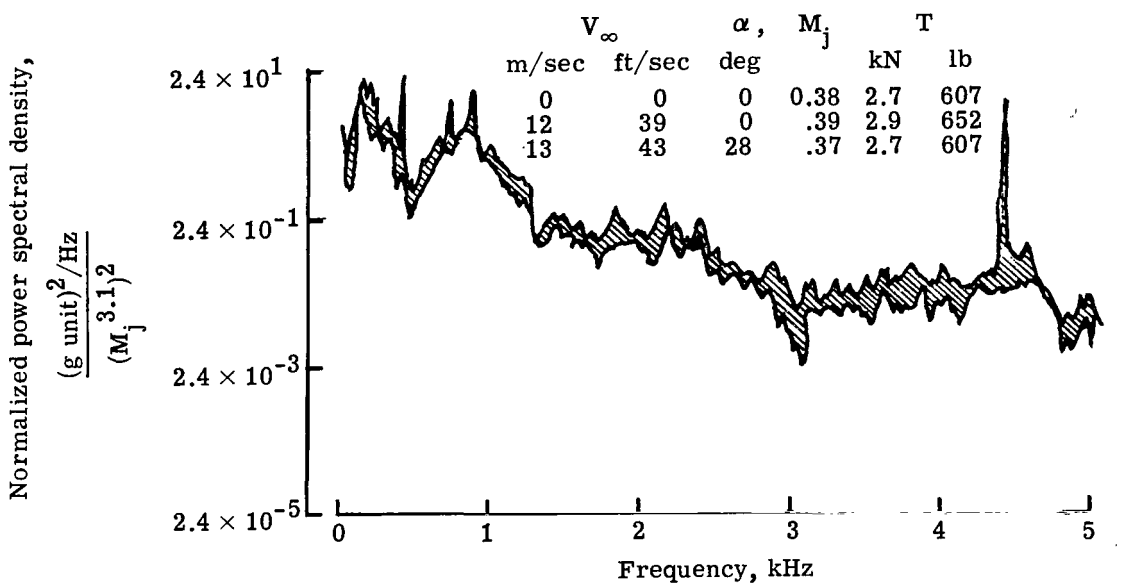

(a) Location 1.

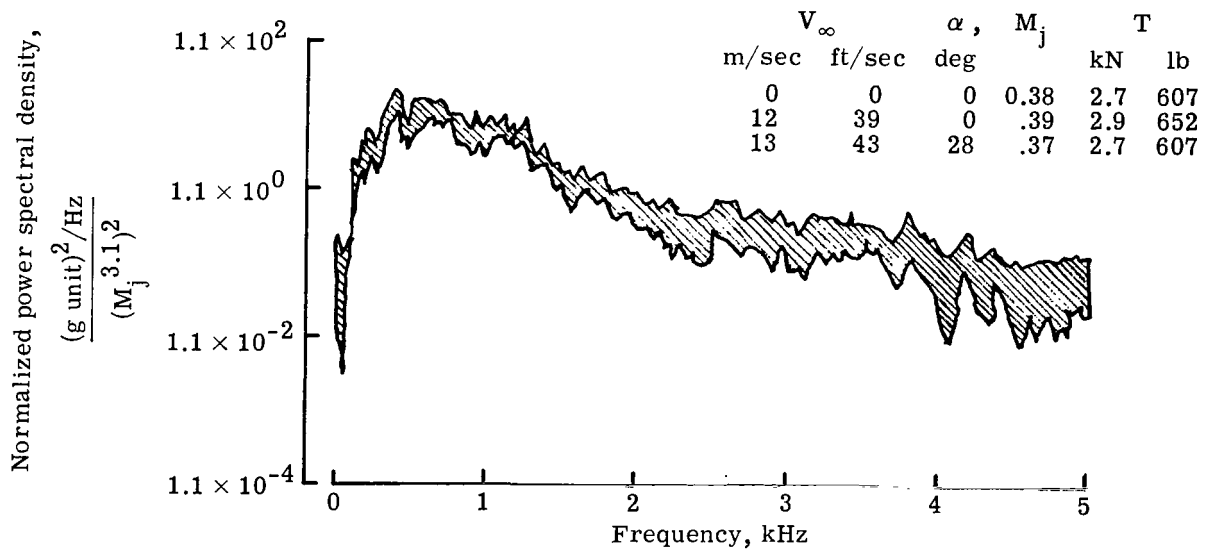

(b) Location 3.

Figure 6.- Effect of airspeed and angle of attack on normalized vibration PSD for 32° flap deflection.

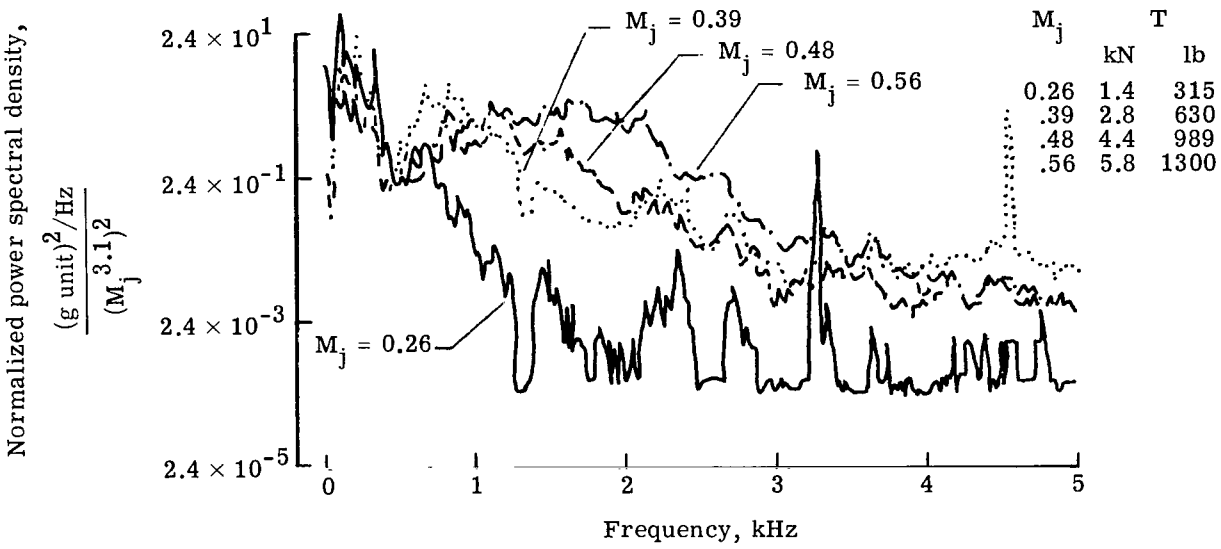

(a) Location 1.

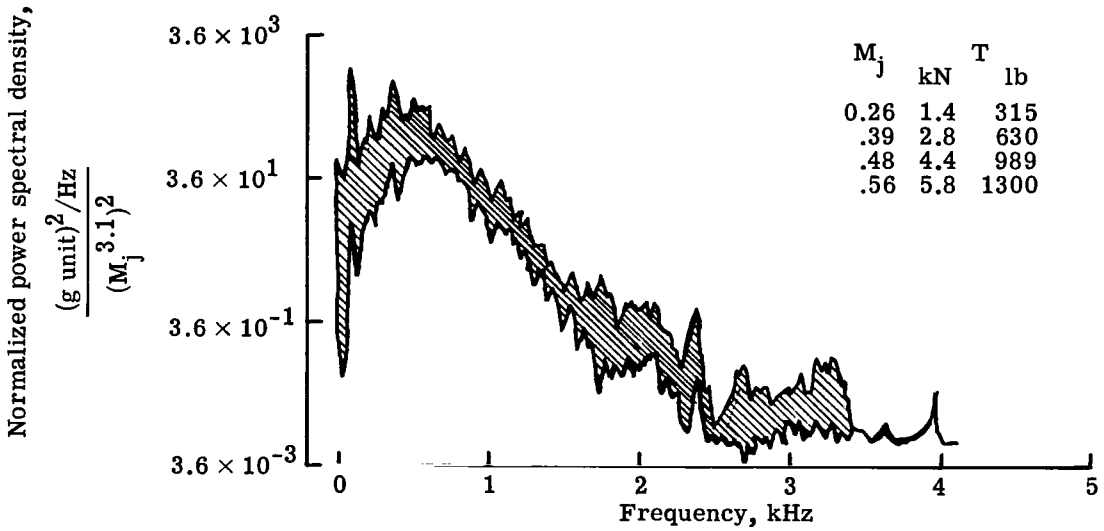

(b) Location 2.

Figure 7.- Effect of jet Mach number on normalized vibration PSD for 72° flap deflection. $V_\infty = 0$; $\alpha = 0°$.

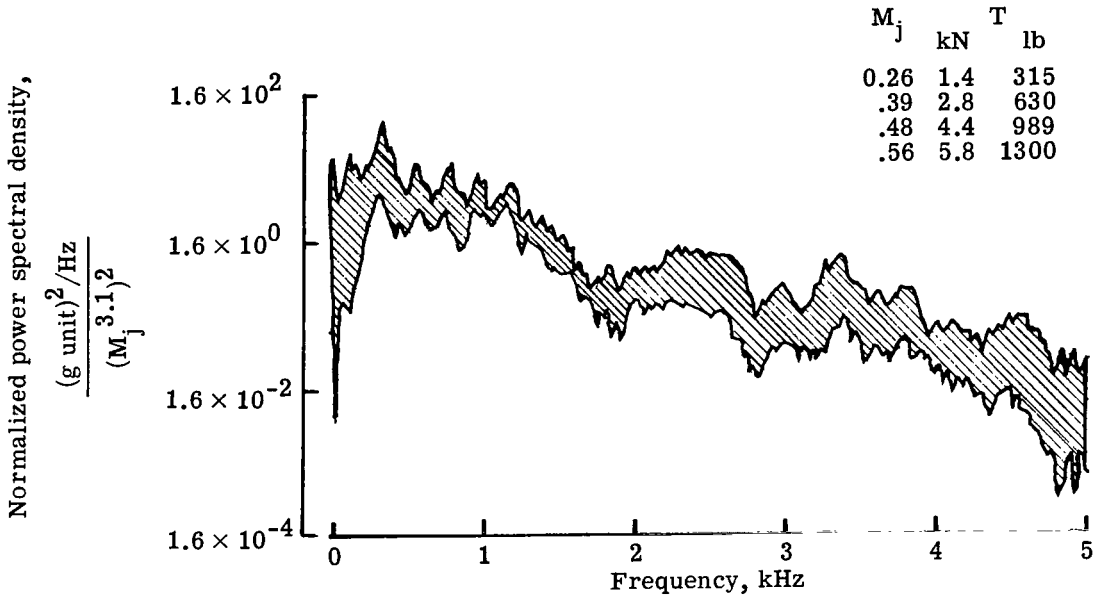

(c) Location 3.

Figure 7.- Concluded.

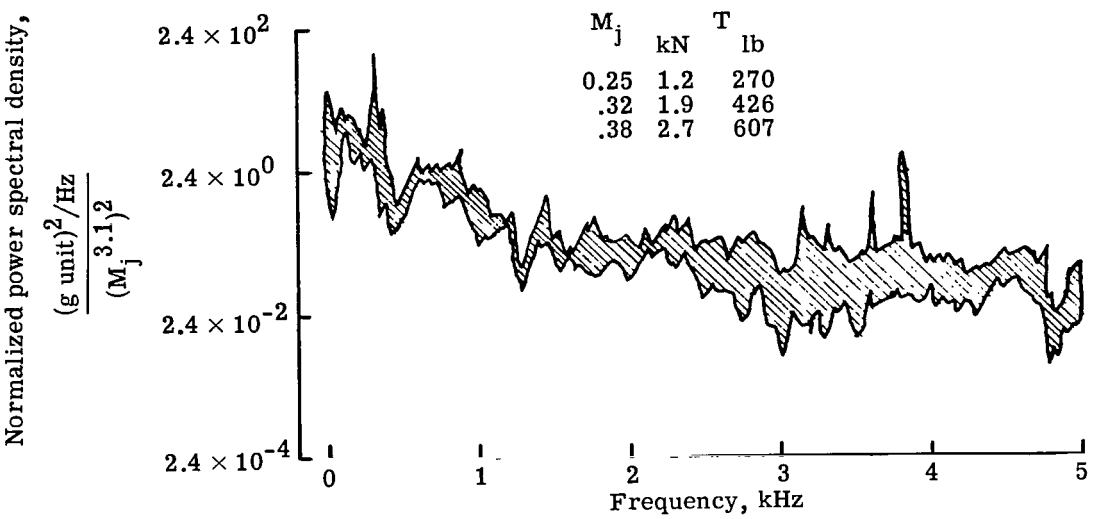

(a) Location 1.

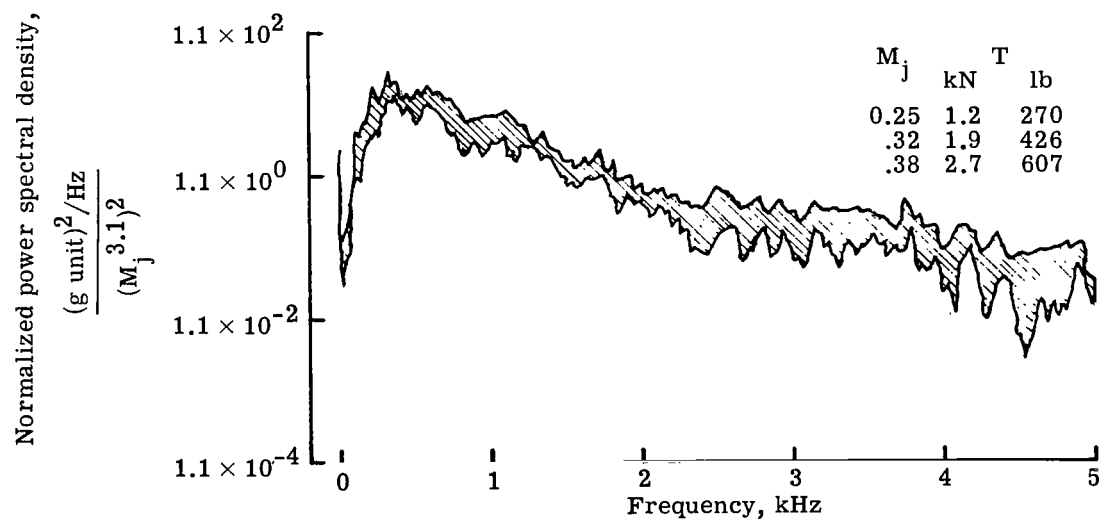

(b) Location 3.

Figure 8.- Effect of jet Mach number on normalized vibration PSD for 32° flap deflection. $V_\infty = 0$; $\alpha = 0°$.

IV. ACOUSTIC CHARACTERISTICS

John S. Preisser and David J. Fratello

SUMMARY

This part of the report presents results from static and low-forward-velocity acoustic tests of a large-scale upper-surface blown model in the Langley full-scale tunnel. Results indicate that the acoustic properties of the upper-surface blown model were characterized, primarily, by an unsymmetrical radiation pattern due mainly to shielding of the high-frequency engine noise and the production of low-frequency noise by jet-surface interaction. The directivity of the low-frequency noise was found to depend on the trailing-edge flap angle for low thrust levels. Normalized sound-pressure-level spectral density data showed good agreement at low Strouhal numbers with other small- and large-scale-model data from previous tests using simulated wing-flap systems. Forward-speed effects were negligible at the low tunnel speeds used during the tests.

INTRODUCTION

To date, there are many published papers on the noise characteristics of a variety of air jets mounted over flat and curved plates which simulate wing surfaces (refs. 1 to 7, for example). Most of the work has been done at small scale and few data are available on both aerodynamics and noise from the same model. The purpose of the present noise tests was to provide baseline acoustic data on a large-scale upper-surface blown configuration having turbofan engines for which acceptable powered-lift performance was obtained. The tests included measurements of noise directivity and spectral content for various flap configurations and various engine thrust settings, a determination of the effect of tunnel flow on noise generation, and a preliminary assessment of the applicability of the small- and large-scale-model data to the more realistic full-scale configuration studied herein. Qualitative results from outdoor static tests of the turbofan engine and a boilerplate wing-flap system are also included.

SYMBOLS

Dimensional data were obtained in U.S. Customary Units and are presented herein in both the International System of Units (SI) and the U.S. Customary Units.

D	equivalent nozzle exit diameter, $\sqrt{\frac{4}{\pi}(\text{Nozzle exit area})}$, m (ft)
f	frequency, Hz
p*	root-mean-square acoustic pressure in specified frequency bandwidth, Pa (lb/ft^2)
p_{ref}	reference acoustic pressure, 20 μ Pa (42×10^{-8} lb/ft^2)
r	radial distance from wing trailing edge (with flaps retracted) to microphone position, m (ft)
V	average nozzle exit velocity, m/sec (ft/sec)
V_∞	free-stream tunnel velocity, m/sec (ft/sec)
δ_f	deflection of USB and double-slotted flap (deflected together), deg (see figs. 2 and 3 of part I)
θ	angle from forward engine axis, measured clockwise, deg (see fig. 2)
θ_f	$= 180^o - \delta_f$

Abbreviations:

OASPL	overall sound pressure level, dB
PSD	power spectral density, $10 \log \frac{p^{*2}}{\Delta f p_{ref}^2}$, dB
SPL	sound pressure level, $20 \log \frac{p^*}{p_{ref}}$, dB
USB	upper-surface blown

TESTS AND PROCEDURES

Test Conditions

Tests were conducted with two different flaps as described in part I. The flaps had upper-surface deflection angles of 72° and 32°, respectively. (Refer to fig. 4(b) in part I of this report.) For each flap setting, both engines were run at four thrust conditions corresponding to average nozzle exit velocities of 131, 189, 236, and 262 m/sec (430, 620, 774, and 860 ft/sec).

Tests were performed both with and without tunnel flow. The tunnel was run at a free-stream dynamic pressure of about 120 Pa (2.6 lb/ft^2), which was determined by scaling requirements of the performance and loads investigations. This condition resulted in a free-stream velocity of approximately 14 m/sec (46 ft/sec). Most of the tests reported herein were performed without tunnel flow. The effect of the acoustical inlet treatment (shown in fig. 6 of part I of this report) on the radiated inlet noise was not studied.

Wind-Tunnel Acoustic Environment

The Langley full-scale tunnel is a large wind tunnel with an open-throat test section. The model was mounted on large struts so that the engine exhaust nozzle was approximately 4.3 m (14 ft) above the ground board (refer to fig. 3 in part I of this report). The ceiling and side walls of the tunnel have had sound-absorbing treatment to reduce reflections for improved aeroacoustic testing. Previous evaluations of the acoustic characteristics of the tunnel (ref. 8) have determined that the ground board is the major reflecting surface affecting noise measurements in the test section. Noise measurements taken 3.0 m (10 ft) above the ground board for an omnidirectional noise source also positioned 3.0 m (10 ft) above the ground board showed that within a radial horizontal distance of approximately 7.6 m (25 ft) the direct noise field exceeded the reflected field. In the vertical direction above the source, the direct field predominated for a distance of about 10.7 m (35 ft).

Ambient overall sound pressure levels measured in the test section were about 70 dB without tunnel flow and 85 dB with the tunnel operating.

Wind-Tunnel Test Procedure

Figure 1 presents a sketch of the model and the microphone setup for the noise tests. Figure 2 presents the coordinate system used throughout this part of the report. During the tests, acoustic data were taken by a microphone with a nose cone, which was traversed in a constant-radius arc (r = 3.7 m (12 ft)) above and aft of the wing on the jet

centerline. In addition, noise measurements were made at two positions beneath the wing by means of flush-mounted microphones on the ground board of the test section, at a sideline position off the wing tip (r = 10.4 m (34 ft)), and at one position far above the wing (r = 12.2 m (40 ft)) out of the tunnel flow. Both the sideline and overhead microphones may have been slightly beyond the maximum distance for which the direct noise field exceeded the reflected field. Hence, no quantitative data are presented for these microphones. The sideline microphone was used for comparing the relative results from the different flap systems. The overhead microphone was used as a reference for comparing noise data with and without tunnel flow. Noise data were measured with 1/2-in. (1.27-cm) condenser-type microphones, analyzed online with a one-third-octave analyzer, and recorded on magnetic tape at 152 m/sec (60 in/sec). The tape data were reduced, by employing a general time series analysis program, to yield power spectral density, one-third-octave band spectrum, and overall sound pressure levels for various frequency ranges. The frequency response curve of the system was flat within ±1.5 dB over the frequency range from 80 to 16 000 Hz. For the microphone measurements on the constant-radius arc, ground-board reflections were assumed to be small and no corrections were made. The readings from the flush-mounted microphones on the ground board and from the sideline and over-the-wing microphones were corrected for distance and reflections based on estimates obtained from reference 8.

Outdoor Static Test Procedure

In addition to the wind-tunnel tests, preliminary noise tests were made by using an outdoor static test setup. A photograph of this test setup is presented as figure 3. A single turbofan engine with a rectangular nozzle was used in conjunction with a partial-span simulated wing-flap system. The wing-flap was mounted in an inverted position to prevent the exhaust from impinging on the ground. Although the setup was far from optimum and had several reflective surfaces nearby, such as buildings and safety screens, it was believed that a qualitative indication of the relative effects of jet noise, deflector noise, and wing-flap interaction noise could be obtained. During the tests, acoustic data were taken by a single microphone which was placed in a position corresponding to the most forward under-the-wing wind-tunnel microphone position (see fig. 1). Data recording and analysis followed the same procedure as that used for the wind-tunnel tests.

RESULTS AND DISCUSSION

Outdoor Static Test Results

Figure 4 presents one-third-octave band spectrum plots from the outdoor static tests of the jet engine alone, the engine with deflector (see figs. 4 and 7 in part I for

details), and the engine with deflector and wing-flap for full engine thrust of 5850 N (1300 lb) with the microphone at a position corresponding to under the wing. The present data show that the high-frequency noise (>3000 Hz) predominates for the engine alone. The peak at 5000 Hz corresponds to the fan-blade-passage frequency and the broadband noise around 1000 Hz is believed to result from other internal sources. Jet exhaust noise for the JT15D-1 has been found to peak around 200 Hz. It is apparent that exhaust noise is not the predominant noise source for this particular jet engine. The addition of the deflector adds several decibels to the measured noise level but does not markedly affect the spectrum shape. When the wing-flap system is added, there is a decrease in noise level for the higher frequencies and an increase for the lower frequencies. This result is in agreement with previous USB noise studies (refs. 1 to 7), where it was found that the wing is effective in shielding the high-frequency noise and that, at the same time, low-frequency jet-surface interaction noise is created.

Wind-Tunnel Test Results

Narrow-band plots of power spectral density for the most forward under-the-wing microphone position in the wind tunnel are presented in figure 5 in order to better define the frequency content of a typical set of data at zero forward speed. Results are shown for four different thrust cases which correspond to nozzle exit velocities of 131, 189, 236, and 262 m/sec (430, 620, 774, and 860 ft/sec, respectively). The velocities are average values obtained from detailed flow surveys of the JT15D-1 with the rectangular nozzle as presented in reference 9. The data, which were obtained for 32° flaps, were analyzed by using a constant filter bandwidth of about 30 Hz. The low frequencies predominate under the wing, as expected. The fan blade tone occurs at about 3100 Hz for the lowest exit velocity. The fundamental fan tone is seen to increase in frequency with increasing exit velocity (or engine rpm), as expected.

Figure 6 shows one-third-octave band plots of sound pressure level for the 32° flaps with engines at full thrust. The data correspond to six different values of θ ranging from directly above the wing ($\theta = 270^{\circ}$) to directly below the wing ($\theta = 90^{\circ}$). The highest frequencies (>5000 Hz) show a very large (30 dB) drop in sound pressure level from above to below the wing. The middle frequencies ($\approx$1000 Hz) indicate a moderate drop (15 dB); whereas the lowest frequencies (<300 Hz) show only a small change. The lack of symmetry in the noise field results from the interaction and modification of the flow by the wing-flap system and the subsequent reflection of some of the noise upward. Thus, the positions beneath the wing are effectively "shielded" from some of the noise that is generated. This result was expected; however, the amount of change indicated in this figure is larger than that which has been reported previously (refs. 1 to 7). The unexpected result can perhaps be explained by the fact that in most previous tests, turbofan engines were not

used and, hence, the high turbofan frequencies were not present. In addition, many of the previous tests had simulated flaps of small span, which would result in some sound being diffracted around the edges; the model reported herein had a large wing span which provided additional shielding in this direction. The large amount of fan-noise shielding agrees with results of a previous test (ref. 10) wherein internal machinery noise was simulated by placing an orifice upstream of a 5-cm-diameter (2-in.) nozzle and up to 10 dB of wing shielding was measured.

The directivity patterns of the overall sound pressure level (OASPL) for the full frequency range (80 to 16 000 Hz) and also for the low-frequency range (<300 Hz) are shown in figure 7 for both the 32° and 72° flaps. The origin of these directivity plots was taken to be the chordwise position which corresponded to the wing trailing edge with no flaps present as indicated by the sketch in the center of the figure. The data were obtained at a radial distance of 3.7 m (12 ft) from this point. The full-frequency-range directivity plots are similar in shape for both the 32° and 72° flaps. For all the velocities shown, there is a systematic decrease in OASPL as θ is decreased from 270° to 90°. This result is consistent with the trend noted in figure 6. The low-frequency plots (figs. 7(c) and 7(d)) show very little change in noise level with variations in θ. In addidion, for the lowest velocity, the 72° flap has a directivity similar to the 32° flap measured relative to the respective flap angle. This similarity can be seen more clearly in figure 7(e). Thus, it appears that for low velocities, the sound field is rotated through approximately the same angle as the nozzle exit flow. On the other hand, for the highest velocity, the low-frequency directivity peaks in the 190° to 210° direction regardless of the flap angle.

Plots of SPL as a function of nozzle exit velocity are presented in figure 8 for both flap angles at selected microphone positions. Note that for $\theta = 192^{\circ}$ (in the aft direction the data vary approximately as a function of V^7. In a direction which is approximately normal to each flap, V^5 (32° flaps) or V^6 (72° flaps) laws predominate. These data, in conjunction with the results of figure 7, would seem to indicate that for low frequencies, jet-surface interaction or dipole noise (which should peak normal to the flap surface) predominates for the low-velocity cases, and quadrupole or flow noise (which should peak in the aft direction) predominates for high-velocity cases. Since there is an apparent rotation of the directivity pattern with changing flap angle for low frequencies, the noise most likely is associated with the trailing edge itself rather than with some other source.

Figure 9 presents a comparison of one-third-octave band spectra for the 72° and 32° flaps at positions above and below the model and at the sideline off the wing tip for full engine thrust. In general, there is not much difference between the noise spectra at the two flap settings. There is a slight difference in the low-frequency range at all three

microphone positions which could indicate that there is slightly more low-frequency flow-surface interaction noise generated for the 72° flaps than for the 32° flaps in these particular directions.

Noise data were also taken with and without airflow in order to ascertain possible "forward speed" effects on the radiated noise. The data were taken by a microphone placed out of the airstream (see reference microphone in fig. 1) to eliminate any noise from airflow over the microphone itself. The data shown in figure 10 indicated little or no change in the noise with forward speed. It should be noted that the tunnel velocity was relatively low (14 m/sec (46 ft/sec)), being dictated by scaling requirements of the performance and loads investigations. Consequently, the small effect of forward speed in this investigation is not unexpected.

Comparison With Other Test Data

In an effort to establish the applicability of the acoustic data to past and future USB configurations, the one-third-octave band spectral data were normalized by the magnitude of the noise signal or OASPL, and the frequency was nondimensionalized to Strouhal number. Results are presented in figure 11 for the 32° flap at $\theta = 134^{\circ}$. The magnitude of the one-third-octave band SPL's for each nozzle exit velocity was converted to a normalized spectral density $\left(\text{SPL} - \text{OASPL} + 10 \log \frac{V}{D\Delta f}\right)$, where Δf is the bandwidth for each of the respective one-third-octave bands, D is the equivalent nozzle diameter, and V is the average nozzle exit velocity. In addition to the present data, results are shown from reference 5 which summarized previous tests of both small- and large-scale circular-nozzle USB models. The present data collapsed into a narrow band when normalized in this fashion. The data also agree very well with those of reference 5 for Strouhal numbers less than 5. For higher Strouhal numbers (higher frequencies) there is a marked difference. In view of the differences in the test hardware of the previous studies, however, it is apparent that the addition of a turbofan engine (with its high-frequency fan noise) to the wing-flap system accounts for this difference. The agreement at the low end of the spectrum would indicate that the flow and flow-surface interaction noise are essentially independent of the upstream source of the jet flow. Whether air is supplied by a compressed-air system or a jet engine, the spectrum shape at low Strouhal numbers is about the same. The good agreement in the data at low Strouhal numbers implies that similar flow spreading and turning were accomplished. Flow surveys of circular nozzles with large-angle deflector plates, such as described in reference 5, yield results similar to those for rectangular nozzles. This similarity most likely accounts for the good agreement in figure 11.

SUMMARY OF RESULTS

Acoustic results have been presented from static and simulated low-forward-speed tests of a large-scale upper-surface blowing model of an aircraft configuration with turbofan engines in the Langley full-scale tunnel. Narrow-band analyses of power spectral density revealed a large low-frequency contribution to the overall power, which is believed to be associated with flow-surface interactions. Fan blade tones contributed prominently to the power at the higher frequencies. One-third-octave band plots at various angular positions relative to the wing trailing edge showed lower noise levels, especially at high frequencies, as the position varied from above to below the wing. Overall sound pressure levels indicated the reduction was of the order of 15 dB. Both low-frequency (<300 Hz) directivity patterns and variations of sound pressure level (SPL) with velocity (or thrust) suggested that the noise was mainly dipole related and dependent on the flap angle at low thrust settings and quadrupole or flow related at high thrust settings. The 72° flaps produced slightly higher noise levels at full thrust than the 32° flaps above, below, and to the sideline. The effects of forward speed were undetectable at the low tunnel speeds used in this investigation. Normalized SPL spectral density showed good agreement at low Strouhal number with other data from tests using simulated upper-surface blown configurations.

REFERENCES

1. Maglieri, Domenic J.; and Hubbard, Harvey H.: Preliminary Measurements of the Noise Characteristics of Some Jet-Augmented-Flap Configurations. NASA MEMO 12-4-58L, 1959.

2. Gibson, Frederick W.: Noise Measurements of Model Jet-Augmented Lift Systems. NASA TN D-6710, 1972.

3. Reshotko, Meyer; Olsen, William A.; and Dorsch, Robert G.: Preliminary Noise Tests of the Engine-Over-the-Wing Concept. I. 30^{o}-60^{o} Flap Position. NASA TM X-68032, 1972.

4. Reshotko, Meyer; Olsen, William A.; and Dorsch, Robert G.: Preliminary Noise Tests of the Engine-Over-the-Wing Concept. II. 10^{o}-20^{o} Flap Position. NASA TM X-68104, 1972.

5. Reshotko, Meyer; Goodykoontz, Jack H.; and Dorsch, Robert G.: Engine-Over-the-Wing Noise Research. J. Aircr., vol. 11, no. 4, Apr. 1974, pp. 195-196.

6. Von Glahn, U.; Reshotko, M.; and Dorsch, R.: Acoustic Results Obtained With Upper-Surface-Blowing Lift-Augmentation Systems. NASA TM X-68159, 1972.

7. Dorsch, Robert G.; Kreim, Walter J.; and Olsen, William A.: Externally-Blown-Flap Noise. AIAA Paper No. 72-129, Jan. 1972.

8. Abrahamson, A. L.; Kasper, P. K.; and Pappa, R. S.: Acoustical Characteristics of the NASA – Langley Full-Scale Wind Tunnel Test Section. NASA CR-132604, 1975.

9. Shivers, James P.; and Smith, Charles C., Jr.: Static Tests of a Simulated Upper Surface Blown Jet-Flap Configuration Utilizing a Full-Size Turbofan Engine. NASA TN D-7816, 1975.

10. Dorsch, Robert G.; Lasagna, Paul L.; Maglieri, Domenic J.; and Olsen, William A.: Flap Noise. Aircraft Engine Noise Reduction, NASA SP-311, 1972, pp. 259-290.

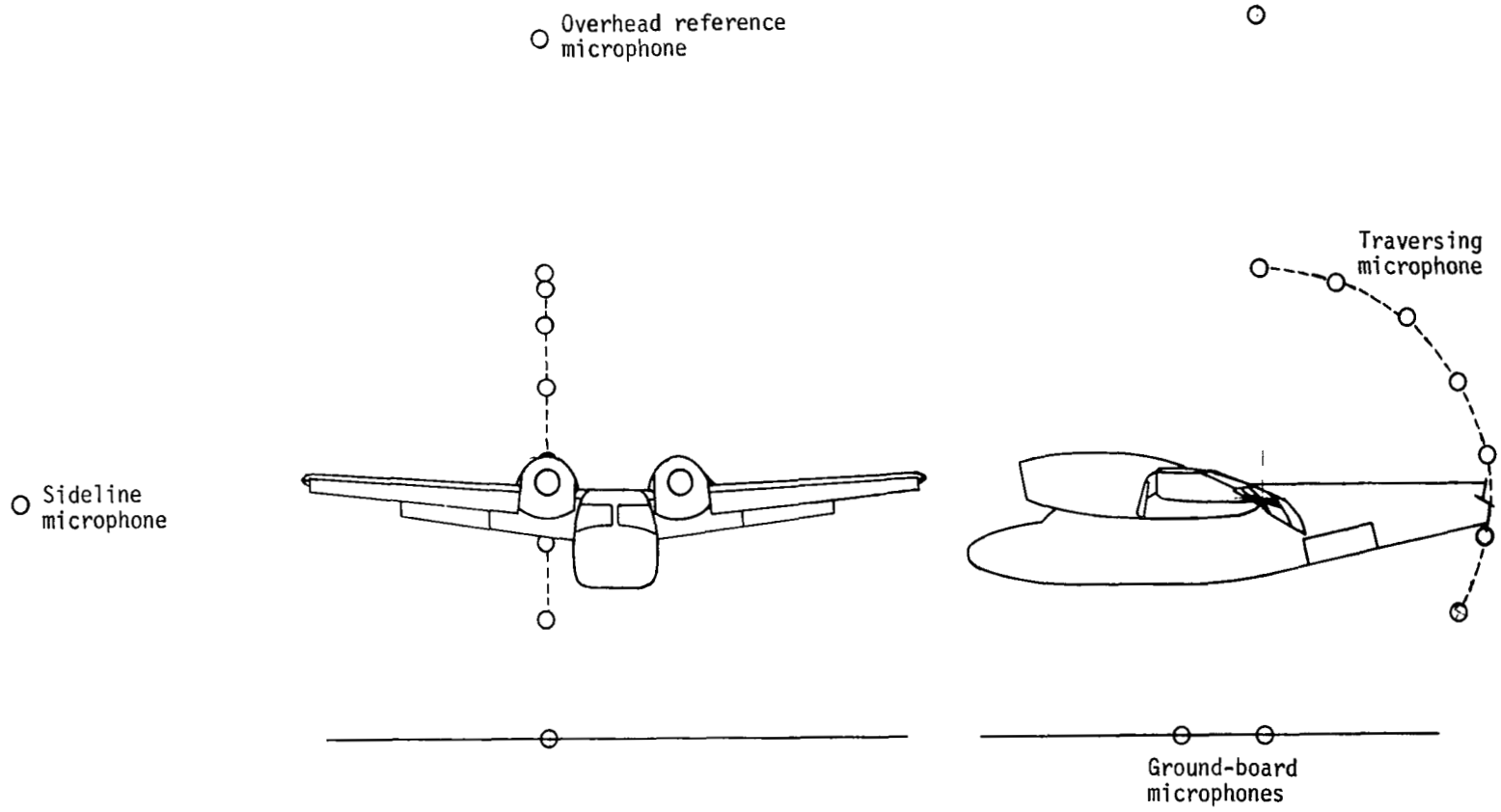

Figure 1.- Sketch of model and microphone locations.

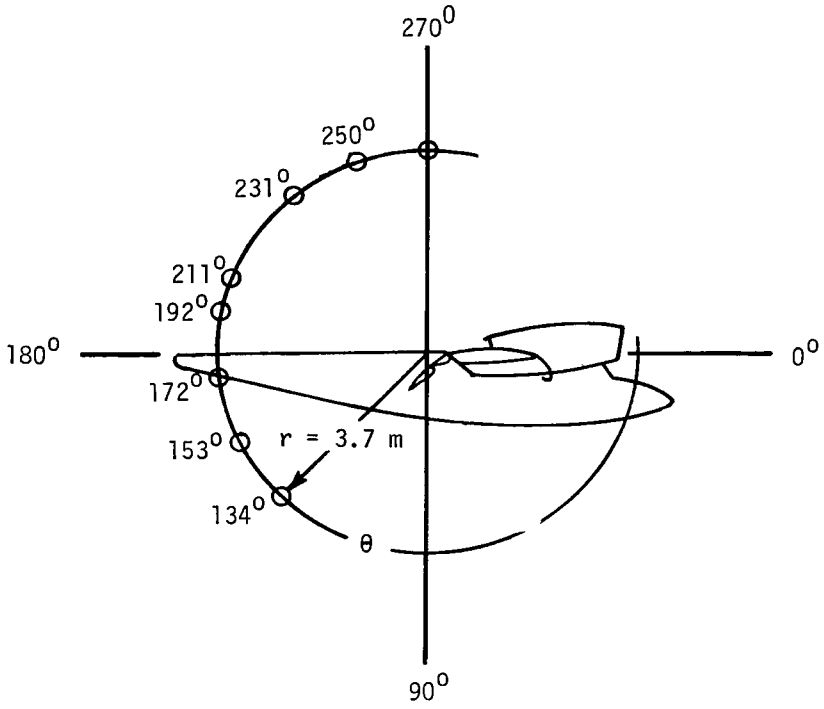

Figure 2.- Coordinate system for microphone locations.

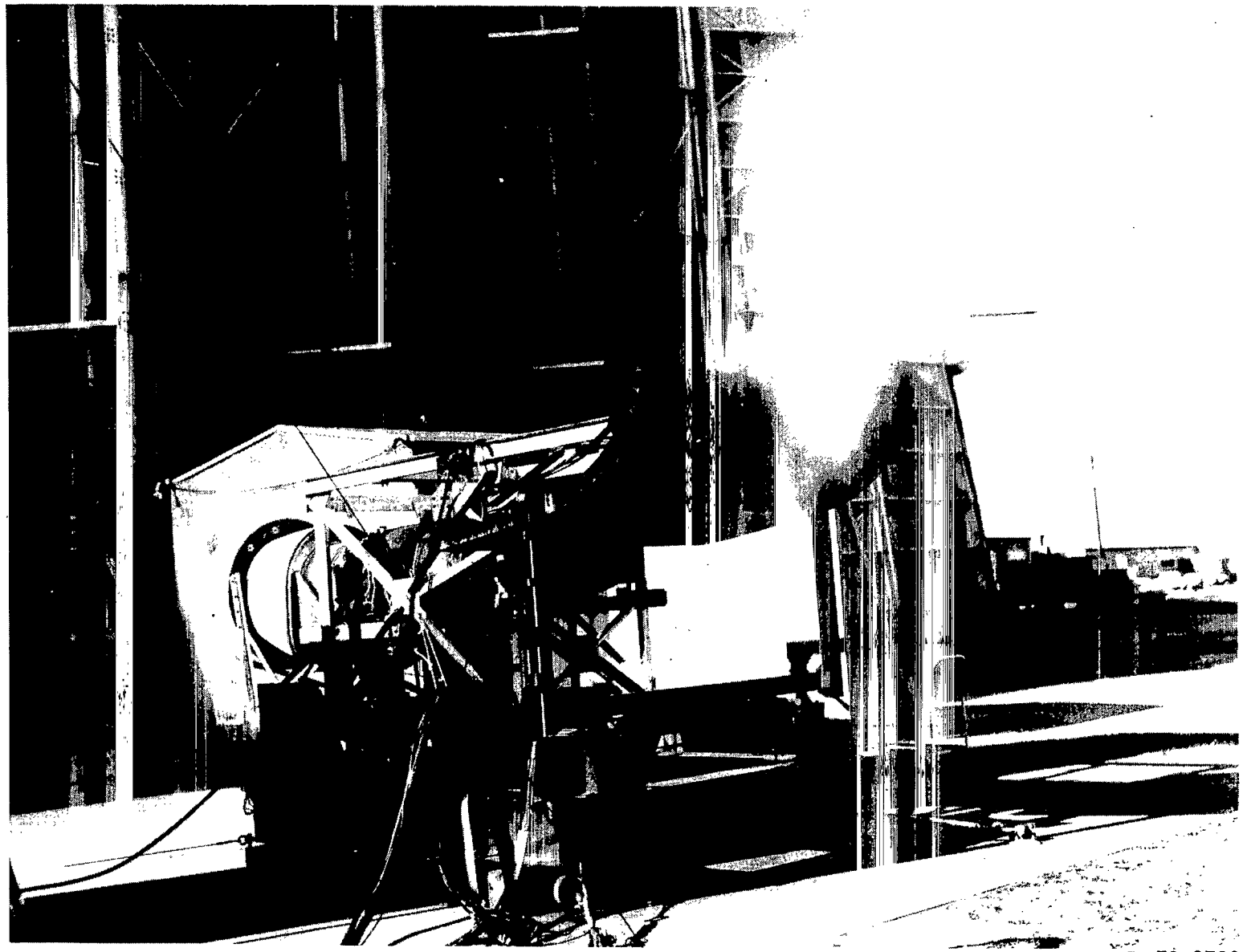

L-73-8709

Figure 3.- Outdoor static test setup.

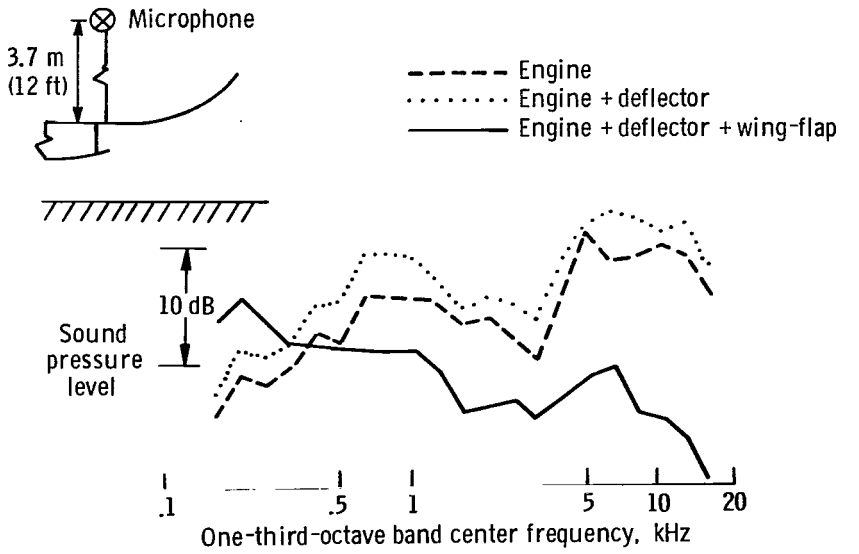

Figure 4.- Sound pressure level under the wing for various system components from outdoor static tests. $\delta_f = 72^o$; engine thrust, 5850 N (1300 lb).

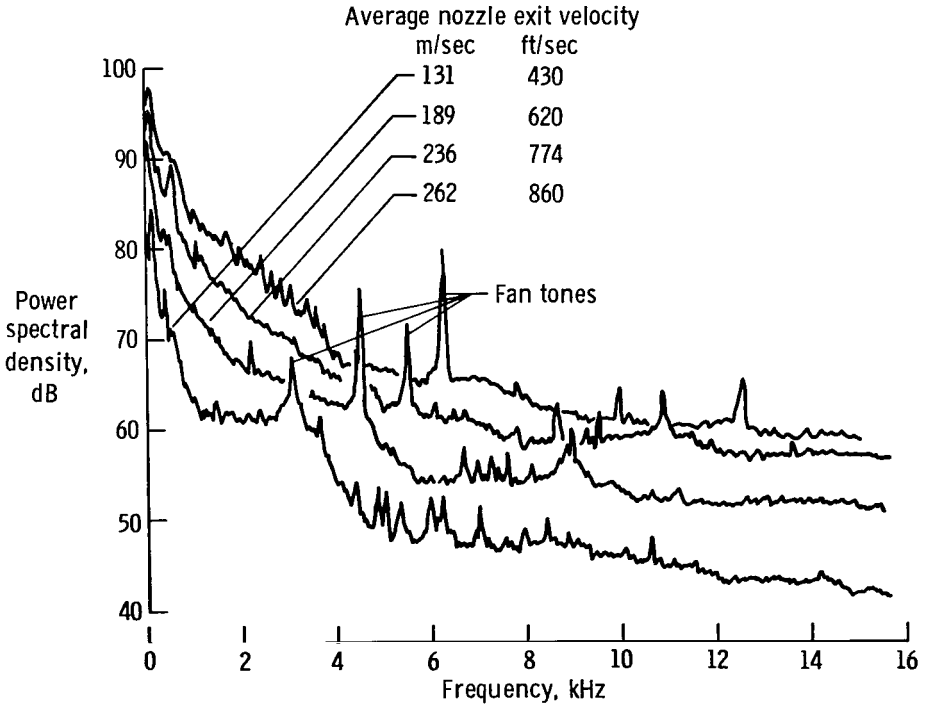

Figure 5.- Narrow-band plots of power spectral density for the most forward under-the-wing microphone position for various thrust conditions. $\delta_f = 32^o$.

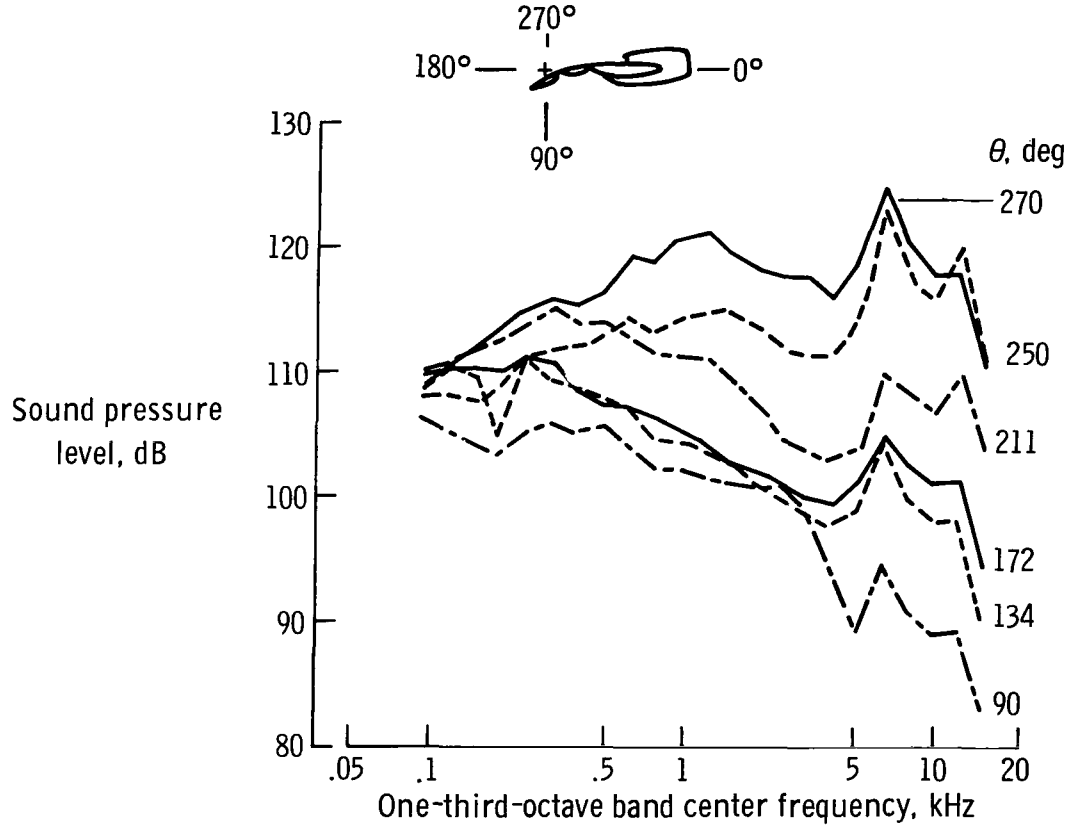

Figure 6.- Sound-pressure-level spectra at various angular positions from jet engine axis. $\delta_f = 32^o$; engine thrust, 5850 N (1300 lb).

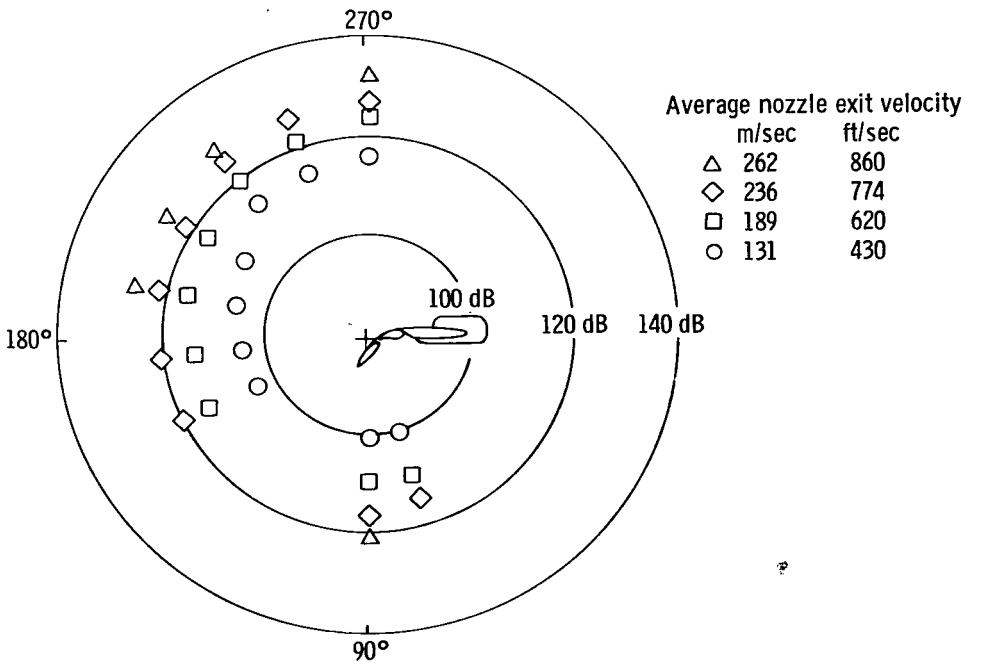

(a) OASPL, $\delta_f = 72^o$.

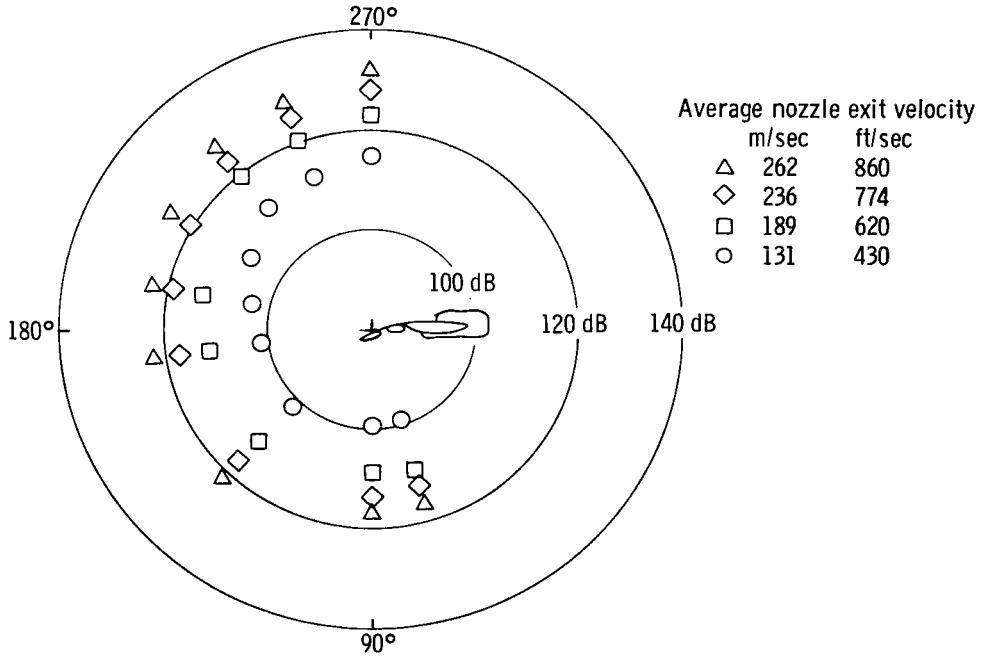

(b) OASPL, $\delta_f = 32^o$.

Figure 7.- Directivity plots. r = 3.7 m (12 ft).

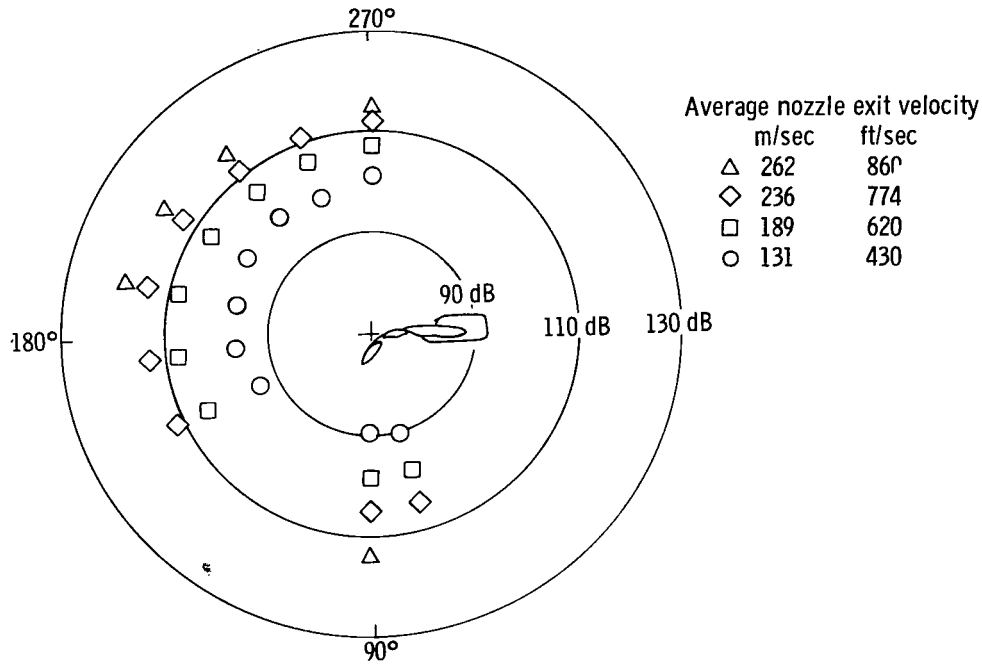

(c) Low-frequency (<300 Hz) directivity. $\delta_f = 72^o$.

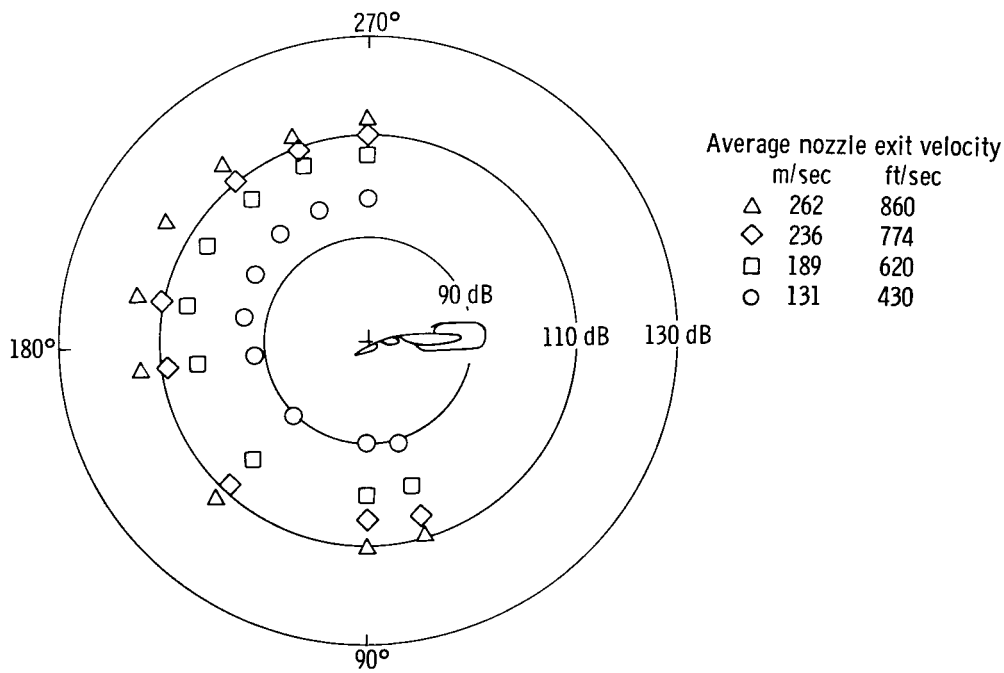

(d) Low-frequency (<300 Hz) directivity. $\delta_f = 32^o$.

Figure 7.- Continued.

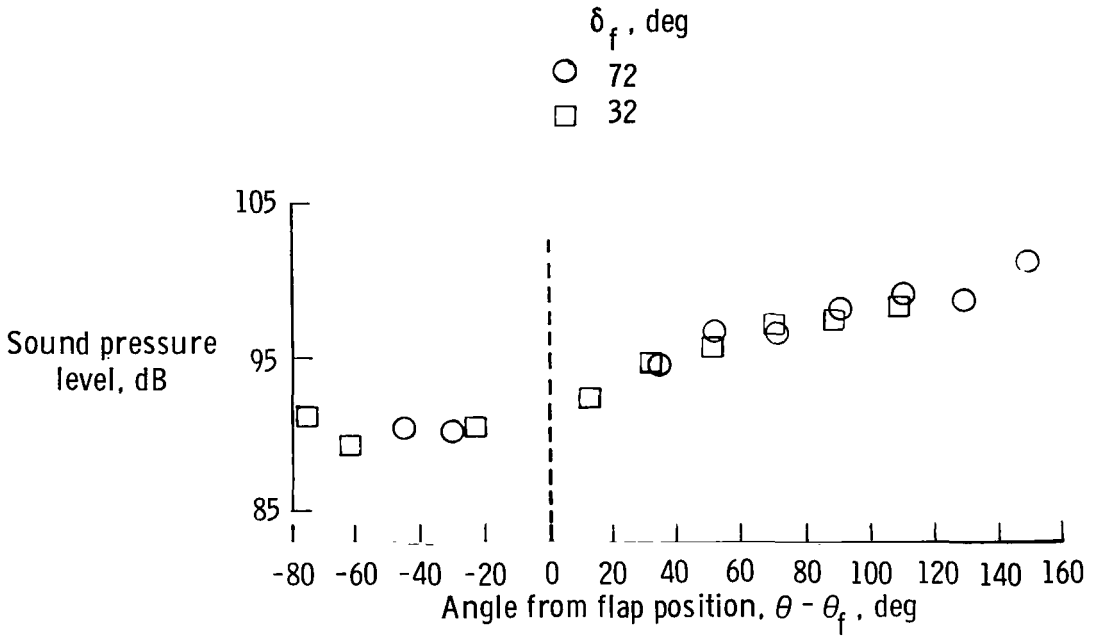

(e) Comparison of low-frequency (<300 Hz), low-velocity (131 m/sec (430 ft/sec)) directivity for 72^o and 32^o flaps relative to their respective flap position.

Figure 7.- Concluded.

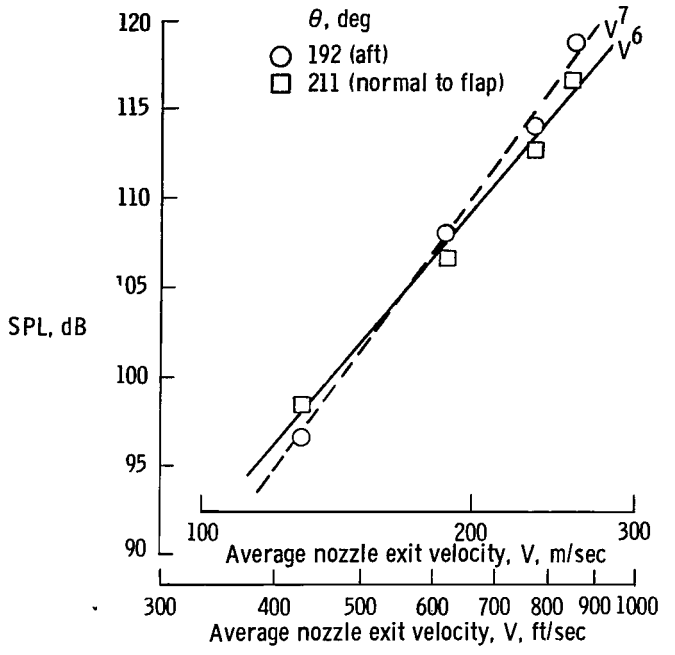

(a) $\delta_f = 72^o$.

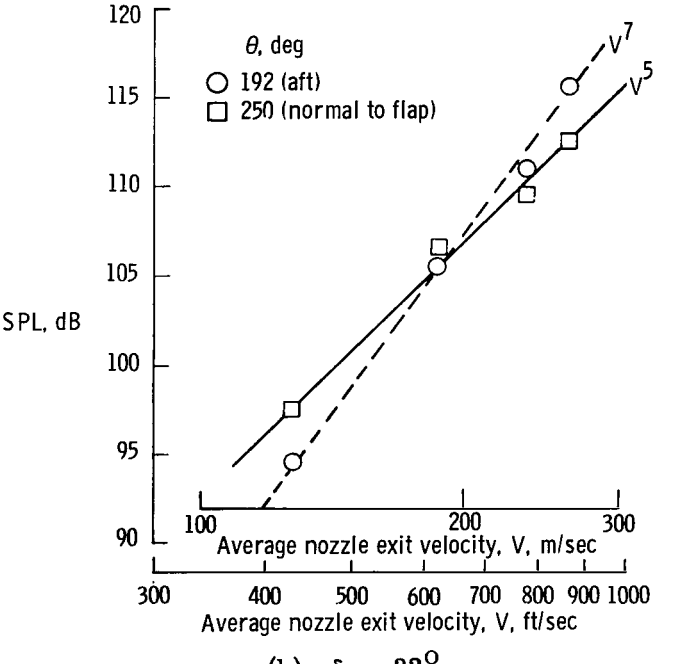

(b) $\delta_f = 32^o$.

Figure 8.- Effect of nozzle exit velocity on low-frequency (<300 Hz) sound pressure level at selected microphone positions.

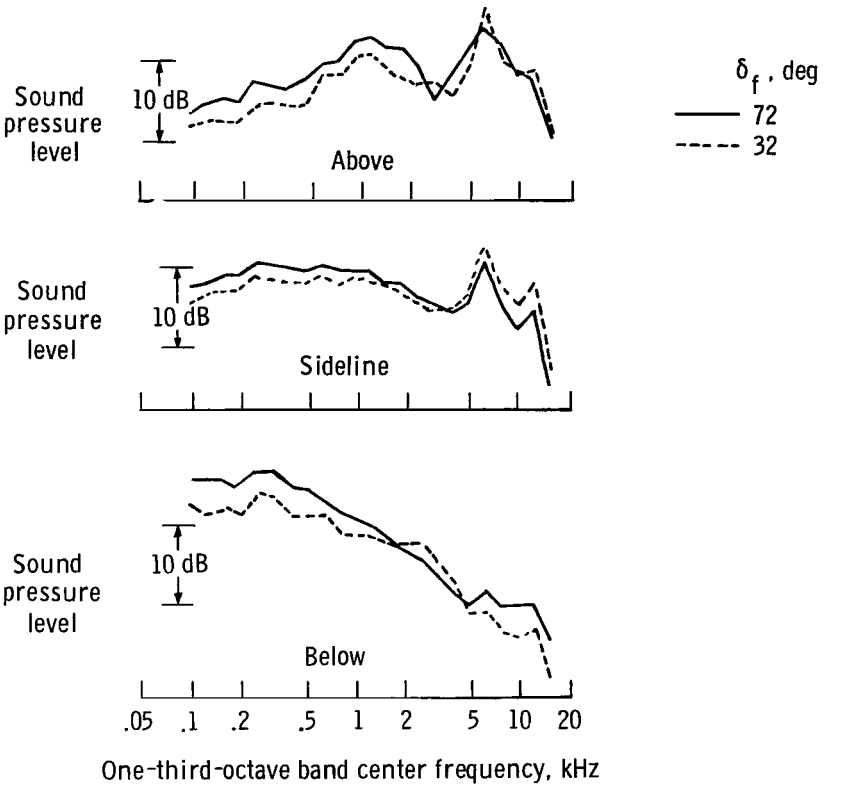

Figure 9.- Comparison of one-third-octave band spectra between different flaps at various microphone positions.

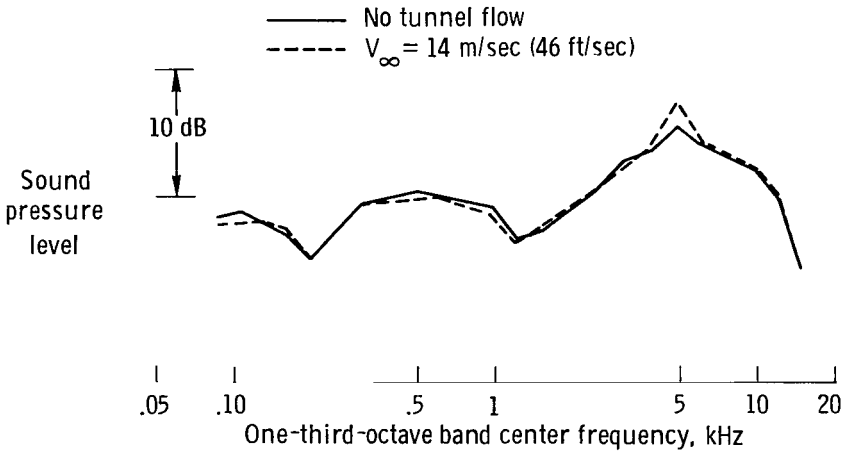

Figure 10.- Comparison of sound-pressure-level spectra with and without tunnel flow. $\delta_f = 72^o$; engine thrust, 1450 N (325 lb); $\theta = 270^o$.

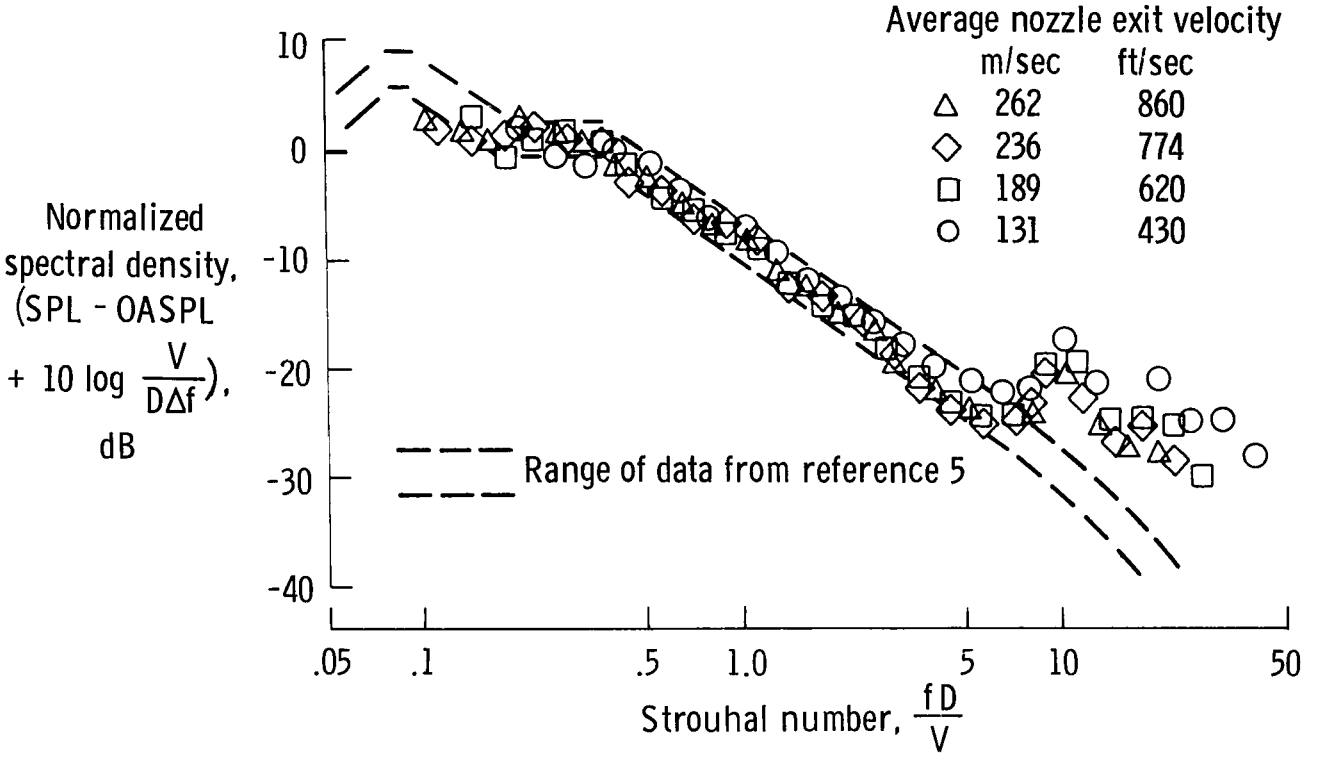

Figure 11.- Normalized spectral density as function of Strouhal number. $\delta_f = 32^o$; $\theta = 134^o$.

NATIONAL AERONAUTICS AND SPACE ADMINISTRATION
WASHINGTON, D.C. 20546

OFFICIAL BUSINESS
PENALTY FOR PRIVATE USE $300

SPECIAL FOURTH-CLASS RATE
BOOK

POSTAGE AND FEES PAID
NATIONAL AERONAUTICS AND
SPACE ADMINISTRATION
451

U.S.MAIL

POSTMASTER: If Undeliverable (Section
Postal Manual) Do Not Re

"The aeronautical and space activities of the United States shall be conducted so as to contribute . . . to the expansion of human knowledge of phenomena in the atmosphere and space. The Administration shall provide for the widest practicable and appropriate dissemination of information concerning its activities and the results thereof."

—NATIONAL AERONAUTICS AND SPACE ACT OF 1958

NASA SCIENTIFIC AND TECHNICAL PUBLICATIONS

TECHNICAL REPORTS: Scientific and technical information considered important, complete, and a lasting contribution to existing knowledge.

TECHNICAL NOTES: Information less broad in scope but nevertheless of importance as a contribution to existing knowledge.

TECHNICAL MEMORANDUMS: Information receiving limited distribution because of preliminary data, security classification, or other reasons. Also includes conference proceedings with either limited or unlimited distribution.

CONTRACTOR REPORTS: Scientific and technical information generated under a NASA contract or grant and considered an important contribution to existing knowledge.

TECHNICAL TRANSLATIONS: Information published in a foreign language considered to merit NASA distribution in English.

SPECIAL PUBLICATIONS: Information derived from or of value to NASA activities. Publications include final reports of major projects, monographs, data compilations, handbooks, sourcebooks, and special bibliographies.

TECHNOLOGY UTILIZATION PUBLICATIONS: Information on technology used by NASA that may be of particular interest in commercial and other non-aerospace applications. Publications include Tech Briefs, Technology Utilization Reports and Technology Surveys.

Details on the availability of these publications may be obtained from:

SCIENTIFIC AND TECHNICAL INFORMATION OFFICE

NATIONAL AERONAUTICS AND SPACE ADMINISTRATION

Washington, D.C. 20546